

**Visualization of *Staphylococcus aureus* infections and antibiotic therapy by bioluminescence and  $^{19}\text{F}$  magnetic resonance imaging with perfluorocarbon emulsions**

**Darstellung von *Staphylococcus aureus* Infektionen und Antibiotikatherapie durch Biolumineszenzbildgebung und  $^{19}\text{F}$ -Kernspintomografie mit Perfluorcarbon-Emulsionen**



Doctoral thesis for a doctoral degree  
at the Graduate School of Life Sciences (GSL),

University of Würzburg

Section: Infection and Immunity

Submitted by Tobias Hertlein

from Gunzenhausen, Germany

Würzburg, 2014

**Submitted on:**

**Members of the Supervisory Committee:**

Chairperson:	Prof. Dr. Thomas Dandekar
Primary Supervisor:	PD Dr. Knut Ohlsen
Supervisor (Second):	Prof. Dr. Peter Jakob
Supervisor (Third):	Prof. Dr. Dr. Bhanu Sinha
Supervisor (Fourth) (if applicable):	

**Date of Public Defense:**

**Date of receipt of Certificate:**

**Eingereicht am:**

**Mitglieder des Promotionskomitees:**

Vorsitzender:	Prof. Dr. Thomas Dandekar
1. Gutachter:	PD Dr. Knut Ohlsen
2. Gutachter:	Prof. Dr. Peter Jakob
3. Gutachter:	Prof. Dr. Dr. Bhanu Sinha
4. Gutachter (falls zutreffend):	

**Tag des Promotionskolloquiums:**

**Doktorurkunde ausgehändigt am:**

## **Affidavit**

I hereby confirm that my thesis entitled “Visualization of *Staphylococcus aureus* infections and antibiotic therapy by bioluminescence and <sup>19</sup>F magnetic resonance imaging with perfluorocarbon emulsions” is the result of my own work. I did not receive any help or support from commercial consultants. All sources and/or materials applied are listed and specified in the thesis.

Furthermore, I confirm that this thesis has not been submitted as a part of another examination process neither in identical nor similar form.

Würzburg,

## **Eidesstattliche Erklärung**

Hiermit erkläre ich an Eides statt, die Dissertation „Darstellung von *Staphylococcus aureus* Infektionen und Antibiotikatherapie durch Biolumineszenzbildgebung und <sup>19</sup>F-Kernspintomografie mit Perfluorcarbon Emulsionen“ eigenständig, d.h. insbesondere selbständig und ohne Hilfe eines kommerziellen Promotionsberaters, angefertigt und keine anderen als die von mir angegebenen Quellen und Hilfsmittel verwendet zu haben.

Ich erkläre außerdem, dass die Dissertation weder in gleicher noch in ähnlicher Form bereits in einem anderem Prüfungsverfahren vorgelegen hat.

Würzburg,



***Meinen Eltern gewidmet***



## *Danksagung*

Am Ende meiner Doktorarbeit möchte ich die Gelegenheit nutzen und die tief empfundene Dankbarkeit gegenüber allen ausdrücken ohne deren Hilfe ich diesen Weg nicht hätte beschreiten können. Zuallererst will ich meinem Doktorvater PD Dr. Knut Ohlsen für seinen hilfreichen Rat und seine großartige Unterstützung während der vergangenen Jahre danken. Darüber hinaus möchte ich auch meinen Dank gegenüber den Mitgliedern meines Promotionskomitees, Prof. Dr. Peter Jakob und Prof. Dr. Dr. Bhanu Sinha, für die vielen wertvollen Hinweise und interessanten Diskussionen ausdrücken. Besonders möchte ich auch Volker Sturm danken, der mich während dieser Zeit als ‚physikalischer Gegenpart‘ begleitet hat, mir eine andere Sichtweise auf unser gemeinsames Projekt ermöglichte und mit dem ich einige schlaflose Nächte vor ‚unserem Biospec‘ verbringen durfte.

Zu großem Dank verpflichtet bin ich der Arbeitsgruppe von Herrn Prof. Dr. Aladar Szalay, insbesondere Dr. Jochen Stritzker und Dr. Stephanie Weibel, für die freundliche Hilfe bei der Unterbringung und Handhabung der Versuchstiere am Biozentrum.

Des Weiteren möchte ich Dr. Stefan Kircher und Dr. Martin Wartenberg für die Unterstützung bei der Herstellung der histologischen Proben und deren anschließender Analyse danken.

Bei Bharat Biotech, insbesondere Frau Dr. Kandaswamy Sumathy bedanke ich mich für die Bereitstellung des rekombinanten Lysostaphins.

Zudem bedanke ich mich bei Dipl.-Chem. Peter Buschmann und Frau Prof. Dr. Anke Krüger für die Größenbestimmung der selbst hergestellten Perfluorcarbon-Emulsionen.

Als ‚Wanderer‘ zwischen zwei Instituten war es mir zudem eine Freude und ein großer Nutzen eine Vielzahl verschiedener Menschen kennenzulernen, die auf die eine oder andere Weise Einfluss auf den Erfolg dieser Arbeit hatten. Leider erscheint es mir unmöglich, alle in diesem Rahmen aufzulisten, doch Einigen möchte ich im Speziellen danken (Nachnahmen in alphabetischer Reihenfolge): Dr. Thomas Basse-Lüsebrink, Christina Daumberger, Dr. Markus Haake, Marcel Jarick, Thomas Kampf, Alexandra König, Dr. Stefanie Krieger, Birgit Lorenz, Dr. Udo Lorenz, Dr. Thomas Menzel, Babett Oesterreich, Annika Parg, Dr. Tina Schäfer, Dr. Tim Schmitter, Martina Selle, Sabine Voll, Uschi Wallner.

Bedanken möchte ich mich auch beim Sonderforschungsbereich 630, dem Institut für Molekulare Infektionsbiologie und der Graduate School of Life Sciences für das hervorragende Arbeitsumfeld, die umfangreiche Unterstützung und die vielfältigen Möglichkeiten.

Vor allem aber möchte ich mich für die Unterstützung meiner Eltern, Schwester und meiner Verlobten Michaela Gilch bedanken, die mir während der letzten Jahre Liebe, Unterstützung und Rückhalt boten, durch alle Höhen und Tiefen der Doktorarbeit und des Lebens.





# Content

Abbreviations.....	1
Abstract .....	2
Zusammenfassung.....	5
<b>1. Introduction.....</b>	<b>8</b>
1.1. Infectious diseases in the 21 <sup>st</sup> century .....	8
1.2. <i>Staphylococcus aureus</i> – a versatile pathogen.....	10
1.3. Preclinical testing and In Vivo Imaging? .....	20
1.4. Aim of this thesis .....	24
<b>2. Materials .....</b>	<b>25</b>
2.1. Chemicals and consumables .....	25
2.2. Kits .....	25
2.3. Antibacterial compounds .....	25
2.4. Instruments .....	26
2.5. Culture media and plates .....	27
2.6. Bacteria.....	27
2.7. Buffers and solutions.....	27
2.8. Contrast agents and tracer .....	28
2.9. Software .....	29
<b>3. Methods.....</b>	<b>30</b>
3.1. General methods.....	30
3.2. Minimal inhibitory concentration testing (MIC).....	30
3.3. Animal models.....	31
3.3.1. Ethics statement.....	31
3.3.2. Thigh infection model.....	31
3.3.3. Catheter related infection model.....	33
3.3.4. Determination of colony forming units.....	34
3.4. In vivo Bioluminescence and Fluorescence Imaging .....	35
3.5. Magnetic Resonance Imaging .....	37
3.6. Histology.....	39
3.7. Perfluorocarbon particle emulgation .....	41
3.8. Flow cytometry.....	42
3.9. Cell sorting.....	43
3.10. Determination of cytokine/chemokine levels.....	45

3.11.	Data analysis and statistics.....	48
<b>4.</b>	<b>Imaging of <i>Staphylococcus aureus</i> infections.....</b>	<b>49</b>
4.1.	Results .....	50
4.1.1.	The <i>S. aureus</i> thigh infection model.....	50
4.1.2.	Native, proton-based magnetic resonance imaging .....	53
4.1.3.	Imaging of iron oxide (CLIO) particles at the site of infection.....	55
4.1.4.	The accumulation mechanism of perfluorocarbon emulsion at the site of infection...	57
4.1.5.	Perfluorocarbon administration does not change the fundamental parameters of infection .....	89
4.2.	Discussion .....	94
<b>5.</b>	<b>Imaging of antibiotic therapy with bioluminescence and <sup>19</sup>F magnetic resonance imaging with perfluorocarbon emulsions.....</b>	<b>110</b>
5.1.	Results .....	111
5.1.1.	Bioluminescence imaging of antibacterial therapy.....	111
5.1.2.	Reduction of bacterial burden by vancomycin or linezolid.....	112
5.1.3.	<sup>19</sup> F MRI of perfluorocarbon emulsion accumulation at the site of infection during antibiotic therapy .....	113
5.1.4.	Quantification of <sup>19</sup> F accumulation volume and signal at the site of infection.....	114
5.2.	Discussion .....	116
<b>6.</b>	<b>Evaluation of lysostaphin efficacy in murine thigh and catheter-related infection models by bioluminescence and <sup>19</sup>F magnetic resonance imaging.....</b>	<b>120</b>
6.1.	Results .....	120
6.1.1.	In vitro activity of lysostaphin against <i>S. aureus</i> .....	120
6.1.2.	Lysostaphin reduced the bacterial burden in the thigh infection model.....	121
6.1.3.	Lysostaphin reduced the bioluminescence signal in the thigh infection model.....	122
6.1.4.	<sup>19</sup> F MR imaging of perfluorocarbon accumulation in the infected thigh muscle.....	124
6.1.5.	Reduction of bacterial burden in the catheter-associated infection model by antibiotic treatment .....	128
6.1.6.	Bioluminescent signal development in the catheter-associated infection model.....	130
6.2.	Discussion .....	132
<b>7.</b>	<b>Influence of antibiotic therapy on immune response.....</b>	<b>140</b>
7.1.	<i>Staphylococcus aureus</i> Xen29 thigh infection model.....	140
7.1.1.	Reduction of bacterial burden by treatment with either vancomycin, oxacillin, linezolid or minocycline .....	140
7.1.2.	Influence of antibacterial treatment on the levels of various cytokines and chemokines at the site of infection .....	142
7.2.	Thigh infection model with ca-MRSA <i>S. aureus</i> Lac (USA300) .....	147

7.2.1.	Influence of antibacterial treatment with either vancomycin, oxacillin, linezolid or minocycline on bacterial burden.....	147
7.2.2.	Imaging of myeloperoxidase activity at the site of infection with luminol.....	149
7.2.3.	Cytokine and chemokine levels at the site of infection .....	150
7.3.	Discussion .....	154
<b>8.</b>	<b>Conclusion and Outlook .....</b>	<b>160</b>
<b>9.</b>	<b>Literature.....</b>	<b>164</b>
	Curriculum Vitae.....	186



## Abbreviations

BL:	Bioluminescence
BLI:	Bioluminescence Imaging
ca-MRSA:	Community-acquired Meticillin resistant <i>Staphylococcus aureus</i>
CCD:	Charge coupled device
CFU:	Colony forming units
CLIO:	Cross-linked iron oxide nanoparticles
CSI:	Chemical Shift Imaging (MRI Sequence)
d:	day
DOPE:	1,2-Dioleoyl-sn-glycero-3-phosphoethanolamine
FL:	Fluorescence
FLI:	Fluorescence Imaging
ha-MRSA:	Hospital-acquired Meticillin resistant <i>Staphylococcus aureus</i>
HE:	Hematoxylin – Eosin staining
IVIS:	In Vivo Imaging System (Bioluminescence and Fluorescence Imaging platform)
la-MRSA:	Livestock-associated Meticillin resistant <i>Staphylococcus aureus</i>
MR:	Magnetic Resonance
MRI:	Magnetic Resonance Imaging
MRSA:	Meticillin resistant <i>Staphylococcus aureus</i>
NaCl:	Sodium chloride solution
p.a.:	post administration
PFC:	Perfluorocarbon emulsion
p.i.:	post infection
<i>S. aureus</i> :	<i>Staphylococcus aureus</i>
SSFP:	Steady-state free precession
TSE:	Turbo Spin Echo (MRI Sequence)
USPIO:	Ultrasmall paramagnetic iron oxide nanoparticles
VISA:	Vancomycin intermediate <i>Staphylococcus aureus</i>
VRSA:	Vancomycin resistant <i>Staphylococcus aureus</i>

## Abstract

*Staphylococcus aureus* is a major threat to public health systems all over the globe. This second most cause of nosocomial infections is able to provoke a wide variety of different types of infection in humans and animals, ranging from superficial skin and skin structure infections to invasive disease like sepsis or pneumonia. But not enough, this pathogen is also notorious in acquiring and/or developing resistance to antimicrobial compounds, thus limiting available treatment options severely. Therefore, development of new compounds and strategies to fight *S. aureus* is of paramount importance. But since only 1 out of 5 compounds, which entered clinical trials, becomes a drug, the preclinical evaluation of promising compounds has to be reconsidered, too. The aim of this thesis was to address both sides of this problem: first, to improve preclinical testing by incorporating in vivo imaging technologies to the preclinical testing procedure in order to acquire additional and clearer data about efficacy of promising compounds and second, by evaluating lysostaphin, which is a promising, new option to fight *S. aureus* infections.

The first aim of this thesis focused on the establishment of a dual modality in vivo imaging platform, consisting of Bioluminescence Imaging (BLI) and Magnetic Resonance Imaging (MRI), to offer detailed insights into the course and gravity of *S. aureus* infection in the murine thigh infection model. Since luciferase-expressing *S. aureus* strains were generated in former studies and enabled thus bioluminescence imaging of bacterial infection, this technology should be implemented into the compound evaluation platform in order to non-invasively track the bacterial burden over time. MRI, in contrast, was only rarely used in earlier studies to visualize and measure the course of infection or efficacy of anti-bacterial therapy. Thus, the first set of experiments was performed to identify benefits and drawbacks of visualizing *S. aureus* infections in the mouse model by different MR methods. Native, proton-based MR imaging showed in this regard increased T<sub>2</sub> relaxation times in the infected thigh muscles, but it was not possible to define a clear border between infected and uninfected tissue. Iron oxide nanoparticles and perfluorocarbon emulsions, two MR contrast agents or tracer, in contrast, offered this distinction. Iron oxide particles were detected in this regard by their distortion of <sup>1</sup>H signal in proton-based MRI, while perfluorocarbon emulsion was identified by <sup>19</sup>F MRI. Mammals do not harbor sufficient intrinsic amounts of <sup>19</sup>F to deliver specific signal and therefore, <sup>19</sup>F MR imaging visualizes only the signal of administered perfluorocarbon emulsion. The in vivo accumulation of perfluorocarbon emulsion can be imaged by <sup>19</sup>F MRI and overlaid on a simultaneously acquired <sup>1</sup>H MR image, which shows the anatomical context in clear detail. Since this is advantageous compared to contrast agent based MR methods like iron oxide particle-based MRI, further experiments were performed with perfluorocarbon emulsions and <sup>19</sup>F MRI.

Experimental studies to elucidate the accumulation of perfluorocarbon emulsion at the site of infection showed robust <sup>19</sup>F MR signals after administration between day 2 and at least day 8 p.i.. Perfluorocarbon emulsion accumulated in all investigated mice in the shape of a

'hollow sphere' at the rim of the abscess area and the signal remained stable as long as the infection prevailed. In order to identify the mechanism of accumulation, flow cytometry, cell sorting and histology studies were performed. Flow cytometry and cell sorting analysis of immune cells at the site of infection showed that neutrophils, monocytes, macrophages and dendritic cells carried contrast media at the site of infection with neutrophils accounting for the overwhelming portion of perfluorocarbon signal. In general, most of the signal was associated with immune cells, thus indicating specific immune cell dependent accumulation. Histology supported this observation since perfluorocarbon emulsion related fluorescence could only be visualized in close proximity to immune cell nuclei.

After establishing and testing of  $^{19}\text{F}$  MRI with perfluorocarbon emulsions as infection imaging modality, the effects of antibiotic therapy upon MR signal was investigated in order to evaluate the capability of this modality for preclinical testing procedure. Thus, the efficacy of vancomycin and linezolid, two clinically highly relevant anti - *S. aureus* compounds, were tested in the murine thigh infection model. Both of them showed reduction of the colony forming units and bioluminescence signal, but also of perfluorocarbon emulsion accumulation strength and volume at the site of infection, which was visualized and quantified by  $^{19}\text{F}$  MRI. The efficacy pattern with linezolid being more efficient in clearing bacterial infection was shown similarly by all three methods. In consequence,  $^{19}\text{F}$  MRI with perfluorocarbon emulsion as MR tracer proved to be capable to visualize antibacterial therapy in preclinical testing models.

The next step was consequently to evaluate a promising new compound against *S. aureus* infections. Thus, lysostaphin, an endo-peptidase that cleaves the cell wall of *S. aureus*, was tested in different concentrations alone or in combination with oxacillin for efficacy in murine thigh and catheter associated infection models. Lysostaphin only in the concentration of 5 mg/kg body weight or combined with oxacillin in the concentration of 2 mg/kg showed strong reduction of bacterial burden by colony forming unit determination and bioluminescence imaging in both models. The perfluorocarbon accumulation was investigated in the thigh infection model by  $^{19}\text{F}$  MRI and was strongly reduced in terms of volume and signal strength in both above-mentioned groups. In general, lysostaphin showed comparable or superior efficacy than vancomycin or oxacillin alone. Therefore, further development of lysostaphin for the treatment of *S. aureus* infections is recommended by these experiments. Overall, the antibiotic efficacy pattern of all applied antibiotic regimens was similar with all three applied methods, demonstrating the usefulness of MRI for antibiotic efficacy testing. Importantly, treatment with oxacillin either alone or in combination with lysostaphin resulted in stronger perfluorocarbon emulsion accumulation at the site of infection than expected compared to the results from bioluminescence imaging and colony forming unit determination. This might be an indication for immunomodulatory properties of oxacillin.

Further murine infection experiments demonstrated in this context a differential release of cytokine and chemokines in the infected thigh muscle in dependence of the applied

antibacterial therapy. Especially treatment with oxacillin, but to a less degree with minocycline or linezolid, too, exhibited high levels of various cytokines and chemokines, although they reduced the bacterial burden efficiently. In consequence, possible immunomodulatory effects of antibacterial compounds have to be taken into account for future applications of imaging platforms relying on the visualization of the immune response. However, this observation opens a new field for these imaging modalities since it might be extraordinary interesting to study the immunomodulatory effects of compounds or even bacterial factors *in vivo*. And finally, a two modality imaging platform which combines methods to visualize on the one hand the bacterial burden and on the other hand the immune response offers an innovative, new platform to study host-pathogen interaction *in vivo* in a non-invasive fashion.

In summary, it could be shown that perfluorocarbon emulsions accumulate in immune cells at the site of infection in the murine *S. aureus* thigh infection model. The accumulation pattern shapes a 'hollow sphere' at the rim of the abscess area and its size and perfluorocarbon content is dependent on the severity of disease and/or efficacy of antibiotic therapy. Thus,  $^{19}\text{F}$  MRI with perfluorocarbon emulsions is a useful imaging modality to visualize sites and course of infection as well as to evaluate promising antibacterial drug candidates. Furthermore, since the accumulation of tracer depends on immune cells, it might be additionally interesting for studies regarding the immune response to infections, auto-immune diseases or cancer, but also to investigate the efficacy of immunomodulatory compounds and immunization.



## Zusammenfassung

*Staphylococcus aureus* ist als zweithäufigste Ursache nosokomialer Infektionen eine ernste Bedrohung für Gesundheitssysteme weltweit. Dieses Pathogen ist in der Lage eine Vielzahl verschiedener Krankheitsformen, von oberflächlichen Wund- und Gewebsinfektionen bis hin zu invasiven Erkrankungen wie Bakteriämie oder Pneumonie, in Mensch und Tier zu verursachen. Zudem erwies sich dieser Krankheitserreger in der Vergangenheit als höchst anpassungsfähig durch den Erwerb oder die Entwicklung von Resistenzen gegenüber antibakterieller Substanzen, wodurch die Verfügbarkeit wirksamer Therapiemöglichkeiten drastisch eingeschränkt wurde. Aus diesem Grund ist die Entwicklung neuer Antibiotika und Behandlungsstrategien gegen *S. aureus* Infektionen von enormem gesellschaftlichem Interesse. Da aber lediglich eine von fünf Substanzen, die in klinische Studien eintreten, später als Medikament zugelassen wird, sollte die präklinische Evaluierung neuer, vielversprechender Therapeutika ebenso verbessert und überdacht werden. Diese Doktorarbeit adressiert in diesem Zusammenhang beide Facetten: zum einen wurde durch Einbeziehung von in vivo Bildgebungstechnologien ein deutlicheres Bild von der Effizienz neuer Substanzen während der präklinischen Evaluierung ermöglicht, zum anderen wurde mit Lysostaphin eine neuartige Substanzklasse zur Behandlung von *S. aureus* Infektionen getestet.

Primärziel dieser Arbeit war deshalb die Entwicklung und Etablierung einer dualen Bildgebungsplattform bestehend aus Biolumineszenz- (BLI) und Kernspintomografischer (MRI) Bildgebung, um detaillierte Einblicke in Verlauf und Schwere von *S. aureus* Infektionen im Muskelinfektionsmodell der Maus zu ermöglichen. Die Biolumineszenzbildgebung bakterieller Infektionen wurde durch die Entwicklung von Luziferase-exprimierenden *S. aureus* Stämmen bereits in früheren Arbeiten ermöglicht und wurde in die Bildgebungsplattform integriert, um die Entwicklung der Bakterienlast nicht-invasiv verfolgen zu können. Kernspintomografie wurde in früheren Arbeiten hingegen kaum zur Darstellung der Effizienz anti-bakterieller Therapien während der Präklinik verwendet. Aus diesem Grund dienten die ersten Experimente zur Erkennung von Vor- und Nachteilen der Darstellung von *S. aureus* Infektionen im Tiermodell durch verschiedene Kernspintomografische Bildgebungsmethoden. Native, Protonen-basierte Kernspintomografie wies verlängerte T<sub>2</sub> Relaxationszeiten im infizierten Muskelgewebe nach, doch eine klare Eingrenzung des infizierten Bereiches war nicht möglich. Die Anwendung von Eisenoxid und Perfluorcarbon Nanopartikeln, zwei Kontrastmittel zur Kernspintomografie, ermöglichte ebendiese. Eisenoxid Nanopartikel wurden durch ihren Signalstöreffekt auf das MR Protonensignal detektiert, während Perfluorcarbon Emulsionen durch <sup>19</sup>F basierte Kernspintomografie nachgewiesen wurden. Säugetiere verfügen nicht über ausreichende Mengen von <sup>19</sup>F Atomen, um ein spezifisches Signal zu liefern, weshalb <sup>19</sup>F Kernspintomografie lediglich applizierte Perfluorcarbon Emulsion in vivo abbilden kann. Dieses Bild kann dann über ein zugleich aufgenommenes Protonen MR Bild gelegt werden, wodurch die Akkumulation des Kontrastmittels im Detail in anatomischer Umgebung dargestellt werden kann. Da es sich

hierbei um einen Vorteil gegenüber anderen Kontrastmittel-basierten MR Bildgebungsmethoden wie Eisenoxid Nanopartikel gestützter Kernspintomografie handelt, wurden nachfolgende Experimente mit Perfluorcarbon Emulsionen durchgeführt. Studien zur Bildgebung der Perfluorcarbon Akkumulation am Infektionsherd des Muskelabszessmodells von *S. aureus* in der Maus zeigten deutliches  $^{19}\text{F}$  MR Signal nach Gabe zwischen Tag 2 und Tag 8 p.i.. In allen untersuchten Tieren zeigte sich eine Ansammlung des Kontrastmittels in Form einer Hohlkugel um den Abszessbereich, wobei das Signal während der gesamten Infektion stabil war. Um den Akkumulationsmechanismus zu identifizieren, wurden Durchflusszytometrie-, Zellseparations- und histologische Experimente durchgeführt. In diesem Zusammenhang erwiesen sich Neutrophile, Makrophagen, Monozyten und Dendritische Zellen als Perfluorcarbon-tragende Immunzelltypen, wobei das Gros an Kontrastmittel in Neutrophilen nachgewiesen werden konnte. Im Allgemeinen war der Großteil des Perfluorcarbonsignals mit Immunzellen assoziiert, weshalb eine spezifische Immunzell-abhängige Akkumulation wahrscheinlich erscheint. Die histologischen Untersuchungen stützten diese Beobachtung, da die Kontrastmittel assoziierten Fluoreszenzmarker nur in der Nähe von Immunzellnuclei gefunden werden konnten.

Die Etablierung von  $^{19}\text{F}$  Kernspintomografie mit Perfluorcarbon Emulsionen als Infektionsbildgebungsmethode ermöglichte im nächsten Schritt die Untersuchung von antibakterieller Therapie auf das MR Signal, um die Eignung dieser Methode für die Präklinik zu evaluieren. Deshalb wurden die Wirksamkeit von Vancomycin und Linezolid, zweier klinisch höchst relevanter Antibiotika zur Behandlung von *S. aureus* Infektionen, im Muskelabszessmodell der Maus untersucht. Beide erwiesen sich als effizient in der Verringerung der bakteriellen Last im infizierten Muskel und des Bakterien-Biolumineszenzsignals, aber auch bei der Reduktion der Stärke und des Volumens der Perfluorcarbon Akkumulation am Infektionsherd, die durch  $^{19}\text{F}$  Kernspintomografie dargestellt und vermessen wurde. Alle drei Methoden zeigten dabei das gleiche Effizienzmuster nach dem Linezolid wirksamer bei der Bekämpfung der Infektion war. Folglich erwies sich  $^{19}\text{F}$  Kernspintomografie mit Perfluorcarbon Emulsionen als effektiv um den antibakteriellen Effekt von Antibiotika in präklinischen Modellen zu untersuchen.

Konsequenterweise wurde im nächsten Schritt eine neuartige Substanz zur Behandlung von *S. aureus* Infektionen mit Hilfe der Bildgebungsplattform untersucht: Lysostaphin. Diese Endopeptidase schneidet spezifisch die Zellwand von *S. aureus* und wurde in verschiedenen Konzentrationen oder in Kombination mit Oxacillin im Muskelabszess- oder Katheterinfektionsmodell der Maus getestet. Lysostaphin in der Konzentration von 5 mg/kg Körpergewicht (Maus) oder Lysostaphin in der Konzentration von 2 mg/kg in Kombination mit Oxacillin führten zu einer starken Verringerung der Bakterienlast und des Biolumineszenzsignals in beiden Modellen. Die Ansammlung von Perfluorcarbon Kontrastmittel war zudem in diesen beiden Gruppen stark reduziert im Vergleich zur Negativkontrolle und den mit Vancomycin und Oxacillin behandelten Tieren. Zusammenfassend kann festgestellt werden, dass Lysostaphin eine vergleichbare oder bessere Wirksamkeit als Vancomycin oder Oxacillin alleine lieferte. Aus diesem Grund

scheint eine Weiterentwicklung dieser Substanz zur Behandlung von *S. aureus* empfohlen. Der Nutzen der Bildgebungsplattform wurde in diesen Experimenten zudem dadurch deutlich, dass alle drei Methoden zur Bestimmung der Schwere der Erkrankung ähnliche Wirksamkeiten der Antibiotika anzeigten. Dennoch muss festgestellt werden, dass die Gruppen, die Oxacillin entweder alleine oder in Kombination mit Lysostaphin erhielten, stärkere Perfluorocarbon Akkumulation am Infektionsherd aufwiesen als von den Bakterienlast- oder Biolumineszenz-Ergebnissen zu erwarten gewesen wäre. Ein Grund hierfür könnten mögliche immunomodulatorische Effekte von Oxacillin sein. Tatsächlich zeigten weitere Experimente Variationen in den Konzentrationen von Cytokinen und Chemokinen im infizierten Muskel in Abhängigkeit der verwendeten Antibiotikatherapie. Besonders die Behandlung mit Oxacillin, in geringerem Maße aber auch mit Minocyclin oder Linezolid, führte zu erhöhten Konzentrationen, wenngleich die Bakterienlast deutlich reduziert werden konnte. Folglich sollten mögliche immuno-modulatorische Effekte antibakterieller Substanzen bei zukünftiger Anwendung von Bildgebungsplattform, die auf dem Markieren von Immunzellen basieren, mit ins Kalkül gezogen werden. Auf der anderen Seite eröffnet diese Beobachtung ein neues Anwendungsfeld für diese Bildgebungsmethoden, da es außerordentlich interessant erscheint, damit immuno-modulatorische Substanzen oder bakterielle Faktoren *in vivo* zu untersuchen. Zu guter Letzt, ermöglicht diese Bildgebungsplattform, die Methoden zur Darstellung der bakteriellen Last auf der einen und des Immunsystems auf der anderen Seite verknüpft, eine innovative, neue Möglichkeit Wirt-Pathogen Interaktionen nicht-invasiv und *in vivo* studieren zu können.

Zusammenfassend konnte gezeigt werden, dass Perfluorocarbon Emulsionen in Immunzellen am Infektionsherd des *S. aureus* Muskelabszessmodells der Maus akkumulieren. Die Ansammlung formt eine Hohlkugel am Rand des Abszessbereiches, deren Größe und Fluorgehalt von der Schwere der Erkrankung und/oder der Wirksamkeit der angewandten Antibiotikatherapie abhängt. Aus diesem Grund erwies sich <sup>19</sup>F Kernspintomografie mit Perfluorocarbon Emulsionen als Kontrastmittel als nützliche Plattform zur präklinischen Evaluierung antibakterieller Substanzen. Weiterhin erscheint diese Methode wegen der Akkumulation des Kontrastmittels in Immunzellen, als interessant zum Studium der Immunantwort gegenüber Infektionen, aber auch Krebs oder Autoimmunerkrankungen sowie zur Erforschung von immuno-modulatorischen Substanzen und Impfansätzen.

# 1. Introduction

## 1.1. Infectious diseases in the 21<sup>st</sup> century

Infectious diseases, a scourge of humanity since its beginning, seemed to become overpowered in the middle of the last century. The development of antibiotics and vaccines promised the eradication and curing of infectious diseases for all mankind. And indeed, in the golden age of antibiotics, which started in the early 1950s, a large variety of different drugs and compound classes were developed and introduced to the clinics, leading to a strong reduction of deaths caused by infectious diseases, especially in developed countries. In the United States, for example, among the major causes of death in the year 1900 were smallpox, cholera, diphtheria, typhoid fever, plague, tuberculosis, typhus, pertussis, syphilis, and other infectious diseases. In addition, many of these diseases caused, if the patient survived, complications leading to severe disabilities, like paralysis from polio or neurological deficits and heart disease from syphilis (Yoshikawa TT. 2002). In contrast to this, in 2010 only pneumonia and influenza, as well as septicemia were among the top 15 causes of death in the United States (Murphy SL et al. 2013). Vaccination efforts led at the same time to large populations immune against several, in earlier times, life-threatening infectious diseases. The climax of vaccination approaches is, without doubt, the eradication of smallpox in 1979, a disease which was responsible for an estimated 300 to 500 million deaths in the 20<sup>th</sup> century (Koplow DA. 2003, ScienceDaily. 2008).

Nonetheless, the WHO estimated that in 2002 about 25.9 % or 14.7 million of all deaths worldwide were attributed to infectious diseases (The World Health report 2004. Annex Table 2). In consequence, it has to be stated, that infectious diseases are not eradicated or overwhelmed at the beginning of the 21<sup>st</sup> century. Public health systems are struggling with emerging or spreading infectious diseases like human immunodeficiency virus (HIV), severe acute respiratory syndrome (SARS) or reemerging pathogens like tuberculosis (Fauci AS. 2005). In addition, bioterrorism, like the 2001 anthrax attacks in the United States, has now to be recognized as a significant threat to public health (Christian MD. 2013).

Furthermore, we have to face in our days a variety of problems that emerged, at least in parts, with the introduction of anti-infective therapy itself. Within these, two big trends are of special interest due to their gravity: the development of antibiotic resistance and the aging of the human population.

Humankind has encountered a strong increase of life expectancy during its evolution, especially after sedentarization and development of culture (Caspari R, Lee SH. 2004, Caspari R, Lee SH. 2006). The most prominent increase took place after the 'Industrial Revolution'. This was mostly caused by massive improvements of public health and was connected to a strong decrease of deaths in childhood (Centers for Disease Control and Prevention (CDC). 1999). Nonetheless, human longevity is unequally distributed over the globe with developed

countries featuring much higher life expectancy, than developing countries. Moreover, it is estimated that life expectancy is further increasing (Oeppen J, Vaupel JW. 2002).

This increase in life expectancy and the expected increase of human longevity will lead to massive challenges for health care systems in future. Besides the general adaptations which are necessary to treat elderly people, it is of special interest, that infections are more prevalent in elderly people than in young adults (Dhawan VK. 2002, Fein AM. 1999, Leibovici L. 1995, Reacher MH et al. 2000). Furthermore, this is not only due to higher hospitalization rates but also to increased risk of infection per hospitalization day and there is a change of pathogens and greater diversity of pathogens in elderly people than in young adults (Emori TG et al. 1991). At the moment, infectious diseases (pneumonia, influenza and complications during bacteremia) are among the 10 major causes of death in elderly people (Yoshikawa TT. 2000). Thus, infectious diseases have a revival simply because of a larger population of human elderly people which are more prone to infections than younger ones.

The second big challenge for the treatment of infectious diseases in future will be antibiotic resistance. Although genes conferring resistance to antibiotic compounds can be found in 30.000 year old permafrost samples (D'Costa VM et al. 2011), most of the pathogenic bacteria were sensitive to antibiotics when they were introduced to the clinics. Nonetheless, since the first application of penicillin, pathogenic bacteria have evolved or acquired resistance mechanisms against virtually all available antibiotics (Alanis AJ. 2005). Moreover, several factors reinforce the emergence and spreading of antimicrobial resistance, namely increasing levels of antibiotic usage (in human but also animal medicine), the greater movement of people and the increase of industrialization and urbanization (Hawkey PM and Jones AM. 2009).

Most importantly, both developments, aging of human populations and the development of antibiotic resistance, can reinforce their individual danger, since the increased hospitalization rates and the elevated risk of infection per hospitalization day for elderly people offer pathogens a higher chance to develop or acquire antibiotic resistance mechanisms (Yoshikawa TT. 2002).

A number of bacterial pathogens has developed or acquired antibiotic resistance during the last 70 years and lead in our days to massive problems in health care worldwide (Alanis AJ. 2005, Hawkey PM and Jones AM. 2009). Infections with gram-negative pathogens like *Pseudomonas aeruginosa* and *Acinetobacter* spp. as well as *Escherichia coli*, *Klebsiella* spp. or gram-positive bacteria like *Staphylococcus aureus*, *Enterococcus faecium* and *Clostridium difficile* are often associated with a high degree of bacterial resistance, sometimes resulting in only one or none remaining compound to treat disease (Hawkey PM. 2008, Theuretzbacher U. 2012).

Thus, new approaches and compounds are necessary to ensure treatment of infections with above-mentioned pathogens in future. Although a number of novel promising antibiotics are in development at the moment (Ohlsen K. 2009, Theuretzbacher U. 2011), in 2004 only 1.6 %

of all drugs in clinical development by the 15 biggest pharmaceutical companies were antibiotics (Jabes D. 2011). It has to be stated, that although antibiotic resistance among pathogenic bacteria increased strongly during the last decades, while development of novel compounds diminished (Spellberg B et al. 2004). Many pharmaceutical companies left the field of antibiotic discovery or cut their expenses, since it seemed to be more interesting to develop therapies for chronic diseases (Projan SJ. 2003, Thomson CJ et al. 2004). Nevertheless, the stopping of emergence and spread of antibiotic resistance and the need for new antibiotics are now recognized as predominant aims of infectious disease societies, nations and companies (Boucher HW et al. 2009). It is regarded in our days as a public problem that has to be solved and countries and the EU are trying to address this problem with big initiatives (Theuretzbacher U. 2012).

In this context, the DFG (Deutsche Forschungsgemeinschaft) decided to establish and fund the SFB630 (Sonderforschungsbereich 630) with the aim to identify, develop and evaluate novel compounds to fight infectious diseases. Embedded in this scientific setting, this thesis was initiated to establish a non-invasive in vivo imaging platform to evaluate the efficacy of novel compounds to treat *S. aureus* infections in preclinical murine models.

## 1.2. *Staphylococcus aureus* – a versatile pathogen

*Staphylococcus aureus* causes a wide variety of different diseases in humans and animals. They include various life-threatening invasive infections, such as sepsis, bacteraemia, endocarditis, pneumonia, osteomyelitis and meningitis (Lowy FD. 1998), but also the majority of skin and soft tissue infections in humans like impetigo, folliculitis, cellulitis and infected wounds and ulcers (McCaig LF et al. 2006, Talan DA et al. 2011). Overall, MRSA only, without methicillin-sensitive *S. aureus*, caused more than 80.000 invasive infections in 2011 in the USA (Dantes R et al. 2013). Interestingly, another study showed in addition that incident rates for invasive MRSA infections for persons 65 years or older (127.7 per 100,000) are very high, higher than for younger adults, suggesting increased susceptibility to MRSA infection with aging (Klevens RM et al. 2007). To get an impression about the impact of *S. aureus* on public health: the number of deaths by invasive MRSA disease outnumbered in the United States in 2005 the deaths caused by tuberculosis, viral hepatitis and AIDS combined (Boucher HW, Corey GR. 2008).

In Europe, healthcare associated MRSA infections are estimated to affect more than 170.000 patients per year, causing more than EUR 380 million extra in-hospital costs for the health care systems (Köck R et al. 2010). Interestingly, the prevalence of MRSA among *S. aureus* bacteraemia samples are highly diverse among the different countries in Europe, ranging from less than 1 % in Scandinavian countries to 25 – 50 % in Italy (European Antimicrobial Resistance Surveillance Network (EARS-net) data, Fig. 1.1). And although the percentage of MRSA among bacteraemia declined in the last years, the overall numbers of blood-stream

infections with *S. aureus* increased between 2002 and 2009 in Europe (Gagliotti C et al. 2011). MRSA infections are today endemic in hospitals world-wide, requiring laborious and expensive methods to prevent further spread of antibiotic resistant strains.

Above all, in the 1990s, the epidemiology of MRSA changed. While MRSA was limited to hospitals and other long-term care facilities prior this time, first cases about community-acquired MRSA infections reported the emergence and spread of MRSA in the healthy population (Chambers HF. 2001). The first isolated strains showed the pulse-field gel electrophoresis pattern of USA400, but these strains were quickly replaced by USA300, which is now epidemic in the United States (Kennedy AD et al. 2008, DeLeo F et al. 2009). Although it has to be stated that the success of USA300 is object of ongoing discussion, the high virulence might be associated with its ability to prevent killing by neutrophils and by the increased production of virulence factors (Voyich JM et al. 2005).

Ca-MRSA, especially the strain USA300, was reported in several studies in Europe, too, but the cases were associated mostly with small outbreaks or single cases and the overall problem, at least at the moment, seems thus to be rather limited (Johnson AP. 2011). A further big threat in Europe is the spread of MRSA among livestock (LA-MRSA) and the associated transmission to humans in close contact to colonized or infected animals (Graveland H et al. 2011). Most of the LA-MRSA strains in Europe and Northern America are members of the clonal complex 398 (CC398), while sequence type 9 (ST9) is most prevalent in Asia. Although *S. aureus* CC398 seems to be a poor persistent colonizer of humans, it accounts for an increasing number of invasive infections in humans (Schaumburg F et al. 2012, Köck R et al. 2011).

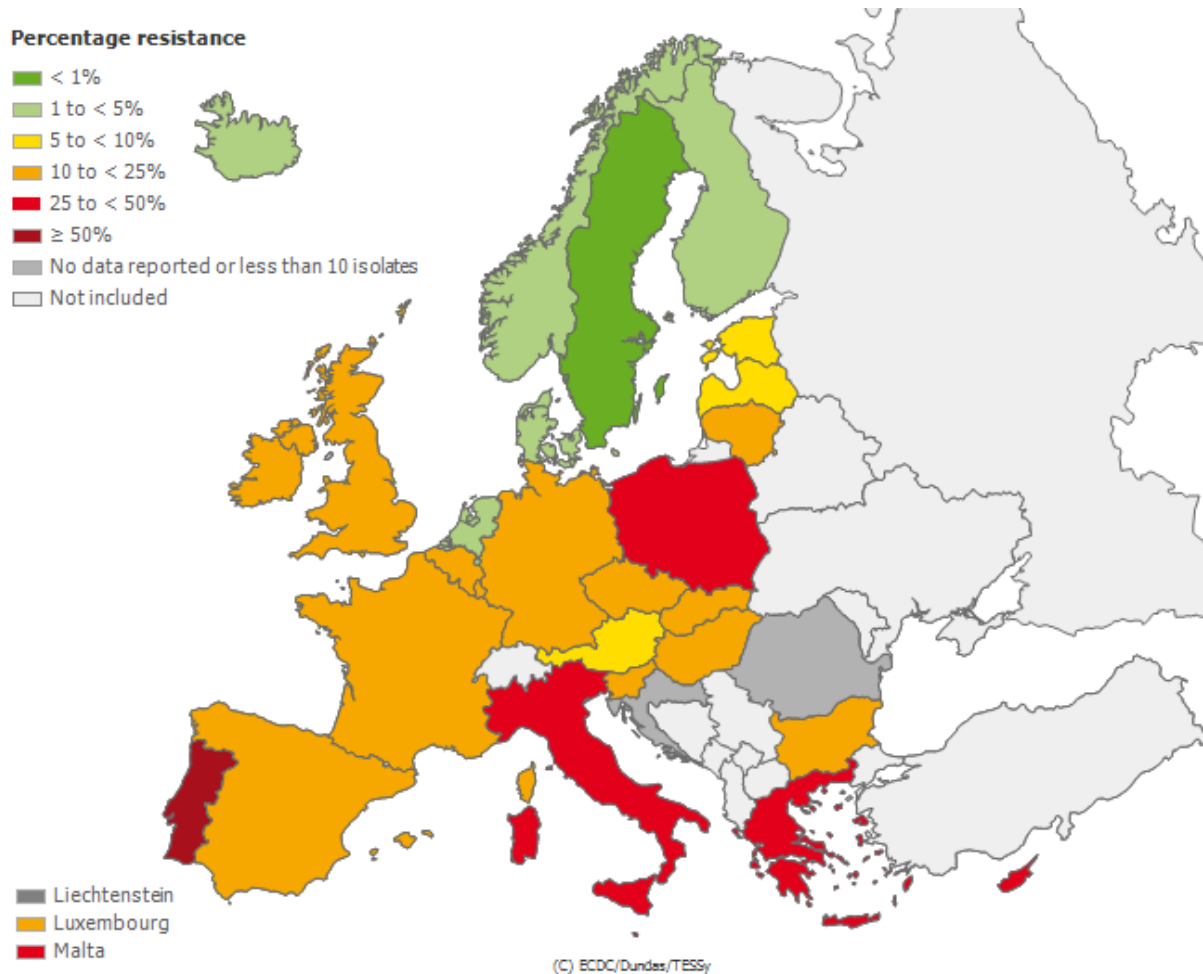


**Fig. 1.1: Prevalence of MRSA among *S. aureus* bacteraemia in Europe in 2012.** Figure derived from [http://www.ecdc.europa.eu/en/healthtopics/antimicrobial\\_resistance/database/Pages/map\\_reports.aspx](http://www.ecdc.europa.eu/en/healthtopics/antimicrobial_resistance/database/Pages/map_reports.aspx)

In Germany, around 132.000 cases of MRSA are registered each year, counting for ca. 20 % of all *S. aureus* cases (Köck R et al. 2011). Most of these cases are associated with hospitalization.

In conclusion, we have to face a very successful pathogen that has adapted to man-made countermeasures to fight infections. The spectrum of diseases that can be caused by *S. aureus* is wide-ranged, but the un-symptomatic colonization of skin and nares in humans is very frequent, too. A survey of carriage in the United States between 2001 and 2004 showed *S. aureus* in nasal samples of about 28.6 % of all tested persons, and 1.5 % of all tested persons carried MRSA (Gorwitz RJ et al. 2008). Similarly, *S. aureus* was found in the nasal swabs of 152 out of 627 patients in an outpatient study in southern Germany (Lietzau S et al. 2004).

To enable survival and growth in such different niches, a diversified genome and flexible gene expression is inevitable. This might be an explanation for the big arsenal of virulence or



virulence-associated genes that are harbored by *S. aureus*. This gram-positive pathogen produces a variety of different microcapsules, although its importance in pathogenesis is still subject of discussion. It was shown that the capsule interferes with complement binding and phagocytic killing (Thakker M et al. 1998, Cunnion KM et al. 2001), while other studies showed either no effect of capsule knock-out or even attenuation of capsule expressing strains in murine models (Albus A et al. 1991, Baddour LM et al. 1992).

As gram-positive bacterium, *S. aureus* has a thick cell wall, which consists to 50 % by weight of peptidoglycan, and no outer membrane. The peptidoglycan consists of alternating subunits of *N*-acetylglucosamine and *N*-acetylmuramic acid. The chains are connected by *S. aureus* specific pentaglycine bridges between tetrapeptide chains bound to the *N*-acetylmuramic acid subunits (Lowy FD. 1998). Further major constituents of the cell wall are ribitol teichoic acids, covalently bound to peptidoglycan, and lipoteichoic acids, which are anchored in the membrane. Interestingly, to reduce susceptibility against antimicrobial peptides, which are produced in tissues and by cells such as neutrophils and platelets, *S. aureus* reduces the negative charge of its surface by the action of Dlt and MprF proteins (Peschel A et al. 1999, Peschel A et al. 2001). Another strategy to neutralize cationic peptides is the secretion of staphylokinase and aureolysin, since both of them bind host derived antimicrobial peptides (Jin T et al. 2004, Sieprawska-Lupa M et al. 2004).

Up to 24 cell-wall anchored proteins can be expressed by *S. aureus*, dependent on the growth phase and condition (Foster TJ et al. 2014). Foster and colleagues proposed to classify the cell-wall anchored proteins into four categories: the microbial surface component recognizing adhesive matrix molecules family (MSCRAMMs), the near iron transporter motif family (NEAT), protein A and the G5-E repeat family. The most abundant family in this context is the MSCRAMM family, which is characterized by at least two subdomains containing adjacent IgG-like folds (Deivanayagam CC et al. 2002). This group of proteins was originally thought to bind extracellular matrix components of the host, but there are members of this family with other functions than adhesion (Foster TJ et al. 2014). The archetype of this family is clumping factor A (clfA), which binds efficiently fibrinogen and thereby on hand promotes adhesion but on the other also hides the bacterium from the immune system (Ganesh VK et al. 2008). The NEAT motif family members participate in capturing haem from haemoglobin and thus help to supply *S. aureus* with iron (Hammer ND and Skaar EP. 2011). Protein A will be described and discussed later in this chapter, while the G5-E repeat family seems to be necessary for biofilm formation, but participates in adhesion, too (Gruszka DT et al. 2012).

Foreign body associated infections with *S. aureus* are prone to biofilm formation. In principle, *S. aureus* biofilms are either polysaccharide intercellular antigen (PIA) dependent or independent (Archer NK et al. 2011). PIA is produced by the proteins of the *ica* operon and anaerobic conditions strongly induce PIA production and biofilm formation (Cramton SE et al. 2001). Nonetheless, the depletion of the *ica* operon did not diminish biofilm formation in *S. aureus*, but PIA-independent biofilm did not longer consist of polysaccharides but of

proteinaceous compounds (Lasa I and Penadés JR. 2006, Merino N et al. 2009). Composition of PIA-independent biofilm seems to be strain specific and not all strains produce this type of biofilm (O'Neill E et al. 2007). Extracellular DNA (eDNA) is another important component of *S. aureus* biofilms and might give structural support (Archer NK et al. 2011).

After entering the host, adhesion and attachment, *S. aureus* has to face the host's immune response and the first line of cellular defense against *S. aureus* infections are neutrophils which migrate in large numbers to sites of infection (DeLeo F et al. 2009). Therefore, *S. aureus* has evolved several proteins which are targeted against neutrophils and their mechanisms to fight bacterial infection. Important for the recognition of invading bacteria by neutrophils are the complement peptide fragments C3a and C5a as well as formylated peptides from growing bacteria. *S. aureus* harbors several proteins to inhibit the detection of these messenger molecules to hinder neutrophil activation and migration to the site of infection. Chemotaxis inhibitory protein of staphylococci (CHIPS) is, for example, one of these proteins and binds specifically to the formyl peptide receptor (FPR) and the C5a receptor (C5aR) on neutrophils and blocks thereby chemotaxis (de Haas CJ et al. 2004). Similar activity was demonstrated for the proteins FLIPr (FPRL1 inhibitory protein) and FLIPr-like. FLIPr binds in this context the formyl peptide receptor-like 1, while FLIPr-like binds this receptor and additionally the formyl peptide receptor, but nonetheless, binding led for both of them to inhibition of neutrophil chemotaxis towards gradients of compounds that are detected by these receptors (Prat C et al. 2006, Prat C et al. 2009). Extracellular adherence protein (Eap or Map) binds to the intercellular adhesion molecule-1 (ICAM-1) on endothelial cells and thus blocks binding of neutrophils to this surface molecule, what in turn prevents extravasation to the site of infection (Chavakis T et al. 2002). If neutrophils enter the site of infection and phagocytose *S. aureus*, this pathogen evolved several strategies to circumvent killing. It expresses two superoxide dismutases to remove  $O_2^-$  and even the yellow carotenoid pigment of *S. aureus* contributes to survival in phagolysosomes by scavenging free radicals (Foster TJ et al. 2009).

Despite its action against phagocytes and especially against neutrophils, *S. aureus* inhibits the complement system, too, the first line of humoral defense against invading pathogens. The complement consists of various proteins which on one hand are able to kill bacteria directly in interplay but on the other hand play an important role in activating or regulating other effectors of the host's immune response (Zipfel PF and Skerka C. 2009). *S. aureus* interferes with the complement cascade at virtually every level utilizing a large arsenal of proteins like SSL7, SSL10, Sbi, CHIPS, SCIN, Spa, Efb and others (Zipfel PF and Skerka C. 2013).

But besides inhibiting the host's innate immune response, *S. aureus* is in addition well stocked with proteins to interfere with adaptive immune response. Both essential parts of adaptive immune response, namely T and B cells, are attacked or manipulated, but that's not all, *S. aureus* is furthermore counteracting the antibody response (Bröker BM et al. 2013). Protein A (Spa), a well studied surface associated and released protein, binds efficiently the Fc part of antibodies, thereby preventing Fc $\gamma$  receptor mediated uptake of bacteria into

professional phagocytes (Parcina M et al. 2008). Further proteins which are able to bind antibodies are Sbi, SSL7 and SSL10. They seem to be predominantly secreted and enable neutralization of antibodies, thus facilitating extracellular lifestyle of *S. aureus* (Langley R et al. 2010, Smith EJ et al. 2011). Alongside to binding and neutralizing antibodies, *S. aureus* expresses serine proteases to cleave and digest antibodies (Prokesová L et al. 1995, Fernandez Falcon MF et al. 2011).

Protein A possesses in addition to its Fc binding domain a Fab' binding domain, which offers direct binding to B cell receptors, which are membrane-bound immunoglobulins that define the antigen specificity of the individual B cell (Graille M et al. 2000). The binding results either in B cell death if soluble Spa has bound or in strong activation of B cells without the otherwise necessary induction by T cells. This leads to short lived differentiated B cells with accompanying release of the anti-inflammatory cytokine IL-10 (Parcina M et al. 2013). Spa is on account of this regarded as 'B cell superantigen' (Bröker BM et al. 2013).

Nonetheless, more attention of the scientific community was attracted by staphylococcal T cell superantigens. The genome of *S. aureus* encodes for no less than 23 superantigens encompassing enterotoxins (SEs) and enterotoxin-like proteins (SEIs) (Fraser JD and Proft T. 2008, Bröker BM et al. 2013). These toxins are of special interest since they are the causative agent of staphylococcal food poisoning and toxic shock syndrome. They are able to bypass the conventional antigen recognition of T cells by directly crosslinking the T cell receptor with MHC II molecules. This results in simultaneous, unspecific activation of a large portion of the total T cell population, causing a life-threatening cytokine storm (Xu SX and McCormick JK. 2012).

In addition to the aforementioned immune avoidance strategies, *S. aureus* harbors several leukotoxins to attack and kill immune cells directly (Grumann D et al. 2013). The most prominent member is  $\alpha$ -toxin or  $\alpha$ -hemolysin. This toxin is secreted as monomer, but forms heptamers in the target's membrane which leads to a 14-stranded  $\beta$ -barrel pore and deaths of the target cell (Montoya M and Gouaux E. 2003). Another group of toxins, the biocomponent leukotoxins, in contrast, consist of two separately secreted subunits that assemble into oligomers with strong affinity for leukocytes. Four types have been identified in *S. aureus* so far: the  $\gamma$ -toxin or  $\gamma$ -hemolysin, the Panton-Valentine leukocidin (PVL), leukocidin E/D and leukocidin M/F-PV-like (Foster TJ. 2005). Of special interest is PVL, since it was suggested to be an important factor in promoting the success of ca-MRSA strains (Gillet Y et al. 2002). But this observation is still topic of ongoing discussion, since other studies showed that PVL is a poor marker for ca-MRSA identification and therefore not necessarily present in ca-MRSA strains (Rossney AS et al. 2007).

Recently, a further group of molecules with cytolytic activity have been identified in *S. aureus*: the phenol-soluble modulins (PSMs). These are short peptides and *S. aureus* harbors four  $\alpha$ -type PSMs, two  $\beta$ -type PSMs and  $\delta$ -toxin (Wang R et al. 2007). Interestingly, ha-MRSA strains lack in contrast to ca-MRSA strains considerable production of PSMs, thus PSMs are suggested to promote ca-MRSA survival and success in healthy population (Wang R et al.

2007). Alongside to their cytolytic activity, PSMs are detected by neutrophils through the formyl peptide receptor 2 which leads in turn to chemotaxis to the site of infection (Kretschmer D et al. 2010).

Another group of toxins produced by *S. aureus* are exfoliative toxins (Ladhani S. 2003). Four serogroups of this family have been identified so far: exfoliative toxin A, B, C and D. They are responsible for the staphylococcal scalded skin syndrome, a blistering skin disorder, which is caused by cleavage of desmoglein-1, an intercellular adhesion molecule (Amagai M et al. 2000).

Besides this plethora of virulence factors, *S. aureus* is able to invade the host's non-professional phagocytes (Fraunholz M, Sinha B. 2012). This mechanism is mainly promoted by the action of fibronectin-binding proteins (Sinha B et al. 2000). This intracellular lifestyle might help to evade the immune system and might open up new nutrient sources.

All these factors or strategies to promote lifestyle as a pathogen but also, not to forget, as a colonizer can be regarded as threat in the case of infection, but the most dangerous factor or mechanism developed or acquired by *S. aureus* is without doubt antibiotic resistance. The lack of adequate therapy during invasive infection due to the resistance of *S. aureus* to various antibiotic compounds endangers patients worldwide. *S. aureus*, naturally susceptible to almost every antibiotic compound developed so far, proved to be a master of antibiotic resistance acquisition or development (Pantosti A et al. 2007).

Only a few years after introduction of penicillin to the clinics in the 1940s, the first penicillin-resistant strains of *S. aureus* emerged. This resistance was facilitated by the action of the extracellular enzyme penicillinase, which inactivated the first  $\beta$ -lactam antibiotics. In the following years a spread of resistant *S. aureus* strains could be seen, leading to a pandemic situation, which made the development of penicillinase-resistant penicillins necessary, with the first and most prominent member being methicillin (Chambers HF and Deleo FR. 2009).

Nevertheless, the introduction of methicillin resulted in a similar development than after introduction of penicillin. Soon after introduction of methicillin, the first resistant clones of *S. aureus* could be detected. But in contrast to penicillin resistance, the pattern was this time not narrow as with penicillinase, but broad, providing resistance to all  $\beta$ -lactam antibiotics. Nonetheless, this second generation of resistant strains was called methicillin-resistant *S. aureus* (MRSA). The resistance was supplied by a genetic element called staphylococcal chromosomal cassette (SCC) *mec*, which harbors the resistance gene cluster *mec*, which encodes for the additional penicillin-binding protein PBP2a and accompanying regulatory proteins, and the *ccr* genes, which enable excision and integration of the genetic element in the *orfX* gene on the *S. aureus* chromosome (Katayama Y et al. 2000). To date, eight variations of the SCC*mec* element have been identified, each of them comprising of at least *mecA* and the *ccr* genes, but some of them harbor additional resistance or virulence associated genes (Chambers HF and Deleo FR. 2009). Interestingly, both types of resistance, against penicillin or methicillin, rely on mobile genetic elements, either the aforementioned

SCC*mec* elements or plasmids. In this regard, it was shown recently, that biofilm formation and/or the expression of the alternative sigma factor H (SigH) promote natural transfer of antibiotic resistance genes on mobile genetic elements, thereby offering *S. aureus* the opportunity to acquire antibiotic resistance, developed in other species (Morikawa K et al. 2012, Savage VJ et al. 2013). This might be an explanation for the rather quick development of resistance, but on the other hand also demonstrates the high adaptability of *S. aureus* when facing new challenges.

After emergence and spread of MRSA in hospitals all over the globe, physicians confided in vancomycin to treat infections (Hiramatsu K. 2001). In 1997, the first case of vancomycin-intermediate *S. aureus* (VISA) phenotype was described and shortly after that the first vancomycin-resistant strains (VRSA) (Appelbaum PC. 2006). Cell wall thickening seems to be a possible origin of vancomycin resistance in *S. aureus* (Hiramatsu K. 2001). Another resistance mechanism was mediated by the transfer of *vanA* from *Enterococcus sp.*, although this seems to be associated with a loss of fitness (Foucault ML et al. 2009). Besides this, it was reported that MRSA developed reduced susceptibility against vancomycin, although they are classified by laboratory techniques as vancomycin sensitive (Sakoulas G and Moellering RC Jr. 2008). This development was accompanied by an increasing number of vancomycin treatment failures (Sakoulas G et al. 2004, Moise PA et al. 2007).

Parallel to the development of vancomycin resistance or insusceptibility, MRSA spread into healthy population. Formerly, MRSA infections were almost exclusively limited to hospitals, thus *S. aureus* was seen as nosocomial pathogen. This pattern changed significantly in the 1990s, when first infections with MRSA, later called community-acquired MRSA (ca-MRSA), in healthy population were reported (Chambers HF and Deleo FR. 2009). Today ca-MRSA has spread worldwide and is even reentering hospital settings again (Seybold U et al. 2006). Although ca-MRSA strains are thought to harbor less many antibiotic resistances than ha-MRSA strains, they seem to be more virulent (Voyich JM et al. 2005).

In conclusion, these developments made it necessary to search for new compounds to fight *S. aureus* infections. Currently, there are linezolid, daptomycin, telavancin, ceftaroline and tigecycline approved as anti-MRSA antibiotics by the US Food and Drug Administration besides vancomycin (Sakoulas G and Moellering RC Jr. 2008, Snyder J et al. 2012). Recently, the FDA has approved another new compound against MRSA, dalbavancin (FDA News Release, May 23, 2014). As with penicillin, first cases of daptomycin treatment failure due to resistance could be described shortly after introduction (Hayden MK et al. 2005, Hirschwerk D et al. 2006). Furthermore, two different mechanisms, namely by the presence of the *cfr* gene or by mutations in the V domain of 23S rRNA, lead to resistance of *S. aureus* against linezolid and resulted in linezolid treatment failures in several cases (Meka VG et al. 2004, Morales G et al. 2010). In conclusion, *S. aureus* has developed strategies to resist or endure treatment with virtually every antibiotic currently available (Stryjewski ME and Corey GR. 2014). Not all of the resistance mechanisms are widespread, but it can be stated nonetheless that *S. aureus* has mastered every challenge faced by man so far. Moreover, emergence of

ca-MRSA strains, that seem to have acquired or developed further strategies to invade, colonize and damage, sometimes even kill the human host, are cause of constant worry today. Therefore, it is inevitable to search for new ways to fight *S. aureus* infections and to prevent the emergence of a *S. aureus* 'superbug'.

Efforts to develop new antibacterial compounds after the emergence and spreading of resistant bacteria, especially of MRSA, has led to the introduction of three new classes of antibiotics: lipopeptides, oxazolidinones and streptogramins (Parisien A et al. 2007), however most efforts were focused on the generation of new compounds based on well-known antibiotic structures (Theuretzbacher U. 2009). In consequence, *S. aureus* and especially MRSA is challenged with new weapons but an old strategy. Maybe, it is time to try something new! And indeed, several new ideas or methods to fight bacterial infections are in preclinical development.

Most importantly, a classical approach has gained renewed attention in the last decades: vaccination. This old approach promises the access to a weapon suitable to eradicate an infectious disease or simply to prevent disease in the immunized population. Vaccines against other pathogens like *Haemophilus influenzae* type b, *Streptococcus pneumoniae* and *Neisseria meningitidis* have led to significant reduction of serious infections after their introduction to the clinics (Seale A and Finn A. 2011). Nonetheless, although a vaccine against *S. aureus* is very appealing to pharmaceutical companies and scientists, every candidate has failed so far, leaving us behind with the question: why did all of them fail, although preclinical data was promising (Proctor RA. 2012a, Proctor RA. 2012b, Spellberg B and Daum R. 2012)? It was supposed that the lack of understanding of the human immune response against *S. aureus* infection has hindered the generation of a protective immune response (Proctor RA. 2012a, Proctor RA. 2012b). Nevertheless, there are further vaccine candidates in different phases of clinical trials and new ideas for a *S. aureus* vaccine in preclinical evaluation.

Besides active immunization with a vaccine, passive immunization with antibodies came into focus of scientists and pharmaceutical companies since advances in the fields of recombinant DNA technology and genetics made production of large amounts of endotoxin-free monoclonal antibodies possible. In principle, several antigens have been proposed as suitable targets for passive immunization, for example MSCRAMMs, lipoteichoic acid, capsule, surface proteins or secreted virulence factors (Ohlsen K and Lorenz U. 2010, Verkaik NJ et al. 2011). One big advantage of passive immunization in comparison to active immunization might be the efficacy of this approach in infants, elderly or immune-compromised patients, who otherwise might lack sufficient immune response (Projan SJ et al. 2006). Some approaches have failed to date, but more monoclonal antibodies are in preclinical or clinical testing for treatment of various diseases caused by *S. aureus* (Ohlsen K and Lorenz U. 2010, Proctor RA. 2012b, Oesterreich B et al. 2014).

Immunomodulators are another new approach to fight bacterial infections. They are based on stimulation or guidance of the host's immune response to fight the infection more

efficiently (Masihi KN. 2000, Pirofski LA and Casadevall A. 2006). Passive immunization with antibodies might, as a matter of principle, classified as immunomodulatory, too, due to the fact that their mode of action depends on the action of the immune system, maybe with the exception of neutralizing antibodies. But there are further approaches to modulate the immune response to fight infection more efficiently. Antimicrobial peptides, for example, have been proposed as promising candidates to fight bacterial infection by their activity upon the immune system (Mookherjee N et al. 2007). Synthetic variants of these peptides with no direct antimicrobial activity are also under investigation as new therapeutics against *S. aureus* (Scott MG et al. 2007, Nijnik A et al. 2010).

Besides these aforementioned approaches which rely on the immune system in one way or another, there are of course further compounds under investigation that act on the bacterium itself. A number of novel compounds targeting similar compartments or structures of/on the bacteria than currently available antibiotics are in preclinical or clinical evaluation including members of the well-known  $\beta$ -lactam class (Fitzgerald-Hughes D et al. 2012). New approaches contain lipoproteins, bacteriophages, enzymes, cationic antimicrobial peptides and novel compounds from natural sources (Ohlsen K et al. 2008).

One novel compound with different mode of action than currently available antibiotics is lysostaphin. It is of special interest for this thesis since it was applied as experimental, novel compound to treat murine *S. aureus* infections in chapter 6. It was originally identified and described in 1964 as an extracellular protein produced by *S. simulans* biovar *staphylolyticus* (Schindler CA and Schuhardt VT. 1964). This zinc metalloprotease glycyl-glycine endopeptidase cleaves specifically the pentaglycine interpeptide crossbridge of *S. aureus* and, to a lesser extent, of *S. epidermidis* (Sloan GL et al. 1977). The species specificity defines lysostaphin as a narrow spectrum anti-infective compound and is therefore different to currently used antibiotics to treat *S. aureus* infection. In vitro tests demonstrated high activity against a broad range of clinical *S. aureus* isolates including antibiotic resistant strains (Harrison EF and Cropp CB. 1965, Zygmunt WA et al. 1965, Schindler CA. 1966) and first in vivo tests, performed shortly after identification, showed increased survival and reduced bacterial burden of treated mice compared to mock treated controls (Harrison EF and Zygmunt WA. 1967, Schaffner W et al. 1967). However, the purification of endotoxin-free lysostaphin formulations remained challenging and thus development was stopped until recombinant lysostaphin formulations became available and renewed interest in this compound (Climo MW et al. 1998, Patron RL et al. 1999, Kokai-Kun JF et al. 2007, Kokai-Kun JF et al. 2009). Interestingly, it was demonstrated that lysostaphin acts synergistic with  $\beta$ -lactam antibiotics in vivo (Climo MW et al. 2001).

To sum up, some novel compounds are currently in different stages of preclinical and clinical development and thus it is possible that some of those new compounds against antibiotic resistant *S. aureus* will reach the clinics sooner or later. Unfortunately, considering the numbers of approvals of novel compounds in the past and comparing this number with the number of compounds that have failed during preclinics or clinical trials, we have to state,

that the probability for new therapies against *S. aureus* in near future is not that high. In consequence, the preclinical evaluation of novel therapeutics has to be reconsidered to reduce the risk of failure.

### 1.3. Preclinical testing and In Vivo Imaging?

Depending on the author, only 5 out of 5,000 or 10,000 compounds enter clinical trials and in the end just one of these 5 is approved by the FDA (Preziosi P. 2004, Willmann JK et al. 2008, DiMasi JA et al. 2010). Importantly, an evaluation of reasons for terminating drug development between 1987 and 1992 showed that more than 50 % of all terminations were related to problems with efficacy (37.6 %) or safety (19.6 %), but further 33.6 % were related to economic reasons (Dimasi JA. 2001). In consequence, more than 50 % of the compounds showed promising results in first evaluations but then failed in subsequent tests. Moreover, 80 % of all drugs that entered clinical trials failed, suggesting insufficient preclinical evaluation. In principle, preclinical testing is limited by the use of the evaluation models, which should mimic the human manifestation of disease, independently of their in vitro or in vivo nature. Animal models play in this context an important role in preclinical evaluation of new promising compounds.

Nonetheless, it is important to note, that the value of animal models is under ongoing discussion. A study that investigated the differences and similarities of the inflammatory response to trauma between mice and humans showed, for example, strong differences in the genomic response and the authors suggested that this differences might be the cause of extensive failure of inflammation blocking agents for critical-ill patients during clinical studies (Seok J et al. 2013). This observation led to strong interest in the public, e.g., even an article in 'The New York Times' (Kolata G. 2013), that insinuated uselessness of animal experiments for all diseases linked to inflammation, including sepsis and trauma. But other scientists stated that the comparison of genetically heterogenous human data with homogenous mouse data (the inbred strain C57BL/6J was used for this study) might not reflect the real benefit of mice in medicinal research (Wanner M. 2013; Hagan CE. 2013). Additionally, the careful selection of animal models for the evaluation of drugs to treat inflammatory diseases has been shown to deliver preclinical results that were predictive for their clinical outcome (Arnett HA and Viney JL. 2007).

But although inflammation and immune response play a very important role in *S. aureus* animal models, there is not necessarily a link to the efficacy of new promising anti-infective agents. It is important, of course, for the evaluation of vaccines to prevent infection and it was indeed a puzzling observation that various *S. aureus* vaccines failed during clinical trials, whereas they have shown protective capacity in murine models (Proctor RA. 2012b). But all other approaches to combat *S. aureus* infections, which are in preclinical or clinical investigation with the exception of antibodies and immune-modulators, have modes-of-



action that do not depend on the immune response and therefore, they should not be affected by differences between mice and humans. A further limitation of mouse models to study *S. aureus* infections is the insusceptibility of mice to human pathogenic *S. aureus* strains, but there are approaches underway to design or identify strains with infectious and pathogenic capacities that are similar to human ones (Holtfreter S et al. 2013).

Besides this experimental design debate, there is also a heated and complex discussion about ethics of animal experiments underway. While opponents of animal experimentation argue either that humans do not have the right to experiment with animals or that animal experiments are not predictive enough for human outcome, supporters argue that animal experiments are vitally important to evaluate efficacy and adverse effects of novel compounds prior to clinical trials and that there are no other methods to achieve this goal (Ellen Frankel, P and Jeffrey, P. 2001, Shaw, WH. 2001, Greaves P et al. 2004). Nonetheless, animal models are at the moment widely used in the preclinical testing of new drugs (Preziosi P. 2004, Beckmann N et al. 2007).

Despite this debate, animal experiments are today subject to the principle of the three Rs: replacement, refinement and reduction. An interesting approach to achieve replacement and reduction of animal experiments might be the application of in vivo imaging technologies (Beckmann N et al. 2007, Willmann JK et al. 2008). In principle, in vivo imaging technologies might be interesting during four out of five phases of drug development, namely target identification and evaluation, profiling during disease models, safety evaluation and clinical studies, only during the phase of lead finding and optimization in vivo imaging technologies cannot have any function (Beckmann N et al. 2007). In principle, several in vivo imaging techniques are available to evaluate efficacy and safety of novel, promising compounds to cure disease, namely ultrasound, positron-emission tomography (PET), single-photon emission computed tomography (SPECT), magnetic resonance imaging (MRI), computed tomography (CT), luminescence and fluorescence imaging (see Tab 1.1). They offer different possibilities and suffer different disadvantages and therefore a careful decision is necessary to decide for one platform or another.

**Tab. 1.1: Different imaging modalities for preclinical evaluation of novel drug candidates, but also for clinical imaging of disease.** The imaging methods have different disadvantages and advantages that have to be considered when chosen. Further methods than the indicated ones suitable for infection imaging in preclinical and clinical approaches are available. The table is sought to give only a glance about interesting techniques for this field of science. Abbreviations: FDG: 2-deoxy-2-[(18)F]fluoro-D-glucose, USPIO: ultrasmall paramagnetic ironoxide particles, \*: Francis KP et al. 2000, \*\*: Gross S et al. 2009, †: Leevy WM et al. 2006, #: Love C et al. 2005, §: Fowler JS et al. 1999, Δ: Niska JA et al 2012, †: Marzola P et al. 1999, ¥: Kaim AH et al. 2002.

Technique	Disadvantages	Advantages	Infection Imaging applications (examples)
<b>Bioluminescence imaging</b>	signal loss due to tissue depths	good sensitivity, high through-put	luminescent pathogens*, luminol imaging**
<b>Fluorescence imaging</b>	signal loss due to tissue depths	good sensitivity, high through-put	fluorescently tagged probes†
<b>PET (positron emission tomography)</b>	costly, radiation	high sensitivity	FDG#, drug labeling§
<b>SPECT (single photon emission computed tomography)</b>	limited spatial resolution	good sensitivity	
<b>CT (Computed tomography)</b>	poor soft tissue contrast, radiation	high spatial resolution	infections of bonesΔ
<b>Ultrasound imaging</b>	imaging through bones and lung difficult	fast, good spatial resolution	
<b>MRI (magnetic resonance imaging)</b>	expensive, time-consuming	high spatial resolution, good soft tissue contrast	soft tissue infection†, USPIO¥

Optical (luminescence and fluorescence) as well as magnetic resonance imaging were of special interest for this thesis since the aim of this work was to establish a multimodal imaging platform consisting of this two methods to evaluate antibiotic drug candidates in murine models of *S. aureus* infection.

Bioluminescence imaging is based on the activity of luciferases in vivo. Luciferases are enzymes that catalyze oxidative reactions which lead to emission of photons. The bacterial luciferase is most suitable for infection imaging due the organization of the *luxABCDE* operon, which does not only encode for the luciferase but also for the enzymes necessary for luciferase compound synthesis (Meighen EA. 1993). In consequence, the introduction of the *luxABCDE* operon enables the bacterial cell to produce all components which are necessary for generation of luminescence signal. This cannot be achieved by other luciferases since they are depended on the additional administration of compounds to emit photons. The heterodimeric bacterial luciferase (encoded by *luxAB*) catalyzes the oxidation

of flavin mononucleotide (FMNH<sub>2</sub>) and a long-chain fatty aldehyde (synthesized by a complex consisting of luxCDE), thereby emitting blue-green light (peak at 490 nm). The introduction of this operon into *S. aureus* led to stable expression of luciferase and correlating photon emission (Francis KP et al. 2000). This enabled in turn imaging of bacterial burden in various models of *S. aureus* infection (Kuklin NA et al. 2003, Kadurugamuwa JL et al. 2003b, Engelsman AF et al. 2009, Funao H et al. 2012). This technique was furthermore applied to investigate the efficacy of antibiotics (Kadurugamuwa JL et al. 2003a, Xiong YQ et al. 2005) or to determine promoter activity in vivo (Steinhuber A et al. 2008). Due to the broad published data about bioluminescence imaging of genetically modified *luxABCDE*-expressing *S. aureus* strains, we decided to include this modality into our two modality platform for antibiotic drug candidate evaluation.

In contrast, much less publications about magnetic resonance imaging (MRI) as infection imaging modality, especially for *S. aureus* infections, in preclinical setting were available at the beginning of this thesis. Regarding native, proton based MRI, few studies demonstrated an increase in T<sub>2</sub> relaxation times in the infected thigh muscle of a murine thigh infection model of *S. aureus* (Marzola P et al. 1999, Kaim AH et al. 2002, Kaim AH et al. 2003). One of these studies demonstrated moreover differences in signal pattern after antibiotic therapy (Marzola P et al. 1999). Furthermore, ultrasmall paramagnetic ironoxide nanoparticles accumulated after intravenous administration at the rim of the abscess area in this model, as shown in a different study (Kaim AH et al. 2002). This could be visualized best by either T<sub>2</sub> or T<sub>2</sub><sup>\*</sup> weighted MR methods. The accumulation was facilitated by uptake of contrast agent in the bloodstream by phagocytes which then migrated to the site of inflammation (Kaim AH et al. 2002, Kaim AH et al. 2003).

In principle, a similar accumulation mechanism was shown for perfluorocarbon emulsions in murine models of stroke, ischemia and pulmonary inflammation (Flögel U et al. 2008, Janjic JM et al. 2008, Ebner B et al. 2010). These perfluorocarbon emulsions could be visualized at the site of inflammation by <sup>19</sup>F MRI. Since mammals do inherently not harbor sufficient amounts of <sup>19</sup>F to deliver signal in <sup>19</sup>F MR images, perfluorocarbon emulsion could be visualized background-free and overlaid upon <sup>1</sup>H MR images to determine accumulation in anatomical context.

Nonetheless, at the beginning of this thesis, no studies about accumulation of perfluorocarbon emulsions at sites of infection were available. Thus, the capability of <sup>19</sup>F MRI with perfluorocarbon emulsions as MR tracer had to be evaluated first. It was furthermore necessary to compare the accumulation and MR visualization of perfluorocarbon emulsions with those of USPIOs in order to decide which method of both should be part of our two modality imaging platform for the evaluation of promising novel antibiotic drug candidates.

## 1.4. Aim of this thesis

The central goal of this thesis was to establish and evaluate a two-modality imaging platform, consisting of bioluminescence and magnetic resonance imaging, for preclinical testing of novel antibiotic drug candidates in small animal models. Bioluminescence imaging was chosen, since the application of luciferase-expressing pathogens offers in vivo and non-invasive monitoring of bacterial burden throughout the course of infection, while magnetic resonance imaging should visualize anatomical changes caused by infection and immune response. Although this imaging platform should be pathogen-independent, *S. aureus* was chosen as model pathogen to establish and test the imaging modalities, due to the enormous clinical importance and the need for novel antibiotics to treat infections caused by this bacterium.

In a second step after establishment, the two-modality platform should be applied to visualize and measure the efficacy of well-known antibiotics against *S. aureus*. And finally, in a third step, if the platform visualizes and indicates differences in the efficacy pattern of antibiotics, a promising novel compound to fight *S. aureus* infections should be evaluated with this system: lysostaphin.

## 2. Materials

### 2.1. Chemicals and consumables

Chemicals and consumables used in this study were purchased from Alfa Aesar (Karlsruhe), BD Biosciences (Heidelberg), Bio-Rad (München), eBioscience (Frankfurt), Eppendorf (Hamburg), Life Technologies (Darmstadt), Merck Millipore (Schwalbach), Miltenyi Biotec (Bergisch Gladbach), Oxoid (Wesel), Pluriselect (Leipzig), Roth (Karlsruhe), Sarstedt (Nürnberg), Sigma-Aldrich (Taufkirchen), ThermoFisher Scientific (Erlangen), VWR (Ismaning). Antibodies used for flow cytometry were supplied by Miltenyi Biotec (Bergisch Gladbach) and eBioscience (Frankfurt).

### 2.2. Kits

**Table 2.1: Kits used in this thesis.**

Kit	Supplier
Anti-Ly6G MicroBead Kit (mouse)	Miltenyi Biotec (Bergisch Gladbach)
Anti-CD11b MicroBead Kit (mouse)	
Anti-FITC MicroBead Kit	Pluriselect (Leipzig)
CD4 S-pluriBeads Kit anti-ms	
CD11b M-pluriBeads Kit anti-ms	
CD19 S-pluriBeads Kit anti-ms	
Ly6G M-pluriBeads Kit anti-ms	
Mouse Chemokine 6plex FlowCytomix Multiplex	eBioscience (Frankfurt)
Mouse CCL2 (MCP-1) ELISA Ready-SET-Go!	
Mouse IFN gamma ELISA Ready-SET-Go!	
Mouse Th1/Th2 10plex FlowCytomix Multiplex	
Mouse Th1/Th2 10plex Ready-to-Use FlowCytomix Multiplex	

### 2.3. Antibacterial compounds

**Table 2.2: Antibiotics used in this study.**

Compound	Supplier	Stock
Linezolid	Sigma-Aldrich (Taufkirchen)	15 mg/ml in PBS or 0.9 % NaCl
Lysostaphin	Bharat Biotech (Hyderabad, India)	2 mg/ml in PBS or 0.9 % NaCl
Minocycline	Sigma-Aldrich (Taufkirchen)	20 mg/ml in PBS or 0.9 % NaCl
Oxacillin		200 mg/ml in PBS or 0.9 % NaCl
Vancomycin		30 mg/ml in PBS or 0.9 % NaCl

All antibiotics were solved in sterile 0.9 % NaCl or PBS and then filtered through 0.22 µm syringe filters (Merck Millipore, Schwalbach) to receive sterile antibiotic solution. Stock solution was then further diluted in either sterile 0.9 % NaCl or PBS in order to receive working solution. Recombinant Lysostaphin was kindly provided by Bharat Biotech as ready-to-use solution. Lysostaphin was expressed as mature lysostaphin in *Escherichia coli*, with no traces of prepro-lysostaphin or pro-lysostaphin (Khatri GS, Sharma R. 2005). The formulation was produced under 'Good Manufacturing Practice' with > 99 % purity and was constituted in 10 mM phosphate buffer (pH 6.9) with 154 mM NaCl.

## 2.4. Instruments

**Table 2.3: Instruments used in this study.**

<b>Instrument</b>	<b>Model</b>	<b>Manufacturer</b>
<b>Centrifuge</b>	Pico 17	Heraeus (Hanau)
	Biofuge 13R	Heraeus (Hanau)
	Multifuge X3R	Heraeus (Hanau)
	Multifuge 1 L-R	Heraeus (Hanau)
<b>Confocal Laser Scanning Microscope</b>	TCS SP5	Leica (Mannheim)
<b>Enzyme linked immunosorbent assay (ELISA) reader</b>	Multiskan Ascent	Thermo Fisher Scientific (Erlangen)
<b>Flow Cytometer</b>	MACSQuant Analyzer	Miltenyi Biotech (Bergisch Gladbach)
<b>Incubator</b>	Tv40b	Memmert (Schwabach)
	BB16	Heraeus (Hanau)
	Mini10	Hybaid (Heidelberg)
	Innova 4300	New Brunswick Scientific (Hamburg)
<b>Luminescence / Fluorescence In vivo Imaging System</b>	FACSCalipur	BD Biosciences (Heidelberg)
	IVIS Lumina II	Caliper Life Sciences (Hopkinton, MA, USA)
<b>Magnetic Resonance Scanner</b>	Biospec, 7 Tesla	Bruker Biospin (Reinstetten)
<b>pH meter</b>	pH720	Inolab (Weilheim)
<b>Photometer</b>	ultraspec 3100 pro	Amersham Biosciences (Nürnberg)
<b>Vortex</b>	Biovortex V1	Lab4you (Berlin)
<b>Sonifier</b>	Sonifier 250	Branson Ultrasonics (Danbury, CT, USA)
<b>Surgical microscope</b>	OPMI	Zeiss (Oberkochen)
<b>Tissue homogenizer</b>	Dispomix	BioLabProducts (Gödenstorf)
<b>Water bath</b>	1002	GFL (Burgwedel)
	1092	GFL (Burgwedel)

## 2.5. Culture media and plates

Table 2.4: Media used in this study.

Media	Ingredient	g/l
<b>B medium</b>	tryptone	10
	yeast extract	5
	NaCl	10
	K <sub>2</sub> HPO <sub>4</sub>	1
<b>BHI medium</b>	Brain Heart Infusion Broth (Oxoid, Wesel)	37
<b>Luria Bertani medium (LB)</b>	tryptone	10
	yeast extract	5
	NaCl	10
<b>Mueller Hinton medium</b>	Mueller Hinton Broth (Sigma Aldrich, Taufkirchen)	23
<b>TSB medium</b>	Difco Tryptic Soy Broth (BD Biosciences, Heidelberg)	30

All media were solved in distilled water and then autoclaved prior to use at 121 °C and 1 bar for 20 min. To receive agar plates, 15 g/l agarose was added to the respective medium prior autoclaving. Sterile filtered antibiotic solutions were added after cooling of medium or agar to 50 °C.

## 2.6. Bacteria

Table 2.5: Bacterial strains used in this thesis.

Strain	Source
<b><i>S. aureus</i> LAC (USA300)</b>	Clinical Isolate, Tübingen, (now in IMIB strain collection)
<b><i>S. aureus</i> NCTC8325</b>	National Collection of Type Cultures, United Kingdom
<b><i>S. aureus</i> HG001</b>	Herbert S et al. 2010
<b><i>S. aureus</i> Xen29</b>	Caliper Life Sciences (Hopkinton, MA, USA)

All strains were stored at – 80 °C in glycerin stocks and plated on B or LB agar plates prior cultivation for experimental application.

## 2.7. Buffers and solutions

Buffers and solutions supplied with the kits were used according to the manufacturer's instructions. Home-made buffers and solutions are either mentioned in materials or methods chapters 2 and 3. Only distilled water was used for buffers and solutions.

## 2.8. Contrast agents and tracer

In principle, magnetic resonance imaging contrast agents/tracer and luminol for luminescence imaging were applied in this study. Luminol sodium salt was purchased from Alfa Aesar (Karlsruhe) and dissolved in sterile 0.9 % NaCl solution to achieve a working solution of 40 mg/ml. Thus, an injection of 100  $\mu$ l i.p. resulted in 200 mg Luminol/kg body weight (average mouse weight of 20 g).

Two different types of contrast agents/tracer for magnetic resonance imaging were used throughout this study: ironoxide nanoparticles and perfluorocarbon emulsions.

The cross-linked ironoxide nanoparticles (CLIO) were kindly provided by the group of Prof. Dr. Schenk (Department of Inorganic Chemistry, University of Würzburg). They had a diameter of 30 nm with a central ironoxide core of 2 – 3 nm and were dextran coated. Emulgated in phosphate buffered saline, 16.8 mg Fe/kg bodyweight were injected intravenously.

Regarding perfluorocarbon emulsions, two different sources of particles were used in this study: commercially available ready-to-use and home-made emulsions. The commercially available emulsion was used for the experiments in the chapters 5 and 6 and for all experiments in chapter 4 with the exception of flow cytometry, fluorescence microscopy and cell sorting experiments. The commercially available particles consisted of a 20 % v/v perfluoropolyether emulsion for direct intravenous administration (VS1000H or VSdmGreen, both from Celsense, Pittsburgh, PA, USA).

At the beginning of this thesis, no fluorescently labeled perfluorocarbon emulsion was commercially available. But the fluorescent label was necessary to uncover the mechanism of accumulation and to identify participating immune cells by flow cytometry, fluorescence microscopy and cell sorting approaches. Therefore home-made fluorescently labeled perfluorocarbon emulsion was used in some indicated experiments in chapter 4. The emulsification protocol is described in chapter 3.7.



## 2.9. Software

**Table 2.5: Software used during this thesis.**

<b>Software</b>	<b>Manufacturer</b>
<b>Adobe Acrobat Pro 9</b>	Adobe (San Jose, CA, USA)
<b>Flow Cytomix Pro</b>	eBioscience (Frankfurt)
<b>Flowing Software 2.5.0</b>	Perrttu Terho, University of Turku, Finland
<b>GIMP 2</b>	The GIMP Team, Freeware, <a href="http://www.gimp.org">www.gimp.org</a>
<b>Graph Pad Prism 5</b>	GraphPad (La Jolla, CA, USA)
<b>Living Image 3.2</b>	Caliper Life Science (Hopkinton, MA ,USA)
<b>MACSQuantify 2.4</b>	Miltenyi Biotech (Bergisch Gladbach)
<b>MS Office 2007</b>	Microsoft (Redmond, WA, USA)
<b>Windows XP and Windows 7</b>	Microsoft (Redmont, WA, USA)

## 3. Methods

### 3.1. General methods

All media and solutions were sterilized prior use either by autoclaving (20 min, 121 °C and 1 bar) or filtered through 0.22 µm syringe filters.

*Staphylococcus aureus* was cultured, if not otherwise stated, in liquid B or LB medium in shaking cultures at 37°C. For storage, 15 ml of liquid cultures (18 h) were centrifuged (10 min, 4000 g/min), the pellet resuspended in 1 ml fresh medium and mixed with 1 ml of sterile glycerin. The resulting culture was then stored at – 80°C.

To generate infectious doses, frozen bacteria (- 80°C) were thawed at room temperature and then plated on B agar plates. After overnight incubation at 37°C, single colonies were picked and incubated in 50 ml shaking cultures of B medium for 18 h at 37°C. 15 ml of the culture were then centrifuged for 5 min at 4000 rpm/min at room temperature, the supernatant discarded and the pellet resuspended in 15 ml 0.9 % NaCl solution. After another centrifugation step (RT, 5 min at 4000 rpm/min) and discarding of the supernatant, the pellet was resuspended in 1 ml 0.9 % NaCl solution. The OD<sub>600</sub> value of this bacterial solution was now measured and the solution diluted to reach the final concentration of bacteria for the animal or in vitro experiments (following the assumption that 1 OD<sub>600</sub> unit equals 7.5 x 10<sup>8</sup> bacteria/ml).

### 3.2. Minimal inhibitory concentration testing (MIC)

The minimal inhibitory concentration is defined as the lowest compound concentration in solution that inhibits bacterial growth completely. To determine this concentration, the experiments followed in principle the recommendations of the CLSI (CLSI. 2012).

The bacteria were incubated overnight in liquid Mueller Hinton medium (MH) at 37°C for at least 18 h. 15 ml of the culture was centrifuged (4000 rpm, 10 min at room temperature) and the pellet resuspended in 1ml MH medium. The OD<sub>600</sub> was measured and the bacterial solution diluted to reach a final concentration of 5 x 10<sup>7</sup> bacteria/ml. Antibacterial substances were diluted serially in MH medium to receive different concentrations and pipetted into different wells of a 96 well plate. 100 µl of the bacterial solution was then administered to each well and the plate incubated for 18 h at 37°C. Each 96 well plate included positive (only bacteria, no antibacterial substance) and negative (only antibacterial substance, no bacteria) controls. The lowest concentration of antibacterial substance resulting in no visible turbidity was defined as MIC value of this compound.

### 3.3. Animal models

#### 3.3.1. Ethics statement

All animal experiments in this thesis were approved by the Committee on the Ethics of Animal Experiments of the government of Lower Franconia (54-2531.01-42/06 and 55.2-2531.01-06/12). All experiments were performed in strict accordance with the German animal protection law. The animals were housed in cages under standardized lighting conditions and had ad libitum access to food and water. All in vivo imaging was performed under isoflurane anesthesia and all efforts were made to minimize suffering. Animals were sacrificed at the end of the experiment by CO<sub>2</sub> inhalation.

#### 3.3.2. Thigh infection model

The standard model of this thesis was the *S. aureus* thigh infection model. It was applied in all experimental chapters of this thesis, especially for magnetic resonance imaging. The *S. aureus* infection in this model is provoked by an intramuscularly injection of bacteria into the thigh muscles of mice. This resulted in localized infection and inflammation and finally in abscess formation in the muscle tissue of the mouse. The bacteria remained in the thigh muscle and did not, as in other *S. aureus* infection models, spread throughout the animal's body and cause systemic infection. Importantly, both acute and chronic phase of inflammation were covered in this rather long-term model, since the infection and immune response did not kill the mouse. These features and the formation of large abscesses (thus loci of infection) seemed to be very interesting and promising to investigate differences in magnetic resonance images and methods as well as the accumulation of contrast agents.

#### The infection model

In principle, female Balb/c mice (Charles River, Sulzfeld) were housed at least for 7 days in the animal facility prior to experimentation. They had ad libitum access to food and water. Animals were around 6 to 8 weeks old, when acquired and reached a body weight of 18 to 22 g at the beginning of experimentation. Before bacteria were administered, animals were shaved at both thigh muscles in order to enable efficient photon imaging and to offer a clear sight onto the site of injection. Animals received inhalation anesthesia (1.5 % isoflurane in O<sub>2</sub>) while bacteria were injected intramuscularly into the left thigh muscle. Bacterial suspension was generated following general methods in B medium, washed and resuspended in 0.9 % NaCl solution or PBS. A variable number of bacteria was administered in the experiments of this thesis, but in all cases, bacteria were in a volume of 50 µl. In principle, only two different *S. aureus* strains were applied in this thesis: the luciferase expressing strain Xen29 and the ca-MRSA strain LAC (or USA300). The *S. aureus* Xen29 strain was in this context a derivative of the strain ATCC 12600 with a chromosomally integrated *luxABCDE* operon from *Photobacterium luminescens* (Francis KP et al. 2000). The exact

number of administered bacteria and the strain is stated in the corresponding results section.

### Antibiotic treatment

Some groups of mice in chapters 5, 6 and 7 received antibiotic treatment during the course of infection. In principle, treatment started, if not otherwise stated, at 2 hours p.i. and was resumed two times a day. The antibiotic concentrations mentioned in the corresponding results section were calculated as mass (antibiotic) per body weight per day. Vancomycin was administered in a dose of 30 mg/kg/day, linezolid in 15 or 20 mg/kg/d, oxacillin in 200 mg/kg/d, minocycline in 20 mg/kg/d, and lysostaphin in either 2 or 5 mg/kg/d. All antibiotics were administered intraperitoneally with the exception of lysostaphin which was injected intravenously. The solvent of the antibiotics is stated in the methods section. The last antibiotic treatment was applied 12 hours prior the end of the experiment and organ recovery.

### Contrast agents and tracer

In chapters 4, 5 and 6, perfluorocarbon emulsions were applied as MR tracer. The emulsions were either acquired (Celsense, Pittsburgh, PA, USA) or home made (see chapter 3.7). The applied perfluorocarbon emulsion for each experiment is stated in the corresponding results section. Independent of their origin, 100 µl of ready-to-inject emulsion was applied intravenously through one of the tail veins. Mice were therefore anesthetized with 1.5 % isoflurane in oxygen and placed on the warming platform of the IVIS system, which is heated to 37 °C (Lumina II, Caliper Life Sciences, Hopkinton, MA, USA).

The iron oxide nanoparticles (CLIO), which were used in MR imaging experiments in chapter 4, were applied in a similar fashion than perfluorocarbon emulsion. The home made contrast agent (AG Schenk, Department of Inorganic Chemistry, University of Würzburg) was dissolved in a final volume of 100 µl and injected into one of the tail veins during anesthesia and after warming of mice.

In chapter 7, mice infected with *S. aureus* LAC received luminol solution in order to visualize myeloperoxidase activity non-invasively and in vivo at the site of infection with luminescence imaging. Therefore, mice received intra-peritoneal administrations of luminol at a concentration of 200 mg/kg body weight in a final volume of 100 µl. The luminol sodium salt (Alfa Aesar) was dissolved in sterile 0.9 % NaCl solution and filtered through 0.22 µm syringe filters to achieve final solution.

### Tissue and blood recovery

At the end of the experiment, mice were sacrificed by administration of inhalable pure CO<sub>2</sub>. The infected thigh muscles were then removed aseptically and either processed immediately after recovery or frozen at – 80°C until processing. In some experiments of chapter 4, inner organs like liver, kidneys, spleen, lungs and heart were removed aseptically and frozen at –

80 °C until processing. The blood was, if necessary, recovered after death of the animal by removing the heart and collecting the leaking blood. Blood samples were immediately after recovery imaged for fluorescence signal with the IVIS system (Lumina II, Caliper Life Sciences), then allowed to coagulate, centrifuged and the resulting serum samples collected and frozen at – 80 °C until the levels of cytokines or chemokines were measured.

### 3.3.3. Catheter related infection model

For evaluation of lysostaphin efficacy in chapter 6, a second animal model besides thigh infection was applied: the catheter-associated infection model. In principle, a catheter was placed in this model in the jugular vein of mice and *S. aureus* was administered into its inner lumen. Bacteria formed a biofilm in the catheter and then spread via the bloodstream to colonize inner organs. This resulted in systemic infection. In general, the model was performed according to a prior study (Lorenz U et al. 2008).

#### The infection model

Female Naval Medical Research Institute (NMRI) mice (Charles River, Sulzfeld) with a weight of 30 to 35 g were housed for at least one week in the animal facility. Prior experimentation, the thorax and neck region of the mice was shaved to enable unobstructed luminescence imaging and surgery. Regarding surgery, mice received an intraperitoneal injection of xylazine (8 mg/kg body weight) and ketamine (100 mg/kg body weight) for anesthesia and a minimal horizontal incision was made into the skin of the left side of the neck. The submaxillary gland was isolated to expose the bifurcation of the anterior and posterior facial veins using a surgery microscope (Zeiss). Next, a venotomy on the anterior facial was performed between loose ligatures and the catheter (polyurethane catheter, Instech Salomon, Plymouth Meeting, PA, USA) was inserted through the incision. After advancing the catheter towards the superior vena cava, the ligatures were tied and the catheter subcutaneously tunneled and exteriorized through a midline scapular incision. The catheter lumen was washed once with sterile 0.9 % NaCl solution and sealed with a plug.

Animals were allowed to recover for 24 hours before the start of the infection experiment. Mice were then anesthetized by inhalation of isoflurane (1.0 to 1.5 % in oxygen). The plug of the catheter was removed and 30 µl bacterial suspension with  $3.7 \times 10^7$  cfu *S. aureus* Xen29 was administered into the catheter lumen. Bacteria were allowed to adhere to the catheter surface for 15 min, before the catheter was flushed with 0.2 ml sterile 0.9 % NaCl solution. Animals were now and at several time points after start of infection imaged for emergence and development of luminescence signal.

#### Antibiotic treatment

Two hours post infection, the antibiotic treatment started. Animals received either sterile 0.9 % NaCl solution (control group, intraperitoneally), 30 mg/kg/d vancomycin (intraperitoneally), 200 mg/kg/d oxacillin (intraperitoneally), lysostaphin in the dosing of 2 or

5 mg/kg/d (intravenously) or a combination of 200 mg/kg/d oxacillin and 2 mg/kg/d lysostaphin. Antibiotics were administered twice a day.

### Tissue and catheter recovery

At the end of the experiment (day 4 p.i.), mice were sacrificed by administration of inhalable pure CO<sub>2</sub>. The location of the catheter in the vena cava was then surgically confirmed and only mice with correctly placed catheter were included in the analysis. The catheter, kidneys, liver, heart and lung were then removed aseptically, their luminescence signal measured *ex vivo* and either processed immediately after recovery or frozen at – 80°C until processing.

#### 3.3.4. Determination of colony forming units

Two different murine models of *S. aureus* infection were applied in this study: the thigh infection model and the catheter-associated infection model. Main and primary site of infection in the thigh infection model was the thigh muscle of the mouse, while major bacterial communities in the catheter-associated infection model were found in the kidneys and catheter of infected mice. Besides these primary sites of infection, the bacterial burden of other organs was in some other experiments of interest, too. In chapter 6, the heart and lung of mice of the catheter-associated infection experiment were recovered in addition to kidneys since bioluminescent imaging indicated infection at these sites. In chapter 4, the bacterial burden in liver, kidneys and spleen of mice of the thigh infection model was determined in order to evaluate whether the infection is localized in this model and whether perfluorocarbon emulsion alters the course of infection or not.

Nonetheless, the colony-forming units and thus bacterial burden in all of these organs was measured, in principle, in the same way. After recovery at the end of the experiment, the organ was placed in a tissue homogenization tube (gentleMACS M tube, Miltenyi Biotech) with 2 ml sterile 0.9 % NaCl solution or PBS. The organ was then homogenized with a tissue homogenizer (DispoMix, BioLabProducts, Gödenstorf) and the resulting cell suspension serially diluted in sterile 0.9 % NaCl solution or PBS. The catheters of the catheter-associated infection (chapter 6) model were sonicated with low-energy, but high frequency sound in 2 ml sterile 0.9 % NaCl solution. Several dilutions of tissue or catheter samples were then plated on B agar plates and incubated for 18 – 24 hours at 37°C. The colonies were counted and multiplied with the dilution factor to determine the number of colony-forming units in the respective organ.

### 3.4. In vivo Bioluminescence and Fluorescence Imaging

In vivo bioluminescence and fluorescence imaging was performed in all experiments with the help of an 'In Vivo Imaging System' (IVIS Lumina II, Caliper Life Sciences).

#### Bioluminescence imaging of bacterial burden

Luciferase-expressing *S. aureus* Xen29 was applied in many of the experiments in order to visualize bacterial burden non-invasively in vivo. This strain harbors a chromosomally integrated *luxABCDE* operon from *Photobacterium luminescens* (Francis KP et al. 2000). This operon is sufficient for the generation of luciferase protein and compound to emit photons in the presence of oxygen and energy in the cell. *S. aureus* Xen29 was applied in the murine thigh infection model in chapters 4, 5, 6 and 7, and in the catheter-associated infection model in chapter 6. Regarding the thigh infection model, bacteria were injected into the left thigh muscle of mice. As a negative control, sterile 0.9 % NaCl solution was injected into the right thigh muscle. The bioluminescence signal was then detected at different time points (indicated in the corresponding results section) pre or post start of infection by the IVIS system. Therefore, mice received inhalation anesthesia (1.5 % isoflurane in oxygen). When asleep, mice were placed on the imaging platform of the IVIS system, which is heated to 37 °C in order to sustain body temperature of the animals during experimentation. Inhalation anesthesia (1.0 % isoflurane in oxygen) was continued until the end of the imaging session. The bioluminescence imaging was performed with following parameters: exposure: 120 s; FStop: 1; excitation: block; emission: open; field of view (FOV): D; and height: 1.5 cm. Images were analyzed with Living Image 3.2 software (Caliper Life Sciences). To determine bioluminescence emission values, an oval area of interest was manually defined at the site of interest and applied with same geometry and size to images of all mice at all time points (of the individual chapter) in order to offer comparability.

#### Bioluminescence imaging of myeloperoxidase activity with luminol

In chapter 7, the experiments focused on the influence of antibiotic treatment on the immune response. Since some of the mice were infected in these experiments with *S. aureus* LAC, which does not harbor a luciferase in its genome and thus does not emit bioluminescence signal, it became possible to administer luminol solution into these mice in order to visualize processing of this compound by neutrophilic myeloperoxidase (Gross S et al. 2009). The reaction results in the emission of blue to green photons that could be detected in principle with same settings than the bioluminescence signal derived from *S. aureus* Xen29.

In general, mice received inhalation anesthesia (1.5 % isoflurane in oxygen) and when asleep, luminol sodium salt (Alfa Aesar), in sterile 0.9 % NaCl solved, in a concentration of 200 mg/kg body weight was administered intraperitoneally. Immediately after injection, mice were placed on the imaging platform of the IVIS system and bioluminescence signal

measured in a series of images (5 to 10), each with following parameters: exposure: 120 s; FStop: 1; excitation: block; emission: open; field of view (FOV): D; and height: 1.5 cm. Images were generated with Living Image 3.2 software (Caliper Life Sciences) and bioluminescence signal was then calculated, similar to *S. aureus* Xen29 derived signal quantification, by defining manually an oval area of interest at the site of infection and applied to all mice and time points.

### Fluorescence imaging of perfluorocarbon emulsions

In chapter 4, home-made perfluorocarbon emulsions were labeled with fluorescence dyes in order to investigate the accumulation at the site of infection by flow cytometry, cell sorting and fluorescence microscopy of tissue sections. The fluorescence labeling offered on the other hand the visualization of the tracer in vivo or in tissue homogenization samples, too. Thus, the accumulation of perfluorocarbon emulsion in mice was studied by in vivo fluorescence imaging, as well as in blood and tissue homogenization or cell sorted samples.

For in vivo imaging, mice received either fluorescently labeled perfluorocarbon emulsion (labeled with either Atto550 or Atto647N, as stated in the corresponding results section) or, as a control, non-fluorescent perfluorocarbon emulsion and fluorescence signal was determined at various time points prior or post administration. Therefore, mice were anesthetized with gaseous isoflurane (1.5 % in oxygen) and placed on the imaging platform of the IVIS system. In the first set of experiments, a large number of different excitation (500 nm, 535 nm, 570 nm, 605 nm, 640 nm, 675 nm) and emission filter (DsRed (575 - 650 nm), Cy5.5 (695 – 770 nm) settings was tested for specific visualization of perfluorocarbon derived fluorescence. Best ratios of fluorescence signal at site of infection compared to signal of control treated mice were achieved with excitation filter: 535 nm and emission filter DsRed for Atto550-labeled perfluorocarbon emulsions and excitation filter: 640 nm and emission filter: Cy5.5 for Atto647N-labeled perfluorocarbon emulsions. Hence, all following imaging sessions were performed with these filter settings and following parameters: exposure: 120 (or 60) s; FStop: 1; excitation: block; emission: open; field of view (FOV): D; and height: 1.5 cm. The area of interest was defined manually in the images generated with the help of Living Image 3.2 software (Caliper Life Sciences) and applied to all mice in the same geometry and size.

The fluorescence signal of blood and tissue homogenization or sorting samples were imaged in equal volumes in 1.5 ml Eppendorf caps. They were placed in racks on the imaging platform of the IVIS system and the imaging was performed with the 535 nm excitation filter and DsRed emission filter for the Atto550-labeled perfluorocarbon samples or with the 640 nm excitation and the Cy5.5 emission filter for the Atto647N-labeled perfluorocarbon emulsion samples. The imaging parameters were: exposure: 120 (60 or 30) s; FStop: 2; excitation: block; emission: open; field of view (FOV): D; and height: 1.5 cm. The images were generated with Living Image 3.2 software (Caliper Life Sciences). In order to measure the fluorescence signal of the individual sample, a circular region of interest was defined manually and applied to all samples in all images in the same size.



### 3.5. Magnetic Resonance Imaging

Magnetic resonance imaging of *S. aureus* infections occupies a central role in this thesis. Since only sparse preliminary studies were published, many imaging experiments had to be performed to evaluate the capability of MRI to visualize sites and course of infection.

In general, magnetic resonance imaging was performed in close collaboration with Volker Sturm (AG Jakob, Department of Experimental Physics 5, University of Würzburg). Volker Sturm developed and adapted all measurement protocols/sequences for the magnetic resonance scanner, operated the MR scanner, generated images and determined values from scanner-derived raw data.

#### Animal handling procedure

The animal imaging experiments were performed on a 7 Tesla small animal scanner (Bruker Biospec system, Bruker BioSpin, Reinstetten), which is located in a biosafety level 1 area in the Department for Experimental Physics 5 (University of Würzburg). Since experiments with *S. aureus* require a biosafety level 2 environment, a special containment device was necessary to separate infected animals and *S. aureus* containing samples from environment. This was achieved with the help of a home-made container (Fig. 3.1). The container had the shape of a cylinder with a bed located inside, on which mice were placed during the imaging experiments. Mice received inhalation anesthesia during the imaging experiment (1.0 to 1.5 % isoflurane in O<sub>2</sub>). The inhalation gas was warmed in order to prevent a decrease of body temperature during the experiment. Heart beat and breathing was monitored with a balloon, placed on the chest of the mice. In the case of a strong decline of breathing or heart beat rate, the experiment was stopped, the inhalation anesthesia aborted and the mouse removed from the container and allowed to recover.

#### Anatomical and iron oxide particle based <sup>1</sup>H MR imaging

All measurements were performed in an adjustable double resonant (<sup>19</sup>F and <sup>1</sup>H) home-built birdcage coil in the scanner. In order to image the anatomy or tissue composition at the site of infection, a turbo spin echo (TSE) sequence was applied to receive either two-dimensional slice images (effective echo time/repetition time [TE<sub>eff</sub>/TR]: 13.4 ms / 2500 ms; inter-echo time: 6.7 ms; turbo factor: 4; FOV: 25 x 25 mm<sup>2</sup>; matrix: 200 x 200; slice thickness: 1 mm; 16 slices; NA: 2) or three-dimensional data sets (effective echo time/repetition time [TE<sub>eff</sub>/TR]: 20.4 ms / 500 ms; inter-echo time: 5.1 ms; turbo factor: 4; FOV: 25 x 25 x 25 mm<sup>3</sup>; matrix: 100 x 96 x 100; NA: 1). In chapter 4, T<sub>2</sub> maps were acquired to visualize edema formation in the infected thigh muscle or to visualize CLIO particle accumulation, thus a multi slice spin echo (MSME) sequence was used (effective echo time/repetition time [TE<sub>eff</sub>/TR]: 6 ms / 6000 ms; NE: 40; FOV: 25 x 25 mm<sup>2</sup>; matrix: 128 x 128; slice thickness: 1 mm; 10 slices interlaced; NA: 1). The second MR method to image the accumulation of iron oxide nanoparticles at the site of infection was the application of T<sub>2</sub><sup>\*</sup> sequences. Therefore 3D multi gradient echo

(MGE) scans were performed (effective echo time/repetition time [ $TE_{eff}/TR$ ]: 2 ms / 100 ms; inter-echo time: 2.7 ms; NE: 16; FOV: 40 x 25 x 25 mm<sup>3</sup>; matrix: 128 x 80 x 80; NA: 2). The signal decay parameters were then fitted pixel per pixel with a  $T_2/T_2^*$  maximum likelihood estimation based on Rice distribution (Sijbers J et al. 1999).



**Fig. 3.1:** Animal imaging container for magnetic resonance imaging of mice with *S. aureus* thigh infection. The container was constructed to comply with biosafety level 2 restrictions. Mice were placed on the inner bed and received inhalation anesthesia during the imaging experiment. Heart beat and breathing was controlled with the balloon, which was placed on the chest of the mice.

### **<sup>19</sup>F MRI with perfluorocarbon emulsions**

The MR active agent applied in this thesis was perfluorocarbon emulsion. These particles are detected not by <sup>1</sup>H MRI, as iron oxide particles are, but by <sup>19</sup>F MRI. In chapter 4, 3D steady state free precession chemical shift imaging (SSFP-CSI) sequences were used with the same geometry than the anatomical <sup>1</sup>H – TSE scans (Pulse shape: hermite; Pulse bandwidth: 5400 Hz; TACQ / TR: 10.24 ms / 13.6 ms; FOV: 25 x 25 x 16 mm<sup>3</sup>; spectral points: 512; matrix: 48 x 48 x 8; - NA: 4). The signal of the <sup>19</sup>F peak was integrated and the data afterwards interpolated into a matrix of 200 x 200 x 16 pixel by zerofilling. After defining the <sup>19</sup>F threshold, the image was overlayed onto the <sup>1</sup>H TSE scan in order to show perfluorocarbon emulsion accumulation in anatomical context.

In chapters 5 and 6, quantification of perfluorocarbon emulsion accumulation at the site of infection became necessary to determine differences between antibiotic treatments. To reach this goal, the total <sup>19</sup>F signal at a given location in the infected thigh muscle had to be determined. In this regard, a problem might be variations in the  $B_1$  field. In order to circumvent this or minimize this effect, only mice of equal size and weight were chosen for experimentation and all of them were placed in the same position in the rather homogenous

$B_1$  field of the birdcage coil. Furthermore, the  $^{19}\text{F}$  MR signal intensity was normalized to the apparent noise amplitude of the measurement in order to receive an estimate of the  $^{19}\text{F}$  content in a given voxel. The apparent mean noise amplitude of the  $^{19}\text{F}$  measurement was determined by fitting the pixel intensity histogram with a Gaussian noise model. Furthermore, in order to avoid false – positive results, each voxel was considered as ‘fluorine filled’ only if the  $^{19}\text{F}$  peak amplitude was at least four times higher than noise amplitude. This threshold was applied to all measurements in these chapters.

The  $^{19}\text{F}$  MR sequence in these chapters was composed of two acquisition weighted 3D steady state free precession chemical shift imaging (SSFP-CSI) sequences with different pulse phase increments but the same geometry than the anatomical  $^1\text{H}$  TSE scans ( $\theta$ :  $0^\circ$  /  $180^\circ$ , Pulse shape: hermite; pulse bandwidth: 5400 Hz; TACQ/TR: 10.24 ms /13.1 ms; FOV: 25 x 25 x 16 mm<sup>3</sup>; spectral points: 512; matrix: 31 x 31 x 20; NA: 4). Both data sets were combined by ‘sum-of-square’ (SoS) and the  $^{19}\text{F}$  spectral line summed. The data was then zero-filled into a matrix of 100 x 100 x 64 pixels.

MR measurement protocols needed between 1 and 3 hours per mouse.

### 3.6. Histology

Histological examination of the abscess area in the thigh infection model was performed to address three questions: first, what is the histological appearance of the primary site of infection in this model, second, how and where accumulate iron oxide nanoparticles and perfluorocarbon emulsions at the site of infection, and third, is the histological appearance of infection altered by administration of contrast agents?

Therefore, three groups of mice received either CLIO (iron oxide particles), perfluorocarbon emulsion (Atto647N-fluorescent or non-fluorescent home-made emulsions) or 0.9 % NaCl solution as negative control at day 2 p.i.. The infected thigh muscles were recovered either at day 3 or day 8 p.i. to cover both acute and chronic phase of inflammation. In addition, the liver and the spleen of perfluorocarbon and negative control group mice were recovered to compare differences in histologic appearance by the accumulation of the tracer.

The muscles for general histology and iron staining, as well as liver and spleen of perfluorocarbon and negative control group mice were immediately fixed in a 10 times the volume of 10 % neutral buffered formalin solution (Sigma-Aldrich) than the organ, while half of the infected thigh muscles from perfluorocarbon group mice and of the negative control group mice were immediately frozen at  $-80^\circ\text{C}$  for cryotome cutting and immunohistochemistry.

The formalin fixed muscles, spleens and livers were brought to Dr. Stefan Kircher (Institute of pathology, university of Würzburg), who kindly conducted further steps of sample

preparation and analysis. The fixed samples were therefore embedded in paraffin and cut to 2 µm thick transversal slices. The sections were stained with haematoxylin-eosin according to the standard protocol at the Institute of Pathology in order to visualize immune cells at the site of infection. Another set of sections from infected thigh muscles of iron oxide group and negative control group mice was stained with Berlin blue staining to reveal intracellular iron content and thus iron oxide nanoparticles. This staining was achieved with a mixture of equal volumes of 20% hydrochloric acid solution (SigmaAldrich) and 10% potassium ferrocyanide solution (SigmaAldrich). Counterstaining with eosin led to visualization of cells by microscopic analysis. All stained tissue sections were analyzed together with Dr. Stefan Kircher (Institute of pathology, university of Würzburg).

The frozen infected thigh muscles from perfluorocarbon and negative control group mice were frozen immediately after recovery at – 80°C. The frozen specimen were then brought to Dr. Martin Wartenberg (Institute of pathology, university of Würzburg), who kindly conducted cryotome cutting of samples to slices of 10 µm thickness. The slices were either fixed in 3.7 % formaldehyde solution at room temperature in the dark for 10 minutes and then stored at – 80°C until staining and/or microscopy or not fixed at all and immediately stored at – 80 °C. Prior to staining, samples were thawed at room temperature in the dark and rinsed once with PBS. 4 drops of Image-iT Fx signal enhancer (Life Technologies, Darmstadt) to reduce background fluorescence was added and the slices incubated for 30 minutes in a humid environment at room temperature in the dark.

After rinsing with PBS, one third of the samples was incubated with anti-Ly6G biotin-conjugated antibody (eBioscience or Miltenyi Biotech) overnight in humid environment at 4 °C in the dark. After incubation, slices were rinsed with PBS and stained with a mixture of streptavidin-conjugated Atto550 (5 µg/ml, Atto-Tec, Siegen), phalloidin-Atto425 conjugate (0.5 nmol/ml, Atto-Tec) and NucBlue Live Cell Stain (2 drops/ml, Life Technologies, Darmstadt) for 60 minutes at room temperature in the dark.

The second third of samples was incubated for 60 minutes in the dark with a mixture of phalloidin-Atto425 conjugate (0.5 nmol/ml, Atto-Tec) and NucBlue Live Cell Stain (2 drops/ml, Life Technologies), while the last third of samples was stained only with NucBlue Live Cell stain for 60 min.

All samples were rinsed with PBS after staining and covered with ProLong Gold antifade reagent (Life Technologies). The mounting medium was allowed to cure overnight before samples were investigated with the confocal laser scanning microscope (Leica TCS SP5, Mannheim).

### 3.7. Perfluorocarbon particle emulgation

For some experiments in chapter 4, fluorescently labeled perfluorocarbon emulsion was mandatory. Since all commercially available emulsions at the beginning of this thesis lacked proper fluorescence labels, this emulsion had to be made by our own. To achieve this, fluorescently labeled 15 % v/v perfluorocarbon emulsion was generated by a sonication approach. In general, 2 ml perfluorocarbon emulsion was produced by mixing 300  $\mu$ l perfluoro-15-crown-5-ether (Chempur Feinchemikalien GmbH, Karlsruhe) with 80 mg of surfactant commixture (resulting in 4 % w/v of final emulsion). Two different compositions of the surfactant commixture were applied in this thesis: one with fluorescent labeling and another one without fluorescent labeling. The exact composition of particles is stated in table 3.1.

**Table 3.1: Composition of surfactant commixture of home-made perfluorocarbon emulsions.** \*: Soy L- $\alpha$ -phosphatidylcholine (Otto Nordwald GmbH, Hamburg), +: cholesterol (Sigma-Aldrich),  $\sim$ : Atto550- or Atto647N-1,2-Dioleoyl-sn-glycero-3-phosphoethanolamine (Atto550- or Atto647N-DOPE, Atto-Tec)

Perfluorocarbon particle	surfactant compounds	molecular weight (g/mol)	mol% of final particle	m/2ml final emulsion
non-fluorescent control particle	L- $\alpha$ -phosphatidylcholine*	775.037	75	68.59 mg
	cholesterol <sup>+</sup>	386.654	25	11.41 mg
fluorescent particle	L- $\alpha$ -phosphatidylcholine*	775.037	74.5	67.78 mg
	cholesterol <sup>+</sup>	386.654	25	11.35 mg
	DOPE-Atto647N or DOPE-Atto550 <sup><math>\sim</math></sup>	1485	0.5	0.87 mg

Following mixing, 1.7 ml sterile 0.9 % NaCl solution was added and the crude emulsion sonicated (Sonifier 250, Branson Ultrasonics, Danbury, CT, USA) with following settings: 20 min non-stop, output control: 7, duty cycle: 22 %. This resulted in perfluorocarbon-filled liposomes of various sizes and thus, to receive a homogenous emulsion with small liposomes, a filtering approach was chosen to exclude large particles. Serial filtration through 1.2  $\mu$ m, 0.7  $\mu$ m and 0.45  $\mu$ m (all filters from msscientific, Berlin) syringe filters proved to be the most efficient way to prevent clogging of filters with liposomes by simultaneously delivering sufficient amounts of final emulsion consisting only of small liposomes. The size distribution of the various perfluorocarbon liposomes was kindly determined by Peter Buschmann (AG Krüger, Organic Chemistry, University of Würzburg) via laser-scattering microscopy. The <sup>19</sup>F signal of three exemplary perfluorocarbon emulsions was measured by magnetic resonance.

### 3.8. Flow cytometry

Flow cytometry was used to identify the immune cells that harbor perfluorocarbon emulsion at the site of infection. Since perfluorocarbon emulsion do not deliver inherent fluorescence signal, fluorescently labeled emulsion had to be applied in order to identify the tracer in cells. Therefore Atto647N-fluorescent perfluorocarbon emulsion was produced according to previously mentioned protocol (see chapter 3.7) and intravenously administered in mice with infection of *S. aureus* in the left thigh muscle at day 2 p.i.. A control group of infected mice received 0.9 % NaCl solution instead of perfluorocarbon emulsion. The infected thigh muscles of both groups were recovered 16 hours post administration and homogenized via pressing through a cell strainer (BD Biosciences, Heidelberg). The resulting cell suspension was diluted with 0.9 % NaCl or PBS and filtered through another cell strainer to exclude cell clumps that might have interfered with flow cytometric analysis. In order to prevent unspecific binding of fluorescently labeled antibodies to Fc receptors, which are frequent on neutrophils, samples were incubated first with FcR Blocking reagent (Miltenyi Biotech, Bergisch Gladbach) for 10 minutes at 4 °C in the dark. Afterwards, the cell suspensions were incubated with either 0.9 % NaCl or various antibody cocktails for 1 hour at 4 °C in the dark. All antibody cocktails consisted of anti-CD11b FITC and anti-Ly6G PE conjugated antibodies (both Miltenyi Biotech, Bergisch Gladbach) but differed in their third antibody. The third was coupled to a fluorescence marker which excited at 405 nm and emitted at 450 nm and was targeted either against CD11c, B220, CD68, CD90.2 or F4/80 (see table 3.2).

**Table 3.2: Antibody mixtures applied in the flow cytometry analysis for the identification of perfluorocarbon emulsion accumulation in immune cells at the site of infection in the *S. aureus* thigh infection model.** \*: from Miltenyi Biotech, #: eBioscience

Flow cytometry mix	Flow cytometer (MACS Quant Analyzer) channel		
	V1 channel	B1 channel	B2 channel
1	no antibodies, incubation with 0.9 % NaCl as control		
2	anti-CD11c-VioBlue*	anti-CD11b-FITC*	anti-Ly6G-PE*
3	anti-B220-VioBlue*		
4	anti-CD68-VioBlue*		
5	anti-CD90.2-VioBlue*		
6	anti-F4/80-PacificBlue#		

After incubation, samples were washed with 1 ml PBS, centrifuged (400 g, 10 min) and the pellet resuspended in 150 – 200 µl FACS buffer. Ten to fifty thousand cells were then analyzed on the flow cytometer (MACS Quant Analyzer, Miltenyi Biotech) using the violet laser (405 nm) and the blue laser (488 nm) with their corresponding FL channels 1 (V1), 2 (B1) and 3 (B2) for determination of cell type by expression of specific antigens and the red laser (635 nm) with its corresponding FL channel 6 (R1) for measuring the perfluorocarbon

emulsion's fluorescence. Results were analyzed with either MACSQuantify (Version 2.4, Miltenyi Biotec) or with Flowing Software (Version 2.5.0 by Perttu Terho, University of Turku, Finland).

### 3.9. Cell sorting

Cell sorting of the immune cell populations at the site of infection was applied as second method besides flow cytometry to identify the cell populations that harbor perfluorocarbon emulsion. Female Balb/c mice were therefore challenged with *S. aureus* Xen29 into the left thigh muscle. 100 µl of commercially available (VS1000H, Celsense) or home-made fluorescent perfluorocarbon emulsion (Atto550 or Atto647N labeled) was administered intravenously at day 2 p.i. and the infected thigh muscle were recovered 16 – 20 hours after tracer administration. The abscess was excised from the surrounding muscle tissue and homogenized by pressing through a 70 µm cell strainer (BD Biosciences, Heidelberg). The resulting cell suspension was further diluted with sterile PBS and filtered through another cell strainer to receive a single cell suspension and remove cell aggregations which might have interfered with cell sorting. Three different cell sorting methods were used in this study: density gradient centrifugation, magnetization-activated cell sorting (MACS) and cell sieving with pluriBeads (Pluriselect, Leipzig).

#### Density gradient centrifugation

First, Histopaque-1083 solution (Sigma-Aldrich) was added to a conical tube. Histopaque-1077 (Sigma-Aldrich) was then carefully layered above. The tissue homogenization single cell suspension was layered on top of the Histopaque gradient and the tube was then centrifuged for 30 minutes at 700 x *g* at room temperature. Granulocytes should aggregate at the Histopaque-1083 / Histopaque-1077 interface, whereas lymphocytes and monocytes should be found at the Histopaque-1077 / aqueous sample remnant.

#### Magnetization-activated cell sorting

The muscle homogenization was filtered through a second 70 µm filter (BD Biosciences, Heidelberg) to exclude cell clumps. The number of cells was then counted and diluted to gain a final concentration of  $1 \times 10^7$  cells / ml. The following cell separation was then performed with either the 'Anti-Ly-6G MicroBead Kit', 'Anti-CD11b MicroBead Kit' or with anti-F4/80-FITC antibodies and 'anti-FITC MicroBeads' (all Miltenyi Biotec). To note, all following steps prior sorting were done without washing the samples in order to prevent loss of perfluorocarbon emulsion that is not incorporated or attached to cells. Single cell suspension was pre-incubated with 'FcR Blocking Reagent' (Miltenyi Biotec) to prevent unspecific binding of antibodies to immune cells via Fc receptors according to manufacturer's instructions. For F4/80+ cell sorting, single cell suspension was then incubated for 30 minutes with anti-F4/80-FITC antibodies (eBioscience, Frankfurt or Miltenyi Biotec) at 4° C

in the dark. Next, anti-FITC MicroBeads (Miltenyi Biotech) were added following manufacturer's instructions and suspension was incubated for 30 minutes at 4 °C in the dark. Regarding Ly6G<sup>+</sup> or CD11b<sup>+</sup> cell sorting, single cell suspension was incubated with anti-Ly6G-biotin or anti-CD11b-biotin antibodies (Miltenyi Biotech) for 30 minutes at 4 °C in the dark. After incubation, anti-biotin MicroBeads were added and the suspension was incubated for 30 minutes at 4 °C in the dark. In the meantime, either XS or LD columns (Miltenyi Biotech) were placed in the separation magnet and rinsed with buffer. Samples were poured after incubation onto the selection / depletion columns and the flow through collected. The column was removed from the separator and the sorted cells were flushed out of the column with an appropriate amount of buffer. Flow-through and sorted cells were then investigated for <sup>19</sup>F signal in the MR scanner.

### Cell sieving with pluriBeads

The number of cells / ml of the single cell suspension (derived from tissue homogenization) was counted with the help of a 'Neubauer chamber' and diluted to achieve a final concentration of  $1 \times 10^7$  cells / ml. The following cell separation was performed with either M-bead kits targeting CD11b or Ly6G antigens (CD11b M-pluriBeads Kit anti-ms or Ly6G M-pluriBeads Kit anti-ms, Pluriselect) or with S-bead kits targeting CD4 or CD19 antigens (CD4 S-pluriBeads Kit anti-ms or CD19 S-pluriBeads Kit anti-ms, Pluriselect) according to the manufacturer's instructions. To note, all following steps prior sorting were done without washing the samples in order to prevent loss of perfluorocarbon emulsion that is not incorporated or attached to cells. Prior sorting, single cell suspension was pre-incubated with 'FcR Blocking Reagent' (Miltenyi Biotech, Bergisch Gladbach) to prevent unspecific binding of antibodies to immune cells via Fc receptors according to manufacturer's instructions. For CD11b and Ly6G, 1.5 ml of single cell suspension was mixed with 500 µl of anti-CD11b or anti-Ly6G-M-beads and for CD4 and CD19, 1 ml of single cell suspension was mixed with 350 µl anti-CD4 or anti-CD19-S-beads. The samples were then incubated for 30 min at room temperature on a roller mixer. The beads are coated with antibodies against the indicated surface antigens, which are characteristic for specific immune cell populations. Thus, cell with the specific antigens on their surface bind to the beads. In the meantime, Pluriselect cell strainers were prepared and after incubation loaded with the bead-sample mixture. The suspension of beads and cells were then pipetted into the proper cell strainer (either S-pluriStrainer or M-pluriStrainer). The beads and thus the bound cells remained in the strainer since they were too large to fit through. The flow-through, containing all antigen-negative cells was collected for analysis. The beads were then taken up into an equally large volume than the original sample. To check for cell sorting filter passage of perfluorocarbon emulsion, a 1:1000 diluted Atto550-labeled tracer sample was pipetted onto either a Ly6G- or a CD4-sorting filter unit. The flow-through was collected and the fluorescence signal (measured by the IVIS system) compared to the pre-sorting sample.

The fluorescent signals of the single cell suspension (prior to sorting), the flow-through and the beads with the bound cells were analyzed in the IVIS system (IVIS Lumina II, Caliper Life



Sciences) with following parameters: exposure, 30 s; FStop, 2; excitation, 535 nm; emission, DsRed; Epi-illumination; lamp level; R, low; field of view (FOV), 12.5; and height, 1.5 cm. The signal was measured in a circular region-of-interest of same size for all samples. As controls served the S- and M-beads only and the single cell suspension of the infected thigh muscle of an infected mouse which had not received fluorescent perfluorocarbon emulsion.

Cell sorting efficiency was investigated by flow cytometry. Therefore, sorted cells were detached from beads by incubation with detachment buffer (supplied with the kit) for 10 minutes in the cell strainer. After incubation, the luer lock of the cell strainer was opened and the released cells collected. Those released cells, the unsorted muscle homogenizate and the flow-through cells were first incubated with FcR Blocking reagent (Miltenyi Biotech, Bergisch Gladbach) for 10 minutes at 4 °C in the dark and then either with a mixture of anti-CD90.2-VioBlue and anti-Ly6G-APC (both Miltenyi Biotech) or with anti-B220-VioBlue (Miltenyi Biotech) and anti-CD11b-PerCP antibodies (eBioscience) for 1 hour 4 °C in the dark. Cells were then washed with 1 ml FACS buffer and the cell pellet resuspended in 200 µl FACS buffer. Flow cytometry was performed on the MACS Quant Analyzer (Miltenyi Biotech). Cell populations were thereby visualized in APC vs. VioBlue or PerCP vs. VioBlue density blots and by histograms of VioBlue, PerCP and APC. The number of CD90.2, B220, Ly6G or CD11b positive cells was measured for all samples in histograms and plotted as ‘% of all visible’ with MACSQuantify (Version 2.4, Miltenyi Biotec) or with Flowing Software (Version 2.5.0 by Perttu Terho, University of Turku, Finland).

### 3.10. Determination of cytokine/chemokine levels

#### Flow cytometry based bead assays

The levels of various cytokines and chemokines at the site of infection in the *S. aureus* thigh infection model were measured with the ‘Mouse Th1/Th2 10plex Ready-to-Use FlowCytomix Multiplex’ or ‘Mouse Chemokine 6plex FlowCytomix Multiplex’ (both eBioscience). In general, infected thigh muscles were recovered and immediately homogenized with a tissue homogenizer (DispoMix, BioLabProducts). The resulting cell suspension was then centrifuged (4000 g, 5 min, room temperature) and the resulting supernatant filtered through a 0.22 µm syringe filter (Merck Millipore) to exclude all cells. 12.5 µl of the resulting cell-free muscle homogenization was then analyzed according to manufacturer’s instructions with the above-mentioned kits.

Briefly, the samples, serial dilutions of defined cytokines/chemokines (12.5 µl each) solutions or buffer (12.5 µl) as negative control were mixed with the corresponding bead mixture (12.5 µl) and detection antibody-biotin mixture (25 µl) in 1.5 ml tubes. The mixture was incubated for 2 h RT in the dark. Cytokines/chemokines bind to the specific beads and detection antibodies during this incubation period. Following incubation, 1 ml of Assay buffer (provided in the kit) was added and all tubes were centrifuged for 5 min at 200 x g at

room temperature. The supernatant was discarded, leaving 100 µl in each tube. In the next step, Streptavidin-PE solution (25 µl) was added and all tubes were incubated for 1 hour at room temperature in the dark. After another washing step with Assay buffer, further 200 µl Assay buffer were added to the residual 100 µl liquid in the tubes and all samples analyzed on the flow cytometer (FACSCalibur, BD Biosciences, Heidelberg).

In principle, the cytokine/chemokine bead kits consisted of various antibody-conjugated beads to target specific cytokines or chemokines in solution. The beads could be distinguished from each other by two parameters: by size and by fluorescence in the FL-3 channel (far red emission) of the cytometer. The different sizes could be distinguished in the FSC vs. SSC plot. The beads bound with their conjugated antibody specifically to cytokines or chemokines in solution. This resulted in concentration dependent bead-cytokine/chemokine complexes. The detection antibody was conjugated to biotin and bound the cytokines/chemokines either in solution or at the surface of the beads. The Streptavidin-PE solution finally bound to the biotin part of the detection antibody. The washing steps removed all soluble components with exception of the beads due to their sedimentation during centrifugation. In the end, this resulted in bead-antibody-cytokine/chemokine-detection antibody-biotin-streptavidin-PE complexes in the final flow cytometry sample. To note, the higher the cytokine/chemokine concentration in serum or homogenate, the more was bound to the beads, the more could be bound by detection antibodies on the beads and the more PE fluorescence marker accumulated at the bead. In consequence, the more cytokine/chemokine was bound to the bead, the higher was the PE fluorescence of the bead. This could be measured in a FL-2 vs. FL-3 density or dot plot and was visualized as 'migrating' bead populations to higher FL-2 fluorescence for higher cytokine/chemokine concentrations.

The flow cytometry gating strategy aimed therefore at measuring the FL-2 fluorescence of each individual bead population in the sample (Fig. 3.2). In order to achieve this goal, the beads were first gated in the FSC vs. SSC dot plot to discriminate the two different sized bead populations. Two FL-2 vs. FL-3 density plots enabled discrimination of the different antigen-specific beads by their intrinsic FL-3 fluorescence. The mean fluorescence intensity of bound PE fluorescence was measured in this plot by defining rectangular regions around the individual beads (same size and geometry for all measurements). A series of samples with defined cytokine/chemokine concentration enabled the generation of a calibration curve and automatic calculation of cytokine/chemokine concentration in the samples with FlowCytomix Pro software (Version 3.0, eBioscience, Frankfurt).

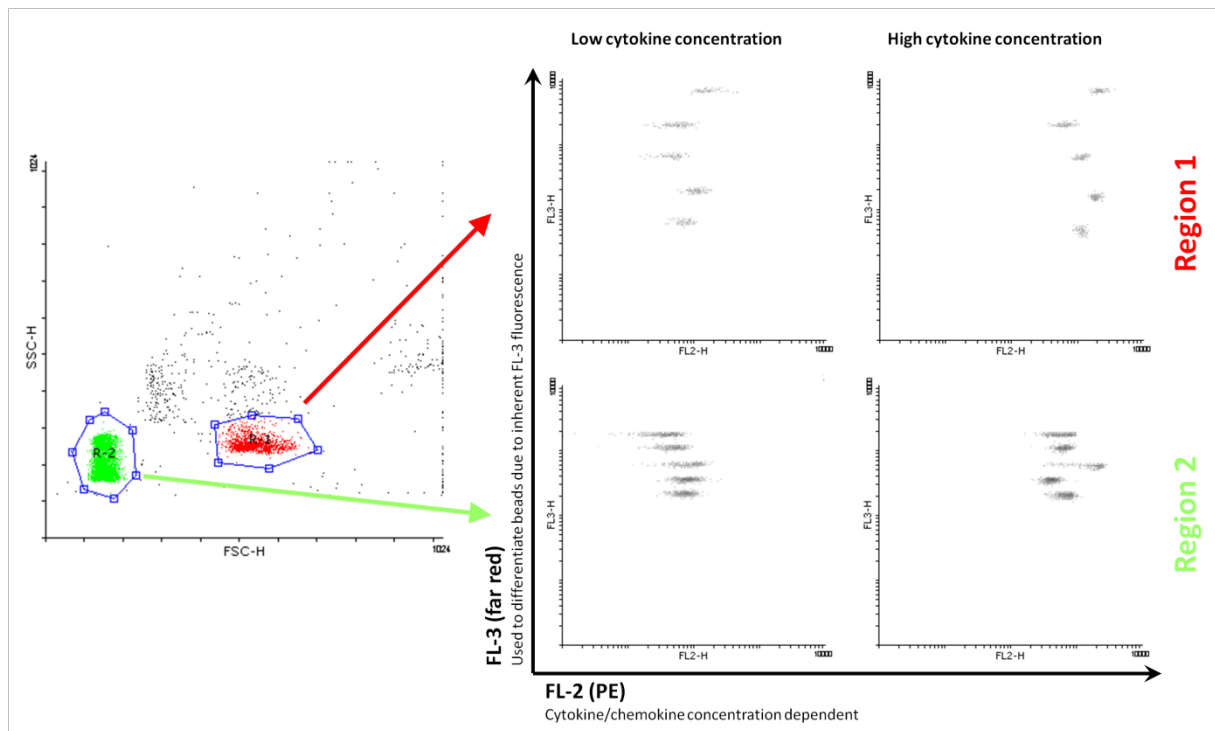


**Fig. 3.2:** Gating strategy of flow cytometry based bead assay to measure cytokine/chemokine concentration at the site of infection. Beads consisted of two different sized populations which could be differentiated in the FSC vs. SSC dot plot. Two FL-2 vs. FL-3 density plots showed then individual antigen-specific bead populations (distinguished by their inherent FL-3 fluorescence) with their cytokine/chemokine concentration dependent FL-2 fluorescence.

### Enzyme-linked immunosorbent assays (ELISA)

As second method to confirm the cytokine results from flow cytometry based assays, two ELISAs were performed to measure the amounts of MCP-1 and IFN $\gamma$  at the site of infection. Both assays were performed according to manufacturer's instructions (Mouse CCL2 (MCP-1) ELISA Ready-SET-Go and Mouse IFN gamma ELISA Ready-SET-Go, both eBioscience).

Briefly, 96well plates were coated with capture antibody in coating buffer overnight at 4 °C. The next day, wells were washed five times (with 1 minute incubation) with wash buffer. Each well was then blocked with assay diluents for 1 h at room temperature. After 5 washing steps with wash buffer, the standard curve was defined by serially diluting a defined cytokine / chemokine concentration. These standard curve samples and the experimental tissue homogenization samples were then added to the 96 well plate and incubated for 2 h or overnight at 4 °C. Following 5 washing steps, the detection antibody – biotin conjugate was added and the well plates were incubated for 1 h at RT. After washing, avidin – HRP (horse radish peroxidase) conjugate was added and incubated for further 30 minutes at RT. Plates were then washed and substrate solution added. After 15 minutes at RT, enzyme reaction stop solution was added and the plates investigated at 450 nm in the ELISA reader.

Standard curve was then generated with software Graph Pad Prism 5 (GraphPad, La Jolla, CA, USA), as well as the concentrations of the unknown, experimental samples determined.

### **3.11. Data analysis and statistics**

Statistical analysis of colony-forming unit, bioluminescence signal and  $^{19}\text{F}$  volume and signal measurements were performed either with GraphPad Prism 5.0 software (GraphPad, San Diego, USA) or with Microsoft Office Excel 2007 (Microsoft, Redmond, WA, USA). Either Kruskal-Wallis with Dunn's post-test or one-way ANOVA with Bonferroni's post test were applied to determine statistical significance between different groups of mice. Bioluminescence values and images were determined/generated with Living Image 3.2 (Caliper Life Science).

## 4. Imaging of *Staphylococcus aureus* infections

*Staphylococcus aureus* infections are a major threat to health care systems worldwide. This opportunistic pathogen is able to provoke a wide array of different diseases including critical, life-threatening ones (Lowy FD, 1998). The emergence of antibiotic resistant *S. aureus* strains has increased the urge for new efficient antibiotics even more. And although a number of new compounds have entered the clinics in the last decade, most novel promising compounds still fail in preclinical or clinical evaluation. Our idea was that in vivo imaging technologies like bioluminescent imaging, positron emission tomography or magnetic resonance imaging might help to get a much clearer picture about the efficacy of promising compounds in preclinical animal models and they might additionally help to identify possible toxic side effects, too. Unfortunately, the above-mentioned imaging technologies, maybe with the exception of bioluminescent imaging, are not evaluated in detail to visualize infections in small animal disease models. Therefore, the first experimental chapter of this work deals with the evaluation of two imaging modalities: bioluminescent imaging (BLI) and magnetic resonance imaging (MRI). Regarding MRI, the basic idea was on one hand to test different native proton-based MR sequences for visualization of tissue changes by the infection itself while on the other hand the application of MR active contrast agents or tracers might lead to an accumulation at the site of infection and thus might visualize the infection indirectly. Two contrast agent/tracer based MR methods should be investigated in this study due to their accumulation in immune cells after intravenous administration: ultrasmall ironoxide nanoparticles and perfluorocarbon emulsions. The imaging experiments were in this context based on one animal model of *S. aureus* infection: the thigh infection model. Thus the following part of this work describes the evaluation of this animal model, the infection imaging experiments and the influence of  $^{19}\text{F}$  magnetic resonance imaging of perfluorocarbon emulsions, a modality applied to investigate these questions for the first time, on the outcome of the infection experiments and possible acute toxic side effects caused by the application of the tracer substance.

## 4.1. Results

### 4.1.1. The *S. aureus* thigh infection model

Before trying to visualize infections in vivo with bioluminescence and/or magnetic resonance imaging, the animal model had to be chosen and evaluated first. The *S. aureus* thigh infection model was selected, because it leads to a localized infection with a bulky abscess and therefore predefines the region of interest for imaging experiments. It is of clinical importance since this type of infection is commonly associated with methicillin-resistant *S. aureus* strains and might lead in human patients to systemic infections like sepsis (King MD et al. 2006, Boucher HW, Corey GR. 2008).

Female Balb/c mice were therefore infected into the left thigh muscle with  $2.2 \times 10^8$  CFU *S. aureus* Xen29, a derivative of *S. aureus* ATCC 12600 with a chromosomally integrated *luxABCDE* operon that confers luciferase expression and activity in metabolically active bacteria (Francis KP et al. 2000). The infected thigh muscle, liver, spleen and the kidneys were recovered at different time points after start of infection to determine the bacterial burden in terms of colony-forming units. The overwhelming number of bacteria (over 99.99 % at all time points) could be found at the site of initial infection, the thigh muscle. The CFU numbers were rather stable in the infected thigh muscle with small increase between day 1 p.i. and day 3 p.i. and a small decrease between day 3 p.i. and day 7 p.i., but the differences were statistically not significant (Fig. 4.1 A). The strongest variation of bacterial burden could be seen between the initial injection of bacteria into the thigh muscle ( $2.2 \times 10^8$  CFU) and day 1 p.i. (slightly above  $10^9$  CFU), suggesting strong growth in the first 24 h p.i.. Small numbers of bacteria could be detected by plate counting regularly in the liver and sporadically in the spleen and kidneys with a similar pattern than in the thigh muscle (Fig. 4.1 B – D): a small increase of median CFU numbers between day 1 p.i. and day 3 p.i. and a slight decrease between day 3 p.i. and day 7 p.i., but the only statistically significant difference was for CFU in the liver at day 3 p.i. vs. CFU in the liver at day 7 p.i., indicating decrease in this organ or decreased systemic spreading from the primary source of infection, the thigh muscle. Overall, the highest isolatable bacterial numbers in the investigated organs could be seen at day 3 p.i., and a slight or significant decrease was measured for all organs until day 7 p.i.. It has to be mentioned, that about 30 – 50 % of the spleen and kidney samples showed no colonies on the agar plates after homogenization, serial dilution and plating of the organs (but due to experimental setup, these samples received values at the detection limit). This proves the lack of systemic infection, a disease that can evolve in human patients following skin, skin-structure or deep tissue infections with *S. aureus* (King MD et al. 2006, Boucher HW, Corey GR. 2008).

The injection of the bioluminescent *S. aureus* strain Xen29 enabled non-invasive bioluminescence imaging in parallel to the tissue recovery for CFU determination. Imaging was performed in a small animal in vivo imaging device for detection of bioluminescence and fluorescence signal (IVIS Lumina 2, Caliper Life Science). The average radiance signal was

very strong immediately after infection (5 – 15 min post infection). After the first 24 h of infection, a strong drop of photon emission was seen, but signal recovered to a lower level than initially until 48 h p.i. (Fig. 4.1 E). The signal then stayed in a slowly increasing plateau phase until the end of the experiment at day 7 p.i.. With the exception of the bioluminescence development within the first 24 h, the results of CFU determination and bioluminescent imaging were congruent in showing a rather stable phase of bacterial burden in the infected thigh muscle.

Histological examination (Fig. 4.1 F) of recovered muscles at day 3 p.i. showed a massive infiltrate of neutrophils with interspersed macrophages/monocytes and the intact muscle fibers (appearing as rose bundles due to hematoxylin-eosin staining). The immune cells surrounded a central necrotic area. Histological slices from muscles recovered at day 7 p.i. showed similarly neutrophils as the predominant immune cell population at the site of infection, but with a slightly higher macrophage/monocyte content and fibroblast-enriched granulation tissue. The immune cells accumulated at this time point around a bulky area of necrosis.

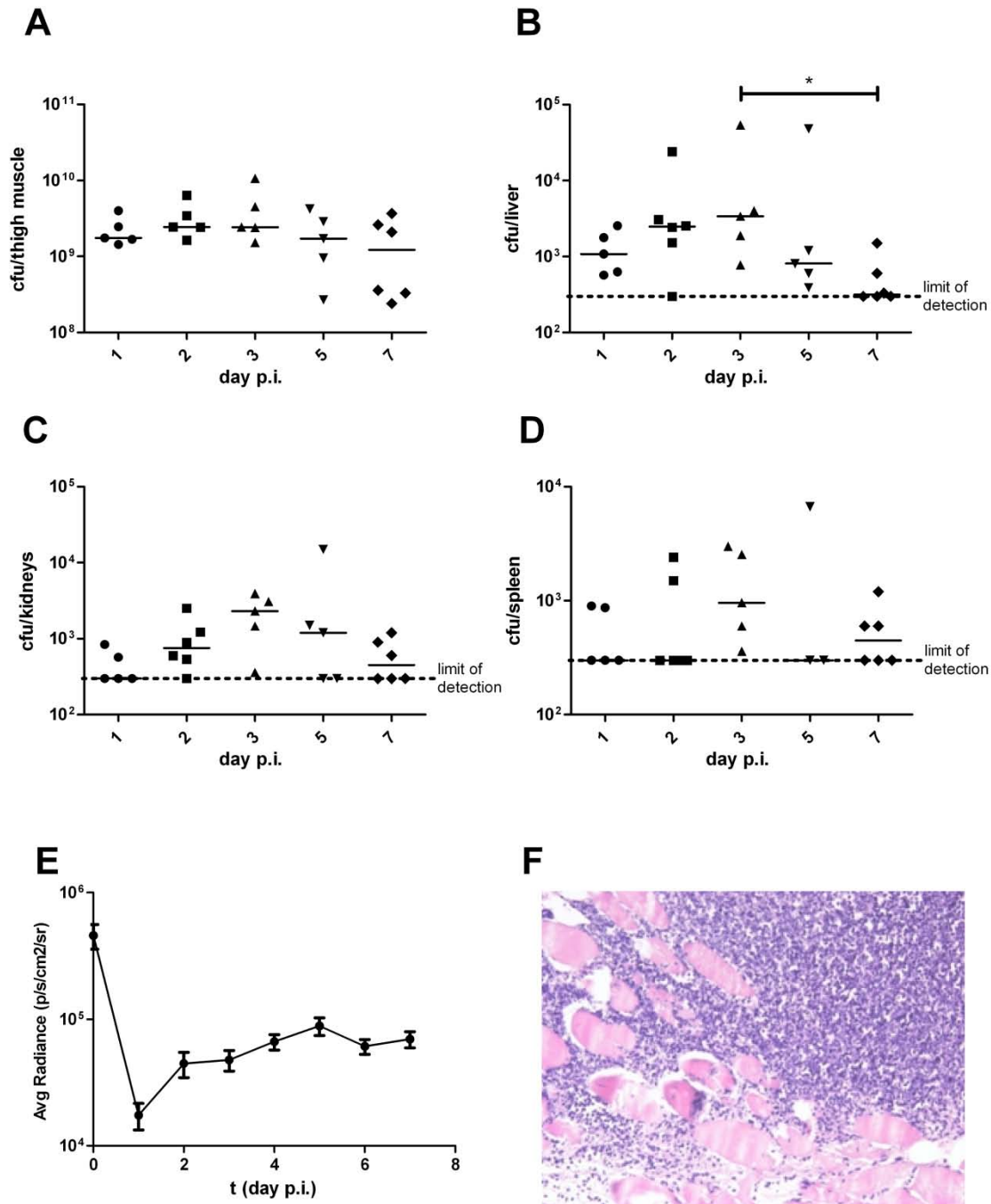


**Fig. 4.1: CFU values and bioluminescence signal over time, as well as histological appearance of infection in the *S. aureus* thigh infection model.** Mice ( $n = 5 - 6$  per indicated time point) were challenged with ca.  $2.2 \times 10^8$  CFU *S. aureus* Xen29 into the left thigh muscle. **A – D:** Shown are the single CFU values and the respective medians determined for the infected thigh muscles (A), livers (B), kidneys (C) or spleens (D) at indicated time points after start of infection. Organs were harvested, homogenized and serial dilutions plated on B-agar. **E:** Development of mean bioluminescent signal  $\pm$  SEM during the course of infection (6 animals). Mice were imaged immediately after infection (+ 5 min, shown as time point 0), and then every 24 h. The average radiance signal was measured in a manually defined region of interest (same size and geometry for all mice). **F:** Exemplary hematoxylin – eosin stained section of a paraffin – embedded, formalin – fixed thigh muscle. Muscle was recovered at day 3 p.i.. Statistical significant differences are indicated with asterisk (\*:  $P < 0.05$ ).



#### 4.1.2. Native, proton-based magnetic resonance imaging

After establishing the thigh infection model with *S. aureus* Xen29 and imaging of bacterial burden via bioluminescence imaging in the first part of this chapter, the experiments in the following were performed to visualize *S. aureus* infections in the thigh muscle with magnetic resonance imaging. Female Balb/c mice were therefore infected with  $2.2 \times 10^8$  CFU *S. aureus* Xen29 and magnetic resonance imaging was performed at several time points after start of infection. A variety of different MR protocols were tested for visualization of changes in signal pattern in the infected thigh muscle (data not shown), but in the end, only T<sub>2</sub> weighted MR methods proved to visualize clear changes in the infected thigh muscle without indicating changes in the control muscle which was inoculated with sterile 0.9 % NaCl solution (Fig. 4.2). Imaging at several different days after start of infection showed increased T<sub>2</sub> values in the infected thigh muscle, but not in the non-infected, 0.9% NaCl solution inoculated one. This was congruent with earlier studies that demonstrated increased T<sub>2</sub> relaxation times at sites of inflammation in *S. aureus* infection models (Marzola P et al. 1999, Kaim AH et al. 2002). The area of prolonged T<sub>2</sub> relaxation times was in these and other studies correlated with an area of massive immune cell immigration, tissue destruction and edema formation (Kaim AH et al. 2003). The differences in T<sub>2</sub> signal between infected and control muscle could at least be seen at day 2 p.i. and lasted until the end of the experiment at day 10 p.i.. Interestingly, the area of heightened T<sub>2</sub> values became slightly larger between day 2 and day 6 p.i., but decreased in size until day 10 p.i.. Nonetheless, the area of prolonged T<sub>2</sub> relaxation times was of rather diffuse shape in most MR images and, even more important, a clear distinction between infected and non-infected thigh muscle tissue remained impossible due the high variations in T<sub>2</sub> relaxation times and the lack of a clear border between heightened and normal T<sub>2</sub> values.

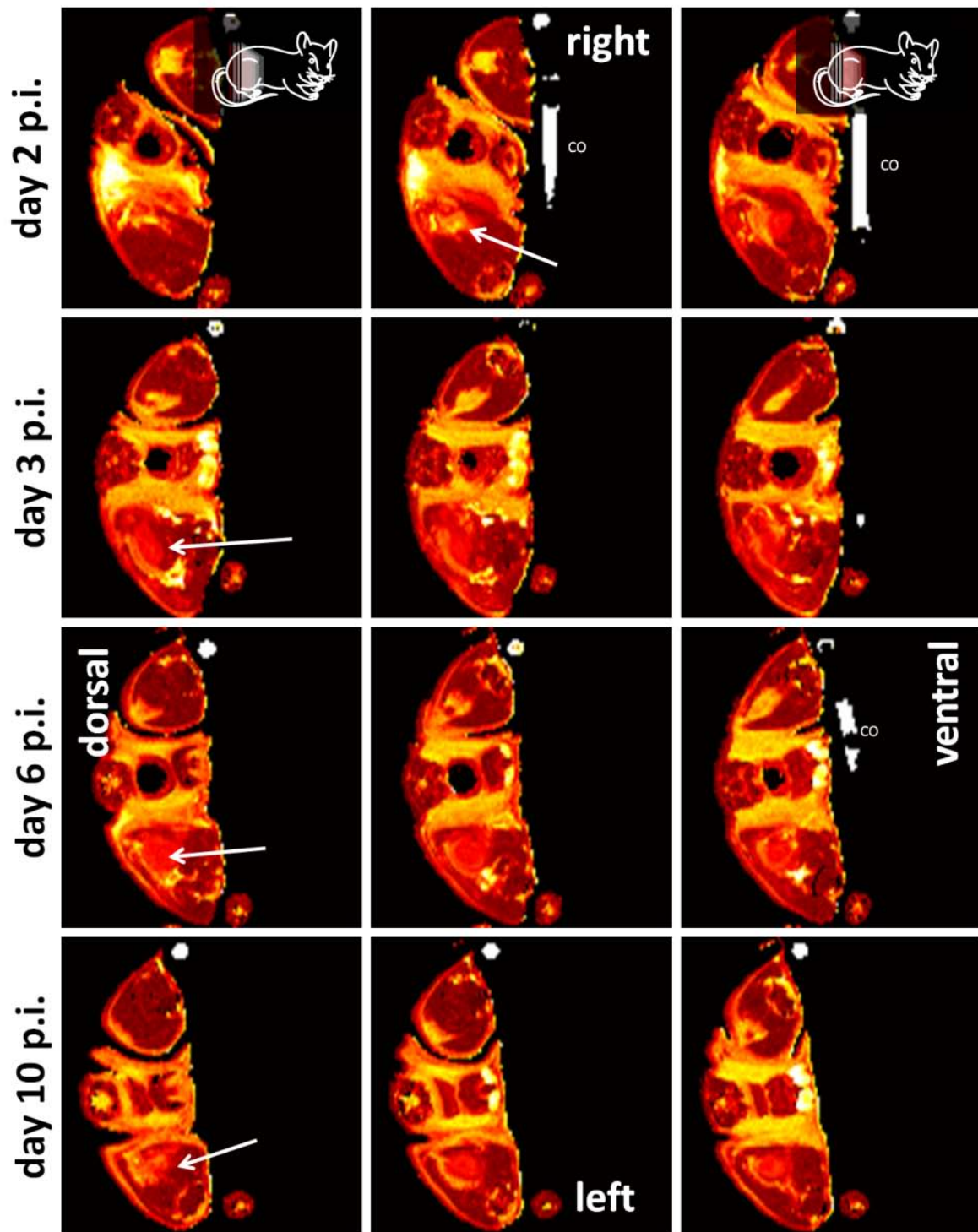


**Fig. 4.2:** Consecutive transversal T<sub>2</sub> maps of one representative mouse imaged at day 2 (first row), day 3 (second row), day 6 (third row) and day 10 p.i. (fourth row). A group of mice (n = 5) was challenged with  $2.2 \times 10^8$  CFU *S. aureus* Xen29 in the left thigh muscle. MR imaging was performed at the indicated time points and three consecutive T<sub>2</sub> map slices of one representative mouse are shown. Mouse drawing indicates the location and orientation of the MR imaging slice. (co: control tube). For illustration, arrows point at the area of elevated T<sub>2</sub> relaxation times (only in the first row of pictures).

### 4.1.3. Imaging of iron oxide (CLIO) particles at the site of infection

The lack of clear identification of infected tissue by native proton-based MR method made it inevitable to evaluate contrast agent based methods to define and visualize the area of infection. Cross-linked ironoxide nanoparticles have been shown to accumulate at sites of inflammation and infection, thus enabling visualization of site of infection and the quantification of severity of disease (Kaim AH et al. 2002, Kaim AH et al. 2003). The most suitable methods to visualize this accumulation are  $T_2$  or  $T_2^*$  weighted methods. The administration of CLIO particles at acute phase of inflammation (day 2 p.i.) led to detectable susceptibility effects at the abscess area 24 h after injection (Fig. 4.3 two upper rows). The 'black' rim could be visualized by both  $T_2$  and  $T_2^*$  maps and indicates accumulation of CLIO particles which induced signal distortion. A similar 'black' rim accumulation pattern in the abscess area could be seen when CLIO particles were administered at day 6 p.i. and imaging was performed at day 7p.i.. To test for specificity of CLIO accumulation at the site of infection, 0.9 % NaCl solution was administered into the right thigh muscle of mice. This injection did not lead to abscess formation, as expected due to the lack of pathogens, and, notably, not to accumulation of contrast agent in the right thigh muscle. But although CLIO accumulated specifically at both time points at the rim of the abscess area, its accumulation pattern did not always allow distinction of infected and not-infected tissue areas. The accumulation was sparse and rather diffuse when visualized by  $T_2$  weighted MRI especially at acute phase of inflammation (day 3 p.i., Fig. 4.3 upper row). Visualization of CLIO accumulation with  $T_2^*$  weighted MRI delivered a much clearer picture, but the intrinsic variation in signal strength complicated the identification of anatomical context. The signal distortion effect prevents furthermore the visualization of edema formation (indicated by longer  $T_2$  relaxation times) in the CLIO accumulation region.

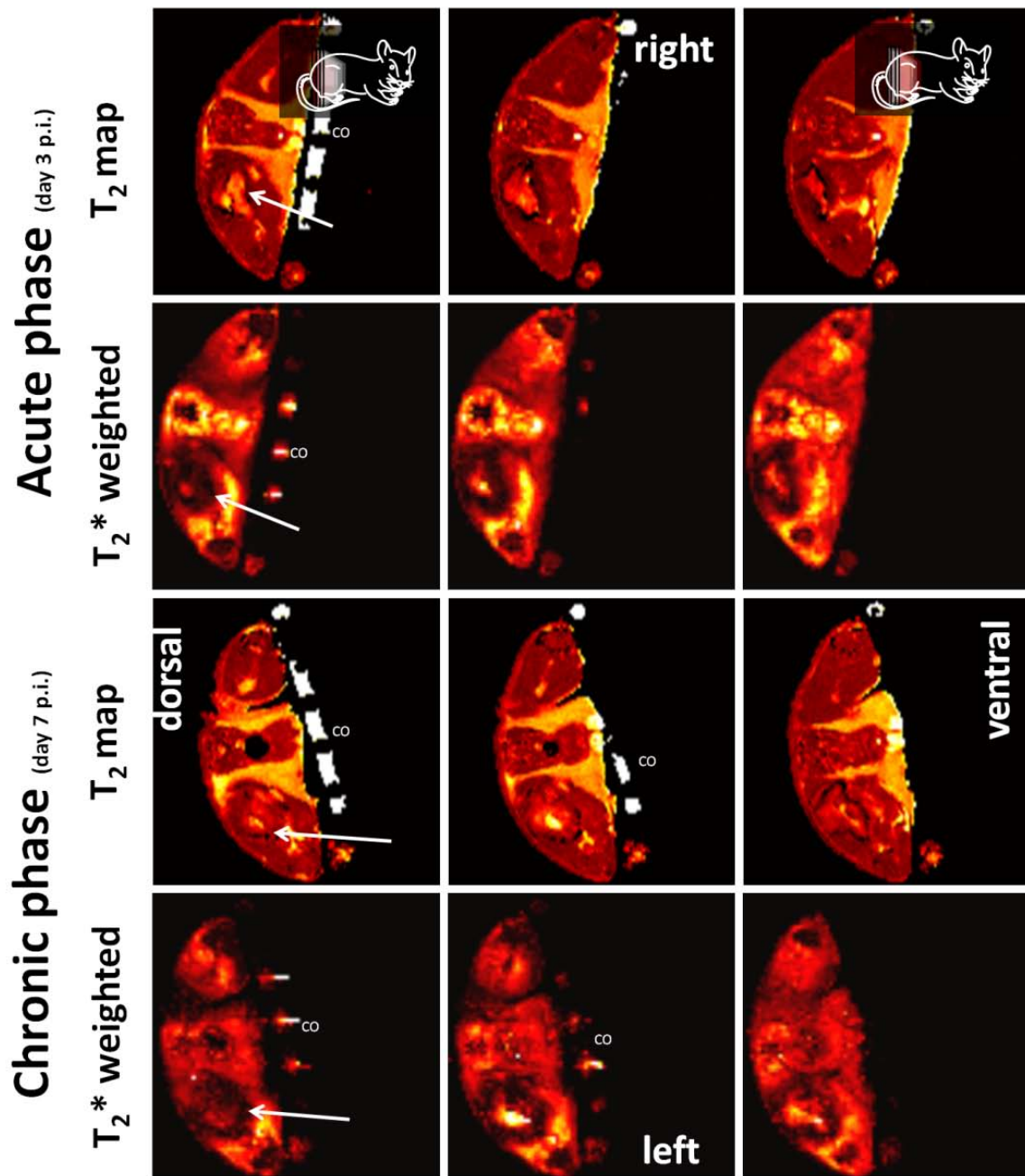


**Fig. 4.3:**  $T_2$  maps and  $T_2^*$  weighted MR images of one representative CLIO treated mouse at day 3 (upper two rows) and day 7 p.i. (lower two rows) visualize signal distortion effects at the rim of the abscess area. A group of mice ( $n = 4$ ) was challenged with  $2.2 \times 10^8$  CFU *S. aureus* Xen29 in the left thigh muscle and with 0.9 % NaCl solution in the right thigh muscle. CLIO particles were administered intravenously at day 2 p.i.. MR imaging was performed 24 h after administration and at day 7 p.i.. Three consecutive slices of one representative mouse are shown for each method at both time points. Mouse drawing indicates the location and orientation of the MR imaging slice. (co: control tube). For illustration, arrows point at the area of CLIO accumulation and thus signal distortion (only in the first row of pictures).

#### **4.1.4. Accumulation of perfluorocarbon emulsion at the site of infection**

A second MR agent based method to visualize inflammation by magnetic resonance imaging is  $^{19}\text{F}$  MRI of intravenously administered perfluorocarbon emulsions. It has been shown recently that the application of perfluorocarbon emulsions during the course of various diseases which are linked to inflammation led to accumulation of  $^{19}\text{F}$  signal at the site of inflammation. Perfluorocarbon emulsion accumulated, for example, at the rim of brain damage in an ischemia model or at the heart muscle in a stroke model (Flögel U et al. 2008). Nonetheless, at the beginning of this PhD thesis, no experiments were described in literature that utilized and evaluated this method to locate and image sites of infection or accompanying inflammation. Consequently, the following experiments were conducted to test whether this method is capable to visualize *S. aureus* thigh infections in the mouse.

##### ***4.1.4.1. Administration of perfluorocarbon emulsion led to a 'hollow sphere' accumulation pattern in the infected thigh muscle***

To test for specific accumulation of perfluorocarbon emulsion at the site of infection, female Balb/c mice were injected with *S. aureus* Xen29 into the left thigh muscle and with the carrier substance 0.9 % NaCl solution into the right thigh muscle. In conclusion, the following experiments are conducted with the same setting than those described in chapter 4.1.3 with the exception of the applied contrast agent/tracer, thus enabling direct comparison of CLIO and perfluorocarbon emulsions as contrast delivering substances to visualize sites of infection with MRI. In contrast to CLIO particles, perfluorocarbons cannot be visualized with  $^1\text{H}$  based MR methods, but only with specific  $^{19}\text{F}$  magnetic resonance methods. Since the mammalian body does not harbor sufficient amounts of  $^{19}\text{F}$ , a second  $^1\text{H}$  based image is necessary to visualize the anatomical context of perfluorocarbon accumulation. Therefore,  $^{19}\text{F}$ -SSFP CSI images were overlaid on  $^1\text{H}$ -TSE images to visualize the anatomy of the site of infection and the accumulation of the PFC tracer (Fig. 4.4).

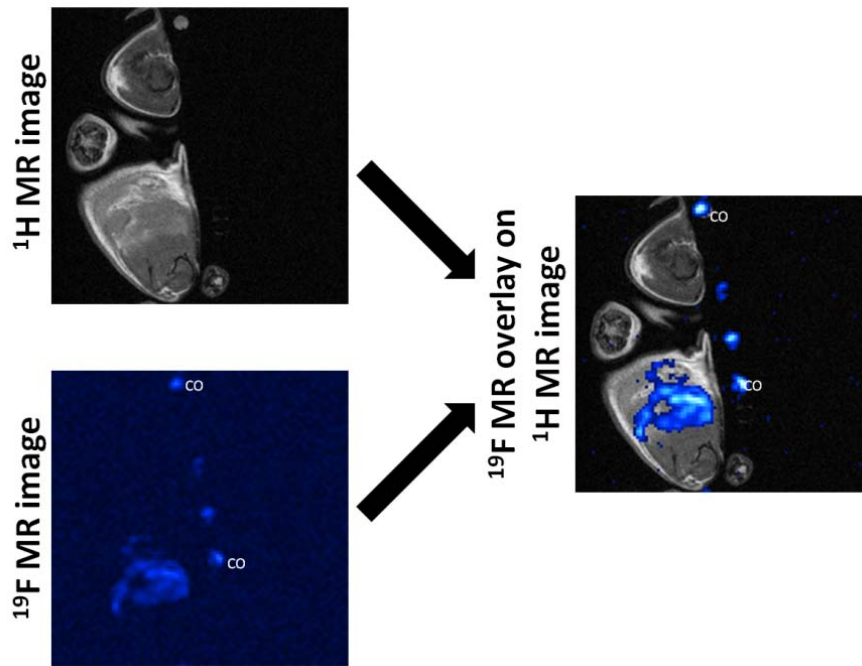


**Fig. 4.4:** Principle of  $^{19}\text{F}$  MR imaging with perfluorocarbon emulsions as MR active tracer.  $^1\text{H}$  TSE MR images served to visualize the anatomy of the infected thigh muscle, while  $^{19}\text{F}$ -SSFP CSI images visualized the accumulation of perfluorocarbon emulsion at the site of infection. Both images can be overlaid, since the investigated animal is quiescent and has not to be moved throughout and between the measurements. In this case, female Balb/c mouse was challenged with  $2.2 \times 10^8$  CFU *S. aureus* Xen29 in the left thigh muscle and with sterile 0.9 % NaCl solution in the right thigh muscle. Perfluorocarbon emulsion was administered intravenously at day 7 p.i. and accumulation at the site of infection was imaged with MRI at day 10 p.i.. (co: control tube)

Intravenous administration of perfluorocarbon emulsion during acute phase of inflammation (at day 2 p.i.) and MR imaging 24 h later showed accumulation of  $^{19}\text{F}$  in the infected left thigh muscle, but not in the 0.9 % NaCl treated right muscle, indicating specificity of perfluorocarbon accumulation at spots of severe inflammation and infection. The tracer accumulated at the rim of the area that showed extended  $T_2$  relaxation times (compared to surrounding muscle tissue), that is, at the rim of the edema area (Fig. 4.4). To note, no accumulation of perfluorocarbon could be detected in the center of the edema area. Consecutive MRI slices or the 3D reconstruction from the site of infection visualized a ‘hollow sphere’ pattern of  $^{19}\text{F}$  accumulation around the abscess area (Fig.4.5).

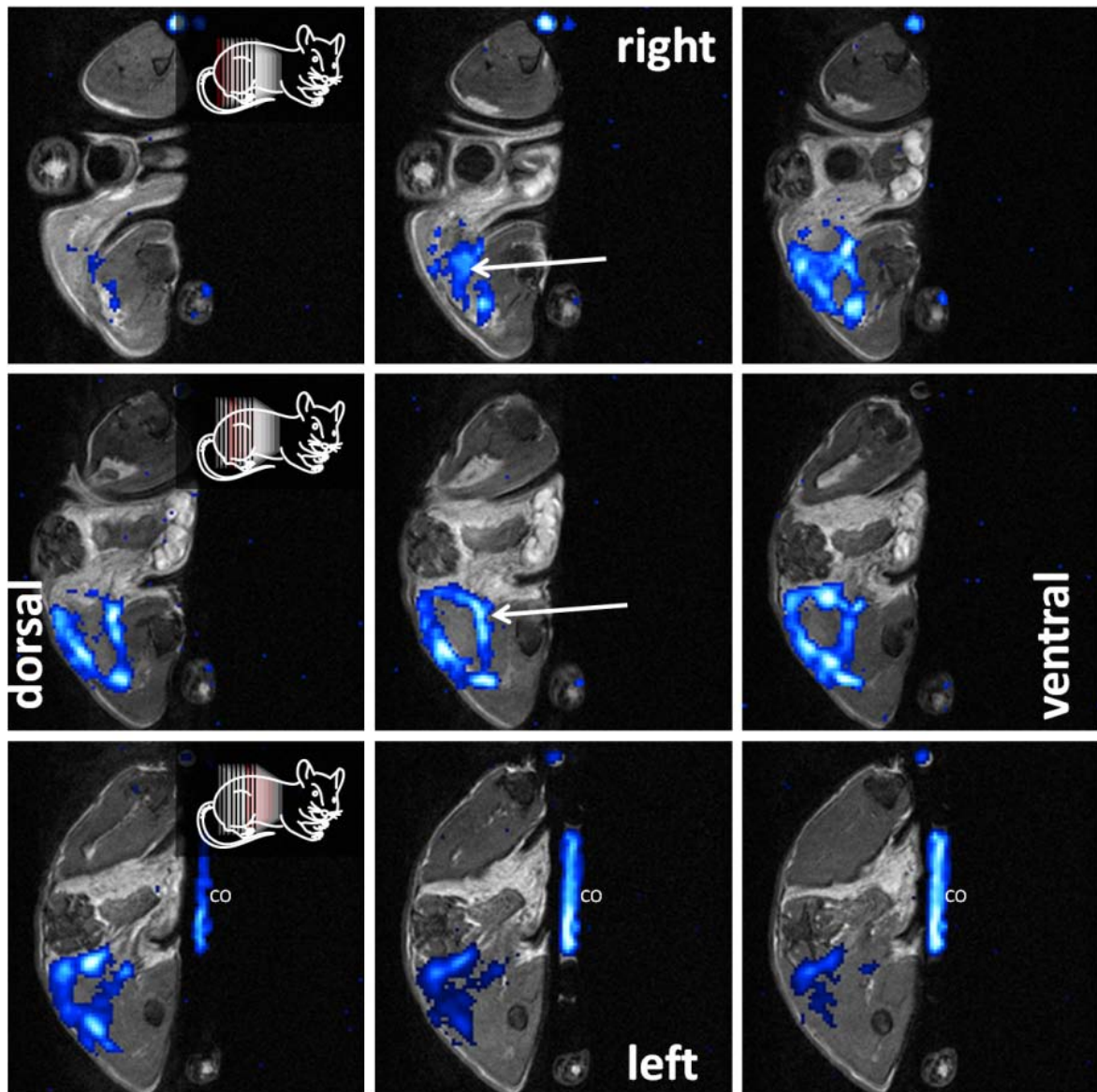


**Fig. 4.5:**  $^{19}\text{F}$ -SSFP CSI overlays (blue color scale) on  $^1\text{H}$  TSE images (grayscale) shows accumulation of  $^{19}\text{F}$  at the rim of the abscess area in the shape of a ‘hollow sphere’ in one representative mouse at acute phase of inflammation. Female Balb/c mice ( $n = 5$ ) were challenged with  $2.2 \times 10^8$  CFU *S. aureus* Xen29 in the left thigh muscle and with sterile 0.9 % NaCl solution in the right thigh muscle. Perfluorocarbon emulsion was administered intravenously at day 2 p.i. and accumulation at the site of infection was imaged with MRI at day 3 p.i.. The mouse drawing indicates location and orientation of the consecutive slices in anatomical context. This whole series of images was generated out of one measurement of one representative mouse. (co: control tube)

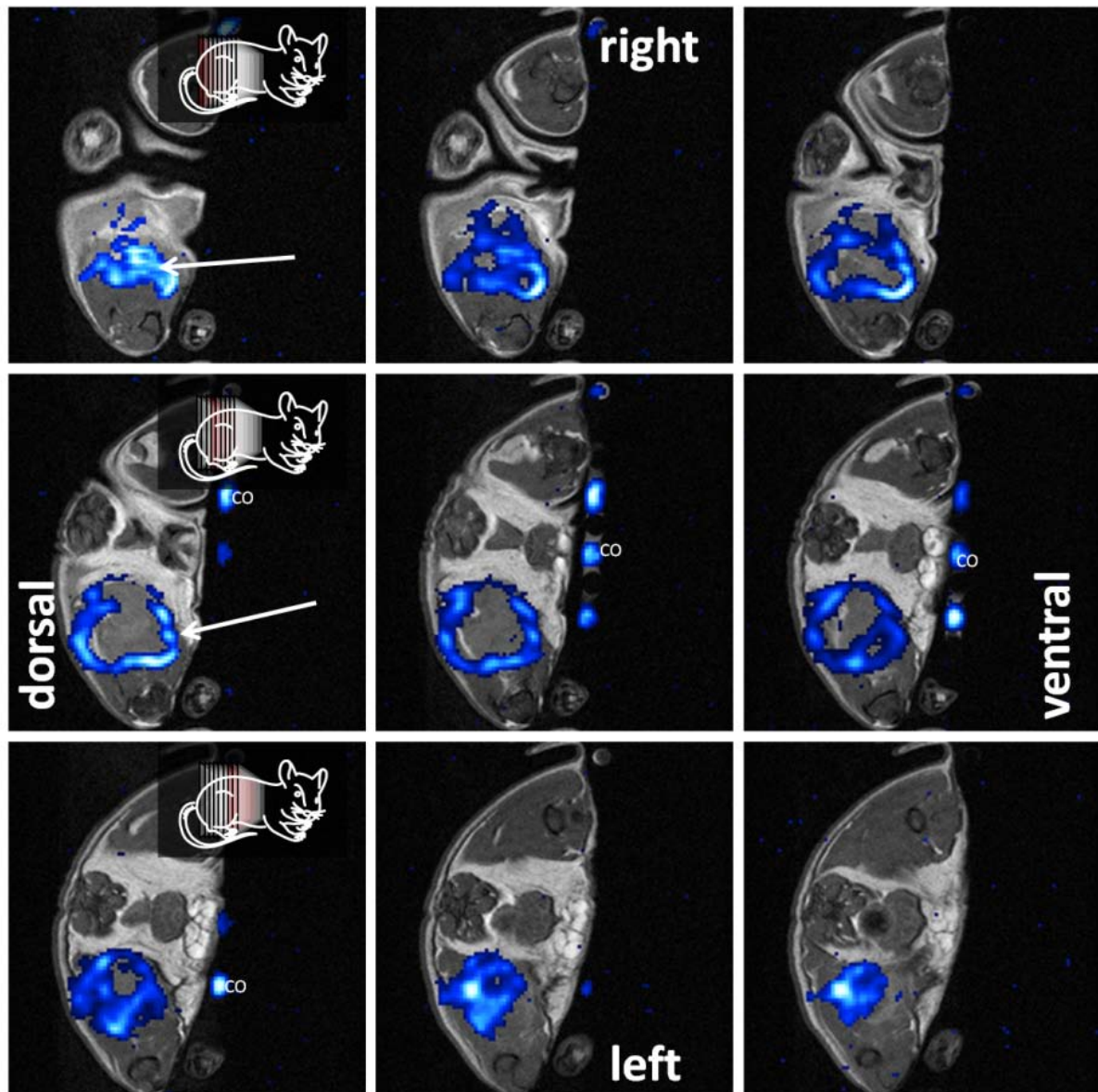


**Fig. 4.6:**  $^{19}\text{F}$ -SSFP CSI overlays (blue color scale) on  $^1\text{H}$  TSE images (grayscale) shows accumulation of  $^{19}\text{F}$  at the rim of the abscess area in the shape of a ‘hollow sphere’ in one representative mouse at chronic phase of inflammation. Female Balb/c mice ( $n = 5$ ) were challenged with  $2.2 \times 10^8$  CFU *S. aureus* Xen29 in the left thigh muscle and with sterile 0.9 % NaCl solution in the right thigh muscle. Perfluorocarbon emulsion was administered intravenously at day 8 p.i. and accumulation at the site of infection was imaged with MRI at day 9 p.i.. The mouse drawing indicates location and orientation of the consecutive slices in anatomical context. This whole series of images was generated out of one measurement of one representative mouse. (co: control tube)



To investigate the accumulation of perfluorocarbon emulsion at the site of infection during chronic phase of inflammation, female Balb/c mice received a single intravenous administration of emulsion at day 8 p.i. and accumulation was imaged 24 h later with  $^{19}\text{F}$  MRI. Congruent with the results from acute phase, only the infected thigh muscle showed  $^{19}\text{F}$  signal, but not the non-infected 0.9 % NaCl solution treated muscle. Perfluorocarbon emulsion accumulated at the rim of the edema area (with higher  $T_2$  values) and formed a 'hollow sphere' pattern, with the lack of  $^{19}\text{F}$  signal in the center of the abscess area (Fig. 4.6).

Importantly, the infection or inflammation itself did not induce higher  $^{19}\text{F}$  values, because without intravenous administration of perfluorocarbon emulsion, no  $^{19}\text{F}$  signal could be detected in the field of view at any time point, neither at acute nor at chronic phase of inflammation (data not shown). Furthermore, intravenous administration of perfluorocarbon emulsion into non-infected mice did not lead to any detectable  $^{19}\text{F}$  signal in the thigh muscle (data not shown).

#### ***4.1.4.2. Variation of perfluorocarbon administration or imaging time points resulted in different $^{19}\text{F}$ accumulation patterns***

Administration of perfluorocarbon emulsion led at both, acute and chronic phase of inflammation, to a stable and strong  $^{19}\text{F}$  'hollow sphere' accumulation pattern in the infected thigh muscle. But to date, the imaging was performed only at 24 h post administration and the following experiments were therefore designed to learn more about the accumulation kinetics of perfluorocarbon emulsion at the site of infection.

To study the durability of  $^{19}\text{F}$  signal and thus perfluorocarbon emulsion accumulation at the site of infection, mice (n = 3 per group) with *S. aureus* Xen29 infection of the thigh muscle received a single intravenous administration of perfluorocarbon emulsion at day 2 p.i.. MR imaging started 24 h later and the mice were then imaged every 48 h until day 9 or 10 p.i. to reveal variations in the  $^{19}\text{F}$  accumulation pattern. But beginning with the first measurement and ending with the last one, a 'hollow sphere' accumulation pattern could be visualized in all mice at all time points when infected with a similar amount of bacteria than applied in the earlier experiments ( $1.1 \times 10^8$  CFU, see Fig. 4.7 third and fourth row). In addition, the  $^{19}\text{F}$  signal remained stable in terms of pattern and intensity in all imaged mice of this group, indicating enduring perfluorocarbon accumulation at the rim of the edema area. In contrast to this showed mice that were infected with smaller numbers of bacteria a different  $^{19}\text{F}$  signal pattern at late stages of the infection. While  $^{19}\text{F}$  MRI at day 3 and day 6 p.i. revealed a similar pattern than seen in mice with higher infectious dose, namely the 'hollow sphere' accumulation of perfluorocarbons at the site of infection, the images generated at days 8 and 10 p.i. showed only sparse and diffuse accumulation at the rim of the abscess area (Fig. 4.7 first and second row). This loss of  $^{19}\text{F}$  signal was accompanied by a reduction of bioluminescence signal at the site of infection (data not shown). The determination of colony-forming units at the end of the experiment showed only minor bacterial burden in this low-infection dose group mice (between  $1.8 \times 10^3$  and  $3.2 \times 10^6$  compared to ca.  $10^9$  CFU

for the high-infection dose group). In conclusion, the disappearance of  $^{19}\text{F}$  signal at the site of infection in the low-infection dose group was accompanied by a reduction of bacterial burden, suggesting spontaneous healing or the failure of *S. aureus* to establish chronic infection in the thigh muscle at this initial inoculum.

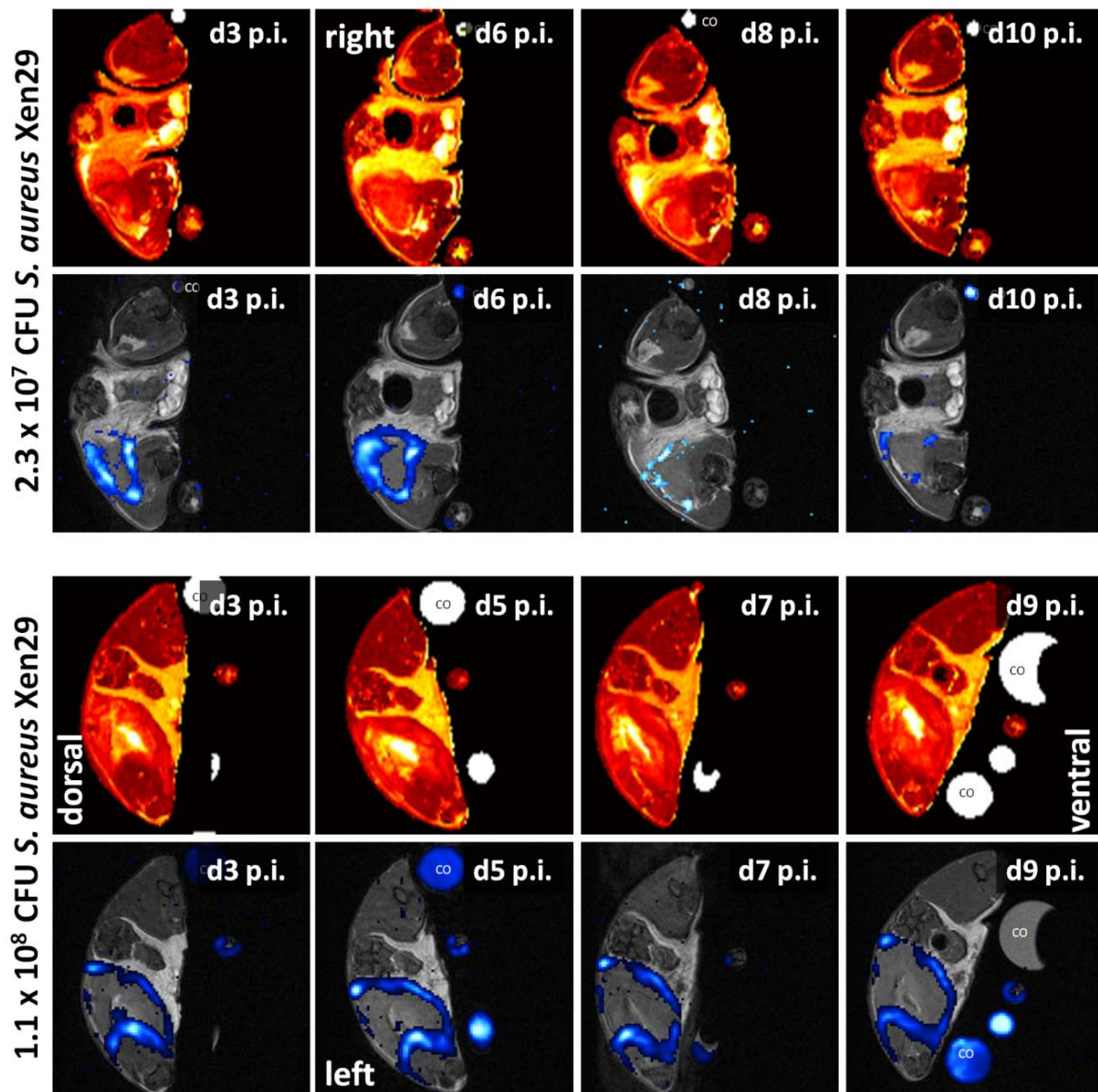


**Fig. 4.7:** Influence of infectious dose on durability of  $^{19}\text{F}$  accumulation at the site of infection. Female Balb/c mice were challenged with either  $2.3 \times 10^7$  (two upper rows) or with  $1.1 \times 10^8$  CFU *S. aureus* Xen 29 in the left thigh muscle. Perfluorocarbon emulsion was intravenously administered at day 2 p.i. and mice were then investigated with MRI at the indicated time points.  $T_2$  maps of the edema formation in one representative mouse of each group are shown in rows 1 and 3, while  $^{19}\text{F}$ -SSFP CSI overlays on  $^1\text{H}$ -TSE images are shown in rows 2 and 4. (co: control tube)

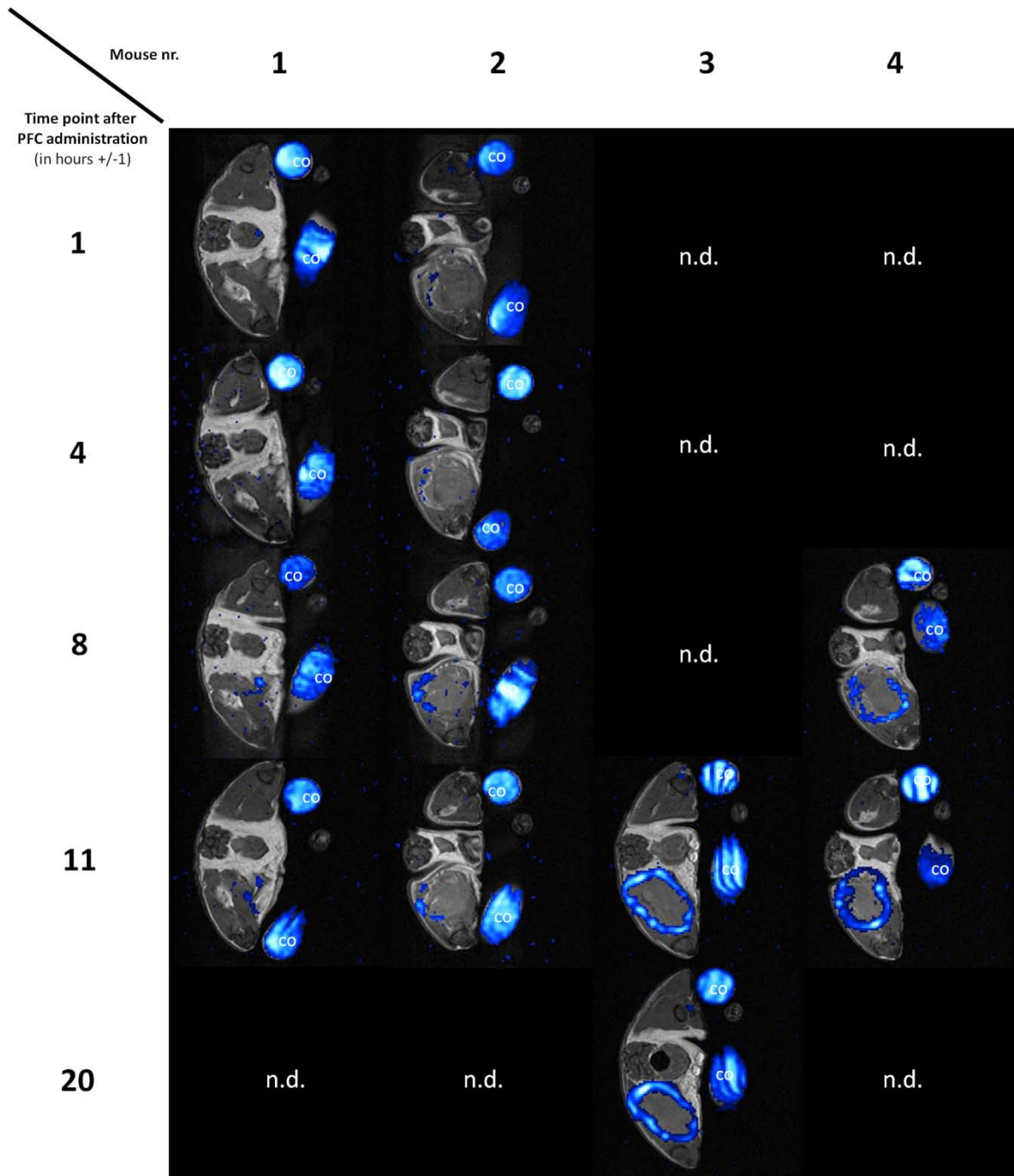


**Fig. 4.8:**  $^{19}\text{F}$ -SSFP CSI overlays (blue color scale) on  $^1\text{H}$  TSE images (grayscale) of four mice at different time points after administration of perfluorocarbon emulsion indicate  $^{19}\text{F}$  accumulation kinetics at the site of infection. Mice were challenged with  $1.9 \times 10^8$  CFU *S. aureus* Xen29 in the left thigh muscle and perfluorocarbon emulsion was administered at day 2 p.i.. Mice were then imaged at indicated time points after administration of perfluorocarbon emulsion to determine the first time point of emergence of visualizable  $^{19}\text{F}$  accumulation pattern in the infected thigh muscle. (n.d.: not determined)

The next aim was to learn more about the accumulation kinetics of perfluorocarbon emulsion at the site of infection. Four mice were therefore infected with  $1.9 \times 10^8$  CFU *S. aureus* Xen29 in the left thigh muscle and perfluorocarbon emulsion was administered intravenously at day 2 p.i.. Former experiments in this chapter demonstrated, that this application leads to a visualizable accumulation of  $^{19}\text{F}$  at the rim of the abscess area, but to date, it was unknown, at which time point exactly the accumulation reaches a signal level that enables imaging. To investigate this, mice were investigated with  $^{19}\text{F}$  MRI at different time points immediately after administration of the emulsion, but before 24 h post administration. Until 8 h post administration almost no  $^{19}\text{F}$  signal could be detected in the infected thigh muscle (Fig. 4.8). Two out of four mice showed the ‘hollow sphere’ accumulation pattern at 11 h post administration, suggesting that the perfluorocarbon accumulation reaches visualization limit at around 10 to 12 h post administration (for this combination of infectious dose and perfluorocarbon administration time point).

Furthermore, by now, only two time points have been tested for administration of perfluorocarbon emulsion during course of infection: acute (day 2 p.i.) and chronic (day 8 p.i.) phase of infection and inflammation.  $^{19}\text{F}$  MR imaging revealed for both cases accumulation of perfluorocarbons at the rim of the abscess area in the shape of a ‘hollow sphere’, but accumulation data to other time points was lacking. Thus, the following experiments sought to investigate the dependence of administration time point and  $^{19}\text{F}$  accumulation pattern. Therefore, the time point of perfluorocarbon emulsion administration was systematically varied from 2 hours p.i. to day 8 p.i. and the accumulation was visualized at several time points after administration (not earlier than 24 h post administration) to get information about the durability of accumulation pattern in the infected thigh muscle (Fig. 4.9). Interestingly, administration of perfluorocarbon emulsion earlier than 2 days p.i. failed to elicit the typical accumulation pattern in the infected thigh muscle. Only very little dispersed  $^{19}\text{F}$  signal could be detected in the field of view. Administration between day 2 p.i. and the last evaluated time point day 8 p.i. led, in contrast, to a steady ‘hollow sphere’ pattern in the infected thigh muscle. The differences in  $^{19}\text{F}$  accumulation pattern size fitted to the size of edema area imaged by  $T_2$  maps, thus suggesting that the differences in size are not connected to the time point of perfluorocarbon administration but to the size of the abscess.

In summary, perfluorocarbon emulsion accumulates in the shape of a ‘hollow sphere’ in the murine *S. aureus* thigh infection model circumscribing the rim of the edema area, which is indicated by higher  $T_2$  values. To note, administration of the contrast media earlier than 2 days p.i. failed to cause the ‘hollow sphere’ pattern. The accumulation reaches detection limit at around 12 h post administration and accumulation remains detectable until the end of the experiment (if the initial inoculum is around  $10^8$  CFU and *S. aureus* is able to establish chronic infection).

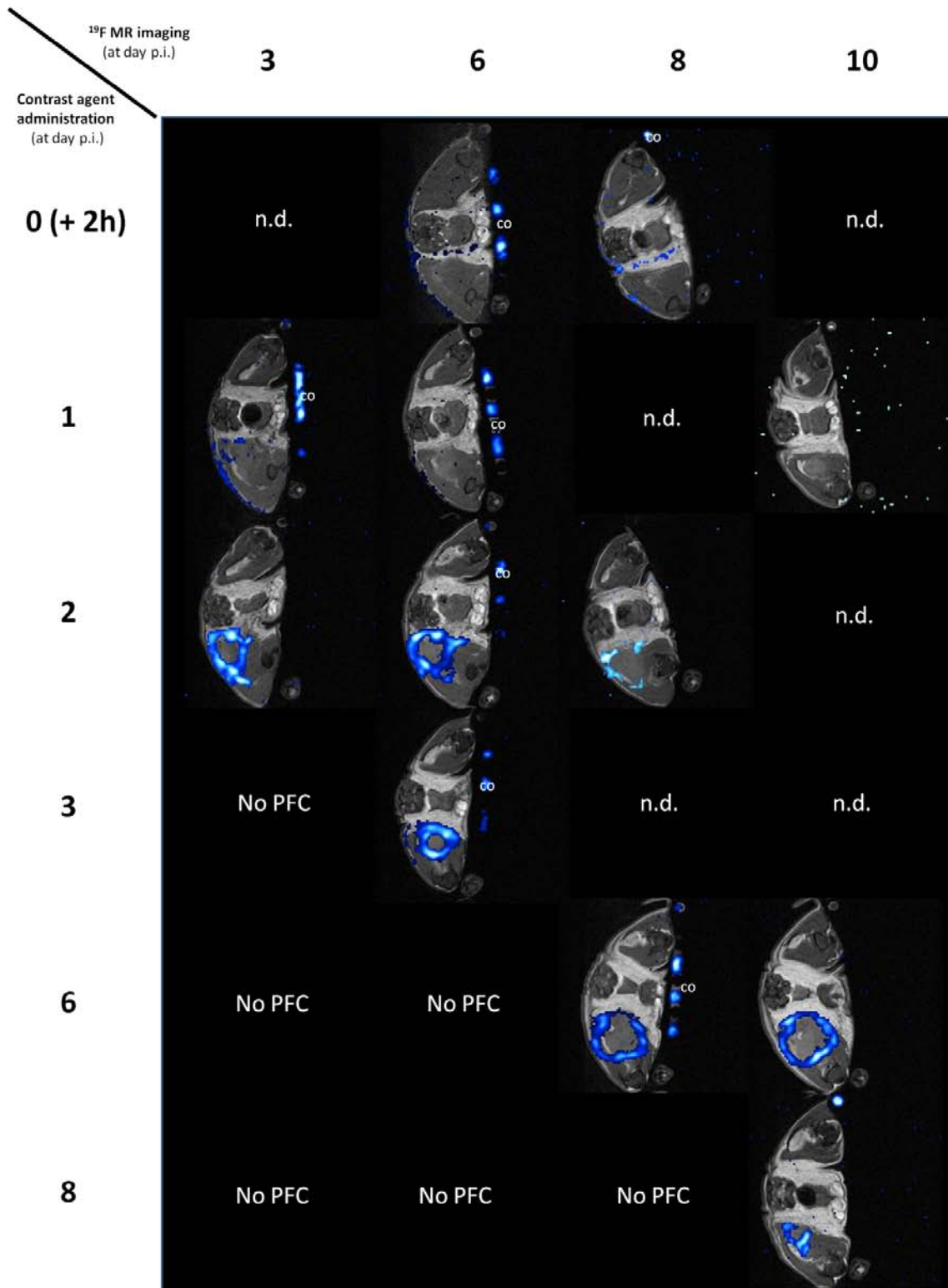


**Fig. 4.9:** Variation of the time point of perfluorocarbon administration leads to differences in <sup>19</sup>F accumulation at the site of infection. Mice were challenged with  $1.9 \times 10^8$  CFU *S. aureus* Xen29 in the left thigh muscle and perfluorocarbon emulsion was administered at indicated time points p.i.. <sup>19</sup>F accumulation was visualized at different time points after start of infection by <sup>19</sup>F-SSFP CSI MR overlays (blue color scale) on <sup>1</sup>H TSE images (grayscale), especially during acute phase of inflammation (day 3 p.i.) and chronic phase of inflammation (days 8 and 10 p.i.). (No PFC: mice have not received perfluorocarbon emulsion at this time point; n.d.: not determined).

#### 4.1.4.3. *The accumulation mechanism of perfluorocarbon emulsion in the S. aureus thigh infection model*

The experiments of the last chapter identified  $^{19}\text{F}$  accumulation in the area of the infected thigh muscle only in a defined field of view that covered the thigh muscles and a few millimeters to the posterior and anterior ends of the mouse. This was caused by the necessary use of a  $^1\text{H}/^{19}\text{F}$  double-resonant birdcage coil with this restricted size to enable imaging with sufficient sensitivity in an acceptable time span. In consequence, other possible sites of perfluorocarbon accumulation in the mouse could not be visualized by these imaging experiments. Thus, in order to identify further spots of accumulation, female Balb/c mice were infected with  $1.5 \times 10^8$  CFU *S. aureus* Xen29 in the left thigh muscle and perfluorocarbon emulsion was administered intravenously at day 2 p.i. (Similar to most of the experiments in the last chapter). Mice were sacrificed 24 hours after administration and fixed immediately in formalin solution. The fixated mice were then measured in a larger birdcage coil. Owing to the worse sensitivity of this coil and the need for good spatial resolution and high signal-to-noise ratio, the measurement time had to be extended to 24 hours to enable enough averaging in order to achieve images with sufficient signal-to-noise ratio. The 3D reconstruction of the measurement revealed strong accumulation of perfluorocarbon in the liver, spleen and infected thigh muscle. These organs could be clearly identified by the shapes drawn with  $^{19}\text{F}$  MR imaging (Fig. 4.10 left column). Additional sites of accumulation were the spinal cord and other bones respectively bone marrows or joints. While the accumulation pattern in the infected thigh muscle forms the well-known 'hollow sphere', congruent with earlier experiments, the liver and the spleen exhibited a continuous accumulation of perfluorocarbon, lacking spots of no signal (Fig. 4.10).

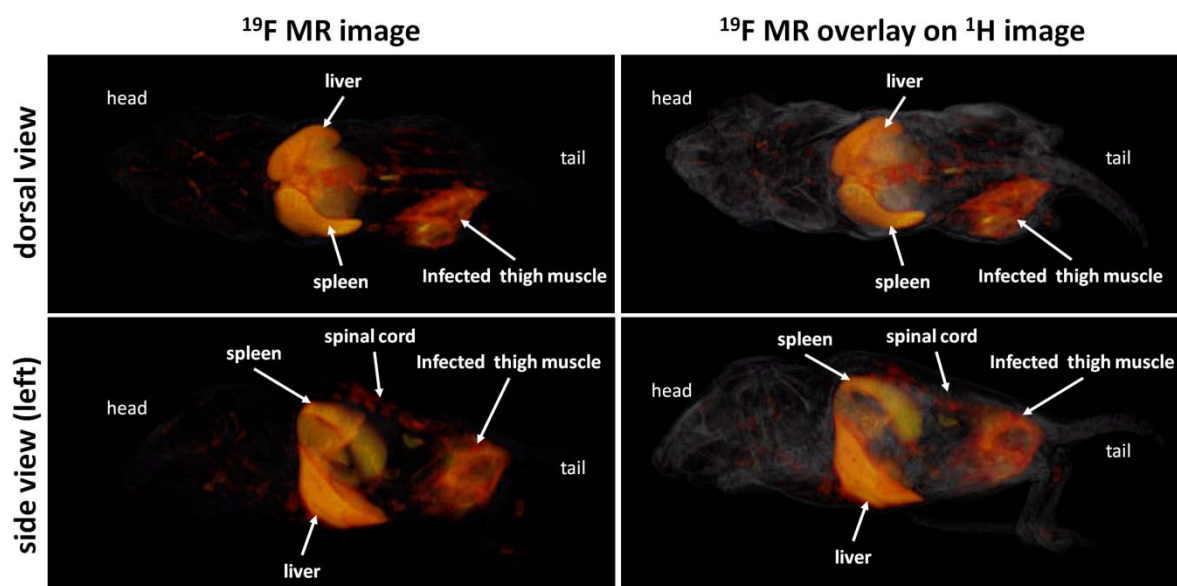


**Fig. 4.10:** Ex vivo whole-animal  $^{19}\text{F}$ -SSFP CSI overlays (hot color scale) on  $^1\text{H}$  TSE images (grayscale) of one representative mouse shows accumulation of  $^{19}\text{F}$  in the thigh infected mouse in anatomical context. Mice ( $n = 3$ ) were challenged with  $1.5 \times 10^8$  CFU *S. aureus* Xen29 in the left thigh muscle and perfluorocarbon emulsion was administered at day 2 p.i.. Mice were sacrificed 24 h after tracer media administration and fixed in 10 % formalin solution. MR imaging was performed after fixation of the mouse and images of the 3D reconstruction from either dorsal (upper row) or side view (lower row) without anatomical context (left images) or with anatomical context (right images) are shown.

The visualization of the  $^{19}\text{F}$  distribution pattern in the whole animal raised the question about the efficacy of perfluorocarbon accumulation at the site of infection and about the mechanism by which the emulsion is transported to the site of infection. The idea to address these questions was to fluorescently label the perfluorocarbon emulsion in order to track their behavior after intravenous administration by in vivo fluorescence imaging. Even more important, the fluorescent marker would help to gather information about the distribution pattern of perfluorocarbon emulsion in tissue, organs and cells by flow cytometry analysis of cell populations at the site of infection, isolation or depletion of specific immune cell populations and fluorescence microscopy of tissue sections. The first experiments were conducted with a commercially available fluorescent perfluorocarbon emulsion (VSdmGreen, Celsense), but the fluorescence label was not sufficient to elicit detectable signals in any of the applied methods. Due to the lack of other sources of fluorescent perfluorocarbon emulsion, it became necessary to develop and produce the emulsions, especially the fluorescent ones, by our own.

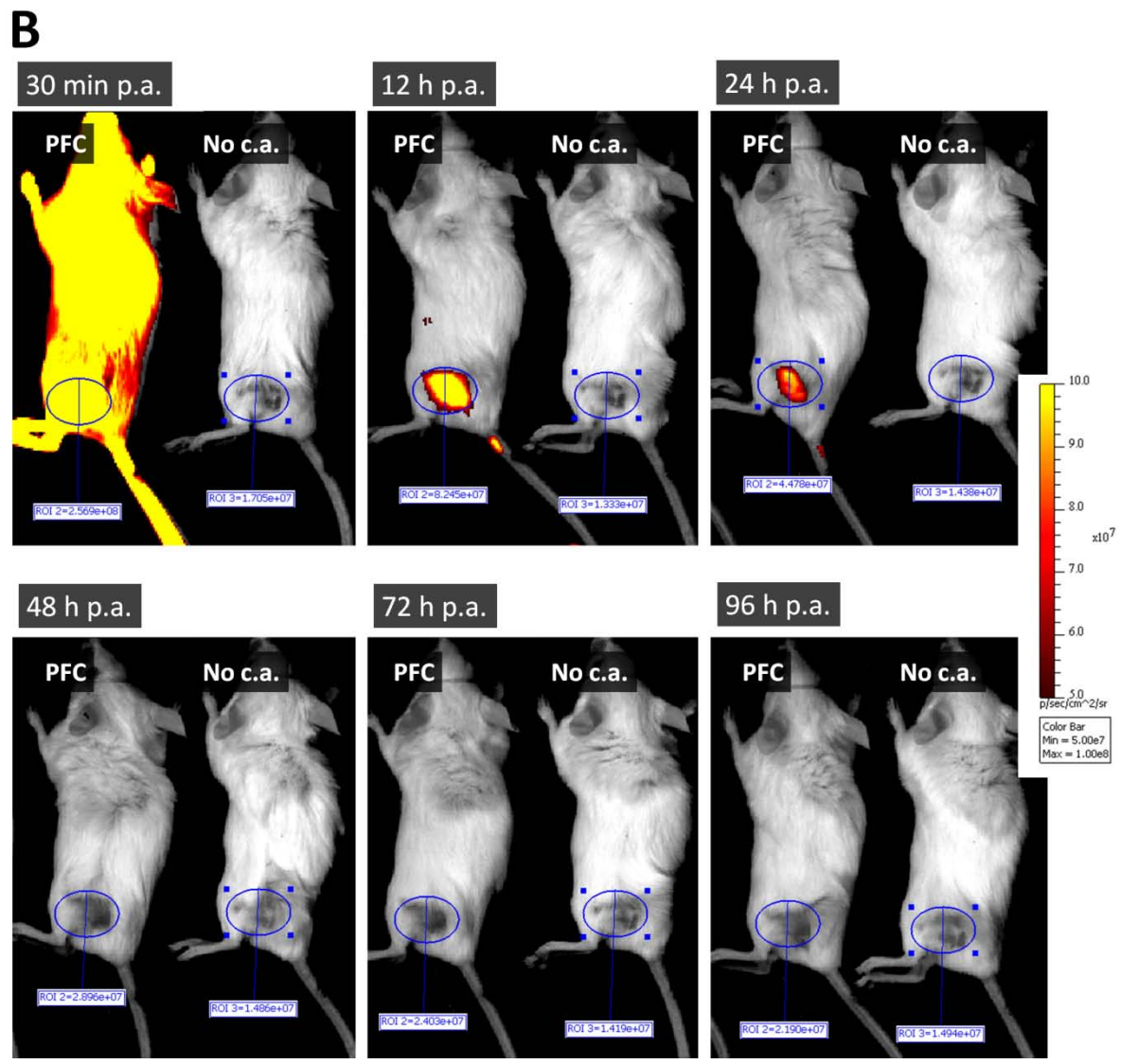
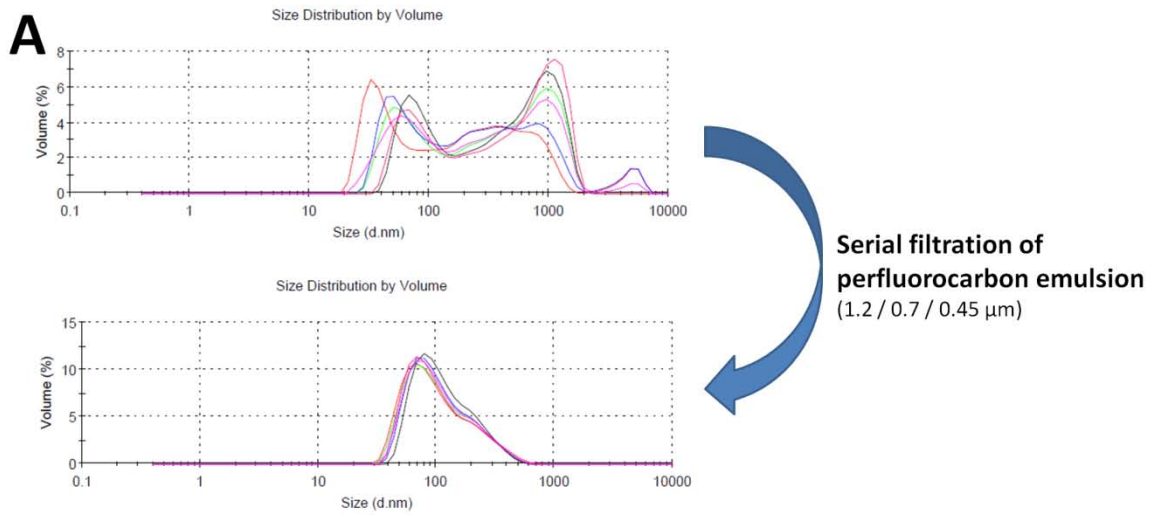
Perfluorocarbon emulsions for magnetic resonance imaging are, in principle, tiny liposomes consisting of a core of perfluorocarbons, which are neither soluble in water nor in lipids. In the emulsion preparation, they are enclosed in a layer of amphiphilic surfactants. This surfactant layer is necessary to enable perfluorocarbons in an aqueous environment. In this study, a sonication approach was applied to emulsify perfluorocarbon compounds into this

liposomal formulation. The standard protocol and particle composition followed, in principle, approaches of other groups and their specifications in literature (Winter PM et al. 2003, Ahrens ET et al. 2005, Flögel U et al. 2008, Southworth R et al. 2009). Perfluoro-15-crown-5-ether (15 % w/v) was therefore mixed with a surfactant commixture (4 % w/v) consisting of L- $\alpha$ -phosphatidylcholine (synonym for lecithin), cholesterol and a fluorescently labeled lipid (Atto647N-DOPE or Atto550-DOPE) in sterile 0.9 % NaCl solution. This mixture was then sonicated and the resulting emulsion filtered through a series of syringe filters for size exclusion (1.2  $\mu\text{m}$ , 0.7  $\mu\text{m}$  and 0.45  $\mu\text{m}$ ). In the resulting emulsion (Fig. 4.11 A), 90 % of the liposomes showed after this filtration process a final size of less than 250 nm in diameter (size determination with laser scattering was kindly performed by Peter Buschmann (AG Krüger, Organic Chemistry, University of Würzburg, Germany)). In vitro  $^{19}\text{F}$  MR measurements of the liposomal perfluorocarbon emulsion showed a resulting perfluorocarbon content of 65 % compared to the original, pre-filtration emulsion, resulting in a 10 % v / v perfluorocarbon emulsion (at initially 15 v / v % perfluorocarbon, otherwise dependent on the initial perfluorocarbon concentration).

The home-made emulsion was then tested in vivo in the thigh infection model for accumulation at the site of infection. Female Balb/c mice were therefore inoculated with  $1.4 \times 10^8$  CFU *S. aureus* Xen29 in the left thigh muscle and perfluorocarbon emulsion was administered intravenously at day 2 p.i.. The accumulation of  $^{19}\text{F}$  at the site of infection was imaged with  $^{19}\text{F}$ -SSFP CSI and overlaid on a  $^1\text{H}$ -TSE image to visualize tracer accumulation in anatomical context. All mice treated with home-made emulsion showed an accumulation pattern congruent with those of the commercially available preparations. All perfluorocarbon emulsions accumulated in the shape of a hollow sphere at the rim of the edema area (which was indicated by extended  $T_2$  relaxation times compared to not-infected thigh muscle tissue).

**Fig. 4.11 (facing page): Size characterization of home-made fluorescently labeled perfluorocarbon emulsion and in vivo fluorescence signal. A. Exemplary size distribution pattern of home-made perfluorocarbon emulsions.** Perfluoro-15-crown-5-ether was emulsified with fluorescence marker containing surfactant commixture by sonication. The upper picture shows size pattern of the emulsion after sonication and prior to filtration. The lower picture shows the size distribution after serial filtration through 1.2, 0.7 and 0.45  $\mu\text{m}$  syringe filters. The particle sizes were kindly measured via laser-scattering microscopy by Peter Buschmann (AG Krüger, Department of Organic Chemistry, University of Würzburg). **B. Fluorescence images of representative mice that received either fluorescent perfluorocarbon emulsion or 0.9 % NaCl solution at day 2 p.i..** Female Balb/c mice ( $n = 10$ ) were challenged with  $2.2 \times 10^8$  CFU *S. aureus* Xen29 in the left thigh muscle. At day 2 p.i., animals received a single intravenous administration of either homemade perfluorocarbon emulsion (with fluorescent Atto647N-DOPE in the surfactant commixture) in 0.9 % NaCl solution or 0.9 % NaCl only. Mice were imaged at the indicated time points and the average radiance signal of the manually defined regions of interest (blue oval frame) then measured (quantification in Fig. 4.12 A).





The fluorescence labeling of the perfluorocarbon emulsion enabled additionally to magnetic resonance imaging, fluorescent imaging as second modality to visualize accumulation and study the kinetics of the applied agent. Thus, Atto647N-labeled perfluorocarbon emulsion was applied intravenously to *S. aureus* Xen29 thigh infected Balb/c mice at day 2 p.i., and fluorescence imaging with the IVIS system (IVIS Lumina II, Caliper Life Science) showed in all animals of the perfluorocarbon group ('PFC group') a strong fluorescence signal at 30 minutes post administration in the whole mouse, suggesting instant dissemination of tracer throughout the whole body via the blood stream (Fig. 4.11). Two control groups were applied in this experiment. The first control group of mice received 0.9 % NaCl solution ('no contrast agent' group) instead of perfluorocarbon emulsion and the second group received perfluorocarbon emulsion with the same composition than the Atto647N-labeled group but without the Atto647N fluorescence label. Administration of non-fluorescent perfluorocarbon emulsion resulted in the same level of fluorescence signal at the site of infection than the 'no contrast agent' group at time point 30 min p.i. and all later time points. Furthermore, it showed in vitro a similar fluorescence signal level in the Cy5.5 channel of the IVIS system than 0.9 % NaCl solution (background level). Fluorescence imaging at 12 and 24 hours post administration revealed localized elevated signal levels in the infected thigh muscle of Atto647N-labeled perfluorocarbon emulsion treated mice, while no further spots of fluorescence signal could be detected in this or one of the other groups. The lack of signal in liver and spleen area, which is suggested by <sup>19</sup>F MRI, might be associated with tissue depths of these organs and the presence of the fur between these organs and the CCD camera. The signal quantification of the regions of interest, drawn in the images shown in Fig. 4.11, demonstrated a strong increase of fluorescence signal at the site of infection at 30 minutes post administration and a strong decline in the first 48 hours post administration (Fig. 4.12 A). The measurements at 30 min, 12 h and 24 h post administration showed significantly elevated average radiance levels, while later measurements signal converged to those of the 'no contrast agent' negative control group. The lack of signal in 'no contrast agent' group mice demonstrated in addition, that luciferase activity of the bioluminescent *S. aureus* strain Xen29 did not lead to detectable photon signal after filtering of fluorescence signal with these settings (Cy 5.5 emission filter was applied for filtering in the IVIS Lumina II imaging device).

Parallel to the in vivo imaging experiments, blood samples of all mice were collected in order to image the fluorescence signal in whole blood (Fig. 4.12 B). Imaging at 30 minutes post administration showed the strongest signal of all blood samples for the group that had received perfluorocarbon emulsion ('PFC group'). Within the first 24 hours most of the fluorescence diminishes from the samples and the signal approximates to the signal derived from the negative control group, indicating rapid clearance of PFC tracer from the blood. Only the measurements at 30 min and 12 h post administration demonstrated significantly higher average radiance values than the control group.

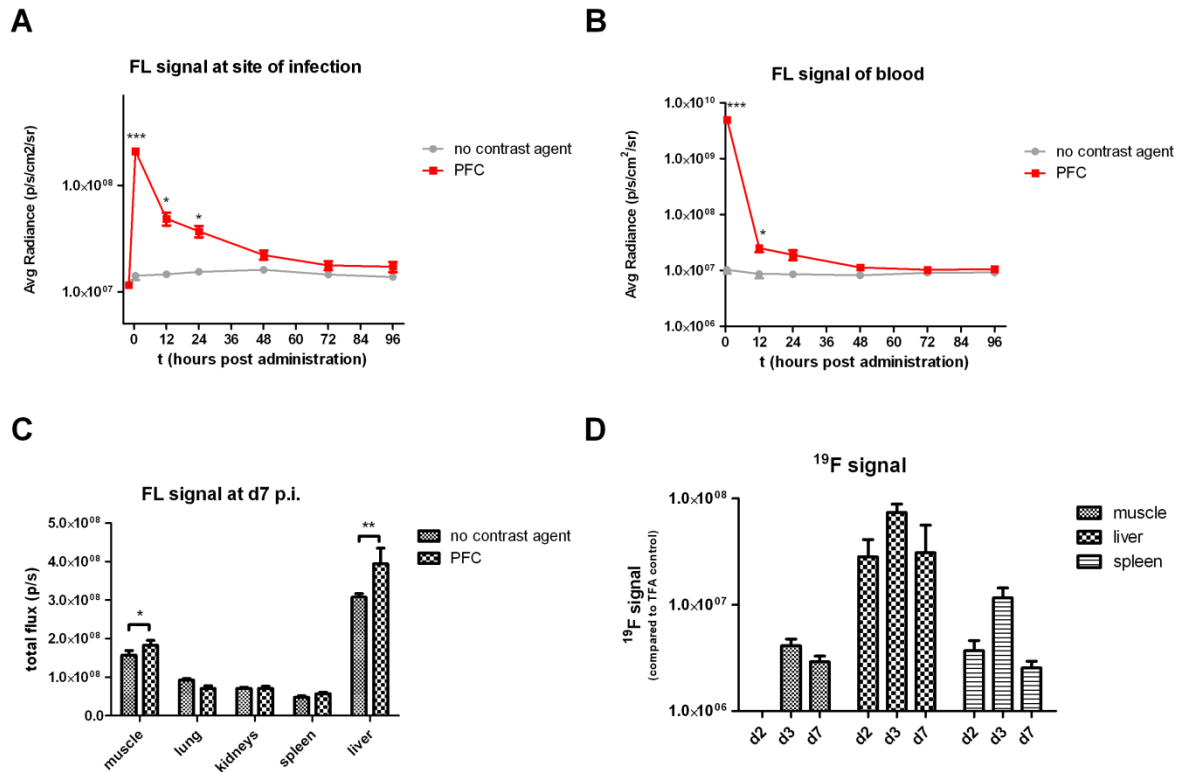


**Fig. 4.12:** In vivo or ex vivo determination of <sup>19</sup>F or fluorescence signal of home-made perfluorocarbon emulsion in blood or organs. Mice were challenged with  $2.2 \times 10^8$  CFU *S. aureus* Xen29 in the left thigh muscle and home-made perfluorocarbon emulsion (with Atto647N-DOPE in the surfactant commixture) or 0.9 % NaCl solution as control ('no contrast agent' group; to note, non-fluorescent perfluorocarbon emulsion delivered in vitro and in vivo similar fluorescence signal levels than 0.9 % NaCl solution) was administered at day 2 p.i.. **A. In vivo fluorescence signal in the manually defined region of interest at the site of infection** (see images in Fig. 4.9). Statistical significant differences between PFC group mice and control group mice (no perfluorocarbon emulsion) are indicated by asterisks (\*:  $P < 0.05$ ; \*\*\*:  $P < 0.005$ ). **B. Fluorescence signal of blood samples of perfluorocarbon treated and control group mice at different time points after administration of tracer.** Statistical significant differences between PFC group mice and control group mice (no perfluorocarbon emulsion) are indicated by asterisks (\*:  $P < 0.05$ ; \*\*\*:  $P < 0.005$ ). **C. Fluorescence signal of homogenized tissue samples of perfluorocarbon treated and control group mice at day 7 p.i..** Statistical significant differences between PFC group mice and control group mice (no perfluorocarbon emulsion) are indicated by asterisks (\*:  $P < 0.05$ ; \*\*:  $P < 0.01$ ). **D. Ex vivo <sup>19</sup>F signal of homogenized tissue samples at different time points after administration.** Time point day 2 represents 30 min post tracer administration.

Organs were recovered at several time points after start of infection in order to measure the  $^{19}\text{F}$  content and the fluorescence signal at the end of the experiments, at day 7 p.i.. Determination of the fluorescence signal of the homogenized organs at day 7 p.i., namely in the infected thigh muscle, the kidneys, lung, spleen and liver, showed significantly elevated fluorescence signal for the PFC group compared to the negative control group only in the thigh muscle and the liver, but not in the spleen (Fig. 4.12 C). But overall, differences in fluorescence of the homogenizations were weak, with the exception of the liver. The  $^{19}\text{F}$  content of homogenizations of the infected thigh muscle, liver and spleen, the main spots of perfluorocarbon accumulation in the whole mouse ex vivo imaging experiment, were determined at 30 minutes (day 2 p.i.), 24 hours (day 3 p.i.) and 120 hours (day 7 p.i.) after administration of perfluorocarbon emulsion (Fig. 4.12 D). Interestingly, there was no detectable  $^{19}\text{F}$  signal in the infected thigh muscle at 30 min post administration, which is congruent with earlier experiments that demonstrated first in vivo measurable  $^{19}\text{F}$  accumulation at the site of infection at around 10 – 12 hours after intravenous injection (compare Fig. 4.8). In contrast, the liver and the spleen, although less pronounced than at later time points, showed accumulation of perfluorocarbon emulsion at this very early time point. The  $^{19}\text{F}$  signal increased in all three organs until 24 h post administration, revealing measurable amounts of perfluorocarbon in the infected thigh muscle. Nonetheless, only about 10 % of the detected total signal accounts for accumulation at the site of infection, while most of the signal is found in the liver. The signal then decreased until day 7 p.i. in all organs, with the strongest reduction seen in the spleen. These results, taken together with the results derived by imaging of fluorescence signal of the Atto647N-labeled emulsion in whole blood samples, suggest clearance of perfluorocarbon emulsion from the mice body by a yet unidentified route and mechanism.

After identifying the accumulation in global scale, the next step was to further narrow the accumulation mechanism down, and to identify whether and which cells are involved. Former studies with this MR tracer imaging modality have shown, that in murine stroke, pneumonia and ischemia models, which are linked to massive monocyte/macrophage migration to the site of inflammation, perfluorocarbon is transported primarily by macrophages/monocytes (Flögel U et al. 2008, Janjic JM et al. 2008, Ebner B et al. 2010), but there were no studies published, which investigated the accumulation mechanism and the participating immune cells in infectious disease models. This is of special importance as *S. aureus* infections are mainly linked to massive neutrophils activation and influx and only to a less severe magnitude to macrophages/monocytes accumulation (Cheng AG et al. 2009). The idea was to identify the immune cell population or populations that participate in perfluorocarbon trafficking to the site of infection by labeling the perfluorocarbon emulsion with a fluorescent dye that can be identified by flow cytometry. In addition, the different immune cell populations which are present at the site of infection could be distinguished by flow cytometry, too, due to prominent and specific surface antigens. Well-known antigens were targeted by antibodies in order to identify crucial and/or important immune cell populations. To identify neutrophils, Ly6G, a prominent antigen on the surface of this cell type, was targeted (Daley JM et al. 2008). CD11b served as marker for macrophages, monocytes and activated neutrophils (Fischer MA et al. 2011). CD11c is a common antigen marker for dendritic cells in mice, although it has been shown recently that dendritic cell down-regulate this marker after activation (Singh-Jasuja H et al. 2013). CD45R (or synonym: B220) is mostly found on B cells (Coffman RL and Weissman IL. 1981), while T cells were identified by their expression of CD90.2 (or synonym: Thy1.2) antigen (Buttke TM et al. 1983).

In order to identify the different immune cell populations at the site of infection, mice were infected with  $1.5 \times 10^8$  CFU *S. aureus* Xen29 in the left thigh muscle and homemade perfluorocarbon emulsion with Atto647N-DOPE in its surfactant commixture or 0.9 % NaCl as control were administered intravenously at day 2 p.i.. The muscles were recovered 16 hours post administration and homogenized via pressing the muscle tissue through a cell strainer. Several samples of the homogenization were incubated with either 0.9 % NaCl solution or different cocktails of antibodies and the resulting cell fluorescence was measured in a flow cytometer (MACSQuant analyzer, Miltenyi Biotec). The samples without further addition of fluorescently labeled antibodies were analyzed first and the analysis of the fluorescence signal in channel R1, which visualizes extinction at 638 nm and emission at 655 – 730 nm (this fits to the extinction/emission spectrum of Atto647N), showed for mice, that had not received perfluorocarbon emulsion, only background fluorescence signal. In contrast to this, Atto647N-emulsion treated mice contained a further population of cells with increased fluorescence signal, resulting in a second peak in the histogram (Fig. 4.13 A).

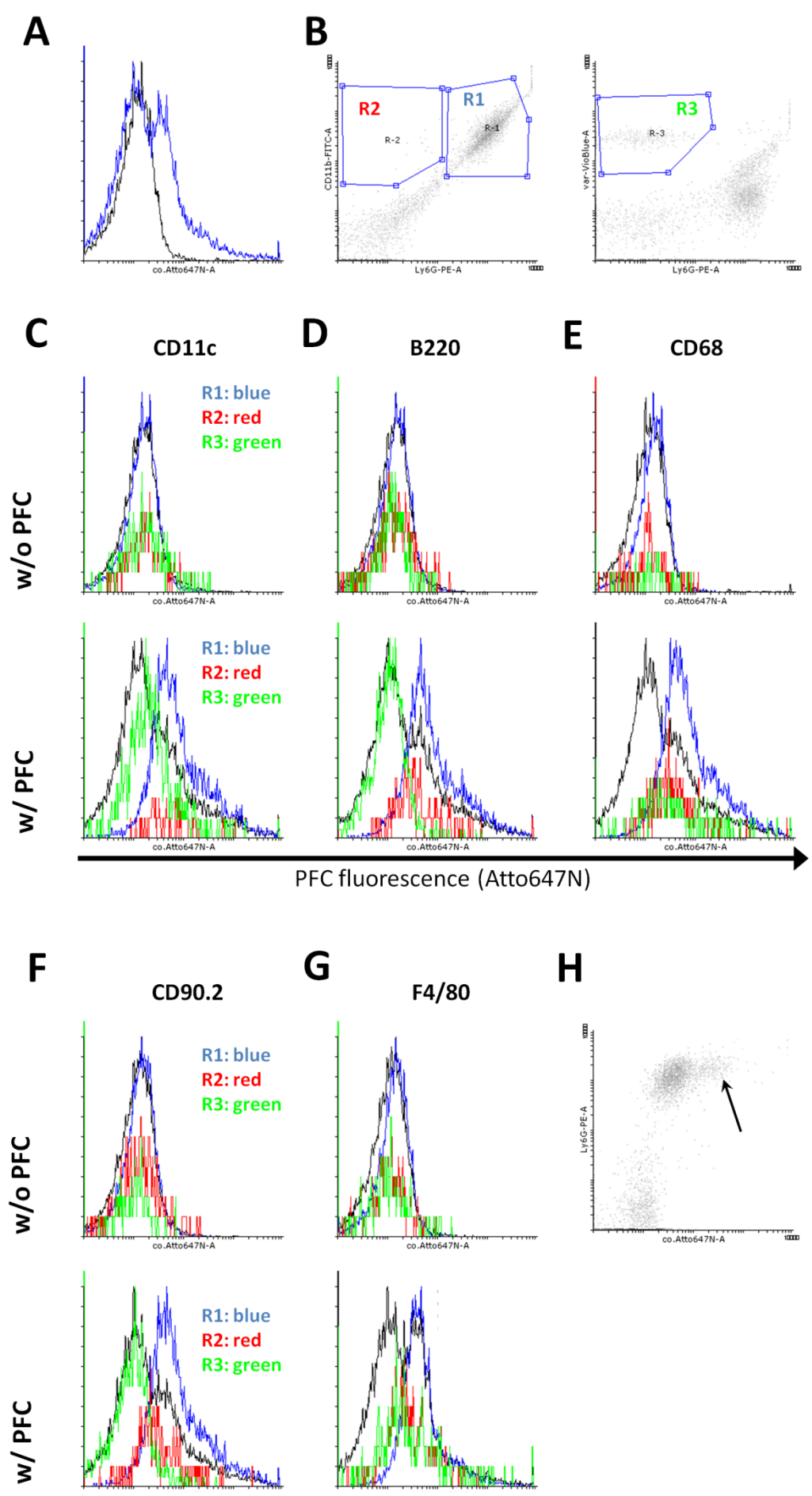
The other samples received different cocktails of antibodies, which consisted of anti-Ly6G PE conjugated, anti-CD11b FITC conjugated and various VioBlue conjugated antibodies. The

last-mentioned antibodies were in this regard used to identify CD11c, B220, CD68, CD90.2 or F4/80 positive cell populations in different measurements of the same samples.

The gating strategy was focused on the prevention of false-positive classification by unspecific binding of antibodies to Fc receptors, which are prominent on neutrophils. Cells were therefore either classified as Ly6G<sup>+</sup> CD11b<sup>+</sup> or Ly6G<sup>-</sup> CD11b<sup>+</sup> in the anti-Ly6G PE vs. anti-CD11b-FITC dot plot (Fig. 4.13 B, regions 1 and 2) or Ly6G<sup>-</sup> VioBlue<sup>+</sup> in the anti-Ly6G PE vs. VioBlue dot plot (Fig. 4.13 B, region 3). Ly6G<sup>+</sup> CD11b<sup>-</sup> cells could not be identified in any of the mice tested, suggesting activation of all neutrophils prior or with their arrival at the site of infection. This corresponds to former experiments demonstrating activation of neutrophils by myeloperoxidase which resulted in enhanced CD11b expression (Lau D et al. 2005, Schymeinsky J et al. 2007).

All regions of all samples derived from control group mice, which had not received Atto647N-labeled perfluorocarbon emulsions, showed only one peak in the histogram of the R1 channel (Fig. 4.13 C – G, upper rows, region 1 (Ly6G<sup>+</sup> CD11b<sup>+</sup>): blue curves, region 2 (Ly6G<sup>-</sup> CD11b<sup>+</sup>): red curves, region 3: (Ly6G<sup>-</sup> VioBlue<sup>+</sup>): green curves). The fluorescence signal strength of the peaks of different regions had, in this context, similar values. This suggests that neither the labels of the antibodies nor auto-fluorescence of the different cell populations lead to detectable signals in channel R1. In consequence, signal from samples derived from Atto647N labeled perfluorocarbon group mice in this channel has to originate from the fluorescence labeling of emulsion.

**Fig. 4.13 (facing page): Flow cytometry investigation of fluorescent perfluorocarbon emulsion accumulation in immune cells.** Mice were challenged with  $1.5 \times 10^8$  CFU *S. aureus* Xen29 in the left thigh muscle and homemade perfluorocarbon emulsion (with Atto647N-DOPE in surfactant commixture) was administered intravenously at day 2 p.i.. The infected thigh muscles were recovered 16 h post tracer administration and homogenized by pressing through a cell strainer. Cells were then incubated with anti-Ly6G-PE, anti-CD11b-FITC and different VioBlue-conjugated antibodies and analyzed with a flow cytometer. **A. Overlay histogram of cells from perfluorocarbon treated and untreated mice showed a second peak with a cell population with higher fluorescence signal in the R1 (Atto647N) channel.** **B. Gating strategy to identify different immune cell population from the infected thigh muscle.** Activated neutrophils are considered as Ly6G<sup>+</sup>CD11b<sup>+</sup> and therefore locate in R1, monocytes/macrophages at the site of infection should exhibit Ly6G<sup>-</sup>CD11b<sup>+</sup> pattern (R2). Other immune cell population were defined by VioBlue<sup>+</sup>Ly6G<sup>-</sup> pattern to exclude unspecific binding of VioBlue-conjugated antibodies to Fc receptors of neutrophils (R3). **C – G. Overlay histograms of signal in the Atto647N channel for the different cell populations from the three Gates/Regions:** R1 (blue curve): Ly6G<sup>+</sup>CD11b<sup>+</sup>, R2 (red curve): Ly6G<sup>-</sup>CD11b<sup>+</sup>, R3 (green curve): either Ly6G<sup>-</sup>CD11c<sup>+</sup> (C), Ly6G<sup>-</sup>B220<sup>+</sup> (D), Ly6G<sup>-</sup>CD68<sup>+</sup> (E), Ly6G<sup>-</sup>CD90.2<sup>+</sup> (F) or Ly6G<sup>-</sup>F4/80<sup>+</sup> (G) and the overall fluorescence signal of all cells (black line) for either perfluorocarbon treated (upper row) or not treated mice (lower row). **H. Atto647N vs. PE dot blot shows a Ly6G<sup>+</sup> population with higher Att647N fluorescence than the bulk of Ly6G<sup>+</sup> cells.**



4.1. Results

And indeed, the R1 channel histograms of samples from Atto647N labeled perfluorocarbon mice (Fig. 4.13 C – G, black curve) exhibited two peaks similar to those seen for samples without antibody addition to the testing (Fig. 4.13 A). The fluorescence histogram overlays of all regions showed a shift of the blue curve (region 1, Ly6G+ CD11b+ cells) to increased fluorescence values in channel R1 (where Atto647N exhibits fluorescence signal) of perfluorocarbon group mice (Fig. 4.13 C – G, lower rows). This shift could be seen in all samples, as both antibodies were applied to all tests, and it was the highest increase of fluorescence signal for all regions. The fluorescence of Ly6G- CD11b+ cells in perfluorocarbon treated mice, visualized as red curve in all measurements, showed similarly an increased signal, although the shift was not as pronounced as with Ly6G+ CD11b+ cells (Fig. 4.13 C – G, lower rows). Regarding samples derived from Atto647N-labeled perfluorocarbon treated mice, a second population with higher fluorescence levels in the R1 channel could be measured for Ly6G- CD11c+, Ly6G- CD68+ and Ly6G- F4/80+ cells (Fig. 4.13 C, E and G; green curves, lower rows), indicating accumulation of fluorescent perfluorocarbon emulsions in these populations. Ly6G- B220+ and Ly6G- CD90.2+ cell populations exhibited, in contrast, no fluorescence shift in the R1 channel (Fig. 4.13 D and F; green curves).

Most interestingly, in the homogenization samples of the thigh muscles of two out of four mice of the perfluorocarbon group, a second population of Ly6G+ cells could be detected, that exhibited elevated Atto647N fluorescence compared to the majority of Ly6G+ cells (Fig. 4.13 H). This suggests a population of neutrophils at the site of infection with increased perfluorocarbon emulsion uptake at 16 h post tracer administration. Nonetheless, the histogram of Ly6G+ cells did not show a clear second peak with increased fluorescence, but a 'thicker right arm' with higher fluorescence values (data not shown).

The results of these flow cytometry experiments were quantified with respect to two parameters: the amount of different cell populations at the site of infection and the mean R1 channel fluorescence signal (Atto647N, labeling of perfluorocarbon emulsions) of single cells of the various populations. The quantification of different immune cell populations in the homogenized infected thigh muscle showed that about 50 % of all cells in the abscess area were Ly6G+ CD11b+ activated neutrophils (Fig. 4.14 A). This was, by far, the largest detectable cell population at the site of infection. Ly6G- B220+ B cells and Ly6G- CD90.2+ T cells were detected, too, but to a much smaller degree, each population representing about 3 – 4 % of all cells. The smallest populations were Ly6G- CD11c+ dendritic cells, Ly6G- CD68+ macrophages or Ly6G- F4/80+ macrophages, comprising around 1 % of total cells, respectively (Fig. 4.14 A).

Each of these cell populations was then measured for their mean fluorescence signal in the R1 channel of the flow cytometer. The mean fluorescence intensity of cells in the samples of control group mice, that had not received Atto647N-labeled perfluorocarbon emulsion, was around 70 – 90 units (data not shown, but indicated in black curve in Fig. 4.13 A). Similar values could be measured for the Ly6G- B220+ B cells and Ly6G- CD90.2 + T cells of



fluorescently labeled perfluorocarbon treated mice, suggesting no accumulation of fluorescence marker and thus of perfluorocarbon emulsion in these cell populations. The other cell populations, namely the Ly6G<sup>+</sup> CD11b<sup>+</sup> neutrophils, Ly6G<sup>-</sup> CD11b<sup>+</sup> phagocytes, Ly6G<sup>-</sup> CD11c<sup>+</sup> dendritic cells, Ly6G<sup>-</sup> CD68<sup>+</sup> macrophages and the Ly6G<sup>-</sup> F4/80<sup>+</sup> macrophages showed significantly higher mean fluorescence in the R1 channel. Dendritic cells and macrophages delivered in this context the highest values, although the variance was especially for the Ly6G<sup>-</sup> F4/80<sup>+</sup> macrophages higher than for the neutrophils. Nonetheless, to identify the source of perfluorocarbon emulsion accumulation at the site of infection, both parameters, the number of cells at the site of infection as well as their inherent Atto647N fluorescence, have to be taken into account. This suggests that the gross of perfluorocarbon is located in neutrophils, especially due to their huge majority at the site of infection.

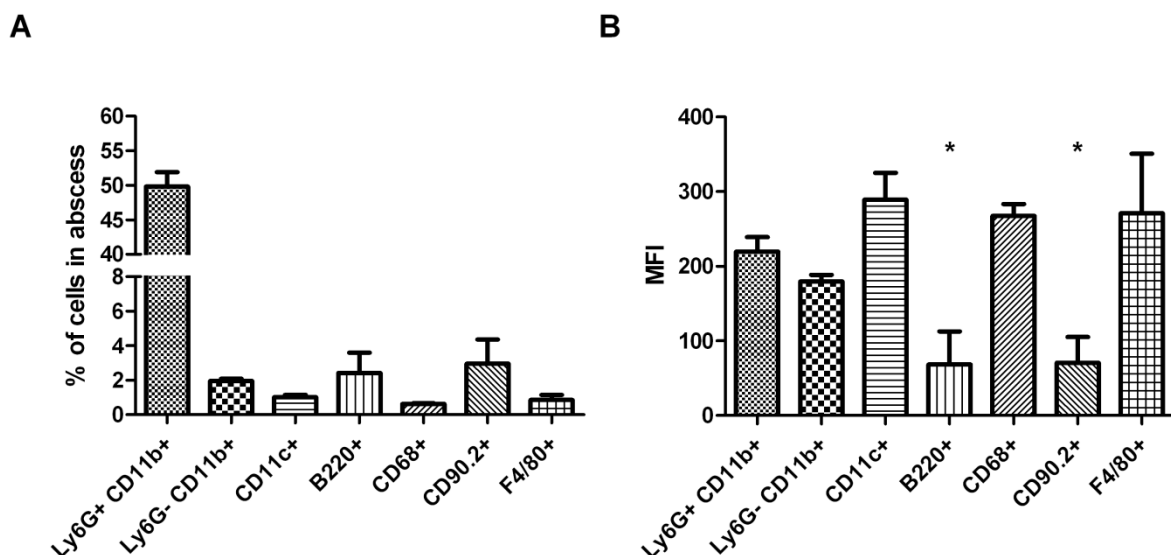


**Fig. 4.14: Quantification of flow cytometry investigation to reveal immune cell populations with increased Atto647N-labeled perfluorocarbon emulsion uptake.** Mice were challenged with  $1.5 \times 10^8$  CFU *S. aureus* Xen29 in the left thigh muscle and homemade perfluorocarbon emulsion (with Atto647N-DOPE in surfactant commixture) was administered intravenously at day 2 p.i.. The infected thigh muscles were recovered 16 h post tracer administration and homogenized by pressing through a cell strainer. Cells were then incubated with anti-Ly6G-PE, anti-CD11b-FITC and different VioBlue-conjugated antibodies and analyzed with a flow cytometer. (Gating strategy shown in Fig. 4.11) **A. Analysis of immune cell frequency in the infected thigh muscle. B. Mean fluorescence intensity (MFI) in arbitrary units of the different immune cell populations at the site of infection.** Asterisks indicate statistically significant lower MFI values for B220<sup>+</sup> and CD90.2<sup>+</sup> cell populations compared to Ly6G<sup>+</sup> CD11b<sup>+</sup>, Ly6G<sup>-</sup> CD11b<sup>+</sup>, CD11c<sup>+</sup>, CD68<sup>+</sup> and F4/80<sup>+</sup> cell populations. Compared to each other, B220<sup>+</sup> and CD90.2<sup>+</sup> cell populations showed no significant differences.

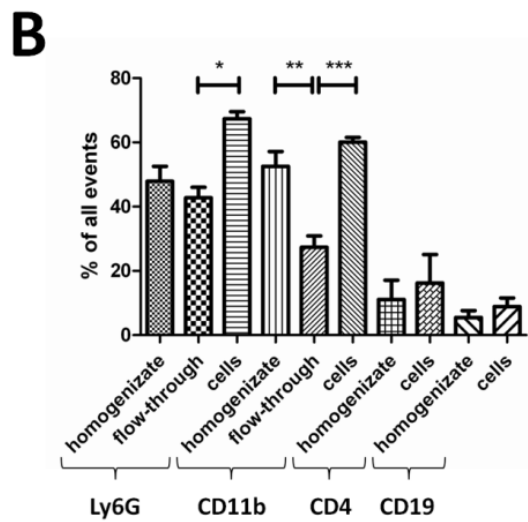
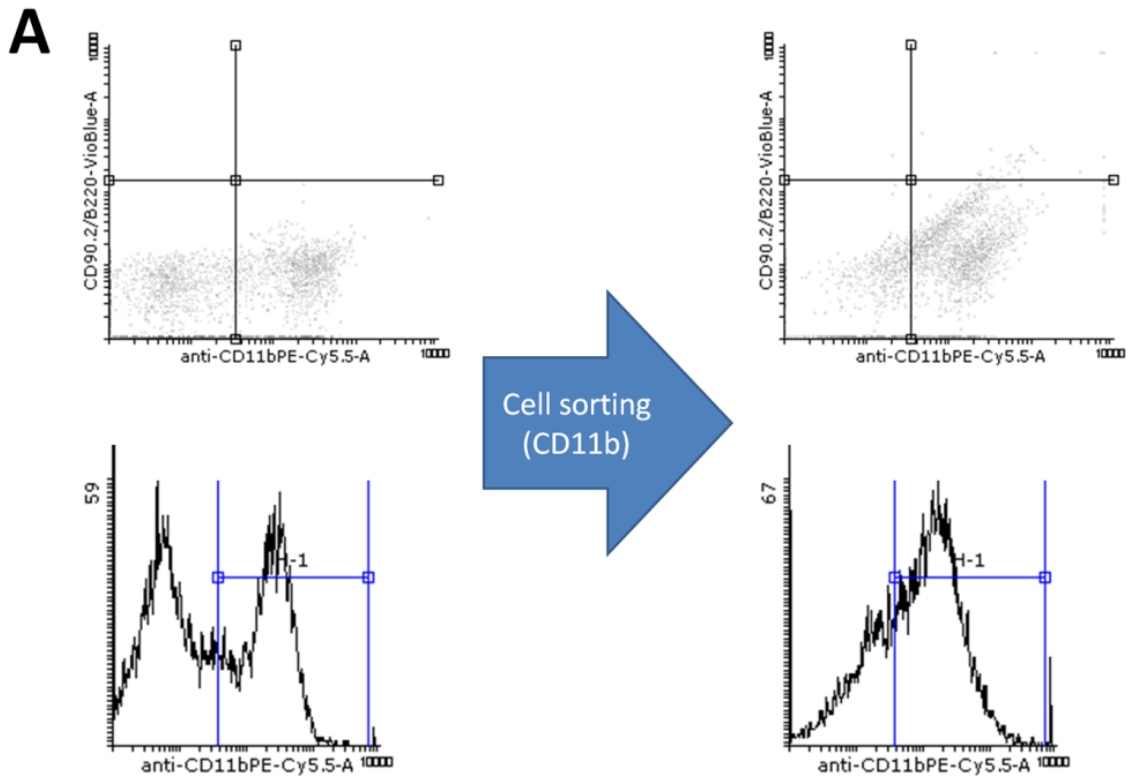
Flow cytometry of fluorescently labeled perfluorocarbons at the site of infection showed perfluorocarbon derived fluorescence in cells, but cannot visualize signal which is not associated with cells. Furthermore, flow cytometry can deliver only information about cell populations that can be identified by specific antibody binding. To address perfluorocarbon accumulation at the site of infection which is not associated with immune cells, cell sorting might be a promising approach. This method might deliver information about perfluorocarbon emulsion distribution at the site of infection by offering information about perfluorocarbon emulsion signal in specific cell populations or in aqueous phase.

Female Balb/c mice were therefore infected with  $1.5$  to  $2.0 \times 10^8$  CFU *S. aureus* Xen29 in the left thigh muscle and received perfluorocarbon emulsion (VS1000H, Celsence, Pittsburg, PA, USA) at day 2 p.i.. The muscles were recovered 16 - 18 hours later and homogenized by pressing them through a cell strainer. Different cell sorting methods were tested to separate specific cells from the crude muscle homogenate, namely magnetization-activated cell sorting (MACS), density gradient centrifugation and cell sieving (Pluriselect). Density gradient centrifugation of infected muscle homogenizations did not result in distinct layers of monocytes and granulocytes in the histopaque gradient. Thus, cell sorting by this centrifugation based method was not possible, maybe due to changes in macrophage and granulocyte cell densities during anti-infective activity, possibly caused by phagocytosis or vesicle release.

The magnetization activated cell sorting approach on the other hand was characterized by the loss of a large and highly variable numbers of cells in the cell separation columns independently of their surface marker composition. In consequence, both the sorted cell samples (from the column) and the flow through samples (which should include all cells and soluble compounds with the exception of the sorted cells) showed much smaller cell numbers than the initial tissue homogenization sample. This led either to comparably high  $^{19}\text{F}$  MR signals for Ly6G+ or CD11b+ sorted cells and for the Ly6G- respective CD11b-column flow through or to detectable  $^{19}\text{F}$  MR signal only in the column flow through samples. But importantly, all of them showed comparable or lower signal levels than the initial homogenization. Sorting of muscle homogenization for F4/80+ cells resulted in only negligible cell numbers and no detectable  $^{19}\text{F}$  MR signal. In consequence, the  $^{19}\text{F}$  signal in flow through samples might indicate perfluorocarbon emulsion accumulation by a cell independent mechanism. To address this, the muscle homogenization was filtered through  $0.45 \mu\text{m}$  syringe filters (msscscientific, Berlin) to exclude cells from the analyte and then the  $^{19}\text{F}$  MR signal was determined. The filtration resulted in a severe to almost complete loss of  $^{19}\text{F}$  MR signal compared to unfiltered samples, suggesting cell dependent accumulation. Importantly, filtration of the perfluorocarbon emulsion itself did only lead to weak or negligible loss of  $^{19}\text{F}$  signal compared to unfiltered samples. In conclusion, the high variance of cell sorting efficiency by this method prohibited quantification of perfluorocarbon emulsion accumulation at the site of infection. The  $^{19}\text{F}$  signal of muscle homogenization could neither be attributed to a specific cell population nor to a cell unspecific accumulation mechanism by this method.

Finally, the third tested method, the cell sieving approach, delivered in this study feasible cell sorting efficiency without interfering with later fluorescence or MR measurements of the sorted samples. For this approach, the intravenous administration of homemade perfluorocarbon emulsion with Atto647N- or Atto550-DOPE in its surfactant commixture or not-fluorescently labeled, but otherwise identical, perfluorocarbon emulsion as control, enabled detection of perfluorocarbon emulsion by fluorescence imaging. The animal experiment was apart from that performed exactly like the other experiments of above-mentioned cell sorting experiments. After muscle recovery, the muscle homogenizations were incubated with antibody-conjugated beads in order to select specific immune cell populations to separate them from the muscle homogenate. The samples were filtered through size exclusion filters, which let all cells pass with the exception of bead-bound antigen-specific immune cells. After this sorting step, the unsorted muscle homogenate, the separated bead-bound cells and the filter-flow-through were investigated for efficiency of sorting and perfluorocarbon derived fluorescence signal.

Four different antigen-specific sorting beads were used to separate immune cell populations from muscle homogenate. First, anti-Ly6G-beads were applied to sort neutrophils out of crude muscle homogenate. Second, anti-CD11b-beads to target activated neutrophils, monocytes and macrophages. The third bead population aimed at the CD4 antigen, which is commonly expressed by T helper cells and finally, anti-CD19-beads to separate B cells from the homogenate.



% of all events	homogenizate	flow-through	sorted cells
Ly6G	47.93 +/- 4.618	42.78 +/- 3.281	67.38 +/- 2.211
CD11b	52.57 +/- 4.573	27.34 +/- 3.592	60.08 +/- 1.483
CD4	11.13 +/- 6.005	n.d.	16.25 +/- 8.877
CD19	5.531 +/- 2.107	n.d.	8.896 +/- 2.674

**Fig. 4.15 (facing page): Efficiency of cell sorting for the identification of perfluorocarbon loaded cells at the site of infection.** Mice were challenged with  $2.0 \times 10^8$  CFU *S. aureus* Xen29 in the left thigh muscle and homemade perfluorocarbon emulsion (with Atto550-DOPE in surfactant commixture) was administered intravenously at day 2 p.i.. The infected thigh muscles were recovered 18 h post tracer administration and homogenized by pressing through a cell strainer. Cells were then incubated with anti-Ly6G-, anti-CD11b-, anti-CD4- and anti-CD19-beads to separate specific immune cell populations out of the muscle homogenate by size exclusion. **A. Flow cytometry analysis of muscle homogenate, separated cells and flow through** (homogenate without separated cells). Samples were incubated with either anti-Ly6G-APC and anti-CD90.2-VioBlue or with anti-CD11B-PerCP and anti-B220-VioBlue and analyzed on the flow cytometer. **B. Sorting lead to an enrichment of antigen-specific immune cell populations in the ‘cell’ samples and a decrease in the ‘flow-through’ samples, indicated by higher or lower frequency.** Shown are the means +/- SEM of all events as measured in the flow cytometer. Statistically significant differences are indicated by asterisks (\*:  $P < 0.05$ , \*\*:  $P < 0.01$ , \*\*\*:  $P < 0.005$ ). (n.d.: not determined)

After sorting, the unsorted muscle homogenate, the filter-flow-through and the sorted cell population were investigated by flow cytometry in order to evaluate the efficiency of sorting. A similar degree of Ly6G+ and CD11b+ cells (about 50 % of all detected events) than in earlier experiments (for comparison: Fig. 4.14) could be seen in the crude muscle homogenate (Fig. 4.15). Cell sorting resulted in a decrease of the ratio of Ly6G+ respectively CD11b+ cells compared to total cells in ‘flow-through’ samples, while the ‘sorted cell’ samples showed increased abundance of these cell types. Likewise, an enrichment of CD4+ respectively CD19+ cells could be seen for sorted cells with the proper antigen-specific beads, although these antigens remained underrepresented in the sample. Overall, cell sorting did not deliver pure samples of Ly6G+, CD11b+, CD4+ or CD19+ cells or, vice versa, muscle homogenates depleted from these cell populations, but nonetheless, the frequency of the cell populations was strongly enriched or reduced after sorting. In consequence, determination of perfluorocarbon emulsion signal in these samples gives a strong hind about the distribution pattern of the tracer at the site of infection.

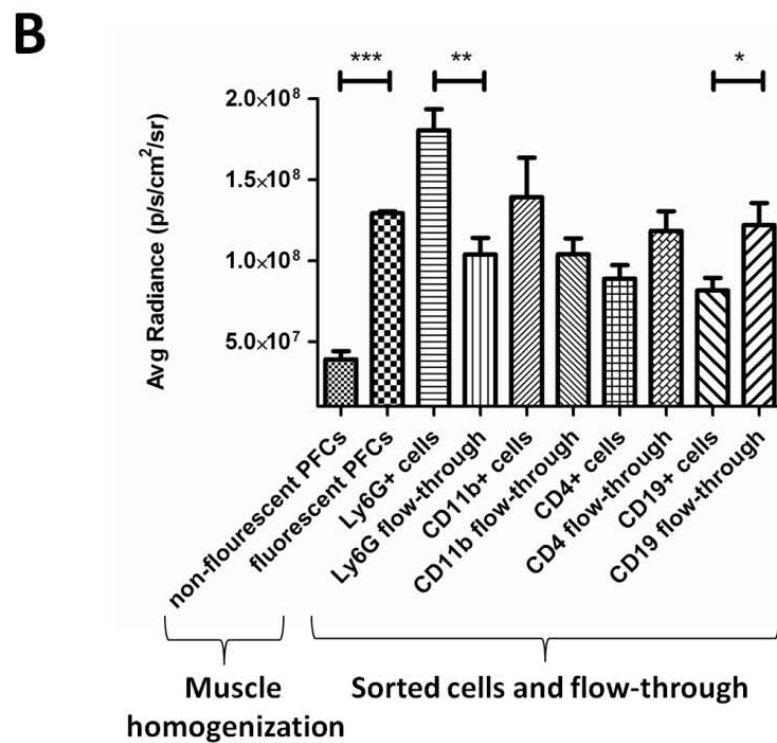
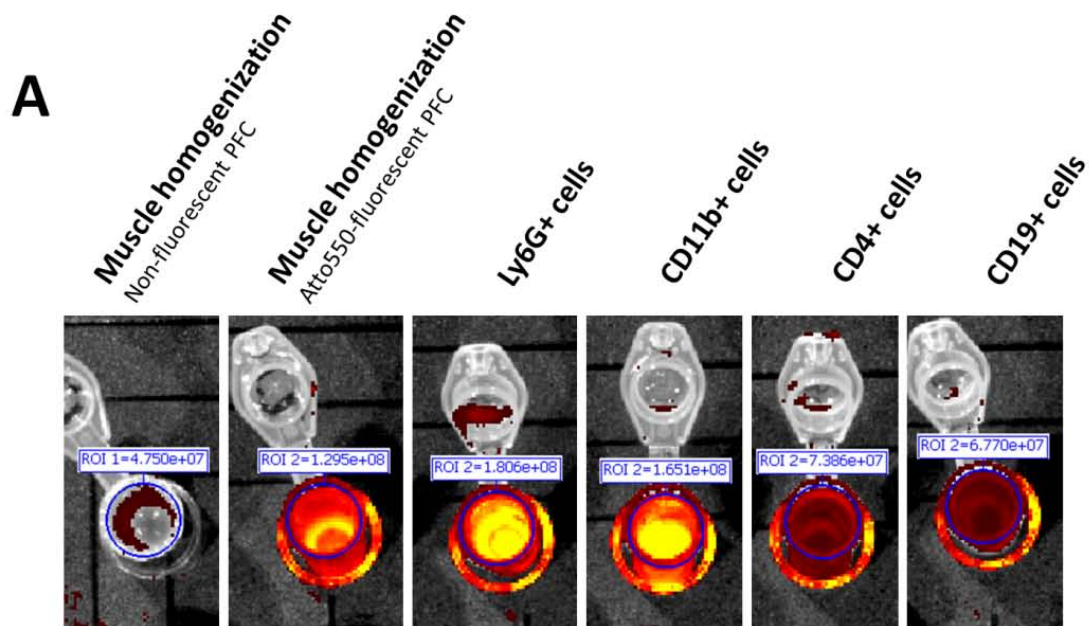
The perfluorocarbon emulsions could be, in principle, detected by two independent methods. First, by their inherent  $^{19}\text{F}$  signal, which can be measured by  $^{19}\text{F}$  MRI, and secondly, by fluorescence imaging of the Atto550 label, which is part of the lipid envelope around the perfluorocarbon core.  $^{19}\text{F}$  MRI of the sorted and crude samples delivered unfortunately only very low signal for all samples, thus it was impossible to compare the different sorted and unsorted samples. One explanation for this might be the rather strong dilution of samples, which is necessitated by the sorting protocol.

Fluorescence imaging of the Atto550-label, in contrast, showed detectable signal for all samples with the exception of non-fluorescent perfluorocarbon control sample, as expected (Fig. 4.16). This resulted in close-to-background fluorescence signal for the control, non-

fluorescent perfluorocarbon emulsion and significantly higher values for the crude muscle homogenate samples. Importantly, one further control sample consisting only of diluted perfluorocarbon emulsion demonstrated, that particles were small enough to fit through the pores of the cell sorting filter and thus fluorescence signal was similarly strong for the 'flow-through' sample compared to the pre-sorting sample. This means, that all perfluorocarbon emulsion signal in the 'sorted cell' samples must originate from cell-associated perfluorocarbon emulsion. In this context, sorting of muscle homogenate for Ly6G+ cells resulted in increased average radiance signal for the bead-bound cells compared to the crude unsorted muscle homogenate and flow-through fraction, which included all cells and supernatant with the exception of Ly6G+ cells. The 'flow-through' sample showed furthermore significantly lower signal than the Ly6G+ 'sorted cell' fraction and the crude homogenate. A similar, but less pronounced, picture could be seen for CD11b sorting. The cells that bound to the antigen-specific beads showed higher fluorescence values than the crude muscle homogenate and the flow-through fraction, which, again, had lower fluorescence than the unsorted homogenate.

Sorting for CD4+ and CD19+ cells resulted in opposite results. The sorted cell population, either predominantly T helper cells for CD4 sorting or B cells in the case of CD19 sorting, showed lower fluorescence signal than the 'flow-through' fraction. This indicates lower perfluorocarbon emulsion content in the T helper and B cell populations than in the crude homogenate, while Ly6G+ neutrophil and CD11b+ activated neutrophils, monocytes and macrophage cell fractions show stronger perfluorocarbon emulsion derived fluorescence signal than the muscle homogenate itself. And furthermore, a reduction of Ly6G+ or CD11b+ cells in the muscle homogenate reduced the fluorescence signal strongly, suggesting that most of the perfluorocarbon emulsion is associated with these cell populations.

**Fig. 4.16 (facing page): Fluorescence signal of muscle homogenate, sorted cells and flow-through.** Mice were challenged with  $2.0 \times 10^8$  CFU *S. aureus* Xen29 in the left thigh muscle and homemade perfluorocarbon emulsion (with Atto550-DOPE in surfactant commixture) was administered intravenously at day 2 p.i.. The infected thigh muscles were recovered 18 h post tracer administration and homogenized by pressing through a cell strainer. Cells were then incubated with anti-Ly6G-, anti-CD11b-, anti-CD4- and anti-CD19-beads to separate specific immune cell populations out of the muscle homogenate by size exclusion. **A. Fluorescence signal of 500  $\mu$ l sample prior ('homogenate') and after cell sorting ('cells') as imaged in the IVIS.** Note, the dilution factors of the individual samples were slightly different, thus the samples cannot be compared directly in this picture. Nonetheless, this image shows that all samples had signals above background levels. **B. Mean fluorescence intensity of homogenates, flow-throughs and cells.** Signal was measured in the IVIS (Caliper Life Science, Hopkinton, MA, USA) and calibrated according to the dilution factor of the sample. Shown are the means  $\pm$  SEM of all groups. Statistically significant differences are indicated by asterisks (\*:  $P < 0.05$ , \*\*:  $P < 0.01$ , \*\*\*:  $P < 0.005$ ).



Most importantly, cell sorting delivered in contrast to flow cytometry information about perfluorocarbon signal distribution over entire cell populations, not individual cells. Therefore, it gives better insights into the global distribution and localization of the tracer at the site of infection. With respect to the cell sorting results, it seems most likely that the majority of perfluorocarbon emulsion is located in Ly6G+ and/or CD11b+ cells. It has to be noted in this context, that flow cytometry of cell populations at the site of infection earlier in

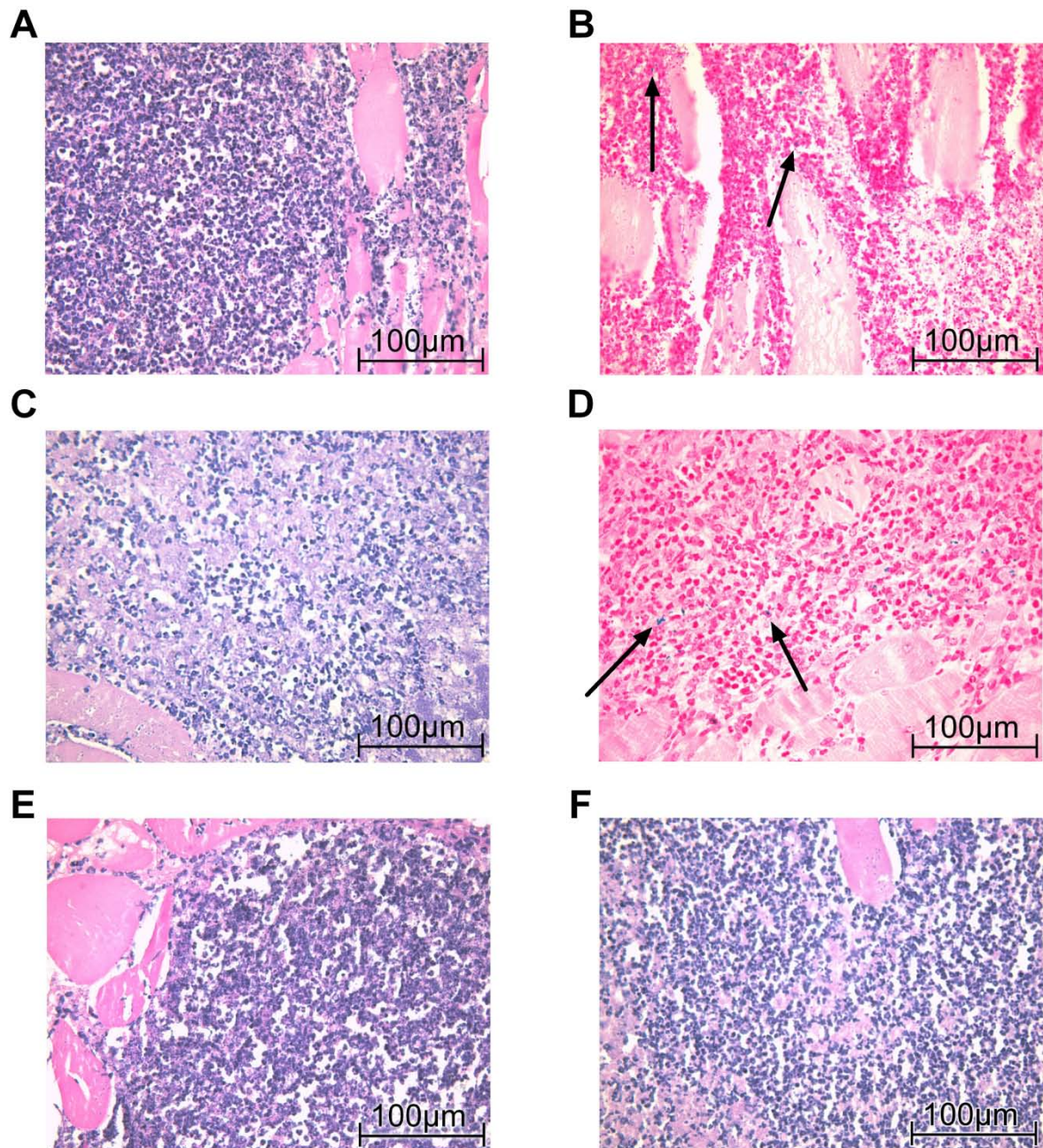
this chapter showed that Ly6G<sup>+</sup> neutrophils express the CD11b antigen at the site of infection, too. Therefore, it is reasonable that both antigens targeted overlapping or congruent cell populations in this experiment. In conclusion, results from cell sorting fit to the flow cytometry results showing accumulation of perfluorocarbon emulsion in neutrophils, monocytes and macrophages. Beyond that, cell sorting showed that the majority of perfluorocarbon emulsion signal is associated with these cell populations and that perfluorocarbon emulsion appears only at low amounts extracellularly at the site of infection.

#### 4.1.4.4. *Histology and fluorescence microscopy*

Flow cytometry analysis of perfluorocarbon accumulation at the site of infection made the homogenization of the tissue sample necessary. This might have led to damaging or destructing of the perfluorocarbon carrying cells and thus to loss of signal or information. Therefore histology was applied as second method to visualize spots of fluorescently labeled perfluorocarbon emulsions. Mice were infected with  $1.9 - 2.2 \times 10^8$  CFU *S. aureus* Xen29 in the left thigh muscle and either CLIO particles (cross linked ironoxide particles), commercially available non-fluorescent or Atto647N labeled homemade perfluorocarbon emulsion or 0.9 % NaCl solution as control was administered intravenously at day 2 p.i. CLIO particles were included in this experiment since it was described in literature, that they have a similar accumulation mechanism than perfluorocarbon emulsions (Kaim AH et al. 2002, Kaim AH et al. 2003).

**Fig. 4.17 (facing page): Histological appearance of abscesses in CLIO and PFC treated mice.** Female Balb/c mice were challenged with  $2.2 \times 10^8$  CFU *S. aureus* Xen29 in the left thigh muscle and either CLIO (A – D) or perfluorocarbon emulsion (E and F) was administered intravenously at day 2 p.i.. Muscles were recovered at acute phase of inflammation (A, B, E) or at chronic phase of inflammation (C, D, F), fixed in formalin, paraffin-embedded and cut to 2  $\mu$ m thick slices. A. Hematoxylin – eosin staining of one representative CLIO treated mouse at acute phase of inflammation (d3 p.i.). B. Berlin blue staining of one representative CLIO treated mouse at acute phase of inflammation (d3 p.i.). C. Hematoxylin – eosin staining of one representative CLIO treated mouse at chronic phase of inflammation (d8 p.i.). D. Berlin blue staining of one representative CLIO treated mouse at chronic phase of inflammation (d8 p.i.). E. Hematoxylin – eosin staining of one representative PFC treated mouse at acute phase of inflammation (d3 p.i.). Hematoxylin – eosin staining of one representative PFC treated mouse at chronic phase of inflammation (d8 p.i.). Arrows point at spots of iron oxide accumulation (They appear as blue spots in the Berlin blue stained tissue sections). (Images adapted from Hertlein T et al. 2011).

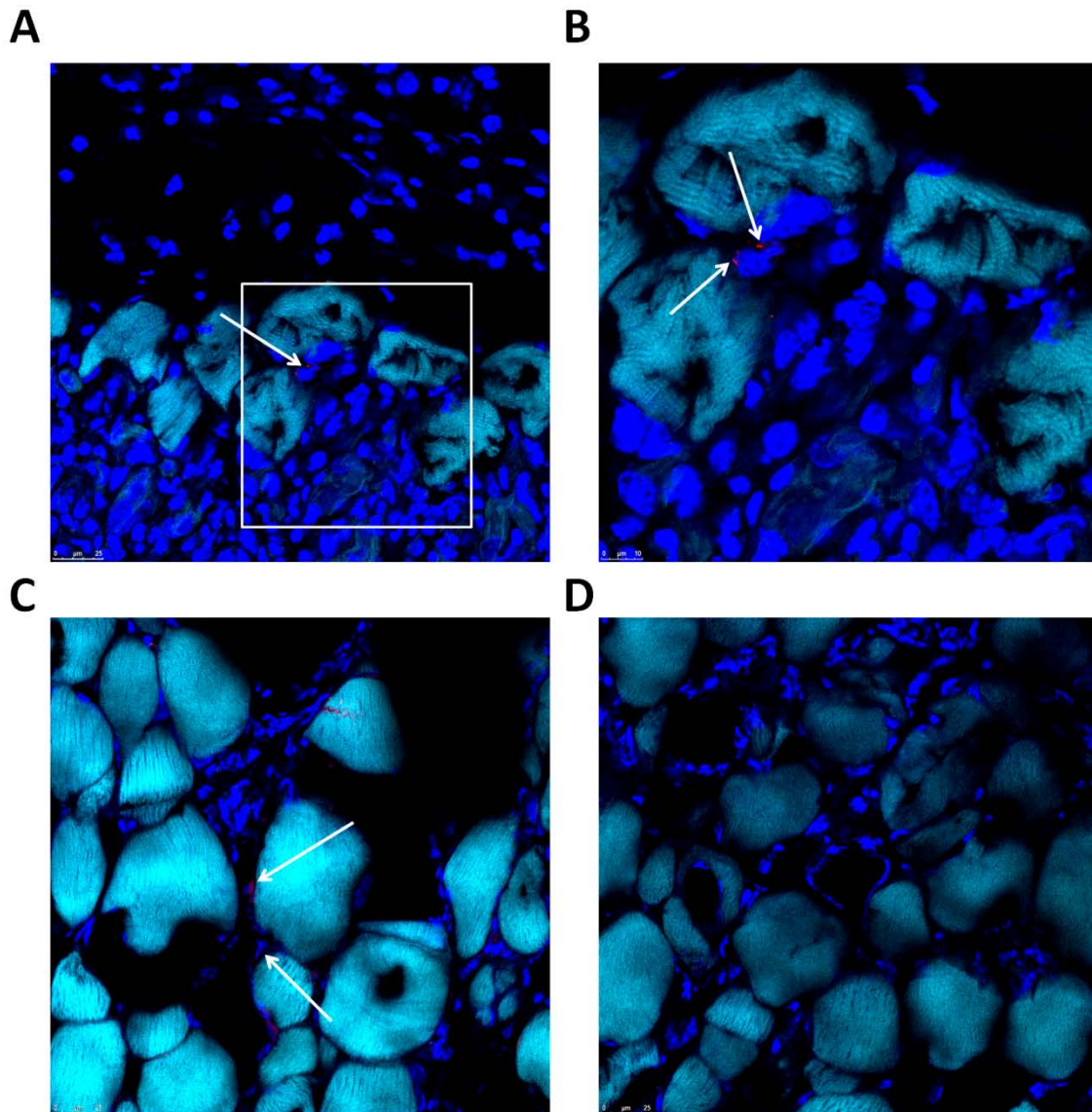




Thigh muscle/abscess samples were in the first approach recovered at days 3 and 8 p.i., fixed in formalin, embedded in paraffin and cut to 2 µm thick slices. Samples of all mice were then stained with hematoxylin and eosin (HE) to visualize different immune cell populations. CLIO treated mouse samples were additionally stained with Berlin blue iron staining to reveal accumulation of iron oxides. All following samples were analyzed together with an experienced pathologist (Dr. Stefan Kircher, Institute for Pathology, University of Würzburg). The HE staining at acute phase of inflammation (day 3 p.i.) showed for all mice a massive infiltration of neutrophils at the rim of the abscess area as well as some interspersed macrophages (Fig. 4.15 A/E). They surrounded a central area of necrosis. There could be seen no difference in immune cell content or density between perfluorocarbon, CLIO and 0.9 % NaCl treated mice. Furthermore, no accumulation of lipid or perfluorocarbon bubbles

could be observed in perfluorocarbon treated mice, which would have indicated growth or fusion of perfluorocarbon emulsions in vivo. The samples of chronic phase of inflammation (day 8 p.i.) showed a bulky central necrotic area encircled by a dense accumulation of granulocytes, macrophages and fibroblasts (Fig. 4.15 C/F). Similar to the results from acute phase of inflammation, no difference in immune cell composition or density could be delineated between perfluorocarbon emulsion, CLIO and 0.9 % NaCl treated mice. Berlin blue iron staining offered the visualization of CLIO particles in the histological samples, they appear as blue spots. Investigation of the acute phase of inflammation (day 3 p.i.) samples showed some blue spots of iron accumulation in granulocytes and macrophages of CLIO treated mice samples. Perfluorocarbon emulsion or 0.9 % NaCl treated mice had, as expected, no blue spots at the site of infection. A slightly stronger accumulation of CLIO particles, especially in macrophages, could be seen for samples from CLIO treated mice at chronic phase of inflammation (day 7 p.i.). The samples from 0.9 % NaCl or perfluorocarbon treated mice were, again, free of blue signal.

Perfluorocarbon emulsion remained undetectable by these methods and there was no further histological method available to stain or visualize fluorine or perfluorocarbon in tissue sections. Therefore, fluorescence labeling of the perfluorocarbon emulsions became necessary to track the emulsion after in vivo application. For this purpose, female Balb/c mice were infected with  $1.9 \times 10^8$  CFU *S. aureus* Xen29 in the left thigh muscle and either homemade perfluorocarbon emulsions with Atto647N-DOPE in its surfactant commixture or non-fluorescent but otherwise equal emulsions were administered intravenously at day 2 p.i.. The infected thigh muscles were recovered 16 h after administration and immediately frozen. The frozen tissue was then sectioned to 10  $\mu\text{m}$  thick slices and either investigated directly with a confocal laser scanning microscope (Leica TCS SP 5, Mannheim, Germany), stained with Hoechst 33425, with Hoechst 33425 and Atto520-phalloidin or with Hoechst 33425, Atto520-phalloidin and different immune cell specific antibodies and afterwards analyzed by fluorescence microscopy.



Hoechst33425  
 Atto425-Phalloidin  
 Atto647N-labeled PFC emulsion

**Fig. 4.18:** Fluorescence microscopy of frozen tissue sections of Atto647N-labeled perfluorocarbon emulsion treated mice. Mice were challenged with  $1.9 \times 10^8$  CFU *S. aureus* Xen29 and perfluorocarbon emulsion was administered intravenously at day 2 p.i.. Muscles were recovered 16 h later and immediately frozen. The tissue samples were then cut with a cryotome into 10  $\mu\text{m}$  thick sections and stained with Hoechst 33425 and Atto425-Phalloidin. **A-C:** Tissue sections of mice from Atto647N-labeled perfluorocarbon emulsion group with varying magnification showed spots of Atto647N fluorescence in close proximity to cell nuclei. Arrows point at spots of Atto647N fluorescence. **D:** Tissue section of control group which had received perfluorocarbon emulsion without fluorescence label showed no fluorescence in the Atto647N channel.

The native unstained slices showed some spots of Atto647N fluorescence, with a pattern ranging from single, intensively fluorescent points to larger areas of weaker signal (data not shown). The Hoechst 33425/Atto520-Phalloidin double stained slices visualized similar accumulation of Atto647N fluorescence in the infected thigh muscle, although the amount seemed to be reduced compared to unstained samples. Nonetheless, the double staining offered a nice anatomic view of muscle bundles and accumulation of immune cells (Fig. 4.16 A - C). The Atto520-phalloidin staining visualized, in this context, muscle tissue by binding to F-actin, while Hoechst 33425 stain visualized DNA and thus, enabled visualization of cell nuclei. The Atto647N fluorescence was in all tested samples in the proximity of the cell nuclei. The pattern was similar to those seen in unstained samples, meaning either single spots of intense signal or larger areas with less pronounced Atto647N fluorescence. The signal sometimes accumulated in a pattern that resembled the shape of cellular plasma. Most importantly, none of the samples exhibited Atto647N fluorescence in muscle bundles, meaning all detectable signal was close to immigrated immune cells. Moreover, no Atto647N fluorescence could be seen with the same microscope settings in samples of mice that had received non-fluorescent perfluorocarbon emulsions (Fig. 4.16 D).

Furthermore, no Atto647N fluorescence could be detected in any of the antibody stained tissue sections. This staining protocol to target specifically immune cell populations required long phases of incubation. During these steps, the slices were covered with buffer. Perfluorocarbon emulsion might be washed out of the sections during the incubation steps, what in turn might be an explanation for the loss of perfluorocarbon derived fluorescence compared to Hoechst 33425/Atto520-Phalloidin stained samples. The loss of perfluorocarbon emulsion derived fluorescence was in this context observed by other investigators, too (Flögel U et al. 2008).

#### 4.1.5. Perfluorocarbon administration does not change the fundamental parameters of infection

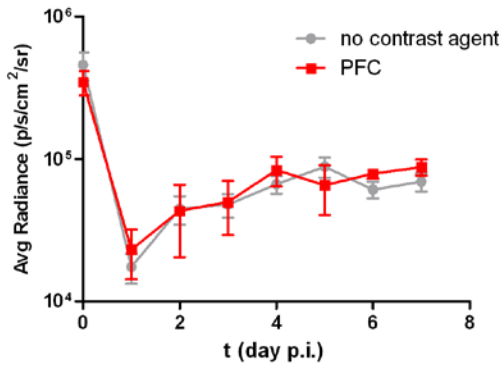
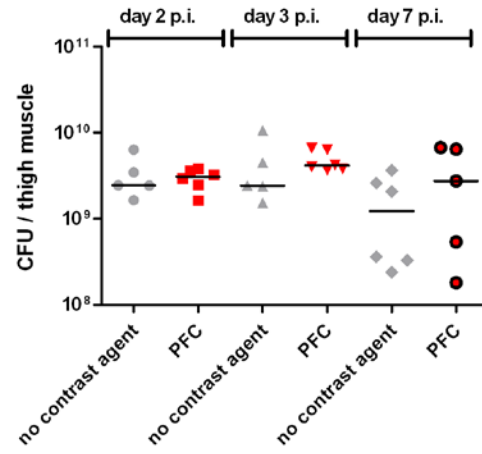
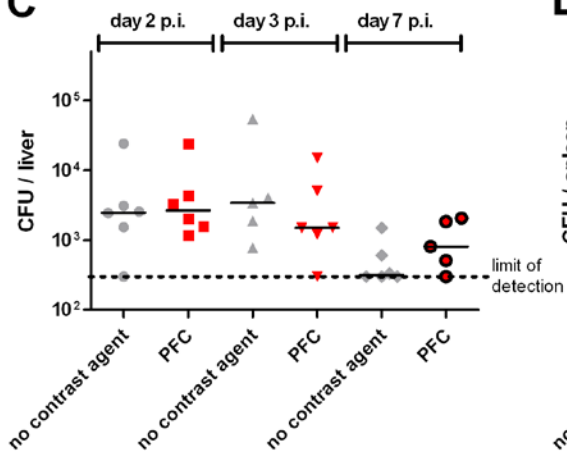
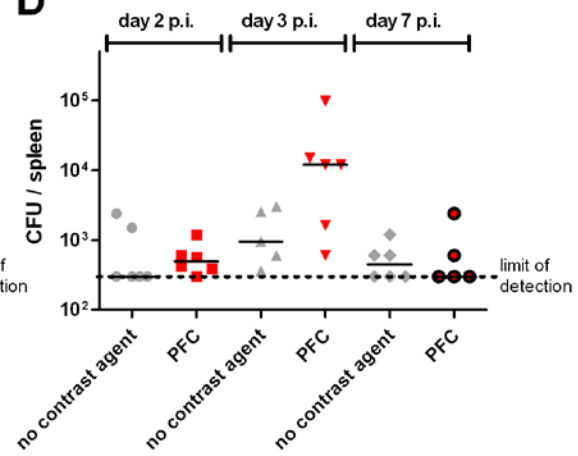
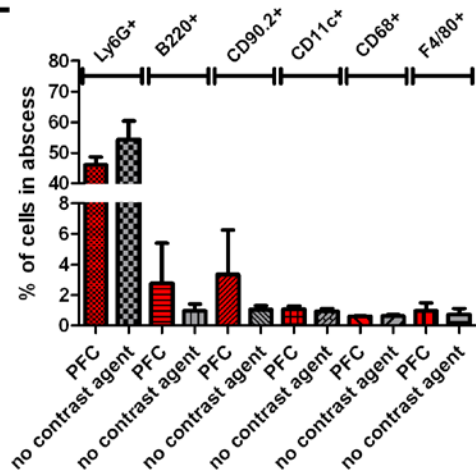
After investigating the accumulation mechanism at the site of infection, the question arose, whether or not, administration of perfluorocarbon emulsion or the following magnetic resonance imaging has any influence on the infection itself. To address this question, two groups of female Balb/c mice were infected with  $2.2 \times 10^8$  CFU *S. aureus* Xen29 and received either 0.9 % NaCl solution at day 2 p.i. or perfluorocarbon emulsion.

The infected thigh muscle, the liver and the spleen were recovered either prior administration, 24 hours (day 3 p.i.) or 5 days (day 7 p.i.) post administration, homogenized and the colony forming units determined. The CFU results were similar to those described in chapter 4.1.1, and showed highest bacterial numbers in the infected thigh muscle and only low numbers or no bacteria at all in the spleen and liver at all examined time points (Fig. 4.19 B – D). There could be seen no significant difference in bacterial burden in the infected thigh muscle, only slightly higher numbers at day 3 and day 7 p.i. for the perfluorocarbon group (PFC), but differences were small and statistically not significant (Fig. 4.19 B). A similar picture could be seen in the liver. The CFU counts were similar between perfluorocarbon treated and not-treated mice at all time points (Fig. 4.19 C). In the spleen, almost no bacteria could be detected at day 2 and day 7 p.i. (Fig. 4.19 D). At day 3 p.i. there might be some difference in bacterial counts between perfluorocarbon and mock treated mice, with higher values for the perfluorocarbon group, but differences were not statistically significant and the results overlapping.

Since the bioluminescent *S. aureus* strain Xen29 was administered to the mice, accompanying non invasive bioluminescence imaging was possible. The time course of bioluminescence signal at the site of infection, measured in a manually defined region of interest with same size and geometry for all mice, showed congruent development of photon emission for both groups (Fig. 4.19 A). Perfluorocarbon treated as well as not-treated mice had a strong decrease of bioluminescent signal within the first 24 hours and a recovery to a stationary phase with slight variations between day 4 and day 7 p.i.. The values of both groups were comparable in signal and differences were very small and statistically not significant.

**Fig. 4.19 (facing page): Comparison of CFU values, bioluminescent signal and immune cell frequency in the abscess between perfluorocarbon treated and not-treated mice in the *S. aureus* thigh infection model.** Mice were challenged with ca.  $2.2 \times 10^8$  CFU *S. aureus* Xen 29 into the left thigh muscle. All mice of 'PFC' groups received a single intravenous administration of perfluorocarbon emulsion at day 2 p.i., while the 'no contrast agent' group mice received a single bolus of 0.9 % NaCl solution. **A: Development of bioluminescent signal in 'PFC' (5 animals) and 'no contrast agent' (8 animals) groups during infection.** Means +/- SEM are displayed. **B – D: CFU counts in infected thigh muscles, livers and spleens of either perfluorocarbon emulsion treated or control mice.** Single CFU counts per mouse and the respective medians per groups for the indicated time points are shown. Time point day 2 p.i. is prior to administration of tracer, day 3 p.i. is 24 hours after administration and day 8 p.i. is 5 days post perfluorocarbon emulsion administration. **E: Flow cytometry analysis of immune cell populations in the infected thigh muscle.** Infected thigh muscles of perfluorocarbon emulsion and control treated mice were recovered 24 hours post tracer administration and homogenized. Single cell suspensions were then incubated with various fluorescently labeled antibodies and analyzed with the flow cytometry protocol described in Fig. 4.13 (only difference to previous experiments: no anti-CD11b antibody). There are no statistically significant differences between both groups (both groups: n = 4).

The establishment of a flow cytometry protocol to analyze the occurrence of perfluorocarbon emulsion derived fluorescence in different immune cell populations at the site of infection in previous experiments (Chapter 4.1.4.3, especially Fig. 4.13) enabled the comparison of incidence of different immune cell populations at the site of infection. The idea was, that the migration behavior of phagocytic immune cells might be altered after uptake of perfluorocarbon emulsion in the blood stream. The frequency of T (CD90.2+) and B (B220+) cells seemed to be, in this context, slightly increased in the perfluorocarbon emulsion treated group, while the incidence of neutrophils (Ly6G+) seemed to be decreased to the same extent (Fig. 4.19 E). Nonetheless, the elevated levels of B and T cells are due to very high numbers in only one out of four mice of the perfluorocarbon group. The other mice of this group showed similar levels than the control group. Most importantly, there are no statistical significant differences between both groups for any of the investigated immune cell populations, indicating unaltered cellular immune response, at least regarding the frequency of cells. The frequency of dendritic cells (CD11c+) and macrophages (CD68+ and F4/80+) were very low and congruent to earlier experiments (compare Fig. 4.14).

**A****B****C****D****E**

At last, cytokine and chemokine levels in the infected thigh muscles were measured and compared between perfluorocarbon treated and not-treated mice. The infected thigh muscles were therefore recovered before (day 2 p.i.), 24 hours after (day 3 p.i.) and 5 days (day 7 p.i.) after intravenous administration of the emulsion. The muscles were then homogenized and the levels of various cytokines and chemokines determined with flow cytometry bead assays (eBioscience). High levels of cytokines IL-1 $\alpha$ , IL-2 and IL-6 as well as of chemokines MCP-1, MIP-1 $\alpha$  and RANTES could be seen at day 2 p.i. in both groups, with no significant differences between them (Fig. 4.20). Lower levels of cytokines IL-4, IL-5, IL-10, IL-17, IFN $\gamma$  and TNF $\alpha$ , as well as of chemokine MCP-3 could be measured, with no differences between perfluorocarbon and control group mice. Almost no detectable levels of GM-CSF and MIP-1 $\beta$  were seen in the infected thigh muscle at all three time points. The level of IL-2 and IL-6 decreased, similar regarding trend and gravity in both groups, between day 2 p.i. and day 7 p.i.. The amounts of IL-1 $\alpha$ , IL-4, IL-10, IL-17, MCP-3 and MIP-1 $\alpha$  remained invariably at their initial level, while the levels of IL-5, IFN $\gamma$  and RANTES ascended between day 2 and day 7 p.i.. But nonetheless, despite some differences in the levels of cytokines or chemokines between perfluorocarbon treated and not-treated mice, for example, in MCP-1 amounts at day 3 p.i. or MIP-1 $\alpha$  at day 7 p.i., the differences were small, statistically not significant and results overlapping. Moreover, the pattern of cytokines and chemokines was similar in both groups and therefore, it has to be stated that perfluorocarbon administration resulted in unaltered cytokine or chemokine release compared to the administration of 0.9 % NaCl solution.



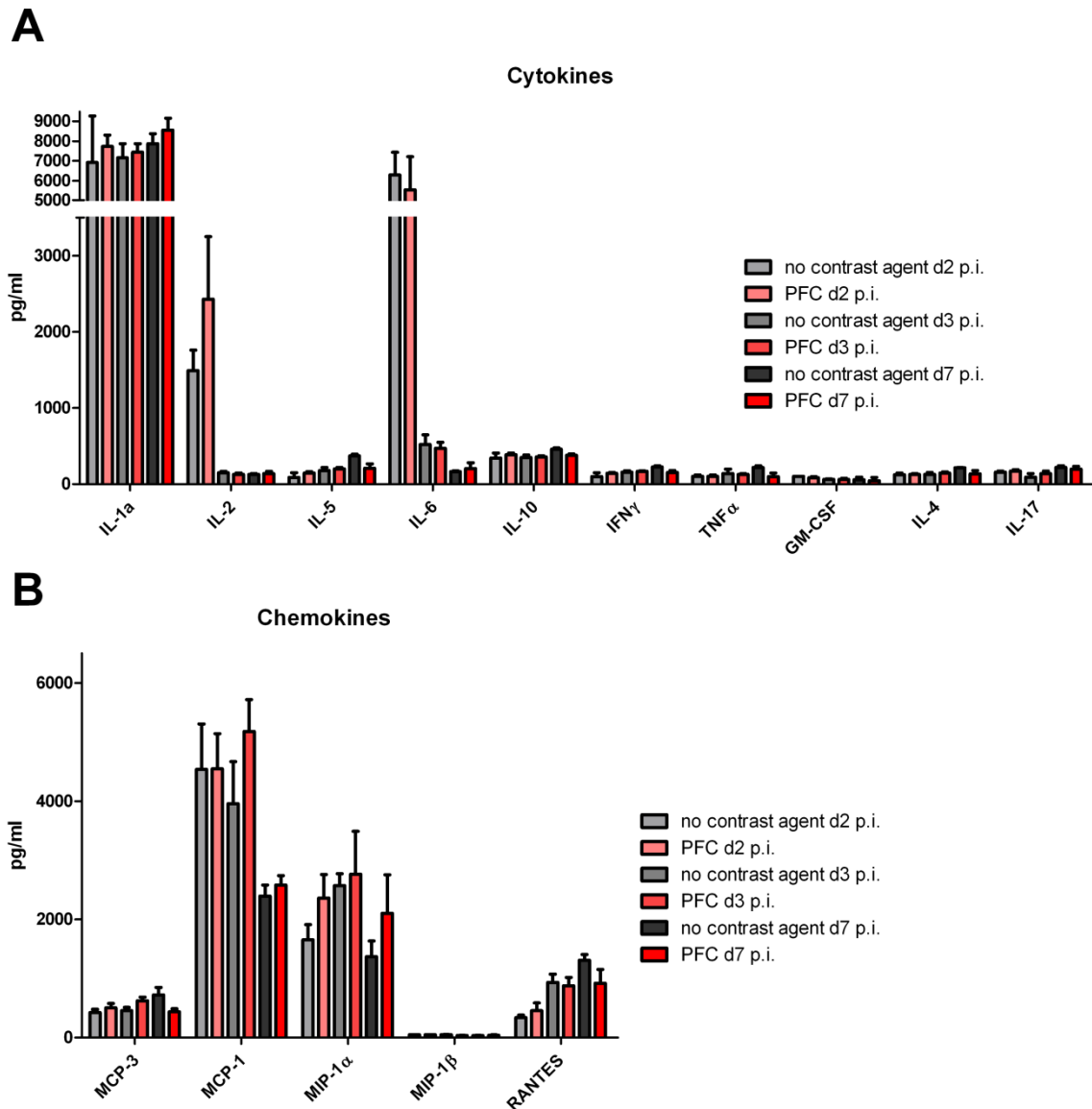


**Fig. 4.20:** Cytokine and chemokine pattern in the infected thigh muscle of PFC treated and untreated mice. Mice were challenged with  $2.2 \times 10^8$  CFU *S. aureus* Xen29 in the left thigh muscle. Muscles were recovered at indicated time points, homogenized and stored at  $-80^\circ\text{C}$  until determination of cytokine or chemokine levels. **A. the mean cytokine levels +/- SEM for PFC treated (5 animals each time point) and untreated groups (5 animals each time point) are shown.** Cytokine levels were measured via flow cytometry with 'Mouse Th1/Th2 10plex FlowCytomix Multiplex Kit' (eBioscience). **B. Shown are the mean chemokine levels +/- SEM for PFC treated (5 animals each time point) and untreated groups (5 animals each time point).** Chemokine levels were measured via flow cytometry with 'Mouse Chemokine 6plex FlowCytomix Multiplex Kit' (eBioscience).

## 4.2. Discussion

Infectious diseases are a constant threat to public health worldwide. Although the identification of antibacterial compounds and its introduction into clinics has led to a strong decrease of deaths caused by infectious diseases, especially in developed countries (Yoshikawa TT 2002), the WHO estimated, nonetheless, that in 2002 about 25.9 % of all deaths worldwide were caused by infectious diseases (The World Health report 2004. Annex Table 2). Moreover, the emergence of new, formerly unknown pathogens, the development and spreading of antibiotic-resistance and the aging of human population exerts a constant, maybe even increasing, pressure on public health systems. In consequence, there is a sustained need for new and more efficient vaccines and antibiotics. Of special interest in this context is the opportunistic pathogen *Staphylococcus aureus*. This pathogen is able to cause a wide variety of diseases, ranging from superficial skin infections to invasive diseases like pneumonia, sepsis or endocarditis (Lowy FD. 1998). *S. aureus* is furthermore notorious in developing or acquiring resistance against antibiotics, thus limiting treatment options to fight life-threatening *S. aureus* infections. For illustration, MRSA infections alone affect more than 170.000 patients per year in the EU, causing more than EUR 380 million extra in-hospital costs (Köck R et al. 2010). In consequence, it is of paramount importance to develop new therapeutics and strategies against this pathogen.

In addition to the mere generation of new antibiotics or vaccines, the identification of sites of infection and the disease-inducing pathogen are of highest importance to enable targeted and efficient therapy. In vivo imaging technologies like positron emission tomography, magnetic resonance or bioluminescence imaging offer in this context non-invasive platforms to visualize and estimate the severity of disease in real-time. Moreover, these platforms might help to elevate the preclinical testing of promising compounds and strategies to fight infections in animal models. Simultaneously, they might help to reduce the number of animals necessary for preclinical evaluation of new compounds by delivering information about the gravity of disease of more than one time point per animal.

The goal of this chapter was therefore to test whether bioluminescence imaging and magnetic resonance imaging are capable to visualize the effects of *S. aureus* infection non-invasively and whether they can be included in a preclinical testing strategy of new compounds, or not. The main focus of the project in this context was the evaluation of magnetic resonance imaging as infection imaging modality, since earlier studies demonstrated the usefulness of bioluminescence imaging with genetically engineered luciferase-expressing *S. aureus* strains in several animal models (Contag CH et al. 1995, Francis KP et al. 2000, Kadurugamuwa JL et al. 2003b, Xiong YQ et al. 2005, Steinhuber A et al. 2008). The benefit of magnetic resonance imaging to visualize sites of *S. aureus* infections, in contrast, was only rarely investigated at the beginning of this study. Interestingly, former investigations concentrated either on the utility of native  $^1\text{H}$  MRI to evaluate the efficacy of antibiotics or on the usefulness of iron oxide particles as contrast

agents to identify the site of infection. It was, for example, depicted that T<sub>2</sub> weighted MRI visualizes sites of edema and inflammation with high resolution and enable identification of sites of infection especially in soft tissue or close to bones (Tang JS et al. 1988, Beltran J 1995). Consequently, MRI was used to assess the efficacy of vancomycin and imipenem/cilastatin in a *S. aureus* thigh infection model (Marzola P et al. 1999). But this study showed, that, although T<sub>2</sub> weighted MRI proved very useful to identify the site of infection, the clear definition of the area of infection as well as the quantification of the severity of disease remained challenging or not feasible with these methods. The variance of the MR results was rather high and the values of vancomycin and mock group overlapping, thus preventing statistically significant differences, although histology proved the efficacy of vancomycin treatment in this experiment. The second approach to apply MRI as infection imaging technology was the evaluation of iron-based contrast agents as infection or inflammation specific imaging probes. It was shown, that ultrasmall superparamagnetic iron oxide (USPIO) particles accumulate after intravenous administration in activated macrophages (Kaim AH et al. 2002). The labeled macrophages migrated in the *S. aureus* thigh infection model to the site of infection, leading to accumulation of USPIOs at the abscess (Gelissen J et al. 1999, Lutz AM et al. 2005).

But these last-mentioned, contrast agent-focused studies did not investigate whether antibiotic therapy has an effect upon accumulation of contrast agent at the site of infection and therefore, the question whether contrast agent based MRI might deliver clearer results about efficacy of antibacterial therapy than native <sup>1</sup>H MRI alone remained unanswered. The main goal of this chapter was in consequence to test different MR methods, especially contrast agent based ones, to visualize sites of infection to enable in the following chapters the application of MRI as an preclinical in vivo antibiotic testing platform.

The first step was to establish and characterize an animal model. The *S. aureus* thigh abscess model was chosen, because it leads to bulky and localized abscesses in the infected thigh muscle. It was furthermore used in the former MR studies of antibiotic efficacy testing (Marzola P et al. 1999) and USPIO evaluation (Kaim AH et al. 2002, Lutz AM et al. 2005). The intramuscular injection of  $2.2 \times 10^8$  CFU *S. aureus* Xen29 led to a stable bacterial community of ca.  $10^9$  CFU after an initial phase (first 24 hours) of bacterial growth (Fig. 4.1). The bacterial burden in the liver, kidneys and spleen were very low or not detectable during the experiment, proving a localized infection in the thigh muscle. The histological examination of the infected thigh muscles showed a dense infiltration of granulocytes at the rim of an emerging abscess area at acute phase of inflammation (day 3 p.i.), surrounding a central area of necrosis. These results were congruent with the MR based imaging studies based on this animal model (Marzola P et al. 1999, Kaim AH et al. 2002, Lutz AM et al. 2005).

Since *S. aureus* Xen29 harbors the *luxABCDE* operon and is thus able to express bacterial luciferase, accompanying bioluminescence imaging was possible. The photon emission of this strain dropped strongly within the first 24 hours of infection from a very strong signal to almost background values (Fig. 4.1 E). Reason for this behavior might be a phase of adaption

from high nutrient medium conditions to nutrient limitation in the murine host. The signal increased from day 1 p.i. until day 4 p.i., but did not reach the initial levels again. From day 4 to day 7 p.i., the signal remained at a stable level, suggesting a constant bacterial community. In summary, the bioluminescence signal between days 4 and 7 p.i. fitted nicely to CFU counts of these time points, both of them indicating constant numbers of bacteria in the infected thigh muscle. The initial phase of infection is in contrast characterized by a large discrepancy in the results derived from CFU counting and bioluminescence imaging. This has to be taken into account when trying to measure the bacterial burden with bioluminescence imaging in the early phase of infection.

The first MR experiments were facilitated to explore the effects of infection in the thigh muscle on native  $^1\text{H}$  MR parameters. As expected from earlier publications (Marzola P et al. 1999),  $T_1$  weighted MRI did not visualize changes in the infected thigh muscle, while  $T_2$  weighted MRI indicated edema formation at least from day 2 p.i. until the end of the experiment. But a clear distinction of infected and not-infected tissue remained impossible since elevated  $T_2$  relaxation times in the center of the edema formation did not form a clear border but a continuous decrease to values of normal, healthy tissue (as measured for example in the right, control muscle). The values showed furthermore high variance between different mice, thus reducing the chance to visualize quantitative differences between antibiotic treatments even more. In conclusion, the MR results were congruent with the study published by Marzola P et al. in 1999, demonstrating the usefulness of  $T_2$  weighted MRI to visualize sites of infection, but lacking on the other hand a sufficient quantification of severity of infection.

One idea to cope with this problem was the application of iron oxide particles (USPIOs) as contrast agents to image the border between abscess and healthy tissue by MRI. These particles accumulate in activated macrophages after intravenous application (Gelissen J et al. 1999). The subsequent migration of the immune cells to the site of infection then leads to accumulation of USPIOs at the rim of the abscess area (Kaim AH et al. 2002). In our experiments, the intravenous administration of cross-linked iron oxide particles (CLIO), which are very similar to USPIOs, at day 6 p.i. led to accumulation of iron particles at the rim of the edema area (which is indicated by increased  $T_2$  relaxation times) at chronic phase of inflammation and enabled thereby a distinction of infected and not-infected tissue (Fig. 4.3). This fits nicely to the above-mentioned former studies, but the application of CLIOs at acute phase of inflammation (day 2 p.i.) caused only sparse and rather diffuse signal distortion effects at the rim of the abscess area, suggesting less pronounced accumulation and avoiding clear distinction of abscess and healthy tissue. But this hampered the quantification of abscess volume and thus the estimation of the disease severity. Another reason against iron oxide particles is the fact, that they are usually detected by their signal distortion effects at the site of accumulation, inducing 'black spots' in the images. Their accumulation can be imaged quite nicely in the thigh muscle, since this tissue delivers sufficient and continuous inherent MR signal, but an application in, for example, systemic infection models, where one

encounters tissues with less inherent signal, an identification of spots of accumulation and their quantification might be very challenging.

Another, recently developed MR tracer based method to identify sites of inflammation, is  $^{19}\text{F}$  MRI with perfluorocarbons. Perfluorocarbons, the imaging 'agent' of this method, are therefore in most studies formulated as emulsion, since this compound class is neither soluble in water nor in lipids. The intravenous application of the perfluorocarbon emulsion in murine models of ischemia, stroke, pulmonary inflammation or arthritis led to accumulation of perfluorocarbons at the site of inflammation (Flögel U et al. 2008, Ebner B et al. 2010, Balducci A et al. 2012). This accumulation can be visualized background-free by  $^{19}\text{F}$  MRI since the mouse does not harbor intrinsically sufficient amounts of  $^{19}\text{F}$ . Nevertheless, the  $^{19}\text{F}$  image can then be overlaid on a  $^1\text{H}$  MR image to visualize the accumulation in anatomical context (Janjic JM, Ahrens ET 2009).

The intravenous administration of perfluorocarbon emulsion in the *S. aureus* thigh muscle infection model at acute phase of inflammation (day 2 p.i.) led to accumulation of  $^{19}\text{F}$  signal at the rim of the edema or abscess area on the MR images 24 hours later (Fig. 4.5). The accumulation formed a 'hollow sphere' circumscribing a central volume with no detectable perfluorocarbon. A similar picture could be seen, when perfluorocarbon emulsion was injected at chronic phase of inflammation (day 8 p.i.). In conclusion, the  $^{19}\text{F}$  signal accumulated at both time points in the shape of a 'hollow sphere' at the rim of the abscess area, thus defining the area of infection in an easy to identify manner.  $^{19}\text{F}$  MRI with perfluorocarbons as tracer substance seems after this first experiments much better suited to investigate the effect of antibiotic therapy than native  $^1\text{H}$  based MRI or MRI with iron oxide nanoparticles. To test for durability of  $^{19}\text{F}$  accumulation at the site of infection, a further group of mice was imaged at various time points after administration of perfluorocarbon emulsion at day 2 p.i.. The imaging at days 3, 5, 7 and 9 showed consistent accumulation of tracer at the site of infection (Fig. 4.7), suggesting stable signal after one single administration of perfluorocarbon emulsion and thus enabling time course imaging of the abscess area. Interestingly, a weaker infectious dose did not only lead to a smaller number of bacteria in the infected thigh muscle after 10 days of infection than initially injected, but also to a reduction or partial loss of  $^{19}\text{F}$  accumulation around the abscess area. This means, that CFU determination as well as  $^{19}\text{F}$  MRI suggests some kind of healing process. But nonetheless, the initial accumulation of perfluorocarbon emulsion at the site of infection led to the well-known 'hollow sphere' pattern around the edema area, which is indicated in the  $T_2$  maps. Taken together, these results suggest a correlation of perfluorocarbon emulsion accumulation or stability at the site of infection and the bacterial burden or severity of disease.

The following experiments sought to investigate the kinetics of accumulation in greater detail. It was unknown till these experiments, whether perfluorocarbon accumulates immediately after intravenous administration at the site of infection, or not. It was furthermore not clear, whether administration of tracer at other time points than day 2 and

day 8 p.i. leads to detectable amounts of  $^{19}\text{F}$  at the site of infection. Thus, in the first experiments, MR imaging was started immediately after administration of perfluorocarbon emulsion to define the first time point of visualizable  $^{19}\text{F}$  'hollow sphere' accumulation at the site of infection. Although, the time points were not congruent in the four investigated mice, a first visualization of perfluorocarbon in the infected thigh muscle was possible at least in two of them at around 11 hours post administration (Fig. 4.8). The results derived from variation of administration time point experiments showed a lack of perfluorocarbon accumulation at the site of infection when the tracer was applied at 2 or 24 hours post infection, while administration at later time points led in all other mice to 'hollow sphere'  $^{19}\text{F}$  pattern around the abscess area (Fig. 4.9). Taken together, these experiments suggest a specific accumulation that depends on the status of the infection or immune response. It seems to be more probable that the status of the immune response is responsible for accumulation or the lack of accumulation at the site of infection, since it was shown in former studies of ischemia, stroke and pulmonary inflammation that perfluorocarbon emulsions accumulate in macrophages and monocytes, whose subsequent migration to the site of inflammation led to fluorine MR signal (Flögel U et al. 2008, Ebner B et al. 2010). Recently, it was shown in addition that macrophages and monocytes, but also neutrophils are able to take up perfluorocarbon emulsion and their migration behavior leads to accumulation of  $^{19}\text{F}$  signal at sites of inflammation (Temme S et al. 2013). Therefore, it seems likely that phagocytes are not attracted in sufficient amounts to the site of infection to induce visualizable MR signal at early phase of infection (until day 2 p.i.), while the activation of phagocytes, especially neutrophils and macrophages/monocytes, becomes strong enough at later stages.

The former MR imaging experiments visualized the accumulation of perfluorocarbon emulsion at the site of infection in a small field of view (approximately 3 cm of the length of the mouse), but gave no hints about further sites of accumulation. To investigate this, whole mice were fixed in formalin solution (24 hours after perfluorocarbon administration), after being challenged with *S. aureus* and having received a single emulsion application at day 2 p.i., and were imaged by  $^{19}\text{F}$  MRI in different, larger  $^1\text{H} / ^{19}\text{F}$  double-resonant MR coil, which enabled whole animal imaging. The 3D reconstruction of these ex vivo measurements showed strong accumulation of perfluorocarbon in the liver, spleen and infected thigh muscle, as well as low amounts in spinal cord and bones (Fig. 4.10). This highly selective pattern, seen in all investigated mice, suggests a specific mechanism causing the accumulation of tracer. It seems probable that perfluorocarbon emulsions are filtered from the blood by cellular uptake in liver cells and phagocytes in the blood, bone marrow or spleen.

In order to address this question, methods to measure the perfluorocarbon emulsion content of organs and cells became necessary. In a first approach the  $^{19}\text{F}$  amounts in organ homogenizations were determined with ex vivo MRI. The distribution in the perfluorocarbon signal in the liver, spleen and thigh muscle proved that most of the signal could be detected in the liver (Fig. 4.12), covering about 80 % of the total signal, while only about 10 % of the

total signal counted for the infected thigh muscle.  $^{19}\text{F}$  signal was in this context very early (30 min after injection) measurable in liver and spleen, but not in the infected thigh muscle. This suggested a filtration-like mechanism for the accumulation in liver and spleen, while the accumulation at the site of infection seems to depend on a more time-consuming mechanism, maybe cellular uptake in the blood and their subsequent migration to the abscess area. In consequence, most of the applied perfluorocarbon emulsion did not reach the area of interest. Therefore, future developments of perfluorocarbon emulsions should aim for targeted approaches to increase the specificity of accumulation. Maybe even an approach to hide the emulsion for phagocytes or liver filtration might become necessary or beneficial. Most importantly, due to low amounts of blood that could be recovered during course of infection, an ex vivo  $^{19}\text{F}$  measuring approach with MR failed. An idea to circumvent this problem was the application of fluorescently labeled perfluorocarbon emulsions. Unfortunately, the commercially available formulations exhibited too weak fluorescence labeling to identify them in vivo or in blood samples. This made the home production of emulsion with higher amounts of fluorescence labels necessary.

A sonication approach was used to emulsify perfluorocarbons in a lipid surfactant commixture to receive liposomal formulations for intravenous application. The composition of the particles followed in principle former descriptions in literature (Partlow KC et al. 2007, Southworth R et al. 2009). The core of the particles consisted in this context of perfluoro-15-crown-5-ether, a compound with 20 magnetically equivalent  $^{19}\text{F}$  atoms, which was surrounded by a layer of lecithin stabilized with cholesterol. The sonication led to particle populations with different sizes in each preparation, but after serial filtration through different sized syringe filters, a single particle population with a size of less than  $0.45\ \mu\text{m}$  remained in the preparation. The intravenous administration in the *S. aureus* thigh infection model led to the well-known 'hollow sphere' accumulation pattern around the abscess area in the infected thigh muscle and to further spots of accumulation in the liver and spleen. No differences between homemade and commercially available emulsions could be determined, suggesting comparability of the results derived from both preparations. The addition of Atto647N-DOPE to the surfactant commixture enabled strong fluorescent labeling of the emulsion and thus fluorescence imaging of perfluorocarbon emulsions in ex vivo and in vivo samples.

The intravenous application at day 2 p.i. led to a very strong fluorescence signal in the whole mouse at 30 min post administration, indicating global distribution via the blood stream and availability of emulsion in the whole animal. At 12 hours p.i., this extensive fluorescence signal was gone, but a specific accumulation at the site of infection could be imaged. Surprisingly, the fluorescence signal at the site of infection decreased steadily between 12 hours and 48 hours post administration and reached almost the background level of control mice, which had not received fluorescent perfluorocarbon emulsion at 72 hours post administration. No fluorescence signal could be detected in liver or spleen areas of the mice. The fur of the mouse, which was not removed at these spots, but at the infected thigh muscle, might have decreased the signal as well as the depths of both organs in the body of

the mouse. This seemed to be a reasonable explanation for the surprising lack of in vivo fluorescence signal from these organs, although the ex vivo  $^{19}\text{F}$  MR experiments indicated perfluorocarbon accumulation in both of them. This hypothesis was furthermore corroborated by measuring the fluorescence signal of the homogenizations of organs, which were collected at day 7 p.i.. The fluorescence signal of liver and infected thigh muscle homogenizates were significantly higher in mice treated with fluorescently labeled perfluorocarbon emulsion than in mice treated with non-fluorescent control emulsions (Fig. 4.12). Nonetheless, the spleen, one major source of  $^{19}\text{F}$  MR signal in ex vivo measurements, delivered only slightly but not significantly higher values for fluorescent emulsion vs. control. Since less sample volume was needed for fluorescence imaging than for  $^{19}\text{F}$  MRI, measuring the content of fluorescence signal of perfluorocarbon emulsions in the blood became feasible. The fluorescence signal in the blood of mice treated with fluorescently labeled preparations showed a very robust signal immediately after injection, that strongly decreased in the first 24 hours to reach the signal level of control treated mice at least at 72 hours post infection. This suggests a rapid clearance or uptake of the perfluorocarbon emulsion. One has to take into account for all these experiments that it is highly likely that the fluorescence label, which is exposed at the surface of the emulsions, gets bleached or inactivated in the mouse's body under in vivo conditions, although Atto647N was chosen because of its high pH stability. This might lead to lower values or stronger reduction of signal than indicated by  $^{19}\text{F}$  MRI. The perfluorocarbon in the core of the emulsion is in contrast to this biologically and chemically inert and in addition shielded from the surrounding environment, thus  $^{19}\text{F}$  signal reduction or loss is less probable.

Taken together, the fluorescence imaging results suggest in principle the same distribution pattern of perfluorocarbon emulsion than  $^{19}\text{F}$  MRI, with some technical advantages like faster gathering of images or values and smaller sample sizes for ex vivo measurements, but could not, as initially expected, deliver higher sensitivity. The fluorescence labels are furthermore prone to bleaching or inactivation in the in vivo environment. But on the other hand they inaugurated a whole new choice of methods to investigate the accumulation of perfluorocarbon emulsions like flow cytometry or fluorescence microscopy.

In order to characterize those immune cells who take up perfluorocarbon emulsion in vivo, the infected thigh muscles were recovered early after administration of perfluorocarbon emulsion, namely 16 hours, since the in vivo  $^{19}\text{F}$  MR imaging results suggested a detectable accumulation at around 11 to 12 hours post administration. To recover as much viable immune cells as possible, a gentle and fast approach for homogenization via pressing through a cell strainer was chosen. The resulting homogenizate was then incubated with different fluorescently labeled antibodies to identify those immune cell populations who exhibit perfluorocarbon associated Atto647N fluorescence. Former studies have demonstrated the accumulation of perfluorocarbon emulsions in macrophages/monocytes (Flögel U et al. 2008, Ebner B et al. 2010) and a very recent study, which was not available during the experimental part of this thesis, additionally in neutrophils (Temme S et al. 2013). Therefore the flow cytometry analysis was primary focused on neutrophils and macrophages



and secondary on other immune cells like dendritic cells, T cells and B cells. The binding of antibodies to immune cell population specific surface-exposed antigens should serve to identify them. Ly6G was applied to identify neutrophils since it was described that this antigen is primarily expressed on neutrophilic granulocytes and expression increases during maturation (Fleming TJ et al. 1993). Macrophages were identified by their expression of the antigens F4/80 or CD68 (Zhang X et al. 2008). CD11b is mainly expressed on macrophages/monocytes and microglia in mice, but upon activation neutrophils start to express this antigen in larger amounts, too (Anderson DC et al. 1986). Mouse CD11c is present on dendritic cells in lymphoid organs and blood and serves as predominant marker to identify or deplete this immune cell population (Rahman S et al. 2010). The CD45R (B220) antigen served as marker for B cells due to its expression on this set of immune cells until they differentiate to plasma cells (Kroese FG et al. 1985). T cells were identified by antibodies against the antigen CD90 (Thy1.2), which is highly expressed on thymocytes and peripheral T cells in blood and lymphoid tissue (Ledbetter JA et al. 1979).

The gating strategy of the flow cytometry analysis was based on the exclusion of unspecific binding of antibodies to neutrophils via their binding to Fc receptors, which are highly expressed on activated neutrophils (Huizinga TW et al. 1990). Therefore, the B1 and B2 channels of the MACSQuant flow cytometer were occupied by detecting anti-CD11b FITC and anti-Ly6G PE conjugated antibodies. Neutrophils were expected to show either CD11b+ Ly6G+ (activated neutrophils) or CD11b- Ly6G+ (not activated) pattern. The other antibodies were used in conjugation with VioBlue or PacificBlue, both of them were detected in the V1 channel. Cells were only regarded as dendritic cells, T cells, B cells or macrophages, if they lacked binding of anti-Ly6G antibody. This means, they were gated and quantified in a B2 (anti-Ly6G PE) vs. V1 (anti-CD11c, anti-CD68, anti-CD90.2, anti-B220 or anti-F4/80 VioBlue) dot plot as PE signal negative but VioBlue positive cells. The majority of the isolated cells at the site of infection were Ly6G+ CD11b+ activated neutrophils, representing about 50 % of total cells. Minor amounts (about 2 - 4 % of total cells) of Ly6G- B220+ B cells and Ly6G- CD90.2+ T cells could be identified, as well as the same amount of Ly6G- CD11b+ cells. The macrophage specific antigens CD68 and F4/80 could be identified in only about 1 % of total cells, and dendritic cells (Ly6G- CD11c+) accounted for further 1 % of total cells. In summary, the results are congruent with former studies proving that neutrophils constituted the main part of the immune cells at the site of infection, and their action is essential for the immune response against *S. aureus*. (Cheng AD et al. 2009, Cho JS et al. 2012).

The fluorescence of the perfluorocarbon emulsion label (Atto647N) could be visualized in the R1 channel of the flow cytometer. Hence, Atto647N was the only fluorescence label in this experiment that was excited by the red laser at 638 nm, thus preventing signal spillover from other fluorescence labels and preventing the need for compensation. When measuring the Atto647N fluorescence of cells, two peaks could be seen in the histograms of Atto647N-labeled perfluorocarbon emulsion treated mice, while control emulsion treated mice showed only one peak. In conclusion, perfluorocarbon emulsion conjugated signal could be detected in cells, indicating intracellular or cell-bound perfluorocarbon emulsion

accumulation. The identification of different cell types with specific antibodies showed, that a shift to increased R1 channel signal could be detected for Ly6G<sup>+</sup> cells, but only in the samples of fluorescently labeled perfluorocarbon emulsion treated mice. Interestingly, some samples showed in the Atto647N vs. anti-Ly6G PE dot plot a second Ly6G<sup>+</sup> neutrophil population with higher Atto647N fluorescence signal than the main population. Source for this second neutrophil population with stronger perfluorocarbon emulsion uptake might be the portion of neutrophils that circulated in the blood stream, when the tracer was administered. They might have incorporated the fluorescent perfluorocarbon emulsion in the blood stream prior to their migration to the site of infection. It seems reasonable that this population vanishes rather fast from flow cytometry analysis due to the short life span of neutrophils. And when dying, they might release the perfluorocarbon emulsion, which might be subsequently taken up by other neutrophils at the site of infection. Overall, the elevated levels of Atto647N fluorescence prove the accumulation of perfluorocarbon emulsion in or with Ly6G<sup>+</sup> neutrophils.

However, Ly6G<sup>+</sup> neutrophils were not the only cell population at the site of infection with elevated Atto647N fluorescence, Ly6G<sup>-</sup> CD11c<sup>+</sup> dendritic cells as well as macrophages (Ly6G<sup>-</sup> CD11b<sup>+</sup>, Ly6G<sup>-</sup> CD68<sup>+</sup> as well as Ly6G<sup>-</sup> F4/80<sup>+</sup> cell populations) showed increased Atto647N fluorescence, too, while Ly6G<sup>-</sup> CD90.2 T cells and Ly6G<sup>-</sup> B220<sup>+</sup> B cells lacked elevated R1 channel signal levels. In summary, fluorescently labeled perfluorocarbon emulsion accumulated in neutrophils, macrophages and dendritic cells at the site of infection, all of them phagocytotic active cell types. Thus, the flow cytometry analysis of perfluorocarbon emulsion accumulation showed in principle results similar to those of former studies (Flögel U et al. 2008, Ebner B et al. 2010). These studies demonstrated accumulation in phagocytes, too, although, in contrast to our results, the main portion of perfluorocarbon emulsion was taken up by macrophages and monocytes. Explanation for this might be the different disease models used to study perfluorocarbon emulsion. These former studies investigated the accumulation in models of stroke, ischemia and pulmonary inflammation, while this study focused on the accumulation at sites of *S. aureus* infection. A further study, which was published after the experimental part of this PhD thesis, showed interestingly <sup>19</sup>F accumulation in neutrophils and macrophages in a subcutaneous model of inflammation (Temme S et al. 2013). This fits very nicely to the results of this study.

Altogether, fluorescent perfluorocarbon emulsion could be detected in neutrophils, macrophages and dendritic cells at the site of infection in the *S. aureus* thigh infection model. The main part of identified immune cells at the site of infection was assigned as neutrophils, accounting for about 50 % of total cells. Since macrophages, dendritic cells and neutrophils displayed similar Atto647N fluorescence, the lion's share of fluorescently labeled perfluorocarbon emulsion should be assigned to neutrophils at the site of *S. aureus* abscesses in the thigh infection model due to their predominant number.

Flow cytometry of fluorescently labeled perfluorocarbons at the site of infection showed nicely perfluorocarbon derived fluorescence in cells, but could not visualize emulsion which

is not associated with cells. Furthermore, flow cytometry can deliver only information about cell populations that can be identified by specific antibody binding and moreover, it visualizes the perfluorocarbon emulsion content of individual cells but not of the global accumulation strength in cell populations. To address the question whether perfluorocarbon emulsion accumulates at the site of infection outside of immune cells and moreover, which immune cell population carries the biggest load of emulsion, cell sorting experiments were conducted.

The hypothesis, that perfluorocarbon emulsion is transported to the site of infection by the action of immune cells, suggested and shown by former models of inflammatory diseases, but not infection models (Flögel U et al. 2008, Ebner B et al. 2010), can be addressed in two ways by this method: first by sorting of individual immune cell populations in order to measure their perfluorocarbon emulsion signal and second, by depletion of individual cell populations in order to measure the residual perfluorocarbon emulsion signal in the homogenate. The second approach might provide information not only about the emulsion content of the depleted immune cell population, but also about perfluorocarbon emulsion that accumulates outside of cells at the site of infection. This in turn might indicate an unspecific, not necessarily infection-associated accumulation mechanism.

A variety of different cell sorting methods were applied to answer these questions: density gradient centrifugation, magnetization-activated cell sorting (MACS) and cell sieving (Pluriselect). Density gradient centrifugation did not result in clearly separated cell populations, maybe due to changes in density of immune cells after entering the inflammatory environment at the site of infection. Magnetization activated cell sorting was characterized by the loss of many cells in the separation columns, independently of the expression of specific surface antigens. In consequence, the sorted Ly6G<sup>+</sup> and CD11b<sup>+</sup> cell samples exhibited only small <sup>19</sup>F MR signal, while F4/80<sup>+</sup> cells showed no detectable signal. But the flow through samples (all cells and soluble components with the exception of sorted cells and cells that were lost in the column) displayed similar strong signal than the sorted cell samples. Nonetheless, the exclusion of cells from these samples by filtration led to a strong decrease of <sup>19</sup>F MR signal. These results indicate cellular accumulation of perfluorocarbons, although the majority of <sup>19</sup>F MR signal was lost in the sorting columns and could not be addressed to any source.

The cell sieving approach, finally, enabled sorting of immune cells without losing too much cells and perfluorocarbon signal. This method is based on the binding of immune cells via specific antigens to antibody-conjugated beads. In the following filtering step remained the bead-bound cells in the filter since the beads are too large to fit through the pores. Hence, the depletion of specific immune cell populations from crude muscle homogenate was possible, but the bead-bound cells could be recovered from the filter, too, by simple reuptake in buffer. Four bead populations were applied to cell sorting to target different surface antigens and thus different immune cell populations. Ly6G<sup>-</sup> and CD11b<sup>-</sup> targeted beads were used to identify the perfluorocarbon emulsion signal in neutrophils (Ly6G, Daley

JM et al. 2008) and neutrophils, monocytes and macrophages (CD11b, Fischer MA et al. 2011). CD4-targeted beads to aim at T helper cells (Zhu J et al. 2010) and CD19-targeted beads for B cells (Kehrl JH et al. 1994). Unfortunately, flow cytometry of sorted cells, filter-flow-through and crude muscle homogenate showed that pure immune cell populations or complete depletion from crude muscle homogenate failed for all four beads. But strong enrichment of the specific immune cell populations in the 'sorted cell' samples or reduction of abundance in the 'flow-through' samples (Fig. 4.15) resulted nonetheless in samples with variations in their immune cell content and thus comparison of the perfluorocarbon emulsion signal might give insights into the tracer distribution pattern at the site of infection.

Determination of perfluorocarbon content of the samples by  $^{19}\text{F}$  magnetic resonance imaging delivered only signals close to background, maybe due to the strong dilution of samples during sorting process, which was necessitated by the sorting protocol. And furthermore, only around  $1.0$  to  $1.5 \times 10^7$  cells could be applied in the sorting approach, which might not be sufficient for  $^{19}\text{F}$  MR determination of perfluorocarbon content. But the emulsion could, in principle, be detected moreover by fluorescence imaging since fluorescently labeled emulsion was administered. And indeed, fluorescence imaging showed detectable signals for all samples with exception of negative control samples.

Sorting of crude muscle homogenate resulted in variations of fluorescence signal. Sorting of Ly6G+ and CD11b+ cells led to increased fluorescence in the 'sorted cell' sample while the 'flow-through' samples showed decreased signal. It has to be noted in this context, that flow cytometry of immune cell populations at the site of infection earlier in this chapter demonstrated that Ly6G+ cells express additionally CD11b in the infected thigh muscle. Therefore it is reasonable that both beads targeted similar or overlapping cell populations. Overall, the sorted cells had an even stronger fluorescence signal than the crude emulsion, suggesting higher concentration of fluorescence marker and thus perfluorocarbon emulsion in the sorted cells than in other cell populations at the site of infection. The fluorescence signal in the 'flow-through' sample was much lower, but still above the signal of non-fluorescent perfluorocarbon treated mice samples (control). This might suggest further sources of perfluorocarbon emulsion at the site of infection than Ly6G+ and/or CD11b+ cells, but it is equally possible, that the residual fluorescence signal originates from Ly6G+ and/or CD11b+ cells that remained in the flow-through since sorting did not deplete these cell populations completely. In summary, enrichment of Ly6G+ or CD11b+ cells resulted in elevated fluorescence levels while the reduction of Ly6G+ or CD11b+ cell numbers (in the flow-through samples) decreased the fluorescence signal. Thus, Ly6G+ and CD11b+ cells are carriers of perfluorocarbon emulsion at the site of infection.

CD4 and CD19 sorting led to lower fluorescence signal in the 'sorted cell' samples than in the crude muscle homogenate and in the 'flow-through' samples. Moreover, reduction of CD4+ or CD19+ cell concentration in the homogenate (flow-through) had no effect upon fluorescence signal. This suggests low or no amounts of perfluorocarbon emulsion in T and B

cells at the site of infection, although sorting led only to enrichment in the 'sorted cell' samples. In conclusion, cell sorting indicates perfluorocarbon emulsion accumulation in Ly6G<sup>+</sup> and CD11b<sup>+</sup> cells at the site of infection, but not in CD4<sup>+</sup> or CD19<sup>+</sup> cells. A reduction of fluorescence signal in samples with reduced Ly6G<sup>+</sup> and CD11b<sup>+</sup> cell concentration suggested furthermore, that the majority of perfluorocarbon emulsion signal arises from these cell populations. Importantly, a control filtration of diluted perfluorocarbon emulsion through cell sorting filters demonstrated, that these particles fit through the pores, thus all signal from 'sorted cell' samples must originate from cell-associated emulsion. Consequently, an unspecific, cell independent accumulation mechanism of perfluorocarbon emulsion at the site of infection seems unlikely in the light of these results.

Flow cytometry and cell sorting delivered a nice analysis of fluorescently labeled perfluorocarbon emulsion accumulation in immune cells at the site of infection, but the homogenization of the infected thigh muscle was inevitable to analyze the samples. Histology, in contrast, might give a hint about the spatial distribution of perfluorocarbon emulsion and might help to identify further spots of accumulation that could not be addressed by flow cytometry. The first approach to identify immune cell populations and contrast agents/tracer (CLIO particles and perfluorocarbon emulsion) at the site of infection was to perform standard fixation (formalin fixation with following paraffin embedding) and hematoxylin-eosin (HE) staining of the slices. Samples of two different time points after administration of the agents were of interest: day 3 p.i. (24 hours after administration of agents) to visualize immune response and contrast agent accumulation at acute phase of inflammation and day 8 p.i. (6 days after administration of contrast agents) to cover the chronic phase of inflammation. Histological examination of acute phase samples from CLIO and perfluorocarbon groups revealed a strong neutrophil community in the infected thigh muscle with some macrophages, both of them surrounding a central area of necrosis. The samples from chronic phase of inflammation showed strong aggregation of neutrophils, but in addition macrophages, lymphocytes and eosinophiles. In the center of the immune cell accumulation, a large necrotic area could be seen. The HE staining of tissue slices from CLIO, perfluorocarbon emulsion or control (0.9 % NaCl) group mice showed comparable results, indicating no impact on immune cell activation and migration pattern by perfluorocarbon or CLIO. But neither perfluorocarbon emulsion nor CLIO accumulation could be visualized by this staining. This means in consequence, that either perfluorocarbon emulsion does not lead to a different staining pattern than cytoplasm or it is not incorporated in cells and therefore maybe washed away during staining procedure or the emulsion liposomes are too small to be visualized by standard light microscopy. Since the fluorescence label of emulsion could be detected in immune cells by flow cytometry, one would expect at least in some of the neutrophils or macrophages at the site of infection some emulsion accumulation. In conclusion, it seems reasonable that the emulsion cannot be visualized by this method and it might furthermore give a hint that the liposomes did not fuse and grow *in vivo*, which seemed to be possible due to their hydrophobic nature and amphiphilic surface.

CLIO particles cannot be visualized by HE staining, but by Berlin's blue staining in fixed, embedded tissue sections. This iron-specific staining showed iron accumulation in some macrophages and granulocytes during acute phase of inflammation and in macrophages, lymphocytes and granulocytes during chronic phase of inflammation in CLIO group mice. Therefore, this experimental data is congruent with former studies investigating the accumulation of USPIO particles at *S. aureus* induced thigh abscesses (Kaim AH et al. 2002, Kaim AH et al. 2003).

Unfortunately, there was no method available to stain and visualize perfluorocarbons in a similar way in fixed tissue section. In order to solve this problem, Atto647N-fluorescently labeled perfluorocarbon emulsion was administered intravenously to enable fluorescence microscopy of emulsion accumulation in tissue sections from the site of infection. The infected thigh muscles were not fixed in formalin, but immediately frozen after recovery and cut to 10 µm thick slices in a crytome to offer as native samples as possible. A former study has shown that washing and staining of samples from perfluorocarbon treated mice led to severe or complete loss of perfluorocarbon fluorescence in tissue sections, and furthermore all tested fixation methods led to loss of fluorescence signal in this study (Flögel U et al. 2008). Thus, the first analysis was performed with native, unstained and untreated slices. Several spots of high Atto647N fluorescence or areas with lower fluorescence, that followed in principle the shape of cytoplasm of cells, could be visualized in samples of fluorescently labeled perfluorocarbon group mice, but not in control perfluorocarbon group mice. The fluorescence signal seemed to accumulate in an area close to the border between muscle tissue and immune cell aggregation in the immune cell section, but a clear view upon anatomical context of Atto647N accumulation was not possible due to the lack of anatomical staining.

In the second approach, a short staining protocol was applied to reveal the tissue at the site of perfluorocarbon accumulation. Tissue sections were stained with Hoechst 33425, which stains DNA, and with Atto520-Phalloidin, a fluorescently labeled bicyclic heptapeptide that binds strongly to actin. The advantage of this staining protocol was the short incubation time of the dyes and only one necessary washing step. In result, the staining revealed immune cell nuclei and muscle fibers by fluorescence microscopy (Fig. 4.16). An extensive aggregation of immune cells could be visualized via cell nucleus staining surrounding a central core with less Hoechst 33425 signal (cell nuclei) and absent muscle fibers (imaged by phalloidin dependent actin staining). Atto647N fluorescence could be detected in close proximity to Hoechst 33425 stained cell nuclei, but never overlapping with this signal. The fluorescence signal was similar to the signal of unstained samples, although there seemed to be less many spots or areas of signal. This might be an indication for loss of Atto647N fluorescence or loss of perfluorocarbon emulsion by staining/washing steps. Nonetheless, the detectable signal could be visualized either as small, bright spots or larger areas (in a cytoplasm likewise shape). This and the lack of signal in phalloidin-stained muscle fibers, suggested accumulation of perfluorocarbon emulsion either in the cytoplasm or at the surface of the immune cells at the site of infection. Further approaches to stain the immune cells at the site

of infection with specific antibodies necessitated further staining, washing and incubation steps, but this resulted in complete loss of Atto647N fluorescence and thus failed to identify the immune cell population(s) that carried perfluorocarbon emulsion at the site of infection.

In summary, flow cytometry, cell sorting and microscopy analysis of samples from Atto647N (or Atto550)-fluorescent perfluorocarbon group mice demonstrated accumulation of tracer emulsion in immune cells at the site of infection. All perfluorocarbon related fluorescence signal was in close proximity to nuclei of immune cells at the site of infection and flow cytometry indicated most of the signal in neutrophils, lower amounts in macrophages and dendritic cells, respectively. Cell sorting demonstrated furthermore, that Ly6G<sup>+</sup> and/or CD11b<sup>+</sup> cell depletion (or reduction) led to considerably reduced perfluorocarbon emulsion derived fluorescence, thus suggesting that these cells serve as main source of perfluorocarbon emulsion signal. Consequently, it seems to be very likely that perfluorocarbon emulsion accumulates at the site of infection mainly in Ly6G<sup>+</sup> and CD11b<sup>+</sup> cells. An unspecific, cell-independent accumulation is unlikely since the majority of emulsion derived fluorescence signal is associated with these cells. Nonetheless, two questions could not be answered in this regard: First, what happens to the perfluorocarbon emulsion when the transporter immune cell dies? And second, inasmuch as perfluorocarbon emulsion accumulated in phagocytic immune cells, it raised the question whether perfluorocarbon emulsion might have an impact on immune cell function, or not?

To elucidate the impact of perfluorocarbon emulsion administration on infection and immune response in the *S. aureus* thigh infection model, a series of experiments was performed to measure differences in the outcome between perfluorocarbon treated and untreated mice. The parameters which were necessary to evaluate the efficacy of antibiotics in future experiments were of particular interest. Hence the CFU and bioluminescence signal, but also the cytokine/chemokine pattern and the frequency of immune cell populations at the site of infection were determined. The bioluminescent signal during course of infection showed no difference between perfluorocarbon treated and control mice, both of them exhibited a strong signal reduction in the first 24 hours after initially very strong photon emission. Both groups showed an increase in bioluminescent signal until they reached a plateau phase at around day 4 to day 7 p.i., suggesting comparable development of bacterial burden in the infected thigh muscle. The CFU determination in the liver, spleen and thigh muscle at days 2 (prior administration), 3 (24 hours post administration) and day 7 p.i. showed no statistically significant differences between perfluorocarbon and control group. Almost no bacteria could be detected in both groups at other sites than the initial location of infection, the thigh muscle. In conclusion, perfluorocarbon administration for MR imaging purpose did not affect the overall survival of bacteria at the site of infection or the efficacy of the immune system to combat the bacterial challenge.

Similar results were gathered in the flow cytometry analysis of immune cell populations at the site of infection. Both groups, perfluorocarbon emulsion and control treated animals, had similar frequencies of neutrophils, T cells, B cells, dendritic cells and macrophages in the

infected thigh muscle. This suggests, that uptake of perfluorocarbon emulsion in the blood stream did not affect or alter the migration behavior of phagocytic immune cells.

In order to evaluate whether their activity at the site of infection was inhibited by the perfluorocarbon loading, or not, the levels of various cytokines and chemokines in the infected thigh muscle prior, 24 hours and 5 days post administration were measured via an antibody based bead kit with flow cytometry. No differences could be seen in the pattern or quantity of cytokine/chemokine response. Both groups showed strong induction of IL-1 $\alpha$ , IL-6, MCP-1 and MIP-1 $\alpha$ , and lower levels of IL-10, RANTES and MCP-3. The overall state of inflammation was thus unaffected by the uptake of perfluorocarbon emulsion. Furthermore, the tracer accumulation in the phagocytic immune cells at the site of infection did not interfere with their expression and release of pro-inflammatory cytokine and chemokine since perfluorocarbon treated and not-treated mice did not show differences in their patterns.

In conclusion, these experiments demonstrated that intravenous administration of perfluorocarbon emulsion and its accumulation at the site of infection, liver and kidneys did not alter the general parameters of infection and antibiotic efficacy evaluation in the *S. aureus* thigh infection model. In consequence,  $^{19}\text{F}$  MRI with perfluorocarbons is a suitable method to evaluate the efficacy of antibiotics without distorting the results.

In summary, the experiments shown in this chapter were facilitated to investigate the capability of MRI to visualize the site of infection in a *S. aureus* thigh infection model. Among the tested native  $^1\text{H}$  MR methods, which did not rely on MR agents, mainly  $T_2$  weighted MRI visualized sufficient contrast in the infected thigh muscle. However, as former studies encountered, too, the differences in  $T_2$  relaxation times between infected and not-infected tissue were rather fluctuating and did not offer clear distinction of both areas (Marzola P et al. 1999, Kaim AH et al. 2003). The application of small iron oxide particles (in this case CLIOs) partially solved this problem by their accumulation at the rim of the abscess area, thus defining an area of infection and differentiating between infected and not-infected tissue. However, CLIOs lead to signal distortion effects and are therefore typically visualized as 'black spots'. But since several tissues (like bones, lung or liver) do not deliver much signal in  $T_2$  or  $T_2^*$  weighted MRI (which is used to image CLIO accumulation), it is not feasible to apply this system to other interesting models of *S. aureus* infection like pneumonia, sepsis or catheter-associated infections. A second, recently developed MR agent based modality to visualize sites of inflammation is  $^{19}\text{F}$  MRI with perfluorocarbon emulsions. However, at the beginning of this thesis, it was only shown that perfluorocarbon emulsions accumulate at sites of stroke and ischemia (Flögel U et al. 2008). Hence the first experiments evaluated the qualification of  $^{19}\text{F}$  MR imaging of perfluorocarbon emulsion accumulation to image the site of infection. Administration of perfluorocarbon emulsion at acute and chronic phase of inflammation led to accumulation at the rim of the abscess area. A big advantage of perfluorocarbon emulsion vs. CLIO particles, which served as comparison, was in this regard the background-free visualization, since mice do not harbor sufficient inherent amounts of



<sup>19</sup>F. Further experiments elucidated the accumulation in more detail, showing that intravenous administration of perfluorocarbon emulsion later than 48 hours post infection caused a 'hollow sphere' like accumulation pattern within 12 hours after administration around the edema area in the infected thigh muscle. This 'hollow sphere' like pattern and the background-free visualization are promising for the quantification of antibiotic efficacy or severity of disease in this model. A global approach to elucidate the accumulation of perfluorocarbon emulsion in the mouse showed accumulation of perfluorocarbon primarily in the liver, spleen and the infected thigh muscle. Generation of fluorescently labeled perfluorocarbon emulsions enabled the investigation of accumulation mechanism. Flow cytometry and fluorescence microscopy proved accumulation in immune cells at the site of infection. The main part of perfluorocarbon emulsion was in this context detected in neutrophils, lower amounts in macrophages and dendritic cells. Therefore, <sup>19</sup>F MRI with perfluorocarbon emulsions can be regarded as an imaging modality to visualize the immune response to infection, but it cannot visualize the pathogen itself. Nonetheless, this opens completely new opportunities to investigate host-pathogen interaction in vivo. This modality might be an interesting approach to visualize and measure differences in phagocytic immune cell migration during vaccination or during treatment with immunomodulatory compounds. Moreover, combining <sup>19</sup>F MRI with bioluminescence imaging would offer the visualization of bacterial burden and immune response non-invasively in the same animal during course of infection.

## 5. Imaging of antibiotic therapy with bioluminescence and <sup>19</sup>F magnetic resonance imaging with perfluorocarbon emulsions

Several MR methods were evaluated in the previous chapter for their capacity to visualize sites of *S. aureus* infection in the murine thigh abscess model. And although contrast media-independent T<sub>2</sub> weighted MRI and CLIO particle imaging with T<sub>2</sub> or T<sub>2</sub>\* weighted MRI indicated inflammation and abscess formation in the infected thigh muscle, <sup>19</sup>F MRI with perfluorocarbon emulsions was chosen to investigate the effects of antibacterial therapy upon imaging results. This decision was based on the general aim of this study, which was to establish a multimodal imaging platform to evaluate the efficacy of antibiotics, and <sup>19</sup>F MRI with PFCs delivered, in this context, best results to differentiate infected and not-infected tissue with easy quantifiable parameters.

This chapter describes the establishment and evaluation of a two-modality imaging platform consisting of Bioluminescence and <sup>19</sup>F Magnetic Resonance Imaging to visualize and quantify the efficacy of two clinically highly relevant antibiotics to treat *S. aureus* infections: vancomycin and linezolid. The course of the experiment is schematically shown in Fig. 5.1.

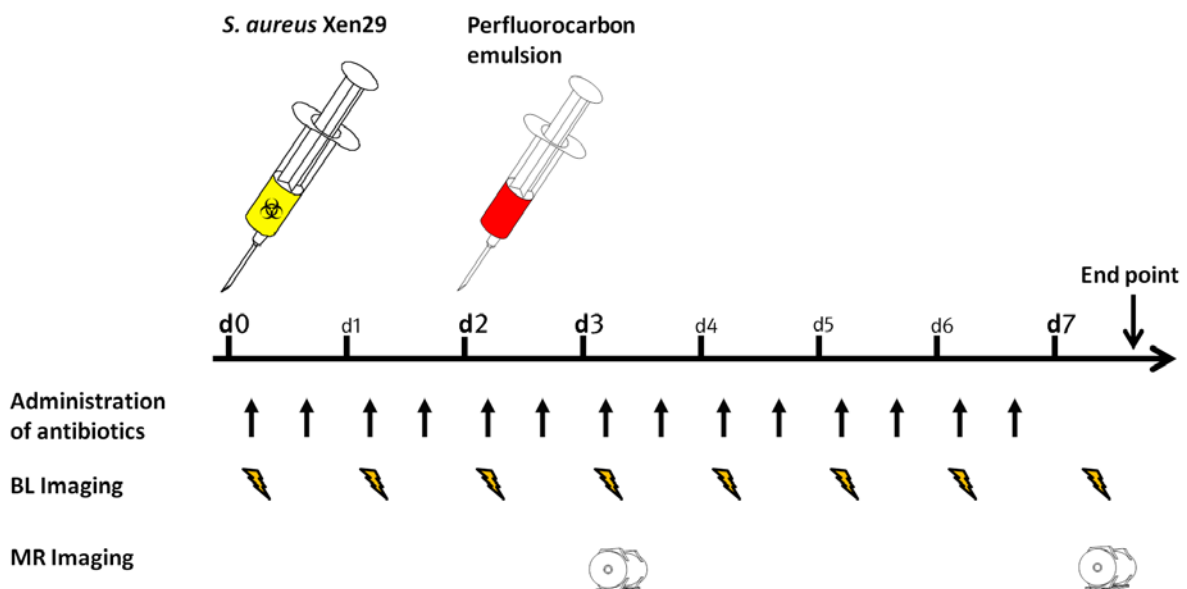


**Fig. 5.1: Schematic representation of the study.** The injection of *S. aureus* Xen29 into the left thigh muscle of female Balb/c mice defined the starting point (day 0) of the experiment. Perfluorocarbon emulsion was administered intravenously at day 2 p.i., while antibiotic or 0.9 % NaCl solutions were applied intraperitoneally at 2 hours p.i. and then every 12 hours. Bioluminescence imaging was performed once every 24 hours and magnetic resonance imaging was conducted at days 3 and 7 p.i. At day 7 p.i., mice were sacrificed and the infected thigh muscles recovered.

## 5.1. Results

### 5.1.1. Bioluminescence imaging of antibacterial therapy

To enable bioluminescence imaging during the course of infection, the luciferase-expressing *S. aureus* Xen 29 was chosen. This MSSA strain harbors a stable chromosomal copy of the *Photorhabdus luminescens luxABCDE* operon, which encodes for all necessary genes which enable *S. aureus* to produce luciferase and accompanying compounds to emit photons (Francis KP et al. 2000). All BL measurements were standardized by applying an oval area of interest at the site of infection to all images and by gathering of average radiance values solely in this region. The injection of  $3.2 \times 10^8$  CFU into the left thigh muscle led to a robust bioluminescence signal of similar value for 0.9% NaCl, vancomycin (30 mg/kg/d) and linezolid (15 mg/kg/d) treated mice at 15 min p.i. (first data point in Fig. 5.2 A). A strong decrease of light emission could be measured for all groups at 24 h after start of infection. The average radiance then increased in the following days in the 0.9% NaCl and the vancomycin group until it reached a plateau phase between day 3/4 and day 7 p.i. (Fig. 5.2 A). Photon emission of the linezolid group remained at the level measured at day 1 p.i. or dropped even further. Treatment with either Vancomycin or linezolid led to reduced average radiance values compared to the vehicle treated group at all time points after the initial signal drop at day 1 p.i. with linezolid showing heavier reduction (Tab. 5.1).

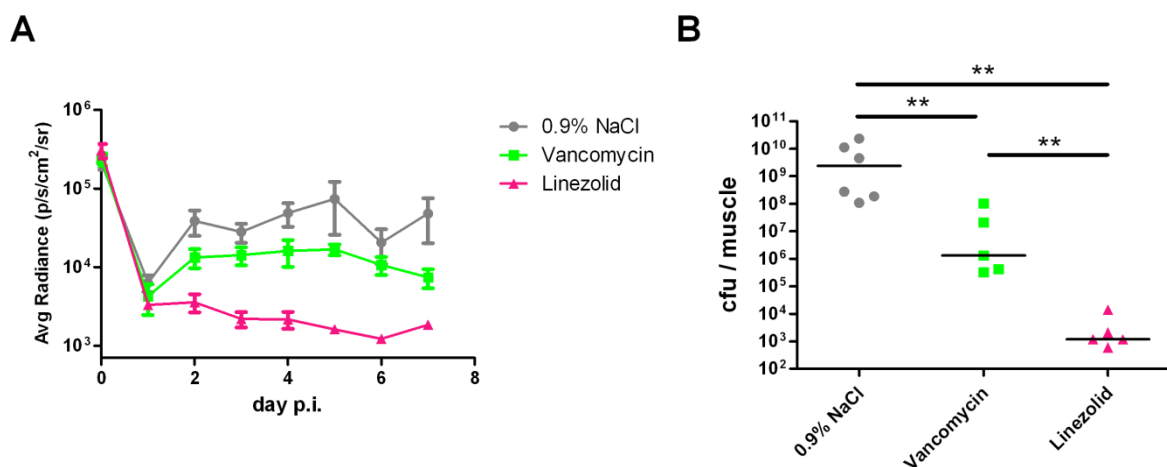


**Fig 5.2: Bioluminescence signal and colony-forming units in response to antibiotic treatment in the thigh infection model with *S. aureus* Xen29.** **A. Development of bioluminescence signal during course of infection.** Female Balb/c mice were challenged with  $3.2 \times 10^8$  CFU *S. aureus* Xen29 in the left thigh muscle. Antibiotic treatment started 2 hours p.i. and was then continued every 12 hours. The first data point (day 0 p.i.) represents the signal from BL measurement at 15 min after injection of  $3.2 \times 10^8$  CFU *S. aureus* Xen29 into the left thigh muscle. Mice were then imaged every 24 h until the end of experiment at day 7 p.i.. Means  $\pm$  SEM per group (5 – 6 mice each) are shown. **B. Colony-forming units in the infected thigh muscles at day 7 p.i..** Muscles were recovered after BL and MR imaging at day 7 p.i., homogenized and serial dilutions plated on agar plates in order to determine the bacterial burden. The results per single mouse and medians of each group are shown. Statistically significant differences between the groups are marked by asterisks (\*\*:  $P < 0.01$ ). (Adapted from Hertlein T et al. 2013).

**Tab. 5.1: Average radiance values at day 3 and day 7 p.i. determined by bioluminescence imaging in the region of interest.** Bioluminescence signal was measured in an oval region of interest, standardized for all mice of all groups. Shown are the mean values +/- SEM for days 3 and 7 p.i.. Statistically significant differences between groups are marked by symbols (\*: P < 0.05 vs. 0.9 % NaCl group, \*\*: P < 0.01 vs. 0.9 % NaCl group, †: P < 0.05 vs. Vancomycin group)

Treatment group	d3 p.i.		d7 p.i.	
	Avg radiance (p/s/cm <sup>2</sup> /sr)	reduction to 0.9% NaCl group	Avg radiance (p/s/cm <sup>2</sup> /sr)	reduction to 0.9% NaCl group
<b>0.9 % NaCl</b>	$2.8 \pm 0.76 \times 10^4$		$4.79 \pm 2.76 \times 10^4$	
<b>Vancomycin</b> (30 mg/kg/d)	$1.4 \pm 0.36 \times 10^4$	49 %	$7.40 \pm 2.02 \times 10^3$ (* )	85 %
<b>Linezolid</b> (15 mg/kg/d)	$2.19 \pm 0.48 \times 10^3$ (** , †)	92 %	$1.85 \pm 0.15 \times 10^3$ (** , †)	96 %

### 5.1.2. Reduction of bacterial burden by vancomycin or linezolid

The infected thigh muscles were recovered and homogenized at day 7 p.i. after bioluminescence and <sup>19</sup>F magnetic resonance imaging. The homogenization was diluted serially and plated on B-Agar plates to determine the colony-forming units following overnight incubation. The injection of  $3.2 \times 10^8$  CFU *S. aureus* Xen29 resulted in a mean CFU value of  $6.55 \pm 3.74 \times 10^9$  CFU in the thigh muscles of vehicle treated mice at day 7 p.i.. Treatment with vancomycin resulted in  $2.5 \pm 1.97 \times 10^7$ , linezolid in  $3.8 \pm 2.58 \times 10^3$  CFU at the site of infection. Both antibiotics reduced the bacterial burden significantly compared to the 0.9% NaCl group with linezolid having a significantly stronger therapeutic effect than vancomycin (Fig. 5.2 B).

### 5.1.3. <sup>19</sup>F MRI of perfluorocarbon emulsion accumulation at the site of infection during antibiotic therapy

Perfluorocarbon emulsion was administered intravenously 48 h after start of infection and the accumulation of <sup>19</sup>F in the thigh muscle area was measured and visualized by <sup>19</sup>F MRI at day 3 and day 7 p.i.. It was shown in chapter 4 and earlier studies that PFC emulsions are incorporated by phagocytes in the bloodstream and their subsequent migration to sites of inflammation leads to accumulation of tracer (Flögel U et al. 2008, Ebner B et al. 2010). It was furthermore shown in chapter 4 that intravenous PFC administration in the thigh infection model leads to a ‘hollow sphere’ like pattern of <sup>19</sup>F signal at the rim of the abscess area in the infected thigh muscle.

<sup>19</sup>F MR imaging of the vehicle group mice of this study showed congruent with the results from chapter 4 accumulation of <sup>19</sup>F tracer at the rim of a sphere-like shape in the infected thigh muscle (Fig. 5.3). Vancomycin treatment resulted in similar but smaller ‘hollow spheres’ in the infected thigh muscle at both time points, while linezolid led to a very small accumulation pattern in the infected thigh muscle.

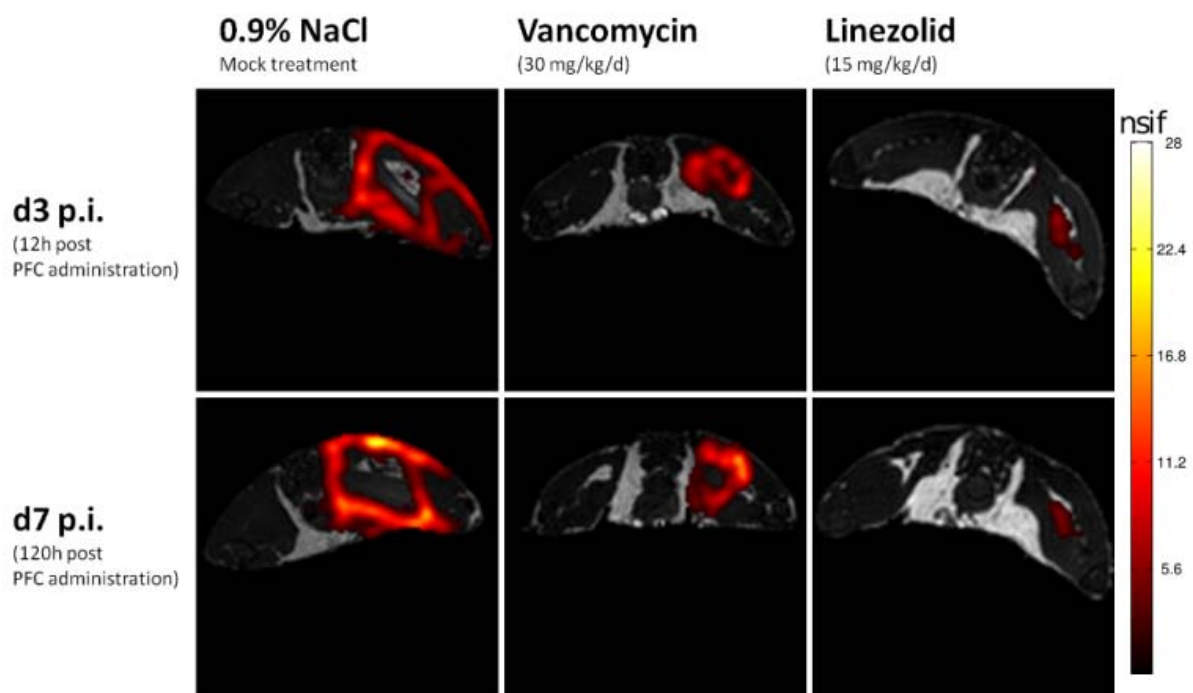


**Fig. 5.3: MR imaging of <sup>19</sup>F accumulation at the site of infection during antibiotic therapy.** Mice were challenged with  $3.2 \times 10^8$  CFU *S. aureus* Xen29 in the left thigh muscle and received either 0.9% NaCl, vancomycin or linezolid solution twice a day. Perfluorocarbon emulsion was administered intravenously 48h p.i. and MR imaging was performed at day 3 and day 7 p.i.. <sup>19</sup>F chemical shift imaging steady-state free precession overlays (hot colors) on <sup>1</sup>H turbo spin echo scans (grayscale) of one representative mouse of each treatment group are shown. (Adapted from Hertlein T et al. 2013).

#### 5.1.4. Quantification of $^{19}\text{F}$ accumulation volume and signal at the site of infection

The idea was to use the 'hollow sphere'  $^{19}\text{F}$  accumulation pattern at the rim of the abscess area to measure the abscess volume as a function of the applied therapy. But the three-dimensional reconstruction of the  $^{19}\text{F}$  accumulation in the infected thigh muscle showed gaps and holes in the surface of the sphere. This made the quantification of total abscess or  $^{19}\text{F}$  circumscribed volume impossible.

The  $^{19}\text{F}$  accumulation itself was nonetheless quantifiable in terms of  $^{19}\text{F}$  filled volume and in terms of total  $^{19}\text{F}$  signal in the infected thigh muscle (Fig. 5.4). In this context, the  $^{19}\text{F}$  filled volume was calculated by adding the overall amount of 'fluorine filled' voxels in the infected thigh muscle. A voxel was in this regard considered as 'fluorine filled' if its  $^{19}\text{F}$  signal intensity was at least four times higher than the mean background signal. The highest fluorine filled volume could be calculated for the 0.9% NaCl group at both MR imaging time points, day 3 and day 7 p.i.. Mice of this group delivered  $3.43 \pm 0.34 \times 10^4$  and  $4.06 \pm 0.58 \times 10^4$  voxels, respectively. Vancomycin treatment led to 83 % reduced  $^{19}\text{F}$  filled volume at day 3 p.i. ( $5.94 \pm 1.48 \times 10^3$  voxels) and 80 % reduction at day 7 p.i. ( $8.25 \pm 2.40 \times 10^3$  voxels). Linezolid showed stronger reduction than vancomycin and resulted in 92 % reduction at day 3 p.i. compared to the vehicle group ( $2.73 \pm 1.17 \times 10^3$  voxels) and 93 % at day 7 p.i. ( $2.66 \pm 0.93 \times 10^3$  voxels).

Total  $^{19}\text{F}$  signal was then calculated by adding the  $^{19}\text{F}$  signal of the individual  $^{19}\text{F}$  filled voxels in the infected thigh muscle. In line with the results from volume calculation, the strongest total signal was measured in the 0.9 % NaCl group at both time points. Vancomycin treatment induced 84 % reduction at day 3 p.i. ( $2.03 \pm 0.67 \times 10^4$  nsif ( $^{19}\text{F}$  MR signal intensity normalized to the apparent noise amplitude of the measurement) for vancomycin vs.  $1.29 \pm 0.22 \times 10^5$  nsif for the vehicle treated group) and 83 % reduction at day 7 p.i. ( $3.41 \pm 1.37 \times 10^4$  nsif vs.  $1.97 \pm 0.41 \times 10^5$  nsif). Linezolid had an even stronger effect and reduced the total signal by 94 % at day 3 p.i. ( $7.31 \pm 3.64 \times 10^3$  nsif) and by 96 % at day 7 p.i. ( $1.21 \pm 0.46 \times 10^4$  nsif).

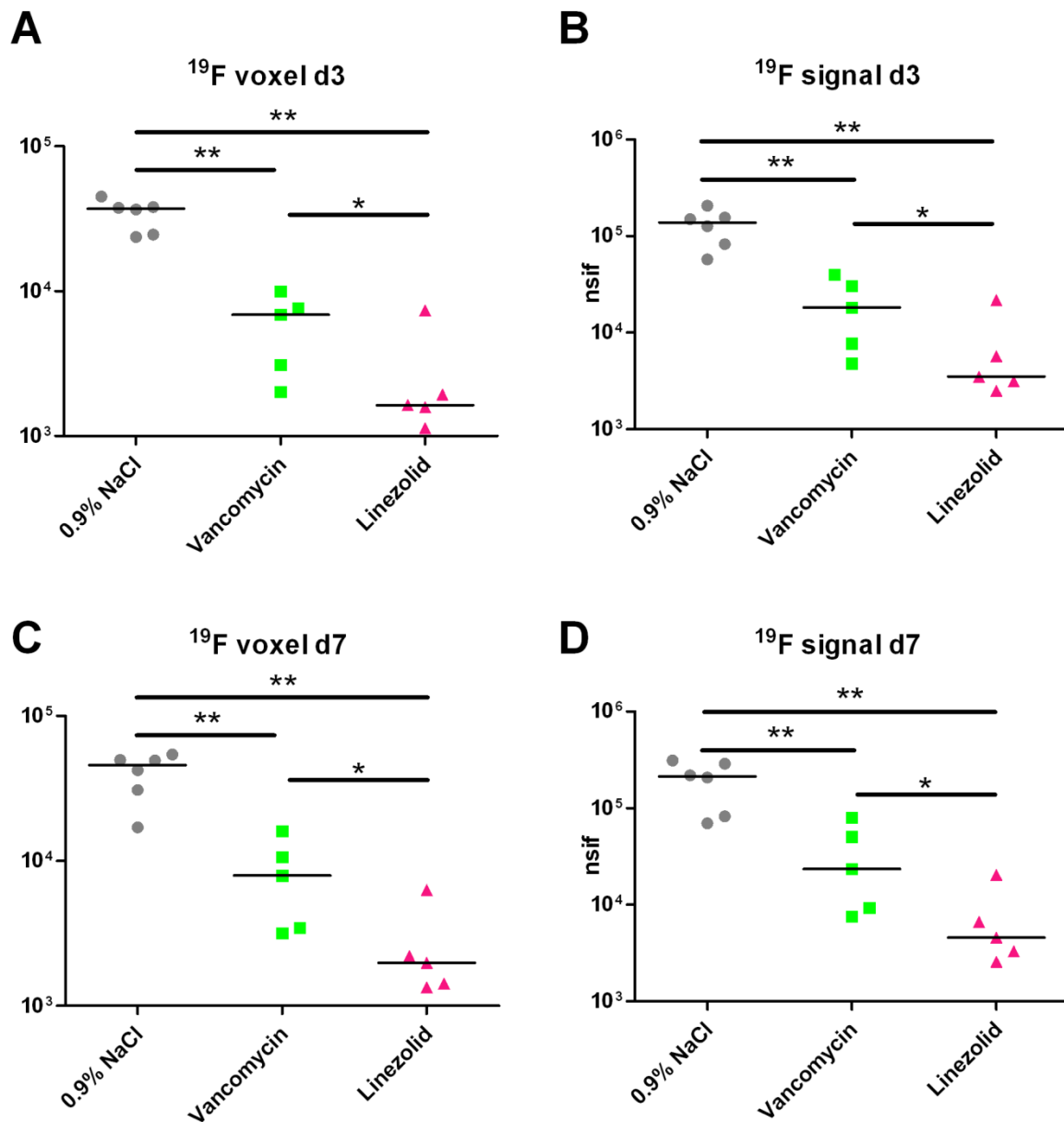


**Fig 5.4: Quantification of  $^{19}\text{F}$  accumulation volume and signal in the infected thigh muscle.** Mice were challenged with  $3.2 \times 10^8$  CFU *S. aureus* Xen29 in the left thigh muscle and received either 0.9% NaCl, vancomycin or linezolid solution via intra-peritoneal injection twice a day. PFC emulsion was administered at day 2 p.i. intravenously. **A/C: Amount of  $^{19}\text{F}$  filled voxel in the infected thigh muscles at day 3 (A) or day 7 (C) p.i.. B/D: Amount of overall  $^{19}\text{F}$  signal in the infected thigh muscles at day 3 (B) or day 7 (D) p.i..** Single data points per mouse and the medians of the groups are shown. Statistically significant differences are marked by asterisks (\*:  $P < 0.05$ , \*\*:  $P < 0.01$ ). (Adapted from Hertlein T et al. 2013).

## 5.2. Discussion

Preclinical testing of new promising drug candidates is a rather challenging task. And although great improvements in the development of in vitro and cell culture based evaluation methods were achieved in the past decades, animal experiments are still regarded as essential in the evaluation of therapies to treat many diseases (Editorial of Nature Medicine 19(10):1191, Winston R 2013). Nonetheless, the principle of the 3 R's is adopted to animal experimentation today, meaning reduction, refinement and replacement of animal experiments.

In vivo imaging technologies such as Positron Emission Tomography, Bioluminescence or Magnetic Resonance Imaging have proven their capability to deliver information about the state and course of disease in different models and their benefit in preclinical evaluation of drug candidates (Wang J et al. 2005, Beckmann N et al. 2007, Sandanaraj BS et al. 2010). Their implementation into the preclinical evaluation process seems to be very interesting because they are fitting nicely to the idea of the 3 R's. Refinement of animal experiments or even models can be achieved through application of in vivo imaging technologies by offering completely new insights into disease development and therapeutic response. Bioluminescence imaging, for example, offers non-invasive determination of bacterial burden in vivo by detection of luciferase-expressing bacteria in infectious disease models (Francis KP et al. 2000). This permits the reduction of animal numbers in the evaluation of antibacterial compounds since organs must not be recovered to determine the gravity of disease or infection at every time point during course of infection. Furthermore, this imaging modality can be extended by photon based imaging methods to visualize and measure the immune response to infection. It is possible, for example, to visualize the migration and accumulation of immune cells like neutrophils (Niska JA et al. 2012) or to visualize the activity of immune cells by imaging myeloperoxidase or elastase activity (Gross S et al. 2009, Kossodo S et al. 2011).

The idea of this study was consequently the implementation of imaging technologies to evaluate the efficacy of antibiotics in vivo and to compare the results with the current state-of-the-art method colony-forming unit determination. The investigations described in chapter 4 allowed the application of  $^{19}\text{F}$  MRI with perfluorocarbon emulsions to visualize the effect of therapy for the first time by this method. Bioluminescence imaging was added as second method due its capability to visualize the efficacy of antibiotic therapy, which was shown by several former studies (Rocchetta HL et al. 2001, Kadurugamuwa JL et al. 2003, Jawhara S et al. 2004, Xiong YQ et al. 2005).



Animals were therefore infected intramuscularly (left thigh muscle) with *S. aureus* Xen29, a MSSA strain derived from strain ATCC 12600 by the insertion of the *luxABCDE* operon from *Photobacterium luminescens* at a single chromosomal site (Francis KP et al. 2000). This led, similar to results from chapter 4, to a strong bioluminescence signal at 15 min p.i., which then dropped to almost background noise strength at day 1 post infection (Fig. 5.1 A). Treatment with either vancomycin (30 mg/kg/d q12h), linezolid (15 mg/kg/d q12h) or vehicle (0.9% NaCl solution) started 2 h p.i. and was continued until the end point of the experiment at day 7 p.i.. The bioluminescence signal of the vehicle treated group recovered after d1 p.i. to reach a plateau phase between day 3 and day 6 p.i., congruent with results shown in chapter 4.1.1.1.. Vancomycin treatment led to lower, but still detectable average radiance signals from day 2 to day 7 p.i., while linezolid treated mice had levels of photon emission that were close to background signal throughout the whole experiment (Fig. 5.2 A). Muscles were recovered at day 7 p.i and the colony-forming units were determined. The highest values were gathered for the 0.9 % NaCl group, vancomycin led to a reduction of approximately 3 log 10 units and linezolid to 6 log 10 units (Fig. 5.2 B). In principle, the efficacy pattern of the three treatment regimens was therefore indicated similarly by BLI and CFU counting in terms of quality, but not in quantity, because differences shown with CFU determination were much more pronounced than with bioluminescence imaging. Of note, the relatively low antibacterial efficacy of vancomycin measured in this study is in line with former studies (Marzola P et al. 1999, LaPlante KL et al. 2008).

The second imaging method applied to investigate the effect and efficacy of antibiotic therapy in this study, namely  $^{19}\text{F}$  MRI with perfluorocarbon emulsions, measures a completely different parameter than bioluminescence imaging or CFU counting. While both later-quoted methods determine the bacterial burden either directly (CFU) or indirectly (BLI),  $^{19}\text{F}$  MRI is based on the accumulation of  $^{19}\text{F}$  tracer at the site of infection. This accumulation is facilitated by inflammation, which accompanies the infection and provokes the immigration of phagocytes like monocytes or neutrophils. In consequence,  $^{19}\text{F}$  MRI with perfluorocarbons images the immune response to infection and not the infection itself. The accumulation of  $^{19}\text{F}$  in the 0.9 % NaCl group in this study, which received no antibiotic therapy and therefore developed an infection similar to the mice described in chapter 4, resembled in terms of pattern and volume the accumulation of the  $^{19}\text{F}$  MR imaging group in chapter 4. This leads, as shown in chapter 4, to a 'hollow sphere'  $^{19}\text{F}$  pattern around the area of inflammation and infection (Fig. 5.3). Vancomycin treatment led to a slightly smaller  $^{19}\text{F}$  circumscribed volume, while linezolid treatment reduced the volume even stronger (Fig 5.3). In conclusion, it can be stated that antibacterial treatment, at least with either vancomycin or Linezolid, does not prevent accumulation and visualization of perfluorocarbons at the site of infection. Furthermore,  $^{19}\text{F}$  MRI with perfluorocarbon emulsions is capable to visualize the therapeutic effect caused by vancomycin or linezolid treatment in vivo in a non-invasive manner. But the accumulation of  $^{19}\text{F}$  was not only visualized, but also measured in terms of accumulation volume and overall  $^{19}\text{F}$  signal in the infected thigh muscle. The results demonstrated, as expected from visualization, the highest accumulation volume and total

signal in the vehicle treated mice, the weakest in linezolid treated mice and an intermediate value for vancomycin treated ones (Fig. 5.4). A small increase of  $^{19}\text{F}$  signal could be observed between the  $^{19}\text{F}$  MR imaging 12 h post administration of PFC (day 3 p.i.) and day 7 p.i., which implies transport of  $^{19}\text{F}$  tracer later than 12 h post administration to the site of infection. The total abscess or  $^{19}\text{F}$  tracer surrounded volume could not be measured by MRI because of gaps and holes in the accumulation pattern.

In general,  $^{19}\text{F}$  accumulation volume and total signal in the infected thigh muscle correlated very well with bioluminescence imaging results. The signal reduction to the 0.9 % NaCl group between bioluminescence signals vs.  $^{19}\text{F}$  volumes/signals were 49 % vs 83/84 % at day 3 p.i. and 85 % vs. 80/83 % at day 7 p.i. for Vancomycin and 92 % vs. 92/94 % at day 3 p.i. and 96 % vs. 93/96 % at day 7 p.i. for Linezolid treatment. This means that BLI and  $^{19}\text{F}$  MRI indicated the same efficacy pattern and overall efficacy of the applied antibiotics in this model. Colony-forming unit determination at day 7 p.i. showed in principle the same efficacy pattern, but different magnitudes of signal reduction for both antibiotics. Vancomycin led to ca. 2 log 10 unit reduction and linezolid to ca. 6 log 10 unit reduction of bacterial burden, both of them being much stronger than the signal reduction achieved with bioluminescence imaging or  $^{19}\text{F}$  magnetic resonance imaging.

Overall,  $^{19}\text{F}$  MRI is capable to visualize and quantify the efficacy of antibiotics to treat *S. aureus* infections in murine models. Based on the results from experiments in chapter 4 and former studies, which showed the accumulation of perfluorocarbon emulsions in phagocytes, which then migrate to sites of inflammation (Flögel U et al. 2008, Ebner B et al. 2010), these results suggest that the number of viable *S. aureus* cells within the abscess depends or influences the number of immigrating phagocytic cells. On the other hand, this imaging method is therefore independent of the infecting pathogen, but dependent on the inflammatory immune response. This, of course, enables the evaluation of clinically relevant, not with genetic markers or reporters equipped strains in relevant animal models and moreover the testing of new inflammation-modulating compounds.  $^{19}\text{F}$  MRI delivers a more detailed picture of the state and course of disease than state-of-the-art CFU determination by delivering additionally information about anatomy and tissue destruction at the site of infection.

The technique might furthermore be clinically interesting to detect infection foci of unknown origin. Several severe and complicated types of infection, such as *S.aureus* induced osteomyelitis, are difficult to recognize and are associated with high rates of treatment failure. The exact localization of infection loci might help to define the most appropriate therapeutic measures and to track and control the efficacy of the applied therapy.

In conclusion, the imaging platform established in this chapter, consisting of bioluminescence and <sup>19</sup>F magnetic resonance imaging, offers the visualization and quantification of antibacterial therapy in vivo in a non-invasive manner. It delivers information about the bacterial burden as well as about the inflammatory response during the course of infection. The results delivered by both imaging modalities indicated the same efficacy pattern of vancomycin and linezolid compared to state-of-the-art CFU determination while proffering additional information like time-course development of bacterial burden and intensity of inflammation.

## 6. Evaluation of lysostaphin efficacy in murine thigh and catheter-related infection models by bioluminescence and <sup>19</sup>F magnetic resonance imaging

<sup>19</sup>F MRI with perfluorocarbon emulsions has proven, as described in chapter 4, its capacity to visualize the abscess formation in a murine thigh infection model of *S. aureus*. It visualized the accumulation of <sup>19</sup>F tracer in vivo in a non-invasive manner, thus enabling serially imaging of the course of infection in the same animal. Chapter 5 then described the combination of this imaging modality with bioluminescence imaging, thereby offering information about the bacterial burden and the effects of infection and therapy upon the host's inflammation at the same time. Nonetheless, up to this point, only clinically applied antibiotics were administered and investigated by this two-modal platform. Consequently, the next step was the evaluation of a new promising compound to treat *S. aureus* infections: lysostaphin. This extracellular zinc metalloprotease glycyl-glycine endopeptidase was selected, because it represents a completely new class of antibacterial compounds. In this regard, a new, recombinant formulation of lysostaphin was tested in murine thigh and catheter-related infection models and efficacy visualized by either <sup>19</sup>F MRI with perfluorocarbon emulsions and bioluminescence imaging or by bioluminescence only.

### 6.1. Results

#### 6.1.1. In vitro activity of lysostaphin against *S. aureus*

Lysostaphin was first described in 1964 (Schindler CA et al. 1964), but a new recombinant formulation of this endopeptidase (Khatri GS et al. 2005), which was supplied by Bharat Biotech (Hyderabad, India) was applied in this study. Therefore, the minimal inhibitory concentrations (MIC) of the antibacterial substances were measured by broth microdilution prior to animal experiments. Vancomycin showed a MIC value of 0.78 µg/ml against *S. aureus* Xen29, the strain used to infect the animals, while oxacillin had a MIC value of 1.56 µg/ml and the recombinant formulation of lysostaphin a value of 0.004 µg/ml.

### 6.1.2. Lysostaphin reduced the bacterial burden in the thigh infection model

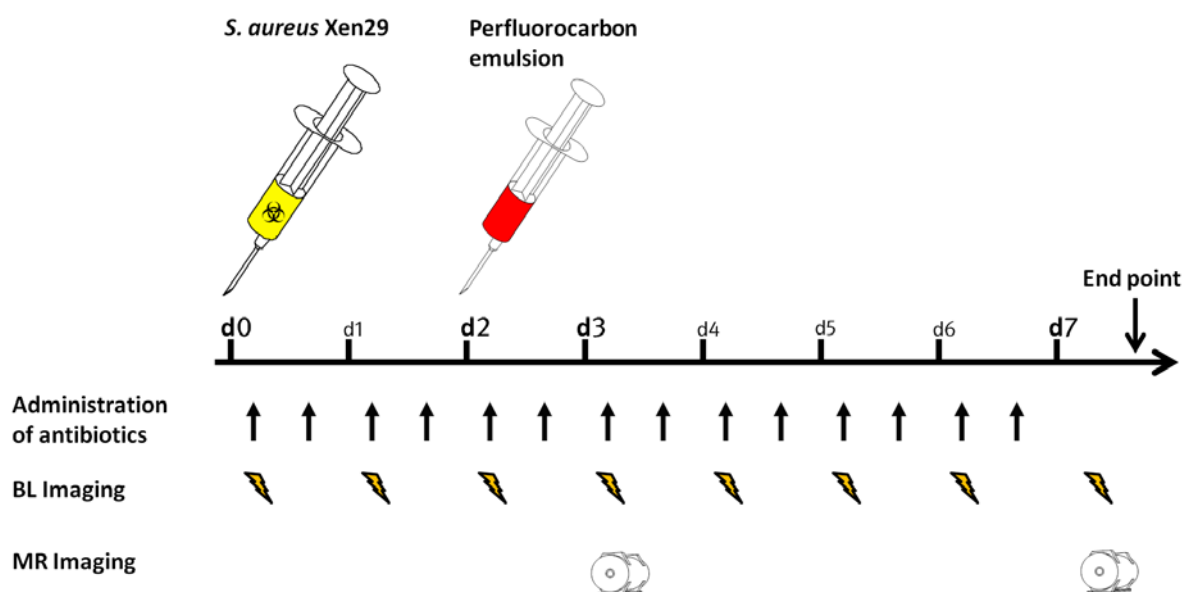


**Fig. 6.1:** Schematic representation of the lysostaphin evaluation study in the murine thigh infection model. The injection of *S. aureus* Xen29 into the left thigh muscle of female Balb/c mice defined the starting point (day 0) of the experiment. Perfluorocarbon emulsion was administered intravenously at day 2 p.i., while antibiotic or 0.9 % NaCl solutions were applied either intraperitoneally (vancomycin and oxacillin) or intravenously (lysostaphin) at 2 hours p.i. and then every 12 hours. Bioluminescence imaging was performed once every 24 hours and magnetic resonance imaging was conducted at days 3 and 7 p.i. At day 7 p.i., mice were sacrificed and the infected thigh muscles recovered.

To test for in vivo efficacy of lysostaphin against *S. aureus* infections, mice were infected intramuscularly with  $2.4 \times 10^8$  CFU *S. aureus* Xen29, a luciferase-expressing strain (Francis KP et al. 2000). The treatment started 2 h after infection and lysostaphin was administered either alone at concentrations of 2 mg/kg/d or 5 mg/kg/d or in combination with oxacillin (200 mg/kg/d) intravenously at two doses the day. It was shown by previous investigations that lysostaphin might exhibit synergistic behavior when combined with  $\beta$ -lactam antibiotics like oxacillin (Climo MW et al. 2001, Kiri N et al. 2002). Three groups were defined as controls and treated either with vehicle (0.9 % NaCl solution), with vancomycin (30 mg/kg/d) or with oxacillin only (200 mg/kg/d), each of them via intraperitoneal application two times a day with the first application at 2 h p.i.. Muscles were recovered after 7 days of infection and treatment and the colony-forming units in the infected thigh muscle after homogenization and serial dilution were determined. The highest CFU values could be detected in the vehicle treated group with approximately  $1 \times 10^9$  CFU (Fig. 6.2 A). Treatment with vancomycin reduced the bacterial burden by ca. 1 log 10 unit, oxacillin-only or low-dose lysostaphin by 1.5 log 10 units. Strongest decrease in bacterial numbers were measured for the high-dose

lysostaphin or the low-dose lysostaphin plus oxacillin group with approximately 4 log 10 units reduction in median.

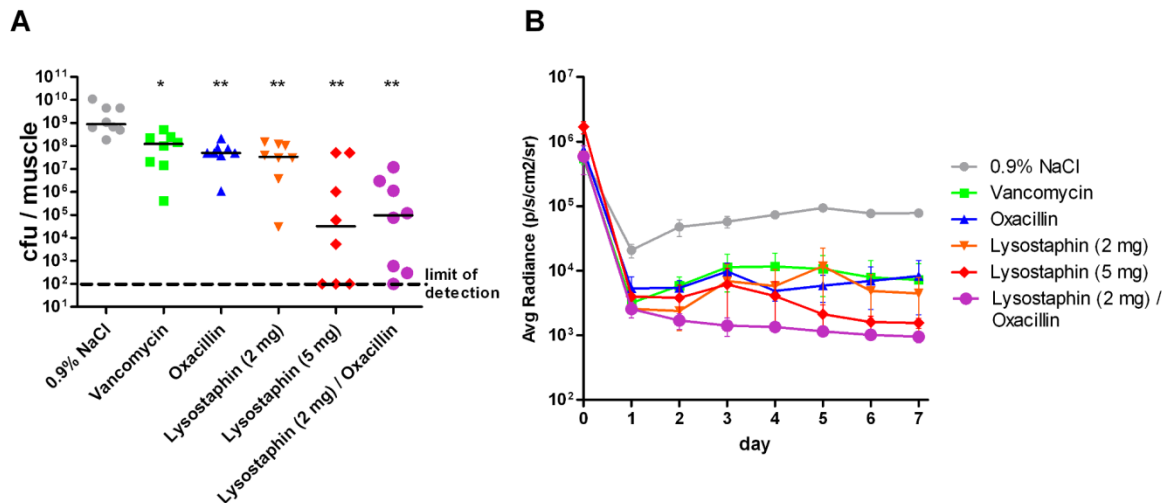


**Fig. 6.2: Bacterial burden in the infected thigh muscles.** Mice were infected with  $2.4 \times 10^8$  CFU *S. aureus* Xen29 in the left thigh muscle. Different treatments, as indicated in the graph, were applied first at 2 h p.i., then every 12 h until day 7 p.i.. **A: Colony-forming units in the infected thigh muscle at day 7 p.i.** Single data points per animal and the median of the corresponding group are shown. Statistically significant differences compared to the 0.9 % NaCl group are indicated by asterisks (\*:  $P < 0.05$ , \*\*:  $P < 0.01$ ). The reduction of CFU by 5 mg/kg/d lysostaphin or 2 mg/kg/d lysostaphin plus oxacillin was additionally significantly lower than the values of the other antibiotic treatment groups. **B: Development of bioluminescent signal during the course of infection and therapy.** Mice were imaged at 1 - 5 min p.i. (time point: day 0 p.i.) and then every 24 h. The means  $\pm$  SEM of the average radiance in a standardized oval region of interest are shown. (Adapted from Hertlein T et al. 2014)

### 6.1.3. Lysostaphin reduced the bioluminescence signal in the thigh infection model

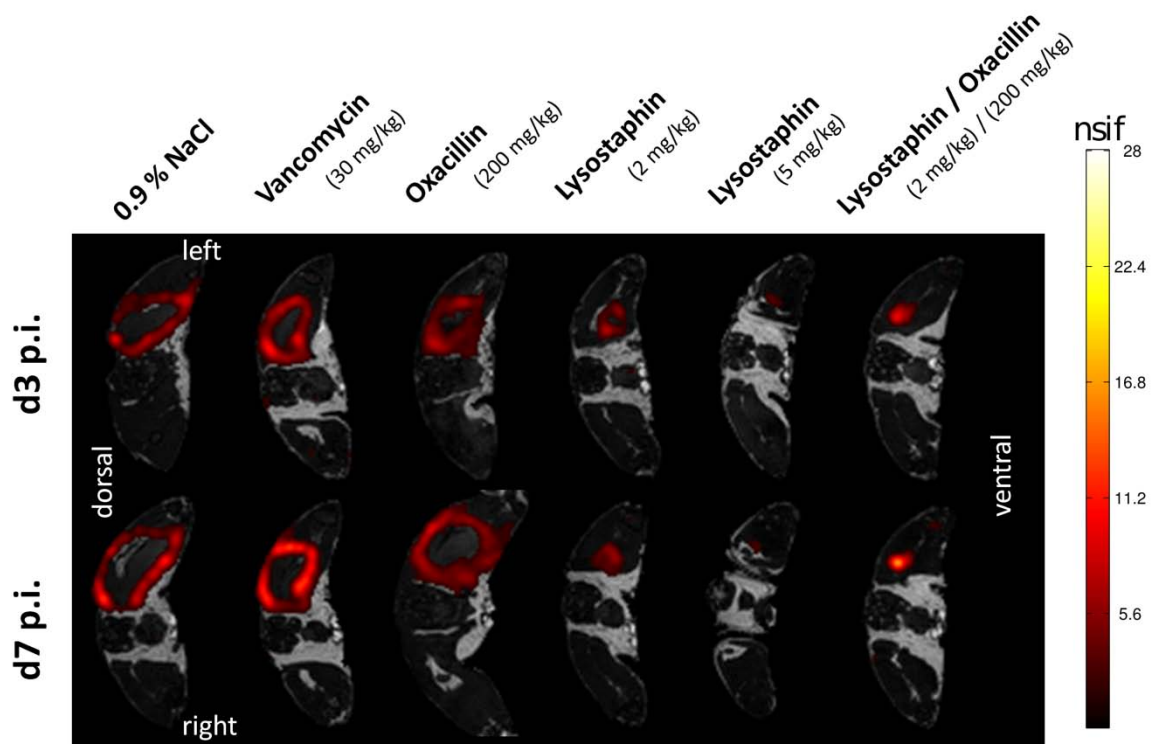
The genomically encoded luciferase of *S. aureus* Xen29 enabled non-invasive bioluminescence tracking of the bacterial burden in this model. The average radiance signal detected 1 – 5 min after start of infection was very strong in all groups (time point: day 0 p.i. in Fig. 6.2 B). All groups showed a significantly lower signal at 24 h p.i.. A gradual increase in photon emission of the 0.9 % NaCl group occurred then from day 2 p.i. until it reached a plateau phase between days 5 and 7 p.i.. The lysostaphin + oxacillin group had the lowest signal of all groups after day 2 p.i., with values close to background signal, which is around  $10^3$  photons/s/cm<sup>2</sup>/sr. Vancomycin, oxacillin or lysostaphin (2 mg/kg/d) treatment reduced the photon emission significantly compared to the vehicle group from day 1 p.i. to day 7 p.i., but the reduction was not as pronounced as for the lysostaphin (5 mg/kg/d) or the lysostaphin + oxacillin groups. High-dose lysostaphin treatment led to average radiance values similar to those of the vancomycin, lysostaphin (2 mg/kg/d) or oxacillin-only groups at days 2 to 4 p.i., but the signal decreased until day 7 p.i. to reach a level close to the

lysostaphin + oxacillin group. The reduction of bioluminescent signal was significantly lower for all groups compared to the vehicle group from day 2 p.i. to day 7 p.i., but the differences between the groups remained statistically non significant. Apart from the infected thigh muscle, no further sources of bioluminescent signal could be detected in the infected mice, indicating a localized infection.

#### 6.1.4. $^{19}\text{F}$ MR imaging of perfluorocarbon accumulation in the infected thigh muscle

After establishing  $^{19}\text{F}$  MRI with perfluorocarbons as infection imaging modality in chapter 4 and demonstrating its capability to visualize the efficacy of antibacterial therapy in chapter 5, this method was now applied to investigate the anti-infective capacity of a new, promising compound: lysostaphin. All animals received therefore a single intravenous administration of perfluorocarbon emulsion at day 2 p.i.. The accumulation of  $^{19}\text{F}$  tracer at the site of infection was then imaged 24 h after administration and at day 7 p.i..

Congruent with former experiments, described in chapters 4 and 5, a ‘hollow sphere’-like  $^{19}\text{F}$  accumulation pattern could be visualized in almost all mice of the vehicle, vancomycin, oxacillin-only and low-dose lysostaphin treated groups. The high-dose lysostaphin and the lysostaphin + oxacillin groups showed very small accumulation patterns that comprised not in all mice a  $^{19}\text{F}$ -free inner volume. Nonetheless, all mice showed accumulation of  $^{19}\text{F}$  tracer only at the rim of the abscess area, no  $^{19}\text{F}$  signal could be visualized outside of the abscess area (Fig. 6.3). The largest  $^{19}\text{F}$  ring structure was visualized in the 0.9 % NaCl group, the smallest ones for the 5 mg lysostaphin group and the lysostaphin + oxacillin group. Vancomycin, oxacillin or 2 mg lysostaphin treatment led to intermediate structures (Fig. 6.3).



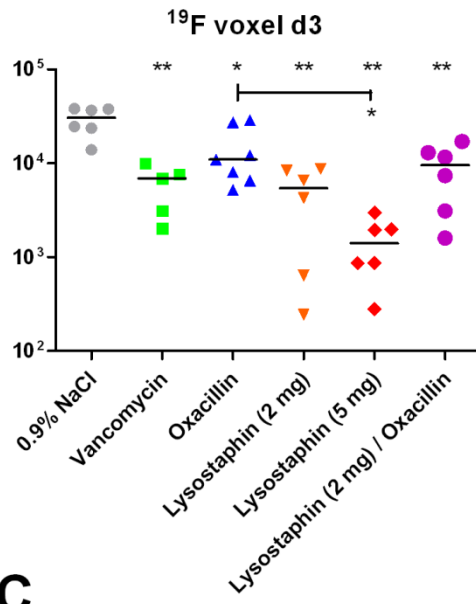
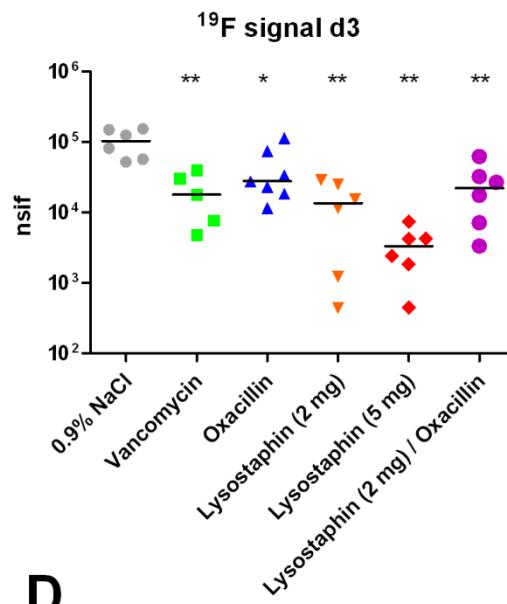
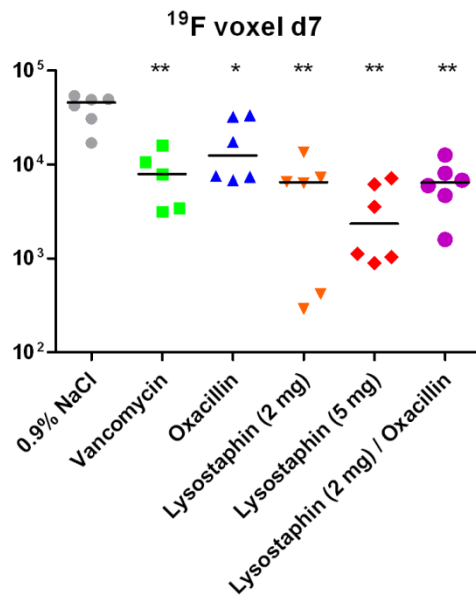
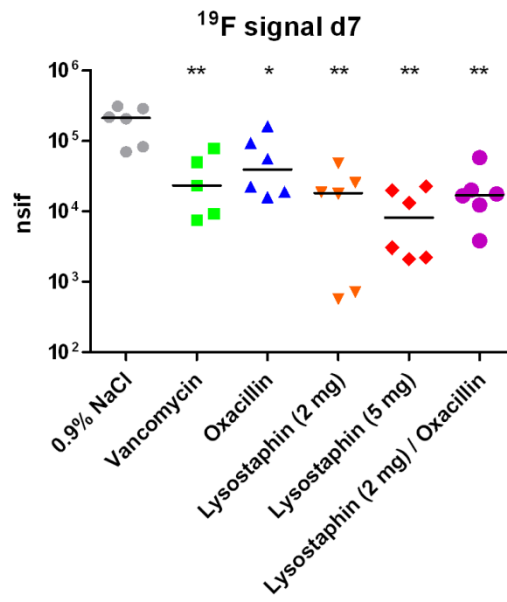


The accumulation pattern was not completely closed in many animals, showing gaps and holes. Thus, quantification of the overall abscess volume was not possible. However, the quantification of  $^{19}\text{F}$ -filled volume and overall signal in the infected thigh muscle, as shown earlier in chapter 5, remained feasible and was done to compare the results with bioluminescence imaging and CFU counting. The highest fluorine-filled volume in terms of  $^{19}\text{F}$ -filled voxels was measured for the vehicle treated group (Fig. 6.4 A/C). Antibacterial treatment led, independently from the administered compound, to statistically significant reduced accumulation volumes at both time points. The smallest volume was measured for the high-dose lysostaphin treatment group, while vancomycin, oxacillin-only, low-dose lysostaphin and lysostaphin + oxacillin treatment led at both time points to intermediate  $^{19}\text{F}$ -filled volumes, which were in numbers close to each other. But the differences between the treatment groups were only significant for lysostaphin 5 mg vs. oxacillin at day 3 p.i. (Fig. 6.4 A).

The overall  $^{19}\text{F}$  signal in the infected thigh muscle was measured in addition to the  $^{19}\text{F}$ -filled volume. Similarly to the fluorine-filled volume results, the highest values were determined for the 0.9 % NaCl group, while high-dose lysostaphin resulted in the weakest signal (Fig. 6.4 B/D). The low-dose lysostaphin, vancomycin, oxacillin-only and lysostaphin + oxacillin groups showed intermediate values. All antibiotic treatment groups had significantly lower values compared to the vehicle group, but the differences between the treatments were not significant.

In summary, both  $^{19}\text{F}$  filled volume and overall  $^{19}\text{F}$  signal determination led to similar signal reduction patterns of antibacterial compounds, indicating similar efficacy patterns. Importantly, the signal was reduced in both parameters significantly for all treatment groups compared to the vehicle group, demonstrating the anti-infective effect and proving the capability of  $^{19}\text{F}$  MRI with perfluorocarbons as infection- and therapy-imaging modality.

**Fig. 6.3 (facing page): Two-dimensional  $^{19}\text{F}$  CSI magnetic resonance overlays on anatomical  $^1\text{H}$  TSE images of representative mice from the different treatment groups.** Mice were infected in the left thigh muscle with  $2.4 \times 10^8$  CFU *S. aureus* Xen29 and treated with different antibiotics or vehicle solution. At day 2 p.i. a single bolus of perfluorocarbon emulsion was administered intravenously into each mouse. MR imaging was performed 24 h later (upper row) and at day 7 p.i. (lower row).  $^{19}\text{F}$  signal is shown in hot colors (red to yellow) upon  $^1\text{H}$  anatomical images in grayscale. (Adapted from Hertlein T et al. 2014)

**A****B****C****D**

**Fig. 6.4 (facing page):  $^{19}\text{F}$  accumulation volume and signal strength in the infected thigh muscle at days 3 and 7 p.i. measured by  $^{19}\text{F}$  MRI.** Mice were infected with  $2.4 \times 10^8$  CFU *S. aureus* Xen29 into the left thigh muscle. Antibiotic treatment started 2 h after infection and was continued two times a day until d7 p.i.. At day 2 p.i., all mice received a single intravenous administration of perfluorocarbon emulsion and MR imaging was performed 24 h later and at day 7 p.i.. **A/C: The  $^{19}\text{F}$ -filled volume of perfluorocarbon emulsion accumulation in the infected thigh muscles of the different treatment groups.** The volume was measured by adding up all voxel from  $^{19}\text{F}$  MR measurements with a signal-to-noise ration of above 4. Only voxel in the infected thigh muscle were included in the calculation. **A:** The  $^{19}\text{F}$ -filled volume 24 h after perfluorocarbon administration. **C:** The  $^{19}\text{F}$ -filled volume at day 7 p.i.. **B/D: The overall  $^{19}\text{F}$  signal of perfluorocarbon emulsion accumulation in the infected thigh muscles of the different treatment groups.** The overall signal was calculated as  $^{19}\text{F}$  MR signal intensity in the infected thigh muscle normalized to the apparent noise amplitude of the measurement. **B:** The total  $^{19}\text{F}$  signal in the infected thigh muscle 24 h after perfluorocarbon administration. **D:** The total  $^{19}\text{F}$  signal in the infected thigh muscle at day 7 p.i.. Single data points per animal and the median of the corresponding groups are shown. Statistical significance between the different treatment groups are indicated by asterisks (\*:  $P < 0.05$ , \*\*:  $P < 0.01$ ). (Adapted from Hertlein T et al. 2014)

### 6.1.5. Reduction of bacterial burden in the catheter-associated infection model by antibiotic treatment

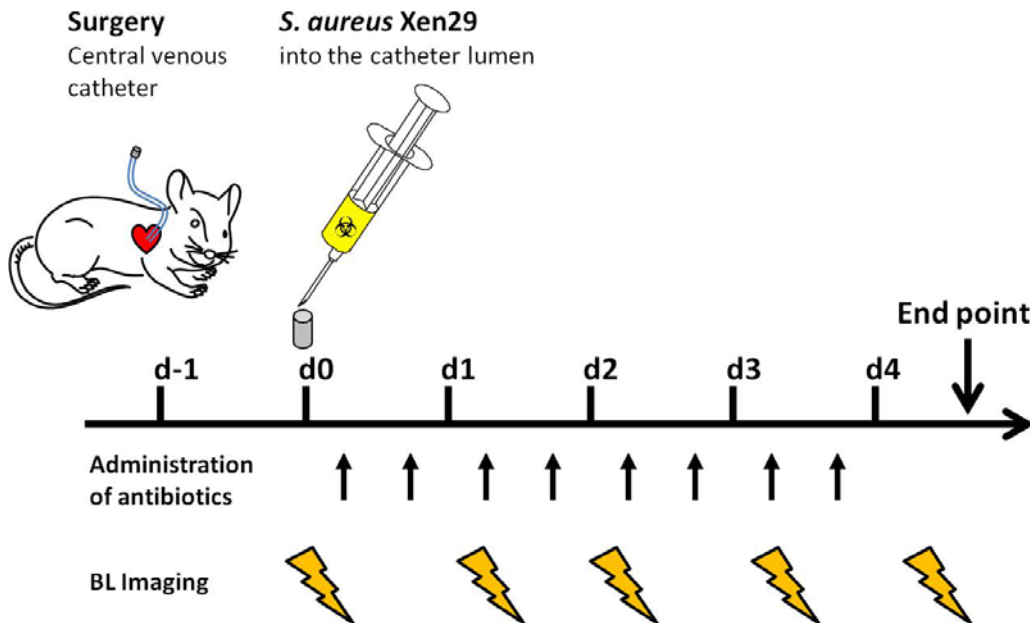


**Fig. 6.5:** Schematic representation of the lysostaphin evaluation study in the murine catheter related infection model. A central venous catheter was placed in female NMRI mice 24 hours prior the experiment start. The injection of *S. aureus* Xen29 into the catheter lumen mice defined the starting point (day 0) of the experiment. Antibiotic or 0.9 % NaCl solutions were applied either intraperitoneally (vancomycin and oxacillin) or intravenously (lysostaphin) at 2 hours p.i. and then every 12 hours. Bioluminescence imaging was performed once every 24 hours. At day 4 p.i., mice were sacrificed and the catheter, heart, lung, kidneys and spleen recovered.

Catheter-related infections account for a significant number of nosocomial infections (Richards MJ et al. 2000). Most of them are associated with a central venous catheter and therefore a murine model with central venous catheter-associated *S. aureus* infection (Lorenz U et al. 2008) was chosen to assess the efficacy of lysostaphin alone or in combination with oxacillin. Thus, NMRI mice were challenged with  $3.7 \times 10^7$  CFU of bioluminescent *S. aureus* Xen29 in the lumen of the catheter, which was placed surgically in the jugular vein. After 4 days of infection and therapy, the kidneys, heart, lung and catheter were recovered and the CFU determined. Five out of eight mice of the vehicle group showed bacteria in the heart, and one out of eight in the vancomycin or lysostaphin (2 mg/kg) groups. Additionally, bacteria were identified in the lungs of four out of eight vehicle treated mice and one out of eight mice of the vancomycin and lysostaphin (2 mg/kg) groups. Mice of other treatment groups had no detectable CFU counts in these two organs.

The highest CFU counts in this model could be measured in the kidneys of the vehicle group, proofing invasive disease (Fig. 6.6 A). Antibacterial treatment with each of the applied therapeutics led to significantly reduced bacterial burden. The strongest effect was exhibited

by the lysostaphin (5 mg/kg) and the lysostaphin + oxacillin groups. Both of them led to complete bacterial clearance in the kidneys of five out of eight mice, which is shown in Fig 6.4 A by plotting them on the detection limit of  $10^2$  CFU. Vancomycin, oxacillin-only or lysostaphin (2 mg/kg) led to a less pronounced reduction of bacterial burden, but reduction was still significant compared to the 0.9 % NaCl group, although vancomycin and lysostaphin (2 mg/kg) were considerably less effective than lysostaphin + oxacillin or lysostaphin (5 mg/kg).

The CFU counts in the catheter showed a similar picture. The highest CFU counts were determined for the vehicle group while treatment with each of the antibiotics or combinations led to significant lower values (Fig. 6.6 B). At this site of infection, the strongest reduction was achieved by either oxacillin alone or in combination with lysostaphin (2 mg/kg). However, a complete eradication of *S. aureus* Xen 29 could not be achieved by any of the therapeutics tested.

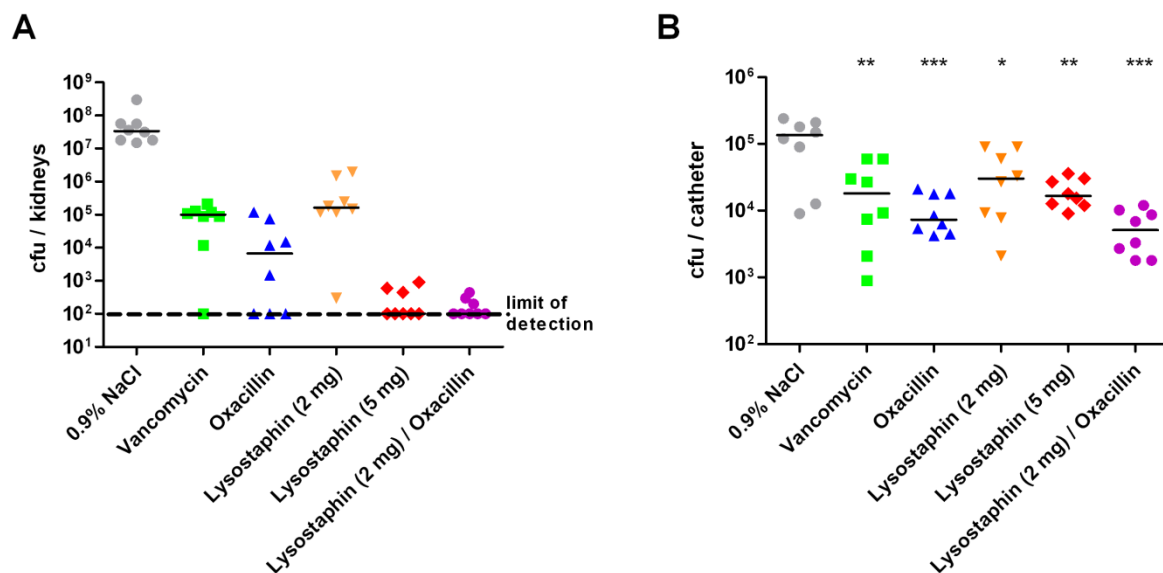


**Fig. 6.6: Bacterial burden at day 4 p.i. in the catheter-associated infection model.** A central venous catheter was placed in the jugular vein of NMRI mice ( $n = 8$  per group) and the lumen was filled with  $3.7 \times 10^7$  CFU *S. aureus* Xen29. The catheter was flushed 15 min after start of infection to remove non-adherent bacteria. Inner organs and the catheter were removed at day 4 p.i., either homogenized or sonicated and dilutions plated to determine CFU counts. **A: CFU counts in the kidneys at day 4 p.i..** All treatment groups had significantly lower CFU values than the 0.9 % NaCl group (vancomycin, oxacillin, lysostaphin 2 mg/kg:  $P < 0.01$ ; lysostaphin 5 mg/kg and lysostaphin+oxacillin:  $P < 0.005$ ). Vancomycin and lysostaphin 2 mg/kg had significantly higher CFU values than lysostaphin 5 mg/kg or lysostaphin+oxacillin ( $P < 0.05$ ). **B: CFU counts in the catheter at day 4 p.i..** Single data points per mouse and the medians of the respective group are shown. Statistically significant differences are indicated by asterisks (\*:  $P < 0.05$ , \*\*:  $P < 0.01$ , \*\*\*:  $P < 0.005$ , n.s.: not significant). (Adapted from Hertlein T et al. 2014)

### 6.1.6. Bioluminescent signal development in the catheter-associated infection model

The bioluminescent *S. aureus* strain Xen29 was applied in this model to enable visualization of colonization and spreading of bacteria following infection via the central venous catheter by BLI. Mice were therefore imaged immediately after infection (1 – 5 min p.i.) and then every 24 h from dorsal and ventral view to visualize sites of emerging photon signal. In principle, bioluminescence signal could be detected at four spots: the catheter area from dorsal and ventral view, the kidney area from dorsal and the heart/lung area from ventral view (Fig. 6.7 A). The signal detected in the catheter area was present from the first measurement immediately after start of infection until the end of the experiment, while the signals in the kidney area and the heart/lung area emerged at later time points. But not all mice of all groups developed bioluminescence signal above background level at all spots. Whereas all mice showed photon emission in the catheter area from ventral view (Fig. 6.7 B, with lysostaphin + oxacillin group being close to background noise), only four out of eight vehicle group and one out of eight vancomycin group mice developed signal in the heart/lung area. Most of the mice, with the exception of the lysostaphin + oxacillin group, showed additionally elevated photon emission in the kidney area from dorsal view. Oval areas of interest were defined at the locations with elevated photon emission and applied to all mice at all time points to guarantee comparable results for all treatment groups.

The quantification of the bioluminescence signal in these areas of interest showed, in general, at the catheter area from ventral view and the kidney area from dorsal view, increasing photon emission levels for the vehicle group and values close to background for the lysostaphin (2 mg/kg) + oxacillin group (Fig. 6.7 B). This led to significantly reduced values from day 3 p.i. until the end of the experiment. Oxacillin treatment led in the catheter area after day 1 p.i. to a signal reduction, which was similar in magnitude than those of the combinatorial group, while the other treatment groups showed intermediate values throughout the whole experiment. Interestingly, the photon emission in the catheter area from ventral view of vehicle, vancomycin, and lysostaphin (2 and 5 mg/kg) treated mice increased until day 2 p.i. and then remained at this level until the end of the experiment. In the kidney area, signal levels increased steadily until the end of the experiment for the vehicle group and slightly for the treatment groups. Lysostaphin + oxacillin and, less pronounced, oxacillin-only group showed a bioluminescence signal close to background levels.

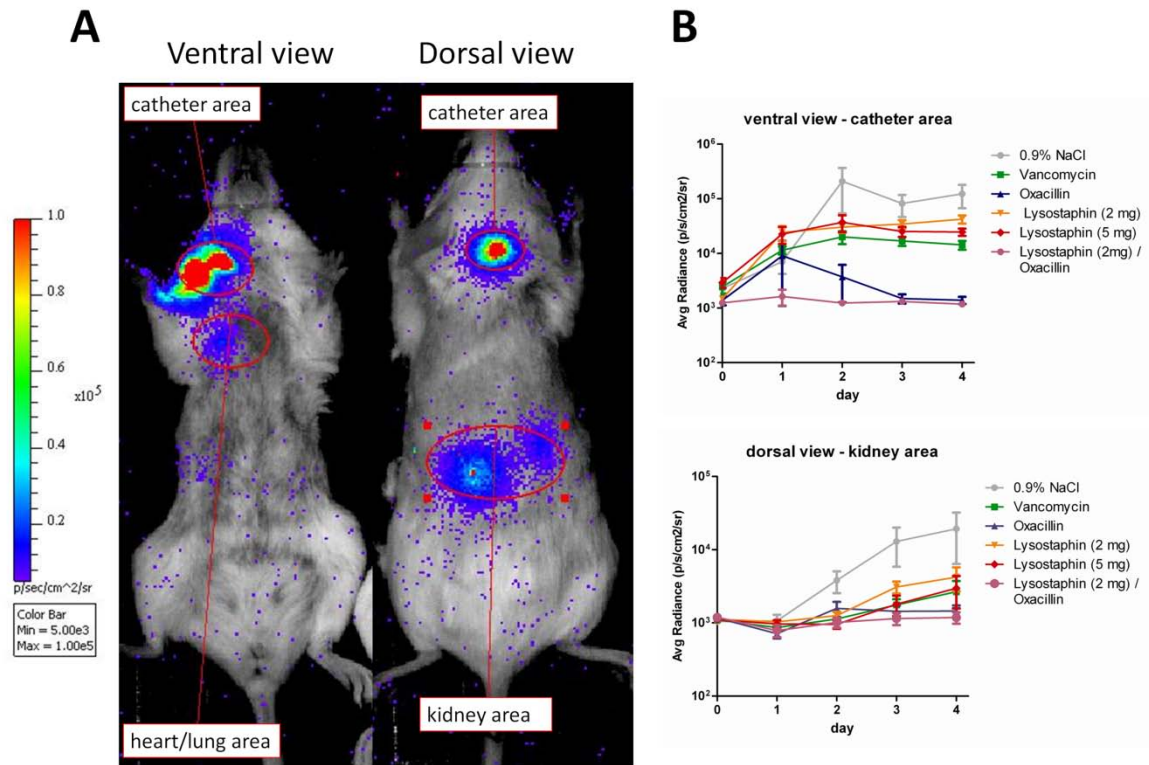


**Fig 6.7: Emergence and development of bioluminescence signal in the catheter-associated infection model.** Mice (Female NMRI,  $n = 8$  per group) were challenged with  $3.7 \times 10^7$  CFU of bioluminescent *S. aureus* Xen29 in the lumen of a central venous catheter. All mice were imaged once every 24 h after start of infection and average radiance signal was determined in manually defined regions of interest. **A:** Exemplary mouse demonstrating areas of bioluminescence signal emergence during the course of infection. The regions of interest, defined from ventral or dorsal view and named catheter, heart/lung or kidney area, were applied to all measurements in same orientation and size to standardize the measurements. **B:** Bioluminescence signal development in the catheter area from ventral view (upper graph) or in the kidney area from dorsal view (lower graph). Shown are the mean values  $\pm$  SEM of each group. (Adapted from Hertlein T et al. 2014)

## 6.2. Discussion

Although a number of new antibiotics has been introduced in the last years, *Staphylococcus aureus* remains a major challenge for public health systems all over the world (Seybold U et al. 2006, Chambers HF and Deleo FR. 2009). The emergence of hospital-acquired Meticillin-resistant *S. aureus* strains (ha-MRSA), community-acquired MRSA (ca-MRSA) and even livestock-associated MRSA strains has increased the pressure to identify and combat spreading of *S. aureus* (Kennedy AD et al. 2008, Schaumburg F et al. 2012). Most of the newly introduced antibiotics are members of long- and well-known substance classes with improved activity especially against MRSA strains (Ohlsen K, Lorenz U. 2010, Theuretzbacher U. 2012). But despite that, there are completely new approaches and compounds to treat *S. aureus* infections in preclinical development like monoclonal antibodies, immunomodulators or enzymes (Scott MG et al. 2007, Ohlsen K, Lorenz U. 2010). Among these, one promising compound in preclinical development is the endopeptidase lysostaphin. The goal of this chapter was therefore to investigate the efficacy of a new, recombinant formulation of lysostaphin in relevant animal models.

In this context, murine thigh and catheter-associated infection models were chosen because of their high clinical relevance. Both models mirror types of human infection, which are characterized by significant morbidity and mortality in the clinical situation and are recognized as difficult-to-treat infections (Lowy FD. 1998). The efficacy of lysostaphin was evaluated in this experiments either directly by measuring the bacterial burden in terms of CFU counts or by reducing the signals measured by the imaging platform established in chapters 4 and 5. Based on the experiments described in these chapters, bioluminescence and <sup>19</sup>F magnetic resonance imaging with perfluorocarbons were applied to investigate the efficacy of lysostaphin: bioluminescence imaging, because it visualizes the development of bacterial burden in vivo during the course of infection, what is, in consequence, similar in target than CFU counting, which measures the number of viable bacteria at the end of the experiment in the infected thigh muscle, while <sup>19</sup>F MRI, in contrast, images the accumulation of perfluorocarbon emulsion at the site of infection dependent on the immigration of phagocytic immune cells and thus the gravity of the innate immune response to infection.

The endopeptidase lysostaphin is member of a new class of antibacterial compounds with high in vitro activity against *S. aureus*, including MRSA (Huber MM et al. 1989, Polak J et al. 1993). Notably, MIC values for the lysostaphin formulation used in this study were 100-fold lower than those of vancomycin. It cleaves the pentaglycine cross-bridge in the *S. aureus* cell wall (Schindler CA et al. 1964, Sloan GL et al. 1977) and has shown in vivo activity in various animal models (Climo MW et al. 1998, Patron RL et al. 1999, Kokai-Kun JF et al. 2007, Kokai-Kun JF et al. 2009). The in vivo efficacy could for example been demonstrated in intraperitoneal infection and kidney abscess models in mice, endocarditis in rabbits or mastitis in cows (Harrison EF et al. 1967, Schaffner W et al. 1967, Goldberg LM et al. 1967, Oldham ER et al. 1991, Climo MW et al. 1998). One study was furthermore published



describing administration of lysostaphin to a neutropenic patient (Stark FR et al. 1974). To sum up, all these studies suggested that lysostaphin has the potential to be applied as a drug of last resort against drug-resistant *S. aureus*.

Lysostaphin was administered at two doses, 2 mg/kg or 5 mg/kg, consistent with the concentrations used in former studies with different, recombinant formulations of lysostaphin (Kiri N et al. 2002, Kokai-Kun JF et al. 2007). The higher dose, 5 mg/kg, reduced significantly CFU values in both murine models and was non-inferior or even superior to the control agents oxacillin and vancomycin, which are commonly used to treat *S. aureus* infections. Only in the catheter lumen oxacillin had a similar or slightly stronger activity than lysostaphin (5 mg/kg). The higher dose was furthermore superior to the lower dose (2 mg/kg) in both models. The values derived by bioluminescence imaging verified the results from CFU determination showing superiority to vancomycin, low-dose lysostaphin and oxacillin with the exception of catheter lumen. Finally, the smallest accumulation of perfluorocarbon emulsion at the site of infection for all groups could be visualized by <sup>19</sup>F MR imaging for lysostaphin (5 mg/kg) treated mice, indicating weak immigration of phagocytic immune cells.

A further group received a combination of low-dose lysostaphin (2 mg/kg) and oxacillin to test for in vivo synergy. Former studies demonstrated synergy between  $\beta$ -lactam antibiotics and lysostaphin by in vitro and in vivo experiments (Polak J et al. 1993, Kiri N et al. 2002). The combination demonstrated efficacies in the reduction of CFU similar to those seen for lysostaphin (5 mg/kg) being superior to oxacillin or lysostaphin (2 mg/kg) alone. In the catheter lumen, the combination of lysostaphin + oxacillin was even better in reducing CFU and bioluminescence values than lysostaphin (5 mg/kg), but only marginally better than oxacillin alone. Regarding the <sup>19</sup>F accumulation at the site of infection, lysostaphin + oxacillin exhibited higher values than lysostaphin (5 mg/kg) and similar ones than vancomycin or lysostaphin (2 mg/kg) suggesting higher influx of phagocytes than the high-dose lysostaphin group. This results suggest not necessarily synergy in both models, because the reduction of CFU, bioluminescence and <sup>19</sup>F accumulation signals compared between lysostaphin (2 mg/kg) and oxacillin-only on the one hand and the simultaneous combination of both on the other hand seemed to be closer to being additive than synergistic. Nonetheless, the combination of the narrow-spectrum lysostaphin with a broad band  $\beta$ -lactam antibiotic might facilitate the application in the clinical situation.

In conclusion, lysostaphin proved to be very efficient either alone or in combination with oxacillin to fight *S. aureus* infection in both thigh and catheter-associated infections. However, concerns have been raised regarding the immunogenicity of and resistance development against lysostaphin. For example, lysostaphin-resistant *S. aureus* clones could be identified after low dose lysostaphin treatment (1 mg/kg) in a rabbit endocarditis model, while high dose treatment (5 – 15 mg/kg) prevented resistance development (Climo MW et al. 2011). The resistance development was connected to mutations in *femA*, resulting in an altered mucopeptide structure in which the normal pentaglycine bridge was replaced by a

single glycine. Resistance development has also been described following the incorporation of other amino acids besides glycine into the peptidoglycan cross bridge (Thumm G et al. 1997, Tschierske M et al. 1997, Strauss A et al. 1998). Interestingly, this kind of resistance development could be prevented by the concomitant application of nafcillin, a  $\beta$ -lactam antibiotic. It was furthermore observed, that MRSA or ORSE strains, which developed lysostaphin resistance after in vivo treatment with low dose lysostaphin, became sensitive to  $\beta$ -lactam antibiotics (Climo MW et al. 2011, Kiri N et al. 2002). A further lysostaphin resistance mechanism was recently identified by using a *Bursa aurealis* insertion approach. This mechanism was independent from alterations in cell wall cross bridges, but the in vivo importance has not yet been determined (Gründling A et al. 2006).

Lysostaphin-resistant clones could, in the experiments of this chapter and congruent with afore mentioned studies, only be identified in the lysostaphin (2 mg/kg) group, but not in lysostaphin (5 mg/kg) or lysostaphin + oxacillin treated mice. This suggests that in vivo resistance development can be prevented by short term treatment with high doses of lysostaphin or by combining lower doses with  $\beta$ -lactam antibiotics. Furthermore, it seems to be recommended to apply lysostaphin only in cases of severe infections with highly-resistant *S. aureus* strains in order to prevent resistance development in the clinical situation.

A further concern regularly mentioned against application of the polypeptide lysostaphin as anti – *S. aureus* drug is the possible occurrence of adverse immunological effects. Nevertheless, studies investigating the topical application of lysostaphin to eradicate nasal *S. aureus* carriage did not induce antibody formation or sensitization (Harris RL et al. 1967, Quickel KE et al. 1971). Additionally, multiple intramammary infusions of recombinant lysostaphin formulations in cows failed to provoke significant serum antibody titers against lysostaphin and did furthermore not show any detrimental effects on the animals (Daley MJ et al. 1992). But nonetheless, additional studies are necessary to assess potential adverse immune reactions to systemic application of lysostaphin during treatment.

The second topic of this study was to evaluate the ability of the imaging platform, which is described in chapter 5, to visualize and quantify non-invasively differences in efficacy pattern of antibiotics, especially new developed ones, in vivo. Challenging the mice with bioluminescent *S. aureus* Xen29 led in both models to bioluminescence signals at the primary sites of infection immediately after infection (Fig. 6.2 B and Fig. 6.7 B). No other sources of photon emission could be detected before or immediately after infection. During course of infection, the vehicle group delivered in both models the strongest bioluminescence signal of all groups and lysostaphin + oxacillin the weakest one. In the catheter-associated infection model, bioluminescence imaging proved useful to identify secondary sites of infection, visualizing emerging signal in the kidney and the heart/lung area of some mice. These results could be confirmed by CFU counting at day 7 p.i.. Moreover, bioluminescence imaging indicated in both infection models the same antibiotic efficacy pattern than CFU counting with the exception of lysostaphin (5 mg/kg) efficacy in the kidneys of the catheter infection model. In this case, one might get from the graph in Fig. 6.5

By the impression, that the kidneys delivered higher mean bioluminescence signal than expected from corresponding CFU counts. Reason for this discrepancy between bioluminescence and CFU results might be the considerable loss of bioluminescence signal due to tissue depths of inner organs. Variations in the localization and orientation of the kidneys (especially if the spinal cord, which strongly absorbs bioluminescence signal of the emitted wavelength, is located between one or both kidneys and the detection-CCD camera) might have led in this rather small animal number approach to these non-distinctive, highly overlapping results. After all, it has to be stated, that the differences in bioluminescence signal of the kidney area between the different treatment groups were statistically not significant and small in value, while the variance of the single values were rather high. In conclusion, bioluminescence imaging has proven its usefulness in preclinical evaluation of antibacterial substances in the catheter-associated infection model by visualizing secondary sites of infection like kidneys, heart or lungs, but the sensitivity, in terms of quantifying the bacterial burden at sites of infection and measuring differences between different treatment regimens, was less sensitive than classical CFU determination.

Regarding the thigh infection model, bioluminescence imaging delivered much more stable and continuous signals than in the catheter-associated infection model (with the exception of the strong bioluminescence signal drop within the first 24 hours after start of infection). Bioluminescence signal was detectable in all groups, with the exception of the lysostaphin + oxacillin group, where signal remained close to background levels. The efficacy pattern fitted in this model nicely between CFU counting and bioluminescence imaging. The discrepancy between the reliability of bioluminescence results of thigh and catheter-associated infection model might be caused by differences in the tissue depths of the respective sites of infection. The signal derived from abscesses of the thigh infection model are more or less standardized by the injection of bacteria at the start of the experiment, while the kidneys and the exact location of the catheter depends on the individual mouse and the emergence of infection loci. It is consequently of high importance to reconsider bioluminescence imaging to quantify bacterial burden in deeper located tissue. Nonetheless, our study is conform with published studies demonstrating the benefits of bioluminescence imaging, to give additional and precious information about the infection process in real time that might, in consequence, help to reduce the number of animals necessary to assess the efficacy of novel antibiotics in preclinical studies (Rocchetta HL et al. 2001, Kuklin NA et al. 2003, Jawhara S et al. 2004).

In addition to bioluminescence imaging,  $^{19}\text{F}$  magnetic resonance imaging was applied as second imaging modality to investigate the efficacy of lysostaphin in the thigh infection model. As shown in chapter 5, the accumulation of perfluorocarbon emulsion, which is visualized by  $^{19}\text{F}$  MRI, at the site of infection is influenced by antibiotic therapy. This modality is in contrast to CFU determination or bioluminescence imaging not directly connected to the bacterial burden, but to the incorporation of perfluorocarbon emulsion by phagocytic immune cells in the bloodstream and their subsequent migration to the site of infection. In

consequence,  $^{19}\text{F}$  MRI with perfluorocarbon emulsions indicates inflammation in distinct areas (Flögel U et al. 2008, Ebner B et al. 2010).

Therefore, all mice received a single application of perfluorocarbon emulsion at day 2 p.i. and were imaged at days 3 and 7 p.i.. The accumulation of  $^{19}\text{F}$  at the site of infection was visualized by MRI and the anatomical context facilitated by underlaying with a  $^1\text{H}$  MR image. In principle, two parameters became measurable by this method: the  $^{19}\text{F}$ -filled volume (in terms of voxels) and the overall  $^{19}\text{F}$  signal in the infected thigh muscle. Both parameters delivered a similar picture regarding the efficacy pattern of the applied antibiotics and dosing regimens. The strongest accumulation in volume and signal could be measured for the vehicle treated group at both time points, while the weakest ones were measured for the lysostaphin (5 mg/kg) group. All treatment groups reached significantly reduced  $^{19}\text{F}$  accumulation volumes and signals at day 3 and 7 p.i., but the differences between the treatment regimens were not significant with the exception of a significantly lower  $^{19}\text{F}$  filled volume in lysostaphin (5 mg/kg) treated mice compared to oxacillin treated ones at day 3 p.i.. Nonetheless, a striking discontinuity between the  $^{19}\text{F}$  MRI results and the CFU/bioluminescence results could be seen regarding the pattern of signal reduction. Oxacillin treatment, both alone or in combination with lysostaphin (2 mg/kg), resulted in higher  $^{19}\text{F}$  values than expected if compared to the efficacy patterns indicated by CFUs or photon emission. This suggests a boost in perfluorocarbon uptake by phagocytes or enhanced migration to the site of infection, indicating immune-modulation by oxacillin treatment. But, to note, the strengthened activation or migration of phagocytes did not lead to better clearance of *S. aureus* in the infected thigh muscle.

In general, it has been shown by former studies that  $\beta$ -lactam antibiotics enhance pro-inflammatory cytokine production by inducing the release of bacterial cell-wall components (Tauber SC et al. 2008). The incubation of *S. aureus* cultures led, for example, to greatly increased concentrations of lipoteichoic acid and peptidoglycan compared to peptide-synthesis inhibitor antibiotic treated cultures. These cultures showed additionally an induction in release of tumor necrose factor alpha and interleukin-10 in human whole blood, which was directly proportional to the concentrations of lipoteichoic acid and peptidoglycan (van Langevelde P et al. 1998). Furthermore, the supernatant of these cultures enhanced the adhesiveness of endothelial cells for granulocytes and induced release of interleukin-8 and monocyte chemotactic protein 1 (van Langevelde P et al. 1999). The induction of pro-inflammatory immune response to  $\beta$ -lactam treated bacterial cultures could be observed for other bacterial pathogens than *S. aureus*, too. Exposure of *Streptococcus pneumoniae* cultures with  $\beta$ -lactam antibiotics led, for example, to activation of TLR2 and elevated levels of IL-8 in HeLa cell cultures (Moore LJ et al. 2007). A systematic testing of several different classes of antibiotics demonstrated differential release of lipoteichoic and teichoic acid from *S. pneumoniae* dependent on class and concentration, with  $\beta$ -lactams delivering the highest levels of all tested antibiotics when applied at concentrations close to their MIC values (Stuertz K et al. 1998, Heer C et al. 2000).

Interestingly, treatment with vancomycin did in this context not provoke TLR2 activation and IL-8 induction (Moore LJ et al. 2004). Since *S. aureus* might lead to similar TLR2 activation after  $\beta$ -lactam treatment, this in vitro experiment might give an explanation for the increased  $^{19}\text{F}$  accumulation for the oxacillin group while vancomycin treatment resulted in lower perfluorocarbon emulsion accumulation at the site of infection, as shown in this chapter. In addition to in vitro studies, several experimental animal models of *Escherichia coli*, *Pseudomonas aeruginosa*, *Streptococcus pneumoniae* and *Staphylococcus aureus* infections have shown that  $\beta$ -lactam treatment induced release of pro-inflammatory bacterial components, fortified inflammation and was associated with impaired survival or elevated bacterial burden (reviewed by Nau R et al. 2005). Therefore, an interesting approach to improve the outcome of antibacterial therapy might be to modulate the immune response that accompanies infection and therapy. Combining  $\beta$ -lactam therapy with either pre-treatment with rifampicin in a *S. pneumoniae* model (Gerber J et al. 2003) or with artemunate in a *S. aureus* model (Jiang W et al. 2011) improved the outcome compared to  $\beta$ -lactam treatment only, suggesting a beneficial effect by anti-inflammatory activity of both compounds. But further studies are necessary to evaluate the efficacy of such combinations in different experimental models in much higher detail. Nonetheless, these studies shift the attention to the problem that measuring the bacterial burden at the site of infection might not be sufficient to determine the real consequences of infection and therapy. Tissue and organ destruction caused by infection and inflammation are of similar importance to the patient and, therefore, those effects should attract more attention in preclinical evaluation of new, promising compounds. Of importance, magnetic resonance imaging, especially  $^{19}\text{F}$  MRI with perfluorocarbons, might give such insights by revealing abscess formation, tissue destruction and phagocyte immigration in vivo.

**Tab. 6.1: Inter-experiment variation of CFU, bioluminescence and <sup>19</sup>F magnetic resonance results for the 0.9 % NaCl and the vancomycin groups.** Shown are the median values (CFU, <sup>19</sup>F volume and <sup>19</sup>F signal) or the mean values (BL signal) for both groups in the experiments described in chapters 5 and 6.

	0.9 % NaCl group		vancomycin group	
	chapter 5	chapter 6	chapter 5	chapter 6
infectious dose in CFU counts	$3.2 \times 10^8$	$2.4 \times 10^8$	$3.2 \times 10^8$	$2.4 \times 10^8$
CFU (d7 p.i.) in counts	$2.39 \times 10^9$	$8.84 \times 10^8$	$2.5 \times 10^7$	$1.25 \times 10^8$
BL signal (d3 p.i.) in p/s/cm <sup>2</sup> /sr	$2.8 \times 10^4$	$5.75 \times 10^4$	$1.4 \times 10^4$	$1.13 \times 10^4$
BL signal (d7 p.i.) in p/s/cm <sup>2</sup> /sr	$4.79 \times 10^4$	$7.81 \times 10^4$	$7.40 \times 10^3$	$7.2 \times 10^3$
<sup>19</sup> F volume (d3 p.i.) in voxels	$3.71 \times 10^4$	$3.06 \times 10^4$	$6.89 \times 10^3$	$7.12 \times 10^3$
<sup>19</sup> F volume (d7 p.i.) in voxels	$4.57 \times 10^4$	$4.58 \times 10^4$	$7.93 \times 10^3$	$8.24 \times 10^3$
<sup>19</sup> F signal (d3 p.i.) in nsif	$1.38 \times 10^5$	$1.04 \times 10^5$	$1.81 \times 10^4$	$1.98 \times 10^4$
<sup>19</sup> F signal (d7 p.i.) in nsif	$2.14 \times 10^5$	$2.31 \times 10^5$	$2.35 \times 10^4$	$2.56 \times 10^4$

The experiments in this chapter were based on the same animal model and the same imaging technologies than those described in chapter 5. Two treatment groups were applied in both chapters as control groups and thus offered the opportunity to investigate the inter-experiment variance of bioluminescence and <sup>19</sup>F magnetic resonance imaging: the 0.9 % NaCl group and the vancomycin group (Tab. 6.1). Regarding bioluminescence imaging results, the 0.9 % NaCl groups showed in both experiments a signal plateau between d3 and d7 p.i. with values of  $5.0 \times 10^4$  to  $1.0 \times 10^5$  p/s/cm<sup>2</sup>/sr and the vancomycin groups had similar signals level between day 3 and 5 p.i. of around  $1.0 \times 10^4$  p/s/cm<sup>2</sup>/sr. In consequence, similar infectious doses led in two independent experiments to similar bioluminescence signals in the same murine model for vehicle and vancomycin treatment, demonstrating the benefit and reliability of bioluminescence imaging in this model. The <sup>19</sup>F accumulation volume and signal values were very similar at days 3 and 7 p.i. for both treatment groups in both experiment sets. The variation was even weaker than with bioluminescence imaging, indicating a highly organized and equivalent immune response. Thus, it suggests that <sup>19</sup>F MRI with perfluorocarbon emulsions is an interesting and reliable imaging modality to investigate the efficacy of promising drug candidates, although the compound's influence upon the inflammatory immune response has to be taken into account. It has to be noted for both imaging modalities, that not only the total values were similar in the experiments of both chapters, but also the signal reduction caused by vancomycin. In consequence, both methods indicated comparable antibacterial capacity of vancomycin by two independent experiment sets.

In general, the results shown in this chapter were comparable regarding vancomycin efficacy and signal magnitude to the results shown in chapter 5. This demonstrates in conclusion that both modalities, bioluminescence imaging and  $^{19}\text{F}$  magnetic resonance imaging with perfluorocarbons, deliver consistent inter-experimental results and are thus suitable and applicable to evaluate antibacterial compounds.

In conclusion, lysostaphin has proven efficacy against *S. aureus* in two clinically relevant murine models, the thigh infection and the catheter-associated infection model. The higher dosing of lysostaphin (5 mg / kg body weight / d) resulted in strong reduction of CFU, bioluminescence signal and  $^{19}\text{F}$  accumulation volume and signal. Similarly efficient was the combination of low dose lysostaphin (2 mg / kg) with the  $\beta$ -lactam antibiotic oxacillin.  $^{19}\text{F}$  MRI with perfluorocarbons visualized the therapeutical effect non-invasively, although the results of the oxacillin only and the lysostaphin + oxacillin group were higher than expected from bioluminescence imaging and CFU determination. This might be an indication for immune-modulation, since perfluorocarbon emulsion accumulates at the site of infection in dependence of phagocytic immune cells, but this question has to be addressed by a different set of experiments.

## 7. Influence of antibiotic therapy on immune response

The unexpected high values of  $^{19}\text{F}$  signal and volume in the oxacillin treated mouse group in chapter 6 raised the question about the origin of the discrepancy between CFU counting, bioluminescence and  $^{19}\text{F}$  magnetic resonance imaging to determine the severity of disease or bacterial burden. Experiments in chapter 4 had shown in this regard that perfluorocarbon emulsion does not accumulate in bacteria at the site of infection, but in phagocytic immune cells, mainly in neutrophils. One obvious explanation for the above-mentioned observation might be therefore differences in the migration behavior or perfluorocarbon uptake of neutrophils during treatment with oxacillin. Literature research proved in this context an increased release of pro-inflammatory cell wall components by the action of  $\beta$ -lactam antibiotics like oxacillin (van Langevelde P et al. 1999, Tauber SC, Nau R. 2008). In order to investigate whether oxacillin can cause immunomodulatory effects in the *S. aureus* thigh infection model, the cytokine/chemokine response, the activity of the myeloperoxidase and the bacterial burden at the site of infection were determined during infection with either oxacillin-sensitive *S. aureus* Xen29 or oxacillin-resistant *S. aureus* LAC.

### 7.1. *Staphylococcus aureus* Xen29 thigh infection model

#### 7.1.1. Reduction of bacterial burden by treatment with either vancomycin, oxacillin, linezolid or minocycline

Female Balb/c mice were challenged with  $2.0 \times 10^8$  CFU *S. aureus* Xen29 in the left thigh muscle, imaged with bioluminescence imaging every 24 hours and the experiment ended at day 5 p.i. with the recovery of the infected thigh muscle. Antibiotic therapy with either vancomycin, oxacillin, linezolid or minocycline was initiated 2 hours p.i. and continued every 12 hours. The bioluminescent signal developed congruent with the experiments from former chapters (Fig. 7.1 A). After very high photon emission values immediately after start of infection, a strong decrease of signal could be detected after the first 24 hours of infection. The bioluminescence signal then recovered to lower values than initially in all groups. The 0.9 % NaCl group had in this regard at all time points after the first imaging session the highest values of all groups. The antibiotic treatment groups started to differ in values at day 4, with vancomycin showing the highest values, followed by linezolid, minocycline and oxacillin. All of them exhibited reduction of bioluminescent signal compared to 0.9 % NaCl group, but differences between the groups were small and results overlapping. In consequence, bioluminescent imaging demonstrated reduction of bacterial burden at the site of infection for all treatment groups, but showed no significant differences between the applied compounds. The determination of CFU values at day 5 p.i. showed highest values for the 0.9 % NaCl group. Antibiotic treatment led for all groups to significantly reduced bacterial burden at the site of infection. Vancomycin treatment reduced the CFU counts in



this regard with the weakest efficacy, followed by oxacillin and linezolid. Minocycline group mice showed strongest reduction of bacterial burden, resulting in no detectable bacteria in 3 out of 7 mice.

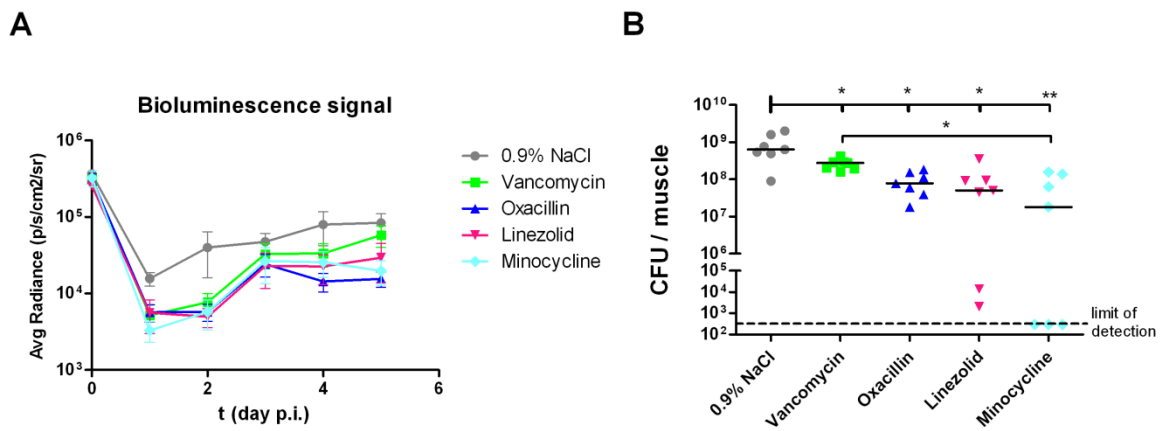


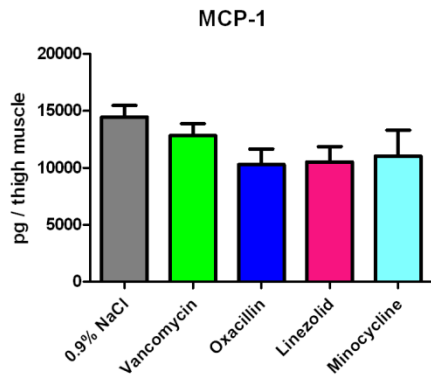
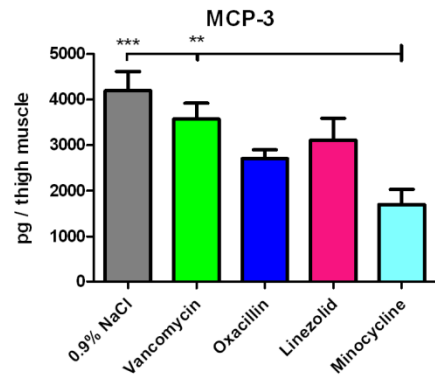
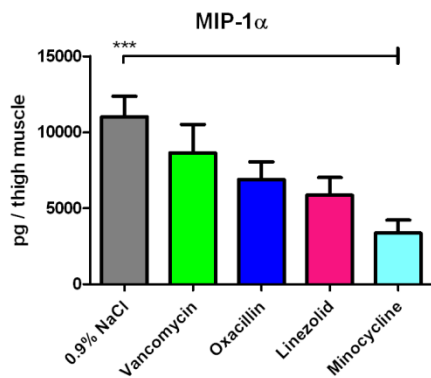
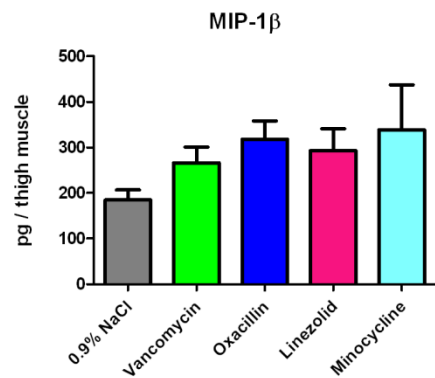
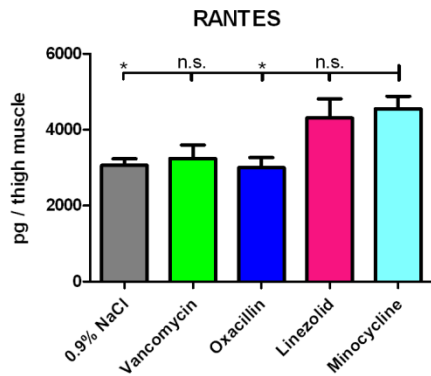
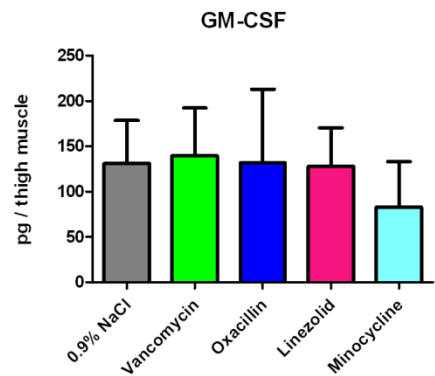
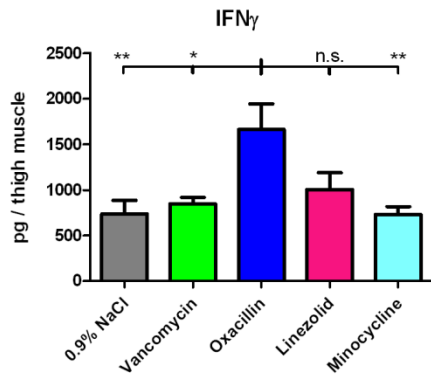
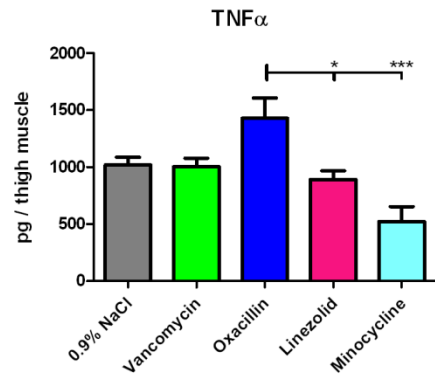
**Fig. 7.1: Bioluminescence signal development and bacterial burden in the *S. aureus* Xen29 thigh infection model.** Female Balb/c mice (n = 7 per group) were challenged with ca.  $2.0 \times 10^8$  CFU *S. aureus* Xen29 in the left thigh muscle. Antibiotic treatment started 2 h p.i. and was continued every 12 h (Vancomycin: 30 mg/kg/d, oxacillin: 200 mg/kg/d, linezolid: 15 mg/kg/d and minocycline: 20 mg/kg/d). **A. Bioluminescent signal derived from the infected thigh muscle during course of infection.** First measurement (time point: day 0 p.i.) was performed 5 – 15 min post infection. Mice were then imaged every 24 h for development of bioluminescence signal in a manually defined region of interest with same geometry and size for all investigated mice. Shown are the means +/- SEM for each group. **B. Colony-forming unit counts in the infected thigh muscles at day 5 p.i.** Muscles were recovered at the end point of the experiment, homogenized and serial dilutions plated on B agar plates. Shown are single data points per mouse and the respective medians per group. Statistical significant differences are indicated by asterisks (\*: P < 0.05, \*\*: P < 0.01).

### 7.1.2. Influence of antibacterial treatment on the levels of various cytokines and chemokines at the site of infection

The recovery of infected thigh muscles enabled additionally to CFU determination the quantification of cytokine and chemokine levels at the site of infection. In order to achieve this goal, the thigh muscles were homogenized and the homogenization filtered through a 0.22  $\mu\text{m}$  syringe filter to remove cells. The filtered homogenizate was then used to quantify the concentration of various cytokines and chemokines with a flow cytometry bead assay. Since we were interested in the state of inflammation and activation of immune cells, the antibody-conjugated beads were selected to cover various pro- and anti-inflammatory cytokines and chemokines.

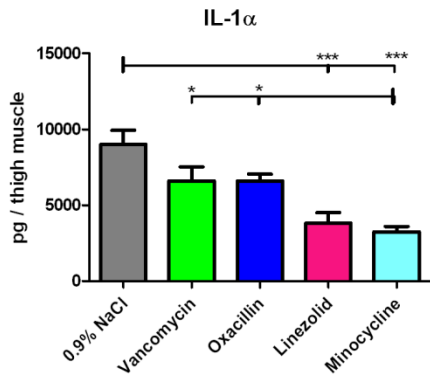
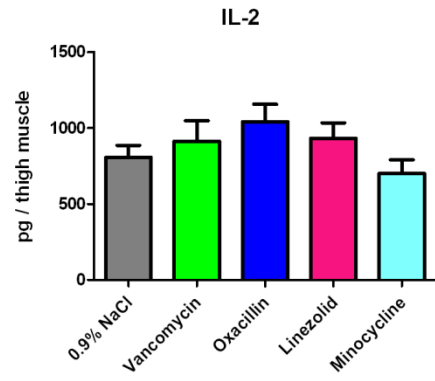
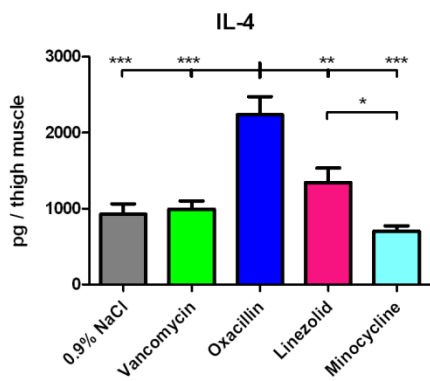
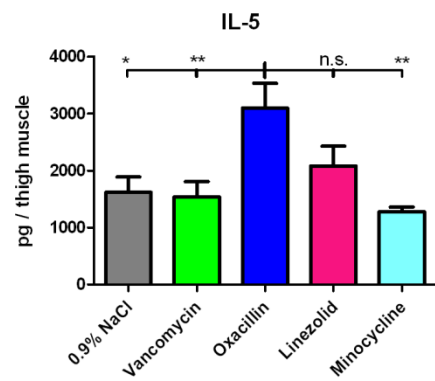
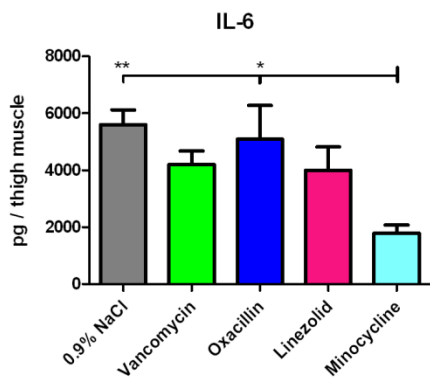
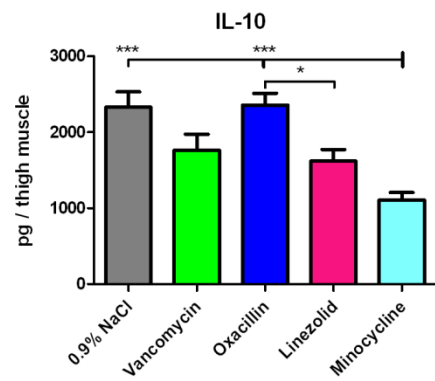
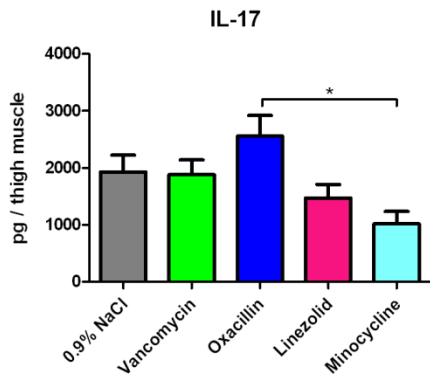
Regarding chemokines, very high amounts of MIP-1 $\alpha$  and MCP-1 as well as high amounts of RANTES and MCP-3 could be found in the infected thigh muscle at day 5 p.i. (Fig. 7.2). MIP-1 $\beta$  was detected only at very low levels with similar values for all groups. Especially interesting is the fact, that they were found differentially among the treatment groups. MIP-1 $\alpha$  and MCP-3 followed in pattern the efficacy of antibacterial therapy with highest values for 0.9 % NaCl group and smallest values for minocycline group. MCP-1 showed this gradient, too, but less pronounced than MIP-1 $\alpha$  and MCP-3. RANTES in contrast was strongest released in minocycline and linezolid groups, and weakest in oxacillin and 0.9% NaCl groups.

**Fig. 7.2 (facing page): Titers of various chemokines and cytokines in the infected thigh muscle of *S. aureus* Xen29 infected mice at day 5 p.i..** Female Balb/c mice (n = 7 per group) were challenged with  $2.0 \times 10^8$  CFU *S. aureus* Xen29 in the left thigh muscle. Antibiotic treatment started 2 h p.i. and was continued every 12 h (Vancomycin: 30 mg/kg/d, oxacillin: 200 mg/kg/d, linezolid: 15 mg/kg/d and minocycline: 20 mg/kg/d). Muscles were recovered at day 5 p.i., homogenized, the homogenate filtered through a 40  $\mu\text{m}$  cell strainer and the cytokine/chemokine concentration measured with either the Mouse Chemokine 6plex FlowCytomix Multiplex or the Mouse Th1/Th2 10plex Ready-to-Use FlowCytomix Multiplex (both eBioscience). Shown are the titers of **A.** monocyte chemotactic protein-1 (MCP-1), **B.** monocyte chemotactic protein-3 (MCP-3), **C.** macrophage inflammatory protein 1 alpha (MIP-1 $\alpha$ ), **D.** macrophage inflammatory protein 1 beta (MIP-1 $\beta$ ), **E.** regulated on activation, normal T cell expressed and secreted (RANTES), **F.** granulocyte macrophage colony-stimulating factor (GM-CSF), **G.** interferone  $\gamma$  (IFN $\gamma$ ) and **H.** tumor necrose factor  $\alpha$  (TNF $\alpha$ ). Shown are the means  $\pm$  SEM per group. Statistical significant differences between different groups are marked by asterisks (\*: P < 0.05, \*\*: P < 0.01, \*\*\*: P < 0.005, n.s.: not significant).

**A****B****C****D****E****F****G****H**

Determination of cytokine values in the infected thigh muscle revealed very high amounts of IL-1 $\alpha$  at the site of infection and high amounts of IL-6 (Fig. 7.3). The highest concentration of IL-1 $\alpha$  was measured for the 0.9 % NaCl group, the smallest one for minocycline. The pattern of IL-1 $\alpha$  concentration among the different treatment groups mirrored thereby the efficacy pattern of the different antibiotics. Lower amounts than IL-1 $\alpha$  could be detected for virtually all other tested cytokines at the site of infection, namely IL-2, IL-4, IL-5, IL-10, IL-17, TNF $\alpha$  and IFN $\gamma$ . GM-CSF, in contrast, delivered no detectable concentration above background values at the site of infection. Interestingly, oxacillin treatment led in this experiment with *S. aureus* Xen29 to the highest measured concentrations of TNF $\alpha$ , IFN $\gamma$ , IL-4, IL-5 and IL-17, all of them (with the exception of TNF $\alpha$  and IL-17) significantly higher than those derived from 0.9 % NaCl group. Other treatments than oxacillin resulted in similar concentrations of this cytokines (IL-4, IL-5, IL-17, TNF $\alpha$  and IFN $\gamma$ ) than the 0.9 % NaCl group, indicating no or weak influence of treatment or reduction of bacterial burden upon expression and release of these cytokines at the site of infection. IL-6 and IL-10 showed with the exception of the oxacillin group a concentration pattern that followed the efficacy pattern of antibiotic therapy. 0.9 % NaCl with the highest values of bacterial burden and IL-6/IL-10 release, minocycline with the smallest values and vancomycin and linezolid groups with intermediate ones, while oxacillin treatment caused values comparable to those of 0.9 % NaCl group. IL-2 was detected at comparable concentrations in all groups.

**Fig. 7.3 (facing page): Titers of various interleukins in the infected thigh muscle of *S. aureus* Xen29 infected mice at day 5 p.i..** Female Balb/c mice (n = 7 per group) were challenged with  $2.0 \times 10^8$  CFU *S. aureus* Xen29 in the left thigh muscle. Antibiotic treatment started 2 h p.i. and was continued every 12 h (Vancomycin: 30 mg/kg/d, oxacillin: 200 mg/kg/d, linezolid: 15 mg/kg/d and minocycline: 20 mg/kg/d). Muscles were recovered at day 5 p.i., homogenized, the homogenate filtered through a 40  $\mu$ m cell strainer and the cytokine/chemokine concentration measured with either the Mouse Chemokine 6plex FlowCytomix Multiplex or the Mouse Th1/Th2 10plex Ready-to-Use FlowCytomix Multiplex (both eBioscience). Shown are the titers of **A.** interleukin 1 $\alpha$  (IL-1 $\alpha$ ), **B.** interleukin 2 (IL-2), **C.** interleukin 4 (IL-4), **D.** macrophage interleukin 5 (IL-5), **E.** interleukin 6 (IL-6), **F.** interleukin 10 (IL-10) and **G.** interleukin 17 (IL-17). Shown are the means  $\pm$  SEM per group. Statistical significant differences between different groups are marked by asterisks (\*: P < 0.05, \*\*: P < 0.01, \*\*\*: P < 0.005, n.s.: not significant).

**A****B****C****D****E****F****G**

In summary, five different patterns of chemokine/cytokine release could be detected at the site of infection. First, IL-2 showed similar levels in all groups independently of the applied antibiotic treatment. Second, MIP-1 $\alpha$ , MCP-3, IL-1 $\alpha$  and MCP-1 (the last one less pronounced) were detected in a pattern that mirrored the CFU reduction efficacy of the different antibiotics with the 0.9 % NaCl group exhibiting the highest, minocycline the smallest and the other compounds intermediate values. Third, IL-6 and IL-10 were released dependent on the efficacy of the applied antibiotic with the exception of the oxacillin group. More precisely, 0.9 % NaCl group showed highest values, minocycline group the lowest ones and vancomycin and linezolid intermediate values, while oxacillin led to levels similar to those of 0.9 % NaCl although the CFU counts and bioluminescence signal were reduced. The fourth group consisted of TNF $\alpha$ , IFN $\gamma$ , IL-4, IL-5 and IL-17. This group exhibited highest amounts for the oxacillin group, while treatment with other antibiotics did not alter the concentration of cytokines compared to 0.9 % NaCl group. RANTES showed the fifth pattern with the highest amounts for the minocycline and linezolid group and lower, but similar ones for oxacillin, vancomycin and 0.9 % NaCl groups. MIP-1 $\beta$  and GM-CSF were detected at very low levels.

## **7.2. Thigh infection model with ca-MRSA *S. aureus* Lac (USA300)**

*S. aureus* Xen29, the strain applied in the thigh infection model in chapter 7.1, is oxacillin sensitive, thus suited to investigate the effect of oxacillin during therapy, but the results could not be differentiated between direct influence of oxacillin on the immune response and indirect influence by killing bacteria and thereby releasing pro-inflammatory cell wall components that stimulate cytokine release. An oxacillin-resistant strain like *S. aureus* LAC (USA300) provides the possibility to measure potential direct effects of oxacillin and was therefore applied in the same infection model to enable the comparison of both results.

### **7.2.1. Influence of antibacterial treatment with either vancomycin, oxacillin, linezolid or minocycline on bacterial burden**

Hence, female Balb/c mice were infected with  $2.2 \times 10^8$  CFU *S. aureus* LAC in the left thigh muscle and antibiotic treatment started 2 hours later. It was continued every 12 hours until the end of the experiment. The infected thigh muscles were recovered at day 5 p.i., homogenized and the CFU counts measured. The highest values could be determined for the 0.9 % NaCl group, although oxacillin treatment resulted in similar, statistically not significant different values (Fig. 7.4 D). Vancomycin treatment led to reduction of approximately one log 10 unit, while linezolid lowered values by 2 and minocycline by 2.5 log 10 units. Both, linezolid and minocycline showed significantly lower values than oxacillin.

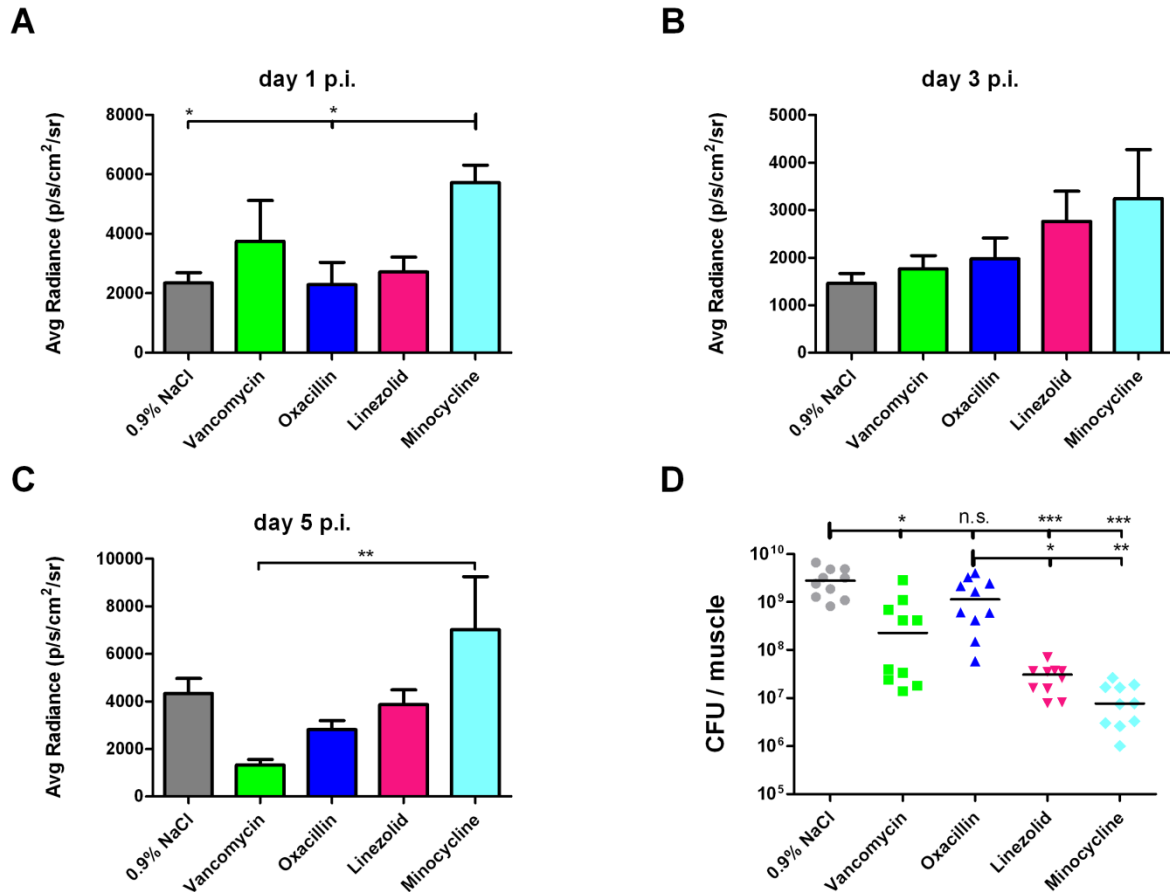


**Fig. 7.4: Bioluminescence signal at the site of infection derived after intra-peritoneal administration of luminol sodium salt and bacterial burden in the *S. aureus* LAC thigh infection model at day 5 p.i..** Female Balb/c mice (n = 10 per group) were challenged with  $2.2 \times 10^8$  CFU *S. aureus* LAC (USA300) in the left thigh muscle. Antibiotic treatment started 2 h p.i. and was continued every 12 h (Vancomycin: 30 mg/kg/d, oxacillin: 200 mg/kg/d, linezolid: 15 mg/kg/d and minocycline: 20 mg/kg/d). **A - C. Bioluminescent signal derived at the site infection after intra-peritoneal of luminol sodium salt.** Each mouse received 200 mg/kg luminol sodium salt (Alfa Aesar), dissolved in 0.9 % NaCl solution, via intra-peritoneal injection after a first bioluminescence control image. A second image was recorded 5 min after application, the photon emission calculated in a manually defined region of interest (same size and geometry for all measurements) and the difference calculated with: average radiance (after luminol administration) – average radiance (before luminol administration). The resulting mean bioluminescence signal differences +/- SEM per group is shown in A – C. **D. Colony-forming unit counts in the infected thigh muscles at day 5 p.i..** Muscles were recovered at the end point of the experiment, homogenized and serial dilutions plated on B agar plates. Shown are single data points per mouse and the respective medians per group. Statistical significant differences are indicated with asterisks (\*:  $P < 0.05$ , \*\*:  $P < 0.01$ , \*\*\*:  $P < 0.005$ , n.s.: not significant).



### 7.2.2. Imaging of myeloperoxidase activity at the site of infection with luminol

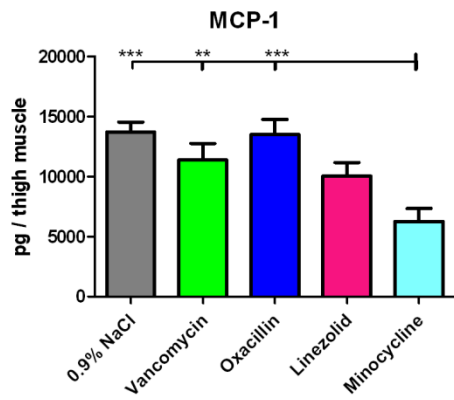
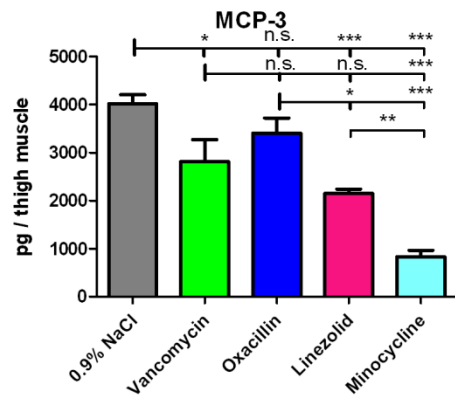
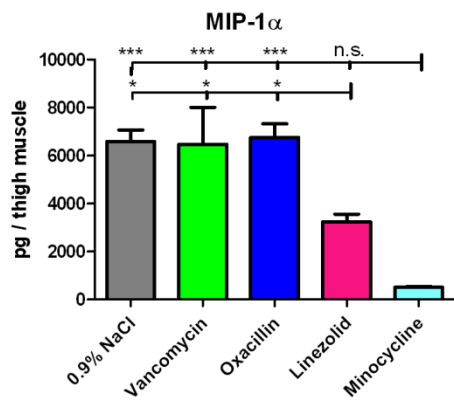
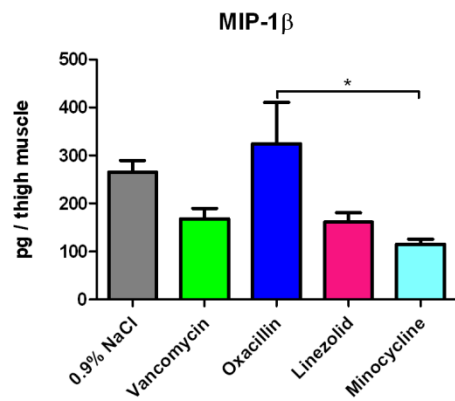
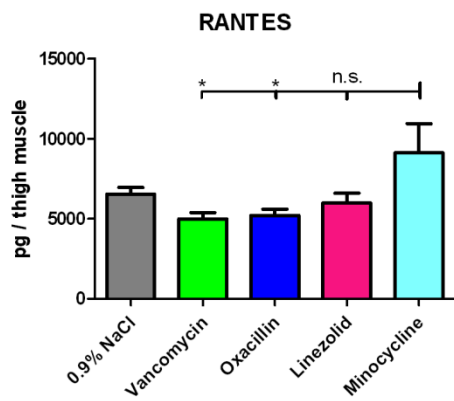
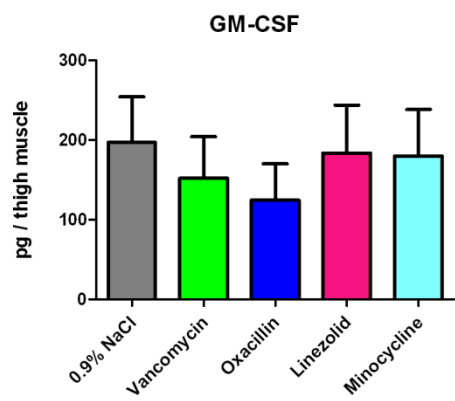
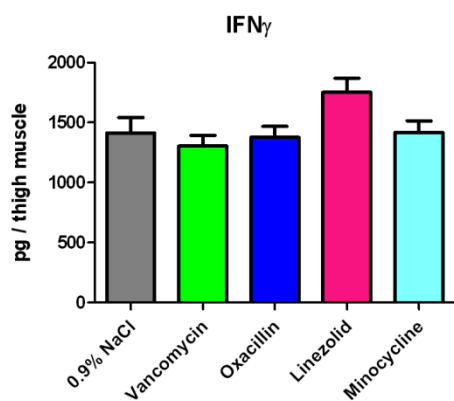
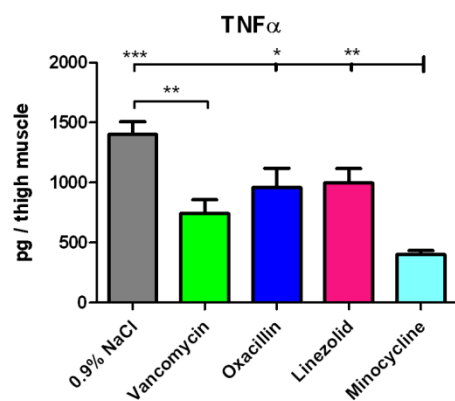
Inasmuch as *S. aureus* LAC does not emit bioluminescent signal, imaging of myeloperoxidase activity at the site of infection with luminol was feasible. This method is based on the intraperitoneal administration of luminol sodium salt that is cleaved in vivo by the action of neutrophilic myeloperoxidase, whereupon light is emitted (Gross S et al. 2009). This photon emission was detected by the IVIS in vivo imaging system in a non-invasive manner, thereby offering repeated sessions of luminol luminescent imaging. To measure the bioluminescent signal derived from luminol cleavage in vivo, first a negative control image was recorded and subtracted from an image after luminol application. Repeated imaging after administration of luminol at day 1 p.i. proved immediate photon signal that lasted for at least 30 minutes at constant signal levels (data not shown). Due to the invariance of photon emission for ca. 30 min after luminol administration, all following luminol luminescence values in a manually defined region of interest were acquired at 2 – 4 minutes post administration. Determination of the signal at day 1 p.i. showed highest luminescence signal for the minocycline group and lowest ones for 0.9 % NaCl and oxacillin treatment (Fig. 7.4 A - C). The difference between these values were statistically significant, the intermediate values from linezolid and vancomycin group, in contrast to this, not. The minocycline group delivered in this regard at days 3 and 5 p.i. the highest values, too. The 0.9 % NaCl group exhibited the second strongest photon emission at day 5 p.i., but the lowest one at day 3 p.i.. Vancomycin treatment led to weakest signal at day 5 p.i., but similar values than 0.9 % NaCl group at day 3 p.i.. Linezolid and oxacillin groups showed at both time points luminol luminescence signal at similar levels than the 0.9 % NaCl group.

### 7.2.3. Cytokine and chemokine levels at the site of infection

The levels of various cytokines and chemokines in the infected thigh muscle were measured at the end of infection with a flow cytometry based antibody-conjugated bead kit. The infected thigh muscles were therefore homogenized and filtered through a 0.22 µm syringe filter to remove cells. The homogenization was then incubated with the cytokine/chemokine specific beads and binding was determined via flow cytometry.

Regarding chemokine levels in the different treatment groups, high amounts of MCP-1, MCP-3, MIP-1α and RANTES could, in general, be determined in the infected thigh muscles (Fig. 7.5). In terms of MCP-1, MCP-3 and MIP-1α, a chemokine release pattern could be seen, that mirrored the efficacy of the applied antibiotics to reduce CFU counts. In more specific terms, this means that 0.9 % NaCl and oxacillin treatment resulted in the strongest release of MCP-1, MCP-3 and MIP-1α, while the weakest one followed from minocycline treatment. Vancomycin and linezolid treatment led to intermediate values. The highest amounts of RANTES, in contrast to this, could be measured for the minocycline group. Other treatments, in the meantime, resulted in similar values.

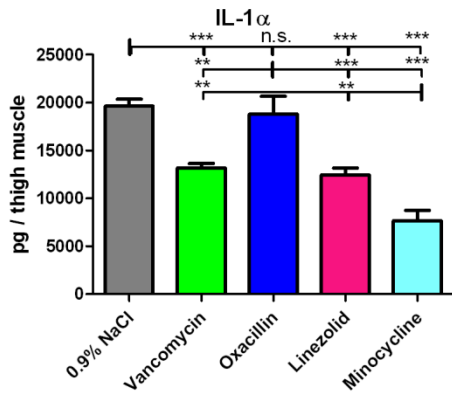
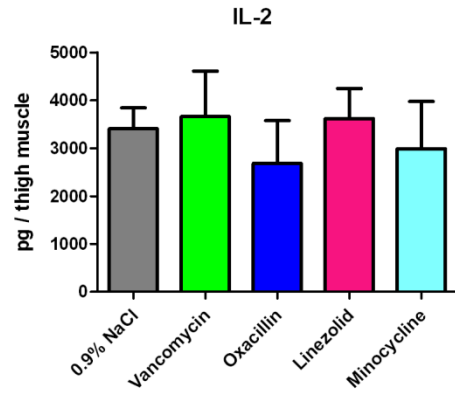
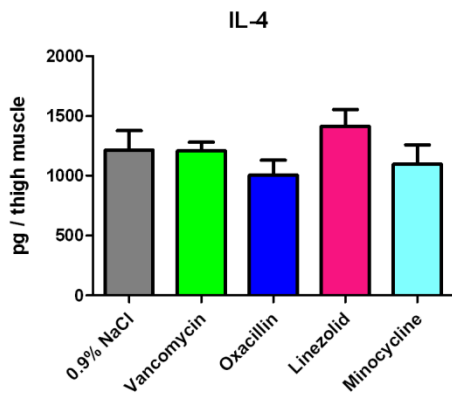
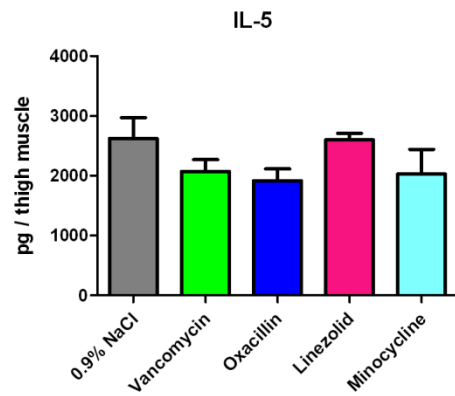
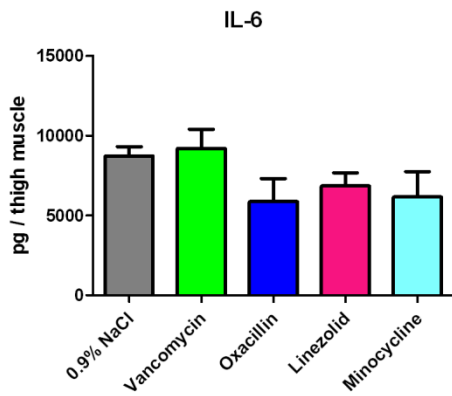
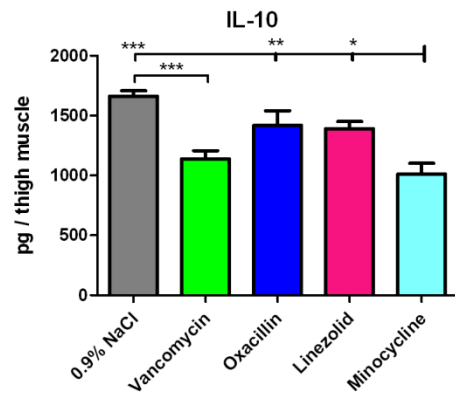
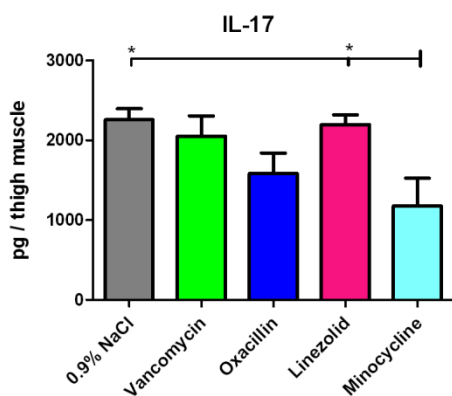
**Fig. 7.5 (facing page): Titers of various chemokines and cytokines in the infected thigh muscle of *S. aureus* LAC infected mice at day 5 p.i..** Female Balb/c mice (n = 10 per group) were challenged with  $2.2 \times 10^8$  CFU *S. aureus* LAC (USA300) in the left thigh muscle. Antibiotic treatment started 2 h p.i. and was continued every 12 h (Vancomycin: 30 mg/kg/d, oxacillin: 200 mg/kg/d, linezolid: 15 mg/kg/d and minocycline: 20 mg/kg/d). Muscles were recovered at day 5 p.i., homogenized, the homogenate filtered through a 40 µm cell strainer and the cytokine/chemokine concentration measured with either the Mouse Chemokine 6plex FlowCytomix Multiplex or the Mouse Th1/Th2 10plex Ready-to-Use FlowCytomix Multiplex (both eBioscience). Shown are the titers of **A.** monocyte chemotactic protein-1 (MCP-1), **B.** monocyte chemotactic protein-3 (MCP-3), **C.** macrophage inflammatory protein 1 alpha (MIP-1α), **D.** macrophage inflammatory protein 1 beta (MIP-1β), **E.** regulated on activation, normal T cell expressed and secreted (RANTES), **F.** granulocyte macrophage colony-stimulating factor (GM-CSF), **G.** interferone γ (IFNγ) and **H.** tumor necrose factor α (TNFα). Shown are the means +/- SEM per group. Statistical significant differences between different groups are marked by asterisks (\*: P < 0.05, \*\*: P < 0.01, \*\*\*: P < 0.005, n.s.: not significant).

**A****B****C****D****E****F****G****H**

Determination of the levels of various cytokines at the site of infection revealed very high amounts of IL-1 $\alpha$  and IL-6 (Fig. 7.6). The cytokines IL-2, IL-4, IL-5, IL-10, IL-17, TNF $\alpha$  and IFN $\gamma$  could be detected at considerable levels, too. GM-CSF and the chemokine MIP-1 $\beta$ , in contrast, could only be measured at very low amounts in the muscle homogenizations. Cytokines IL-2, IL-4, IL-5, IL-6 and IFN $\gamma$  were released at similar levels in all groups, with no significant differences between them. This indicates no influence of reduction of bacterial burden by antibiotic therapy on release of this group of cytokines during infection. Antibiotic treatment led to IL-1 $\alpha$  levels that followed the pattern of CFU reduction. In more detail, 0.9 % NaCl and oxacillin treatment with the highest CFU counts at the site of infection at day 5 p.i. resulted in the strongest IL-1 $\alpha$  levels, while minocycline group with the lowest CFU counts had the smallest IL-1 $\alpha$  amounts. Vancomycin and linezolid group mice showed intermediate levels in both parameters. TNF $\alpha$  and IL-10 levels resembled in pattern the reduction of bacterial burden with the exception of the linezolid group. The linezolid group mice exhibited similar levels than the oxacillin or 0.9 % NaCl group, although having much lower numbers of viable bacteria in their infected thigh muscle. Finally, IL-17 was found at comparable levels in all groups with the exception of the minocycline group, which had significantly lower levels than 0.9 % NaCl or linezolid group.

In summary, several different responses to antibiotic therapy could be seen in chemokine/cytokine pattern. A first group resembled the pattern of antibiotic efficacy, meaning, the lower the CFU counts in the infected thigh muscle, the lower the levels of cytokines/chemokines. Members of this group were the chemokines MCP-1, MCP-3, MIP- $\alpha$  and the cytokine IL-1 $\alpha$ . All of them were released in high amounts. IL-2, IL-4, IL-5, IL-6 and IFN $\gamma$  ranked among the second group, which showed similar levels for all treatments, independent of the reduction of bacterial burden by antibiotic treatment. RANTES levels showed a third, different pattern with minocycline leading to highest amounts while the other treatments resulted in similar levels at the site of infection. For the third group, TNF $\alpha$  and IL-10 levels mirrored the pattern of antibiotic efficacy with the exception of the linezolid group, which displayed similar values than oxacillin or 0.9 % NaCl group.

**Fig. 7.6 (facing page): Titers of various interleukins in the infected thigh muscle of *S. aureus* LAC infected mice at day 5 p.i..** Female Balb/c mice (n = 10 per group) were challenged with  $2.2 \times 10^8$  CFU *S. aureus* LAC (USA300) in the left thigh muscle. Antibiotic treatment started 2 h p.i. and was continued every 12 h (Vancomycin: 30 mg/kg/d, oxacillin: 200 mg/kg/d, linezolid: 15 mg/kg/d and minocycline: 20 mg/kg/d). Muscles were recovered at day 5 p.i., homogenized, the homogenate filtered through a 40  $\mu$ m cell strainer and the cytokine/chemokine concentration measured with either the Mouse Chemokine 6plex FlowCytomix Multiplex or the Mouse Th1/Th2 10plex Ready-to-Use FlowCytomix Multiplex (both eBioscience). Shown are the titers of **A.** interleukin 1 $\alpha$  (IL-1 $\alpha$ ), **B.** interleukin 2 (IL-2), **C.** interleukin 4 (IL-4), **D.** macrophage interleukin 5 (IL-5), **E.** interleukin 6 (IL-6), **F.** interleukin 10 (IL-10) and **G.** interleukin 17 (IL-17). Shown are the means  $\pm$  SEM per group. Statistical significant differences between different groups are marked by asterisks (\*: P < 0.05, \*\*: P < 0.01, \*\*\*: P < 0.005, n.s.: not significant).

**A****B****C****D****E****F****G**

### 7.3. Discussion

Experiments investigating the accumulation of perfluorocarbon emulsions in the *S. aureus* thigh infection model during antibiotic therapy in chapter 6 raised the question whether antibacterial compounds feature an effect on the immune system besides their antibacterial action. In more detail, oxacillin treatment resulted in only slightly lower  $^{19}\text{F}$  values (overall signal and volume) at the abscess area than the 0.9 % NaCl group, although the CFU counts in the thigh muscle were reduced strongly. Other antibiotic treatments in the imaging experiment to evaluate the efficacy of lysostaphin (chapter 6) did not show likewise results. Literature research to explain this observation elucidated that various antibacterial compounds can have immunomodulatory effects in addition to the antibacterial activity. Of special interest for this work was the discovery that  $\beta$ -lactam antibiotics like oxacillin can lead to increased release of pro-inflammatory cell wall components from dying bacteria (van Langevelde P et al. 1998, van Langevelde P et al. 1999). Furthermore, macrolides and tetracyclines can exhibit distinct effects on the release of cytokines and chemokines or upon the migration behavior of phagocytes (Tauber SC, Nau R. 2008). As an example, treatment with minocycline, a tetracycline, resulted in a murine brain abscess model with minocycline-resistant *S. aureus* to reduce the levels of IL-1 $\beta$  and MCP-1 (Kielian T et al. 2007).

In order to evaluate immunomodulatory effects of antibiotics *in vivo*, different antibacterial compounds were administered during course of infection in the murine *S. aureus* thigh infection model. Vancomycin, oxacillin and linezolid were used for this series of experiments due to the comparability with results from former chapters 5 and 6. Minocycline was added to this investigation because of its above-mentioned possible immunomodulatory effects. Since oxacillin should receive special attention due to the observations with  $^{19}\text{MR}$  imaging in the last chapter, two different *S. aureus* strains were used to infect the animals: *S. aureus* Xen29 and *S. aureus* LAC (USA300). *S. aureus* Xen29 is the bioluminescent strain which was applied in former experiments of this thesis and should therefore be included in these experiments. This strain is oxacillin sensitive and hence should display direct and indirect immunomodulatory effects of oxacillin therapy *in vivo*. *S. aureus* LAC in contrast is a ca-MRSA strain and thus oxacillin resistant. Oxacillin should only be able to induce direct immunomodulatory effects in the thigh infection model with this strain, but not indirectly via its antibacterial activity (which might lead, as shown in former publications (van Langevelde P et al. 1998, van Langevelde P et al. 1999), to increased release of pro-inflammatory cell wall components).

The efficacy of the antibiotic treatments to reduce bacterial burden and therefore eliminate or reduce the source of immune stimulating pathogens has, of course, to be taken into account. In order to determine the efficacy, the infected thigh muscles were recovered at day 5 p.i., homogenized and the CFU counts measured. In the MSSA infection experiment with *S. aureus* Xen29 the highest numbers of viable bacteria could be detected for the 0.9 % NaCl group, while every antibiotic regimen led to significantly reduced values. The strongest

reduction was seen for the minocycline group, the weakest one for the vancomycin treated mice. In terms of efficacy pattern, the results are congruent with the experiments in chapters 5 and 6 (Tab. 7.1), although linezolid treatment showed much weaker efficacy in reducing the CFU counts in the experiments of this chapter (around 1 log<sub>10</sub> unit reduction in chapter 7 vs. 6 log<sub>10</sub> units in chapter 5). Moreover, it has to be stated that vancomycin and oxacillin groups showed slightly weaker efficacy in this chapter than in the prior chapters. But important for this comparison is that the infected thigh muscles were not recovered at the same day p.i.. The thigh infection model in chapters 5 and 6 and, more importantly, the antibiotic treatment (twice a day) was continued until day 7 p.i., while the animal experiments of chapter 7 were ended at day 5 p.i.. The experiments of these chapters deliver moreover no information about the development of bacterial burden during these two additional days of infection and therapy. This has to be taken into account when comparing CFU results of these chapters. Besides this discrepancy in the time point of muscle recovery, the differences in infectious dose should be considered, too. The infectious dose was slightly lower than in the former experiments. This resulted in lower CFU counts for the 0.9 % NaCl group at the end of the experiment, too, thus maybe impeding the efficacy of antibiotics to reduce bacterial burden even stronger. And lastly, different batches of antibiotics were employed in chapters 5, 6 and 7, and although they were supplied by the same companies, there might have been slight variations in their composition or efficiency.

**Tab. 7.1: Comparison of CFU values in the infected thigh muscle at the end of the experiment in the different chapters of this thesis.** Different antibiotics were applied with the same dosing and treatment interval in different chapters and thus results are comparable. All mice were infected with *S. aureus* Xen29 in the left thigh muscle and antibiotic therapy was initiated 2 hours p.i. (then continued every 12 hours). The infected thigh muscle was recovered at the indicated time point (different between chapters 5/6 and 7), homogenized and the number of viable bacteria determined after plating of serial dilutions. Shown are the median values of the respective groups. n.d.: not determined, this antibiotic treatment was not included in the experiments of these chapters.

	chapter 5	chapter 6	chapter 7
	infection: $3.2 \times 10^8$ CFU muscle recovered: <b>d7</b> p.i.	infection: $2.4 \times 10^8$ muscle recovered: <b>d7</b> p.i.	infection: $2.0 \times 10^8$ muscle recovered: <b>d5</b> p.i.
<b>0.9 % NaCl</b>	$2.39 \times 10^9$	$8.84 \times 10^8$	$6.39 \times 10^8$
<b>Vancomycin</b> (30 mg/kg/d)	$2.5 \times 10^7$	$1.25 \times 10^8$	$2.76 \times 10^8$
<b>Oxacillin</b> (200 mg/kg/d)	n.d.	$5.1 \times 10^7$	$7.80 \times 10^7$
<b>Linezolid</b> (15 mg/kg/d)	$1.2 \times 10^3$	n.d.	$5.00 \times 10^7$

Since *S. aureus* Xen29 is a genetically modified strain and harbors the *luxABCDE* operon of *Photobacterium luminescens*, in vivo detection of luciferase activity and thus bacterial burden by an optical imaging system was possible (Francis KP et al. 2000). The pattern of photon emission over time was congruent with former imaging experiments in this thesis, namely a strong signal immediately after injection, that drops strongly within the first 24 hours to recover to a lower than initial plateau phase from day 3/4 p.i. until the end of the experiment. All antibiotic treatments led to reduction of average radiance signal from day 1 p.i. on. The degree of signal reduction was dependent on the efficacy of the applied antibiotic and followed the outcome of CFU determination. More precisely, minocycline resulted in lowest values and vancomycin in the highest ones of the antibiotic treatment groups, although all of them entailed significantly lower levels than the 0.9 % NaCl group. In this regard, the reduction of bioluminescent signal by antibiotic treatment was in magnitude similar to those seen in chapters 5 and 6, indicating consistency of bioluminescence imaging as modality to evaluate the efficacy of antibacterial treatment.

The CFU determination in the *S. aureus* LAC thigh infection model of this chapter showed, with the exception of the oxacillin group, the same efficacy pattern of the applied antibiotics than the *S. aureus* Xen29 thigh infection model. Minocycline treatment reduced the bacterial burden strongest, followed by linezolid and vancomycin had the weakest effect. Oxacillin showed no significant reduction of CFU values compared to the 0.9 % NaCl group. This had to be expected since *S. aureus* LAC is resistant to this  $\beta$ -lactam antibiotic. Overall, the reduction of bacterial burden was slightly stronger than the reduction in the *S. aureus* Xen29 infection model, but the overall pattern similar (with the exception of oxacillin due to resistance).

*S. aureus* LAC does not harbor a luciferase gene and thus does not emit luminescent signal, it was possible to apply Luminol based myeloperoxidase imaging, a recently developed in vivo method (Gross S et al. 2009, Tseng JC and Kung AL. 2013). Luminol solution was therefore administered intra-peritoneally at days 1, 3 and 5 p.i.. Neutrophil derived myeloperoxidase cleaves luminol in vivo and this leads to photon emission in the blue light spectrum. This luminescent signal can be detected by an optical in vivo imaging system. Administration of luminol resulted at all three time points to detectable luminescence signal for all groups. Interestingly, the strongest photon emission could be measured for the minocycline group at all three days, even though therapy with this antibiotic led to strongest CFU reduction in this model. The other groups, including the 0.9 % NaCl group showed variations in their signals, but remained at similar levels. This was very surprising, because the activity of myeloperoxidase was thought to be connected to the number of neutrophils. But since abscesses were much smaller in the minocycline group than, for example, in the 0.9 % NaCl group, one would assume that there are higher numbers of neutrophils at the site of infection in the 0.9 % NaCl group and thus higher luminol derived luminescence signal. In this context, it seems more reasonable that luminol imaging signal is not a benchmark for number of neutrophils, but for the activity or myeloperoxidase expression and release of the neutrophils. In consequence, these results suggest modulation of neutrophil activity at the



site of infection by minocycline, but further experiments are necessary to confirm these results and to identify the possible mechanism of modulation.

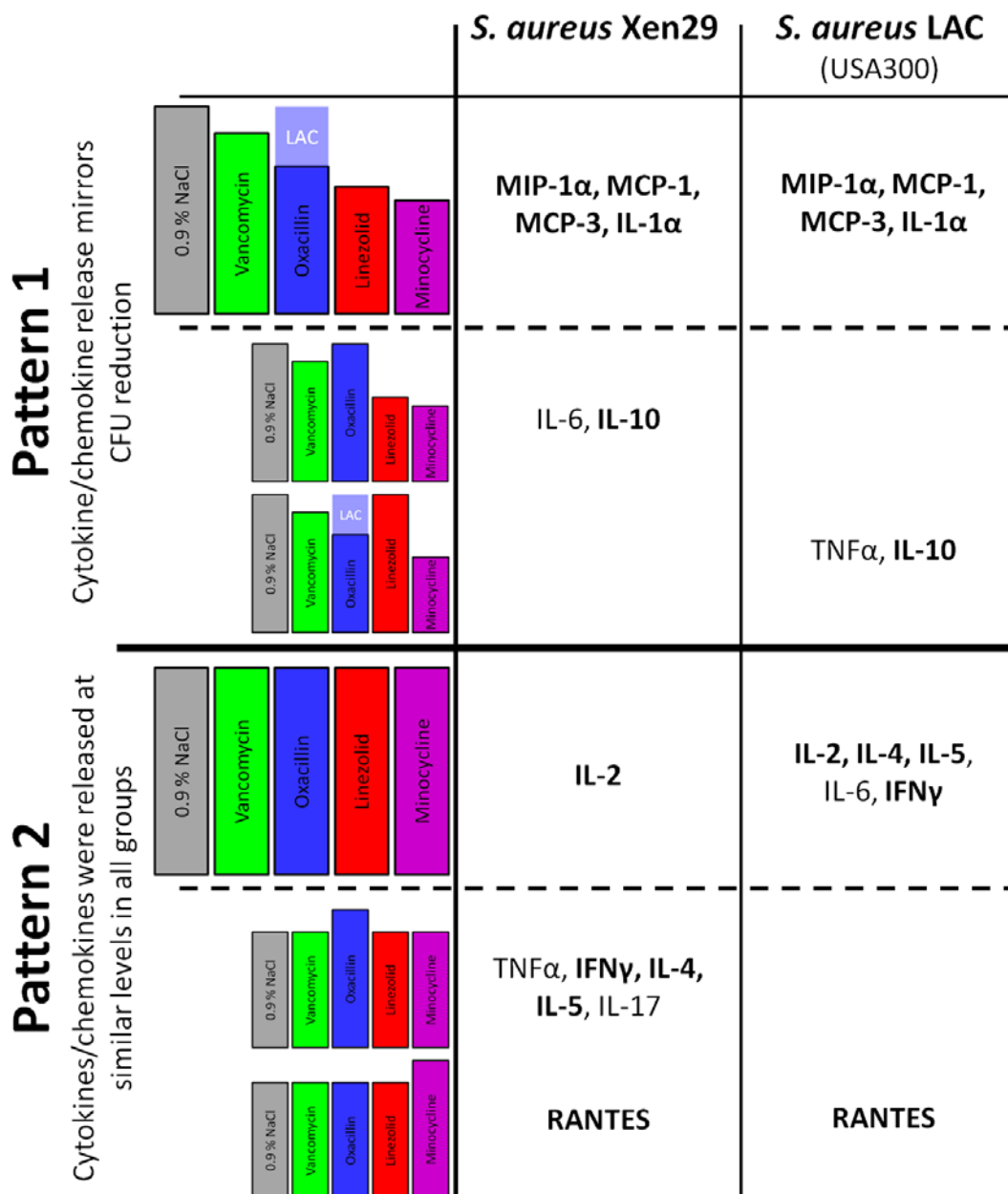
Since *S. aureus* Xen29 expresses a chromosome-located luciferase and thus emits photons in the blue light spectrum (overlapping signal with luminol luminescence) by itself, luminol imaging of myeloperoxidase activity was not possible with this strain.

The main focus to determine possible immunomodulatory effects was the release of cytokines and chemokines at the site of infection since these molecules are central elements in regulation of immune cell attraction, migration and activity. On this account the antibody-conjugated bead assays were selected to measure the concentrations of various highly relevant cytokines/chemokines in the infected thigh muscle. In this context, the chemokine bead assays covered: MCP-1, MCP-3, MIP-1 $\alpha$ , MIP-1 $\beta$  and RANTES, while the cytokine bead assay included beads to measure IL-1 $\alpha$ , IL-2, IL-4, IL-5, IL-6, IL-10, IL-17, TNF $\alpha$ , IFN $\gamma$  and GM-CSF levels. In order to measure the concentration at the site of infection, the thigh muscles were recovered, homogenized and filtered to exclude cells. In general, high amounts of IL-1 $\alpha$ , IL-6, MCP-1, MCP-3, MIP-1 $\alpha$  and RANTES could be detected in the infected thigh muscle, independently of the applied pathogen. GM-CSF and MIP-1 $\beta$ , in contrast, were found only at very low to almost negligible amounts.

Interestingly, two general patterns of chemokine/cytokine release dependent on the antibiotic therapy were found at the site of infection with both *S. aureus* strains (illustrated in Tab. 7.2). The first group of chemokines/cytokines mirrored the efficacy pattern of antibiotics. In more detail, the highest amount of release was detected for the 0.9 % NaCl group and the lowest values for the minocycline group in both murine models, as both groups had either the highest or lowest CFU counts at day 5 p.i. Members of this group in models with both pathogens were the cytokine IL-1 $\alpha$  as well as the chemokines MCP-1, MCP-3 and MIP-1 $\alpha$ . All of them were released in the pattern of CFU reduction by antibiotics therapy, independently of possible immunomodulatory effects.

Two variations of this pattern were found in the murine models. First, in the *S. aureus* Xen29 model, higher titers of cytokines IL-6 and IL-10 were found for the oxacillin group in the thigh muscle homogenizations than expected from CFU determination. In more detail, although oxacillin reduced CFU burden efficiently, the titers of these two cytokines were similarly high than those of the 0.9 % NaCl group. The second variation of this first general pattern was seen in the *S. aureus* LAC infection model. The linezolid group exhibited similar values of TNF $\alpha$  and IL-10 than 0.9 % NaCl and oxacillin groups, although CFU counts were lower.

**Tab. 7.2: Different patterns of cytokine or chemokine levels at the site of infection at day 5 p.i..** Mice were infected either with *S. aureus* Xen29 (center column) or LAC (right column) and received antibiotic or mock therapy during course of infection. Muscles were recovered at day 5 p.i., homogenized and the titers of various cytokines/chemokines in the homogenization measured with flow cytometry based bead assays (FlowCytomix, eBioscience). The two general patterns of release in response to antibacterial therapy and the variations of these general patterns are indicated by the multicolored bar charts.



The second general pattern of chemokine/cytokine titers showed similar values for all treatment groups, independent of the applied antibiotic. IL-2 exhibited this behavior in models of both pathogens, while the titers of IL-4, IL-5, IL-6 and IFN $\gamma$  resembled a similar level between all treatment groups in the *S. aureus* LAC infection model, too. Variations of this general pattern were the elevation of distinct cytokine/chemokine titers in either the oxacillin or the minocycline group. Interestingly, minocycline treatment led in the experiments with both pathogens to increased values of RANTES compared to the other groups, suggesting a general phenomenon. Oxacillin treatment led in the *S. aureus* Xen29 experiment to higher values of TNF $\alpha$ , IFN $\gamma$ , IL-4, IL-5 and IL-17 than all other groups.

In consequence, antibiotic treatment, especially with oxacillin, but also with minocycline or linezolid led to variations in the levels of various cytokines and chemokines in the infected thigh muscle that did not correspond to the reduction of bacterial burden. The hypothesis, the lower the bacterial burden, the lower the level of cytokines and chemokines, especially pro-inflammatory ones like TNF $\alpha$  or IL-1, did not fit for all of the antibacterial treatments. It might be interesting to study these differences in more detail. It might be especially interesting to investigate whether this deregulation of cytokine/chemokine release causes beneficial or harmful effects in the case of resistant bacteria. This might, in consequence, led to approaches to regulate the immune response during infection in order to achieve an increased clearing of the pathogens, more efficient immune response or even accelerated wound healing and faster recovery from disease. In conclusion, the cytokine and chemokine results indicate that oxacillin treatment induced at least slightly a pro-inflammatory environment. This might lead to elevated migration and/or increased level of neutrophil activation, which in consequence causes stronger accumulation of perfluorocarbon emulsion at the site of infection. Nonetheless, to date, no experiments were performed to elucidate the number of neutrophils at the site of infection, therefore this hypothesis has to be evaluated in a further set of experiments in future.

Nonetheless, possible immunomodulatory effects of antibacterial compounds should be taken into account for future imaging studies with this platform. On the other hand, this observation offers completely new applications for  $^{19}\text{F}$  MRI with perfluorocarbons. Since several new approaches to fight *S. aureus* infections are based on the immune system, for example passive or active immunization or immunomodulatory peptides (Mookherjee N et al. 2007, Ohlsen K and Lorenz U. 2010), it might be interesting and maybe even necessary to study the effects in vivo.  $^{19}\text{F}$  MRI with perfluorocarbons might be an interesting choice to study the migration of neutrophils or, with the help of targeted perfluorocarbon emulsions, other immune cell populations. Furthermore, combining this imaging modality with a second imaging modality which enables the visualization of the bacterial burden in vivo, like bioluminescence imaging, might offer completely new insights into host-pathogen interaction.

## 8. Conclusion and Outlook

This study comprised two different goals and questions: first, is in vivo imaging in general and magnetic resonance imaging in particular useful, maybe even beneficial in preclinical evaluation of promising new compounds to fight *S. aureus* infections? And second, how efficient is lysostaphin, a new, promising antibiotic drug candidate, as treatment option against *S. aureus* in clinically relevant murine models?

The experiments of chapter 4 aimed at the first question, a rather new field of scientific investigation. Since bioluminescence imaging of infections in preclinical disease models was in principle investigated by several former studies (Contag CH et al. 1995, Francis KP et al. 2000, Kadurugamuwa JL et al. 2003b, Kuklin NA et al. 2003), the main goal of this thesis was the evaluation of magnetic resonance imaging as preclinical infection imaging modality. Thus, based on the few MR imaging experiments performed so far to visualize sites of *S. aureus* infection in preclinical models (Marzola P et al. 1999, Kaim AH et al. 2002, Kaim AH et al. 2003), different MR methods, native and contrast agent/tracer based, were applied in this thesis and evaluated for their infection imaging capability. In the end,  $^{19}\text{F}$  MRI with perfluorocarbons delivered the best, unobstructed view upon the extend and severity of infection. Most of the experiments in this chapter were consequently conducted to determine the accumulation mechanism and kinetics in more detail. The perfluorocarbon emulsion accumulation was dependent on the number of bacteria in the infected thigh muscle and delivered detectable  $^{19}\text{F}$  signal at earliest when administered at day 1 or 2 p.i., but signal then remained rather stable until the end of the experiment. Interestingly, perfluorocarbon emulsion accumulated in all experiments at the rim of the abscess area, in the shape of a 'hollow sphere'. Taken together, this suggested that accumulation is connected to a robust immune response. Flow cytometry, cell sorting and histology experiments were performed in order to elucidate this hypothesis. They showed that most of the perfluorocarbon derived fluorescence could be detected in neutrophils, smaller amounts were found in monocytes, macrophages and dendritic cells, too. Most of the perfluorocarbon emulsion could be considered as cell associated, proving immune cell dependent accumulation and contradicting unspecific cell-independent accumulation. In conclusion,  $^{19}\text{F}$  MRI of perfluorocarbon emulsion accumulation visualizes the accumulation of immune cells, more specific of neutrophils, at the site of infection. This offers, in consequence, a completely new perspective for this imaging modality. It might be interesting to study differences in the immune response by this modality. For example, since *S. aureus* harbors an extensive amount of factors that interfere with the immune system, it might be extraordinarily interesting to study the effects of depletion or overexpression of these factors upon the migration of neutrophils in vivo in the mouse model. Furthermore, a new, experimental approach to combat infections is the application of compounds that modulate the immune response in order to enable a more efficient clearing or inactivation of pathogens.  $^{19}\text{F}$  MRI with perfluorocarbon emulsion might offer a powerful tool to investigate the influence of these compounds upon immune cell activation and migration. In

consequence, this imaging modality might give completely new insights into host-pathogen interaction and the influence of antibacterial therapy upon the host.

Nonetheless, the aim of this thesis was to integrate MR imaging into a preclinical small-animal antibiotic evaluation platform. Therefore, chapter 5 focused on the application of  $^{19}\text{F}$  MRI with perfluorocarbon emulsion during treatment with clinically relevant antibiotics against *S. aureus*: vancomycin and linezolid. Both antibiotics showed reduction of colony-forming units and bioluminescence signal, the second imaging modality which was integrated into the preclinical testing platform to visualize the photon emission of a luciferase integrated into the genome of *S. aureus*. In consequence, both methods indicated efficient antibacterial activity of both compounds, with linezolid being more efficient.  $^{19}\text{F}$  MRI visualized differences in perfluorocarbon accumulation at the site of infection. Treatment with either vancomycin or linezolid led to smaller abscess areas, indicated by the 'hollow sphere' accumulation pattern of the tracer.  $^{19}\text{F}$  signal strength and volume were reduced for both treatment groups compared to the mock-treated control group, with linezolid showing stronger reduction. In conclusion,  $^{19}\text{F}$  MRI with perfluorocarbon emulsion indicated efficacy of vancomycin or linezolid in the murine *S. aureus* thigh infection model with similar results than colony forming unit determination or bioluminescence imaging.

In chapter 6, a promising compound against *S. aureus* infection was tested in the preclinical antibiotic evaluation platform established in chapters 4 and 5: lysostaphin. This endopeptidase cleaves specifically the cell wall of *S. aureus* and is currently in preclinical testing for application in human disease. Two different clinically highly relevant murine models of *S. aureus*, the catheter-associated and the thigh infection model, were applied to evaluate the efficacy of lysostaphin in two concentrations and in combination with oxacillin. Lysostaphin showed in both models, dependent on concentration, efficient reduction of bacterial burden in terms of colony-forming units and bioluminescence signal. The combination of lower dose lysostaphin with oxacillin showed similar efficacy than higher dose lysostaphin, being in many parameters superior to vancomycin or oxacillin only.  $^{19}\text{F}$  MR imaging showed in the thigh infection model clear reduction of both perfluorocarbon emulsion accumulation strength and volume, indicating smaller sites of infection and less pronounced immune cell immigration than in vancomycin or control groups. Surprisingly, the perfluorocarbon emulsion accumulation in oxacillin and oxacillin/lysostaphin treated groups was stronger than expected from colony forming unit and bioluminescence signal determination. This might indicate a pro-inflammatory modulation of immune response by oxacillin, which led to a stronger migration of neutrophils to the site of infection, although the bacterial burden was reduced efficiently.

In order to investigate this possible immunomodulatory effect of antibiotic therapy in vivo, the levels of various cytokines and chemokines at the site of infection were measured in chapter 7 in order to evaluate differences between different antibiotic treatments. To evaluate whether oxacillin shows its potential immunomodulatory effect either indirectly via its action against the bacteria or directly by influencing the immune cells, two different

strains of *S. aureus* were applied in the thigh infection model: the oxacillin-sensitive strain Xen29 and the oxacillin-resistant strain LAC (USA300). Two principal patterns of cytokine and chemokine release could be seen. The first one showed release dependent on the efficacy of reduction of bacterial burden at the site of infection. In more detail, the fewer bacteria survived the antibiotic treatment, the less cytokines / chemokines could be found. Prominent members of this group were the chemokines MIP-1 $\alpha$ , MCP-1 and the cytokine IL-1 $\alpha$ . The second pattern showed similar levels of cytokines / chemokines at the site of infection independent of the efficacy of the applied antibiotic. This could be seen for the cytokine IL-2. Interestingly, some chemokines / cytokines seemed to be differently released or regulated in oxacillin, linezolid or minocycline treated mice. RANTES was found in minocycline treated mice in higher levels, than in all other groups, who showed a rather uniform level. IFN $\gamma$ , IL-4 and IL-5 showed similar levels for all groups with the exception of oxacillin treatment which exhibited in the Xen29 background higher values. Linezolid and oxacillin, finally, showed elevated levels of IL-10 dependent on the sensitivity of the *S. aureus* strain. In summary, antibiotic treatment led to differential levels of cytokines and chemokines at the site of infection. These differences were not always linked to a reduction of bacterial burden, but indicated in some cases direct or indirect immunomodulation. Nonetheless, these experiments are only the first steps in the investigation of possible immunomodulatory effects of antibiotics in vivo. The effects upon cellular immune response as well as on the immune system's memory were not even addressed by these experiments. But in conclusion,  $^{19}\text{F}$  MRI with perfluorocarbons might be a very interesting method to study the influence of therapy upon immune cell behavior in vivo in more detail. It might visualize differences in neutrophil migration behavior and activation during course of infection and should be applied in further studies dealing with this subject.

In conclusion,  $^{19}\text{F}$  MRI with perfluorocarbon has proven its value as a platform to image both, the course of infection and the efficacy of new promising antibacterial compounds non-invasively. It has furthermore been demonstrated, that this imaging modality is prone to modulation of the immune response. Although this has to be taken into account during antibiotic evaluation, it offers on the other hand a wide field of new applications. The effects of immunomodulatory compounds might be visualized in vivo and non-invasively in various disease models by this method. It might be used to study the effects of active or passive immunization approaches against *S. aureus* or other pathogens, but it might moreover be applied to study immunomodulators or immunization strategies against cancer or disorders of the immune system, too. In this study, only untargeted perfluorocarbon emulsions were applied as tracer, but the establishment of a protocol to emulsify fluorescently-labeled liposomes offers the opportunity to construct surface-functionalized targeted emulsions. These particles might aim at either bacteria in order to visualize bacterial burden directly or at specific immune cell populations to determine their importance, migration behavior or activity during course of infection. Most importantly, the  $^{19}\text{F}$  MR sequence applied in this study, chemical shift imaging, offers the distinction of different perfluorocarbons in the core of the emulsions. Thus, it is possible to target various cell populations, bacteria and immune

cells, during course of infection with different targeted perfluorocarbon emulsions and visualize and distinguish their accumulation at the same time in the same animal. Furthermore, it is possible to study differences in the migration behavior at different phases of infection in the same animal by the administration of emulsions with different core perfluorocarbons at different time points. These ‘multi – color’ options are superior to, for example, gadolinium or iron oxide based MRI, positron emission tomography or classical bioluminescence imaging, since it offers the simultaneous acquisition of more than one parameter. Moreover,  $^{19}\text{F}$  MRI with perfluorocarbon does not interfere with anatomical  $^1\text{H}$  MRI and thus offers unbeatable 3D tissue contrast, which is one of the most important advantages of MRI.

In summary,  $^{19}\text{F}$  MRI with perfluorocarbons proved to visualize sites of *S. aureus* infection by accumulation in neutrophils and other phagocytic immune cells. It furthermore proved to be useful in evaluating the efficacy of antibiotic compounds and drug candidates in preclinical *S. aureus* infection. Nevertheless, perfluorocarbon emulsion imaging with  $^{19}\text{F}$  MRI might offer further interesting applications, for example, in the evaluation of immunomodulators or immunization approaches, but also in revealing deeper insights of host – pathogen interaction by targeting and tracking pathogens or immune cells in vivo.

## 9. Literature

**Ahrens ET, Flores R, Xu H, Morel PA.** 2005. In vivo imaging platform for tracking immunotherapeutic cells. *Nat Biotechnol.* 23(8):983-7. Epub 2005 Jul 24.

**Albus A, Arbeit RD, Lee JC.** 1991. Virulence of *Staphylococcus aureus* mutants altered in type 5 capsule production. *Infect Immun.* 59(3):1008-14.

**Amagai M, Matsuyoshi N, Wang ZH, Andl C, Stanley JR.** 2000. Toxin in bullous impetigo and staphylococcal scalded-skin syndrome targets desmoglein 1. *Nat Med.* 6(11):1275-7.

**Anderson DC, Miller LJ, Schmalstieg FC, Rothlein R, Springer TA.** 1986. Contributions of the Mac-1 glycoprotein family to adherence-dependent granulocyte functions: structure-function assessments employing subunit-specific monoclonal antibodies. *J Immunol.* 137(1):15-27.

**Appelbaum PC.** 2006. The emergence of vancomycin-intermediate and vancomycin-resistant *Staphylococcus aureus*. *Clin Microbiol Infect.* 12 Suppl 1:16-23.

**Archer NK, Mazaitis MJ, Costerton JW, Leid JG, Powers ME, Shirtliff ME.** 2011. *Staphylococcus aureus* biofilms: properties, regulation, and roles in human disease. *Virulence.* (5):445-59. doi: 10.4161/viru.2.5.17724. Epub 2011 Sep 1.

**Attia AS, Schroeder KA, Seeley EH, Wilson KJ, Hammer ND, Colvin DC, Manier ML, Nicklay JJ, Rose KL, Gore JC, Caprioli RM, Skaar EP.** 2012. Monitoring the inflammatory response to infection through the integration of MALDI IMS and MRI. *Cell Host Microbe.* 11(6):664-73. doi: 10.1016/j.chom.2012.04.018.

**Baddour LM, Lowrance C, Albus A, Lowrance JH, Anderson SK, Lee JC.** 1992. *Staphylococcus aureus* microcapsule expression attenuates bacterial virulence in a rat model of experimental endocarditis. *J Infect Dis.* 165(4):749-53.

**Balducci A, Helfer BM, Ahrens ET, O'Hanlon CF 3rd, Wesa AK.** 2012. Visualizing arthritic inflammation and therapeutic response by fluorine-19 magnetic resonance imaging (19F MRI). *J Inflamm (Lond).* 9(1):24. doi: 10.1186/1476-9255-9-24.

**Beckmann N, Kneuer R, Gremlich HU, Karmouty-Quintana H, Blé FX, Müller M.** 2007. In vivo mouse imaging and spectroscopy in drug discovery. *NMR Biomed.* 20(3):154-85.

**Beltran J.** 1995. MR imaging of soft-tissue infection. *Magn Reson Imaging Clin N Am.* (4):743-51.

**Boucher HW, Corey GR.** 2008. Epidemiology of methicillin-resistant *Staphylococcus aureus*. *Clin Infect Dis.* 46 Suppl 5:S344-9. doi: 10.1086/533590.



- Boucher HW, Talbot GH, Bradley JS, Edwards JE, Gilbert D, Rice LB, Scheld M, Spellberg B, Bartlett J.** 2009. Bad bugs, no drugs: no ESKAPE! An update from the Infectious Diseases Society of America. *Clin Infect Dis.* 48(1):1-12. doi: 10.1086/595011.
- Bröker BM, Holtfreter S, Bekeredjian-Ding I.** 2013. Immune control of *Staphylococcus aureus* - Regulation and counter-regulation of the adaptive immune response. *Int J Med Microbiol.* pii: S1438-4221(13)00181-1. doi: 10.1016/j.ijmm.2013.11.008. [Epub ahead of print]
- Buttke TM, Mallett GS, Cuchens MA.** 1983. Positive selection of mouse B and T lymphocytes and analysis of isolated populations by flow cytometry. *J Immunol Methods.* 58(1-2):193-207.
- Caspari R, Lee SH.** 2004. Older age becomes common late in human evolution. *Proc Natl Acad Sci U S A.* 101(30):10895-900. Epub 2004 Jul 13.
- Caspari R, Lee SH.** 2006. Is human longevity a consequence of cultural change or modern biology? *Am J Phys Anthropol.* 129(4):512-7.
- Chambers HF.** 2001. The changing epidemiology of *Staphylococcus aureus*? *Emerg Infect Dis.* 7(2):178-82.
- Chambers HF, Deleo FR.** 2009. Waves of resistance: *Staphylococcus aureus* in the antibiotic era. *Nat Rev Microbiol.* 7(9):629-41. doi: 10.1038/nrmicro2200.
- Chavakis T, Hussain M, Kanse SM, Peters G, Bretzel RG, Flock JI, Herrmann M, Preissner KT.** 2002. *Staphylococcus aureus* extracellular adherence protein serves as anti-inflammatory factor by inhibiting the recruitment of host leukocytes. *Nat Med.* 8(7):687-93. Epub 2002 Jun 24.
- Cheng AG, Kim HK, Burts ML, Krausz T, Schneewind O, Missiakas DM.** 2009. Genetic requirements for *Staphylococcus aureus* abscess formation and persistence in host tissues. *FASEB J.* 23(10):3393-404. doi: 10.1096/fj.09-135467. Epub 2009 Jun 12.
- Cho JS, Guo Y, Ramos RI, Hebroni F, Plaisier SB, Xuan C, Granick JL, Matsushima H, Takashima A, Iwakura Y, Cheung AL, Cheng G, Lee DJ, Simon SI, Miller LS.** 2012. Neutrophil-derived IL-1 $\beta$  is sufficient for abscess formation in immunity against *Staphylococcus aureus* in mice. *PLoS Pathog.* 8(11):e1003047. doi: 10.1371/journal.ppat.1003047. Epub 2012 Nov 29.
- Christian MD.** 2013. Biowarfare and bioterrorism. *Crit Care Clin.* 29(3):717-56. doi: 10.1016/j.ccc.2013.03.015.
- Centers for Disease Control and Prevention (CDC).** 1999. Ten great public health achievements--United States, 1900-1999. *MMWR Morb Mortal Wkly Rep.* 48(12):241-3.

**Climo MW, Patron RL, Goldstein BP, Archer GL.** 1998. Lysostaphin treatment of experimental methicillin-resistant *Staphylococcus aureus* aortic valve endocarditis. *Antimicrob Agents Chemother.* 42:1355-1360.

**Climo MW, Ehlert K, Archer GL.** 2001. Mechanism and suppression of lysostaphin resistance in oxacillin-resistant *Staphylococcus aureus*. *Antimicrob Agents Chemother.* 45:1431-1437.

**CLSI.** 2012. Methods for dilution antimicrobial susceptibility tests for bacteria that grow aerobically; approved standard, 9th ed. CLSI document M07-A9. CLSI, Wayne, PA.

**Coffman RL, Weissman IL.** 1981. B220: a B cell-specific member of the T200 glycoprotein family. *Nature.* 289(5799):681-3.

**Contag CH, Contag PR, Mullins JI, Spilman SD, Stevenson DK, Benaron DA.** 1995. Photonic detection of bacterial pathogens in living hosts. *Mol Microbiol.* 18(4):593-603.

**Cramton SE, Ulrich M, Götz F, Döring G.** 2001. Anaerobic conditions induce expression of polysaccharide intercellular adhesin in *Staphylococcus aureus* and *Staphylococcus epidermidis*. *Infect Immun.* 69(6):4079-85.

**Cunnion KM, Lee JC, Frank MM.** 2001. Capsule production and growth phase influence binding of complement to *Staphylococcus aureus*. *Infect Immun.* 69(11):6796-803.

**Daley JM, Thomay AA, Connolly MD, Reichner JS, Albina JE.** 2008. Use of Ly6G-specific monoclonal antibody to deplete neutrophils in mice. *J Leukoc Biol.* 83(1):64-70. Epub 2007 Sep 20.

**Daley MJ, Oldham ER.** 1992. Lysostaphin: immunogenicity of locally administered recombinant protein used in mastitis therapy. *Vet Immunol Immunopathol.* 31:301-312.

**Dantes R, Mu Y, Belflower R, Aragon D, Dumyati G, Harrison LH, Lessa FC, Lynfield R, Nadle J, Petit S, Ray SM, Schaffner W, Townes J, Fridkin S; Emerging Infections Program–Active Bacterial Core Surveillance MRSA Surveillance Investigators.** 2013. National burden of invasive methicillin-resistant *Staphylococcus aureus* infections, United States, 2011. *JAMA Intern Med.* 173(21):1970-8. doi: 10.1001/jamainternmed.2013.10423.

**de Haas CJ, Veldkamp KE, Peschel A, Weerkamp F, Van Wamel WJ, Heezius EC, Poppelier MJ, Van Kessel KP, van Strijp JA.** 2004. Chemotaxis inhibitory protein of *Staphylococcus aureus*, a bacterial antiinflammatory agent. *J Exp Med.* 199(5):687-95.

**Deivanayagam CC, Wann ER, Chen W, Carson M, Rajashankar KR, Höök M, Narayana SV.** 2002. A novel variant of the immunoglobulin fold in surface adhesins of *Staphylococcus aureus*: crystal structure of the fibrinogen-binding MSCRAMM, clumping factor A. *EMBO J.* 21(24):6660-72.

**Dhawan VK.** 2002. Infective endocarditis in elderly patients. *Clin Infect Dis.* 34(6):806-12. Epub 2002 Jan 31.

**Dimasi JA.** 2001. Risks in new drug development: approval success rates for investigational drugs. *Clin Pharmacol Ther.* 69(5):297-307.

**DiMasi JA, Feldman L, Seckler A, Wilson A.** 2010. Trends in risks associated with new drug development: success rates for investigational drugs. *Clin Pharmacol Ther.* 87(3):272-7. doi: 10.1038/clpt.2009.295. Epub 2010 Feb 3.

**Ebner B, Behm P, Jacoby C, Burghoff S, French BA, Schrader J, Flögel U.** 2010. Early assessment of pulmonary inflammation by <sup>19</sup>F MRI in vivo. *Circ Cardiovasc Imaging.* 3(2):202-10. Epub 2010 Jan 8.

**Editorial [No authors listed]** 2013. Animal research: a balancing act. *Nat Med.* 19(10):1191. doi: 10.1038/nm.3382.

**Ellen Frankel, P and Jeffrey, P.** 2001. *Why Animal Experimentation Matters: the Use of Animals in Medical Research* (Transactions Publishers, 2001)

**Emori TG, Banerjee SN, Culver DH, Gaynes RP, Horan TC, Edwards JR, Jarvis WR, Tolson JS, Henderson TS, Martone WJ, et al.** 1991. Nosocomial infections in elderly patients in the United States, 1986-1990. National Nosocomial Infections Surveillance System. *Am J Med.* 91(3B):289S-293S.

**Engelsman AF, van der Mei HC, Francis KP, Busscher HJ, Ploeg RJ, van Dam GM.** 2009. Real time noninvasive monitoring of contaminating bacteria in a soft tissue implant infection model. *J Biomed Mater Res B Appl Biomater.* 88(1):123-9. doi: 10.1002/jbm.b.31158.

**Fauci AS.** 2005. Emerging and reemerging infectious diseases: the perpetual challenge. *Acad Med.* 80(12):1079-85.

**Fein AM.** 1999. Pneumonia in the elderly: overview of diagnostic and therapeutic approaches. *Clin Infect Dis.* 28(4):726-9.

**Fernandez Falcon MF, Echague CG, Hair PS, Nyalwidhe JO, Cunnion KM.** 2011. Protease inhibitors decrease IgG shedding from *Staphylococcus aureus*, increasing complement activation and phagocytosis efficiency. *J Med Microbiol.* 60(Pt 10):1415-22. doi: 10.1099/jmm.0.027557-0. Epub 2011 Jun 2.

**Fischer MA, Davies ML, Reider IE, Heipertz EL, Epler MR, Sei JJ, Ingersoll MA, Rooijen NV, Randolph GJ, Norbury CC.** 2011. CD11b<sup>+</sup>, Ly6G<sup>+</sup> cells produce type I interferon and exhibit tissue protective properties following peripheral virus infection. *PLoS Pathog.* 7(11):e1002374. doi: 10.1371/journal.ppat.1002374. Epub 2011 Nov 10.

**Fitzgerald-Hughes D, Devocelle M, Humphreys H.** 2012. Beyond conventional antibiotics for the future treatment of methicillin-resistant *Staphylococcus aureus* infections: two novel alternatives. *FEMS Immunol Med Microbiol.* 65(3):399-412. doi: 10.1111/j.1574-695X.2012.00954.x. Epub 2012 Apr 4.

- Fleming TJ, Fleming ML, Malek TR.** 1993. Selective expression of Ly-6G on myeloid lineage cells in mouse bone marrow. RB6-8C5 mAb to granulocyte-differentiation antigen (Gr-1) detects members of the Ly-6 family. *J Immunol.* 151(5):2399-408.
- Flögel U, Ding Z, Hardung H, Jander S, Reichmann G, Jacoby C, Schubert R, Schrader J.** 2008. In vivo monitoring of inflammation after cardiac and cerebral ischemia by fluorine magnetic resonance imaging. *Circulation.* 118(2):140-8. Epub 2008 Jun 23.
- Foster TJ.** 2005. Immune evasion by staphylococci. *Nat Rev Microbiol.* 3(12):948-58.
- Foster TJ.** 2009. Colonization and infection of the human host by staphylococci: adhesion, survival and immune evasion. *Vet Dermatol.* 20(5-6):456-70. doi: 10.1111/j.1365-3164.2009.00825.x.
- Foster TJ, Geoghegan JA, Ganesh VK, Höök M.** 2014. Adhesion, invasion and evasion: the many functions of the surface proteins of *Staphylococcus aureus*. *Nat Rev Microbiol.* 12(1):49-62. doi: 10.1038/nrmicro3161.
- Foucault ML, Courvalin P, Grillot-Courvalin C.** 2009. Fitness cost of VanA-type vancomycin resistance in methicillin-resistant *Staphylococcus aureus*. *Antimicrob Agents Chemother.* 53(6):2354-9. doi: 10.1128/AAC.01702-08. Epub 2009 Mar 30.
- Fowler JS, Volkow ND, Wang GJ, Ding YS, Dewey SL.** 1999. PET and drug research and development. *J Nucl Med.* 40(7):1154-63.
- Francis KP, Joh D, Bellinger-Kawahara C, Hawkinson MJ, Purchio TF, Contag PR.** 2000. Monitoring bioluminescent *Staphylococcus aureus* infections in living mice using a novel luxABCDE construct. *Infect Immun.* 68(6):3594-600.
- Fraser JD, Proft T.** 2008. The bacterial superantigen and superantigen-like proteins. *Immunol Rev.* 225:226-43. doi: 10.1111/j.1600-065X.2008.00681.x.
- Fraunholz M, Sinha B.** 2012. Intracellular *Staphylococcus aureus*: live-in and let die. *Front Cell Infect Microbiol.* 2:43. doi: 10.3389/fcimb.2012.00043. eCollection 2012.
- Funao H, Ishii K, Nagai S, Sasaki A, Hoshikawa T, Aizawa M, Okada Y, Chiba K, Koyasu S, Toyama Y, Matsumoto M.** 2012. Establishment of a real-time, quantitative, and reproducible mouse model of *Staphylococcus* osteomyelitis using bioluminescence imaging. *Infect Immun.* 80(2):733-41. doi: 10.1128/IAI.06166-11. Epub 2011 Nov 21.
- Gagliotti C, Balode A, Baquero F, Degener J, Grundmann H, Gür D, Jarlier V, Kahlmeter G, Monen J, Monnet DL, Rossolini GM, Suetens C, Weist K, Heuer O; EARS-Net Participants (Disease Specific Contact Points for AMR).** 2011. *Escherichia coli* and *Staphylococcus aureus*: bad news and good news from the European Antimicrobial Resistance Surveillance Network (EARS-Net, formerly EARSS), 2002 to 2009. *Euro Surveill.* 2011 Mar 17;16(11). pii: 19819.

- Ganesh VK, Rivera JJ, Smeds E, Ko YP, Bowden MG, Wann ER, Gurusiddappa S, Fitzgerald JR, Höök M.** 2008. A structural model of the *Staphylococcus aureus* ClfA-fibrinogen interaction opens new avenues for the design of anti-staphylococcal therapeutics. PLoS Pathog. 4(11):e1000226. doi: 10.1371/journal.ppat.1000226. Epub 2008 Nov 28.
- Gellissen J, Axmann Ch, Prescher A, Bohndorf K, Lodemann KP.** 1999. Extra- and intracellular accumulation of ultrasmall superparamagnetic iron oxides (USPIO) in experimentally induced abscesses of the peripheral soft tissues and their effects on magnetic resonance imaging. Magn Reson Imaging. 17(4):557-67.
- Gillet Y, Issartel B, Vanhems P, Fournet JC, Lina G, Bes M, Vandenesch F, Piémont Y, Brousse N, Floret D, Etienne J.** 2002. Association between *Staphylococcus aureus* strains carrying gene for Panton-Valentine leukocidin and highly lethal necrotising pneumonia in young immunocompetent patients. Lancet. 359(9308):753-9.
- Goldberg LM, DeFranco JM, Watanakunakorn C, Hamburger M.** 1967. Studies in experimental staphylococcal endocarditis in dogs. VI. Treatment with lysostaphin. Antimicrob Agents Chemother (Bethesda). 7:45-53.
- Gorwitz RJ, Kruszon-Moran D, McAllister SK, McQuillan G, McDougal LK, Fosheim GE, Jensen BJ, Killgore G, Tenover FC, Kuehnert MJ.** 2008. Changes in the prevalence of nasal colonization with *Staphylococcus aureus* in the United States, 2001-2004. J Infect Dis. 197(9):1226-34. doi: 10.1086/533494.
- Graille M, Stura EA, Corper AL, Sutton BJ, Taussig MJ, Charbonnier JB, Silverman GJ.** 2000. Crystal structure of a *Staphylococcus aureus* protein A domain complexed with the Fab fragment of a human IgM antibody: structural basis for recognition of B-cell receptors and superantigen activity. Proc Natl Acad Sci U S A. 97(10):5399-404.
- Graveland H, Duim B, van Duijkeren E, Heederik D, Wagenaar JA.** 2011. Livestock-associated methicillin-resistant *Staphylococcus aureus* in animals and humans. Int J Med Microbiol. (8):630-4. doi: 10.1016/j.ijmm.2011.09.004. Epub 2011 Oct 7.
- Greaves P, Williams A, Eve M.** 2004. First dose of potential new medicines to humans: how animals help. Nat Rev Drug Discov. 3(3):226-36.
- Gross S, Gammon ST, Moss BL, Rauch D, Harding J, Heinecke JW, Ratner L, Piwnica-Worms D.** 2009. Bioluminescence imaging of myeloperoxidase activity in vivo. Nat Med. 15(4):455-61. doi: 10.1038/nm.1886. Epub 2009 Mar 22.
- Grumann D, Nübel U, Bröker BM.** 2013. *Staphylococcus aureus* toxins - Their functions and genetics. Infect Genet Evol. pii: S1567-1348(13)00086-5. doi: 10.1016/j.meegid.2013.03.013. [Epub ahead of print]
- Gründling A, Missiakas DM, Schneewind O.** 2006. *Staphylococcus aureus* mutants with increased lysostaphin resistance. J Bacteriol. 188:6286-6297.

- Gruszka DT, Wojdyla JA, Bingham RJ, Turkenburg JP, Manfield IW, Steward A, Leech AP, Geoghegan JA, Foster TJ, Clarke J, Potts JR.** 2012. Staphylococcal biofilm-forming protein has a contiguous rod-like structure. *Proc Natl Acad Sci U S A.* 109(17):E1011-8. doi: 10.1073/pnas.1119456109. Epub 2012 Apr 9.
- Hagan CE.** 2013. New York Times article misleads on the value of mouse models. *Mo Med.* 110(3):206.
- Hammer ND, Skaar EP.** 2011. Molecular mechanisms of *Staphylococcus aureus* iron acquisition. *Annu Rev Microbiol.* 65:129-47. doi: 10.1146/annurev-micro-090110-102851.
- Harris RL, Nunnery AW, Riley HD Jr.** 1967. Effect of lysostaphin on staphylococcal carriage in infants and children. *Antimicrob Agents Chemother (Bethesda).* 7:110-112.
- HARRISON EF, CROPP CB.** 1965. COMPARATIVE IN VITRO ACTIVITIES OF LYSOSTAPHIN AND OTHER ANTISTAPHYLOCOCCAL ANTIBIOTICS ON CLINICAL ISOLATES OF *STAPHYLOCOCCUS AUREUS*. *Appl Microbiol.* 13:212-5.
- Harrison EF, Zygmunt WA.** 1967. Lysostaphin in experimental renal infections. *J Bacteriol.* 93:520-524.
- Hayden MK, Rezai K, Hayes RA, Lolans K, Quinn JP, Weinstein RA.** 2005. Development of Daptomycin resistance in vivo in methicillin-resistant *Staphylococcus aureus*. *J Clin Microbiol.* 43(10):5285-7.
- Heer C, Stuert K, Reinert RR, Mäder M, Nau R.** 2000. Release of teichoic and lipoteichoic acids from 30 different strains of *Streptococcus pneumoniae* during exposure to ceftriaxone, meropenem, quinupristin/dalfopristin, rifampicin and trovafloxacin. *Infection.* 28(1):13-20.
- Herbert S, Ziebandt AK, Ohlsen K, Schäfer T, Hecker M, Albrecht D, Novick R, Götz F.** 2010. Repair of global regulators in *Staphylococcus aureus* 8325 and comparative analysis with other clinical isolates. *Infect Immun.* 78(6):2877-89. doi: 10.1128/IAI.00088-10. Epub 2010 Mar 8.
- Hertlein T, Sturm V, Kircher S, Basse-Lüsebrink T, Haddad D, Ohlsen K, Jakob P.** 2011. Visualization of abscess formation in a murine thigh infection model of *Staphylococcus aureus* by <sup>19</sup>F-magnetic resonance imaging (MRI). *PLoS One.* 6(3):e18246. doi: 10.1371/journal.pone.0018246.
- Hertlein T, Sturm V, Jakob P, Ohlsen K.** 2013. <sup>19</sup>F magnetic resonance imaging of perfluorocarbons for the evaluation of response to antibiotic therapy in a *Staphylococcus aureus* infection model. *PLoS One.* 8(5):e64440. doi: 10.1371/journal.pone.0064440. Print 2013.

- Hertlein T, Sturm V, Lorenz U, Sumathy K, Jakob P, Ohlsen K.** 2014. Bioluminescence and <sup>19</sup>F magnetic resonance imaging visualize the efficacy of lysostaphin alone and in combination with oxacillin against *Staphylococcus aureus* in murine thigh and catheter-associated infection models. *Antimicrob Agents Chemother.* 58(3):1630-8. doi: 10.1128/AAC.01422-13. Epub 2013 Dec 23.
- Hiramatsu K.** 2001. Vancomycin-resistant *Staphylococcus aureus*: a new model of antibiotic resistance. *Lancet Infect Dis.* 1(3):147-55.
- Hirschwerk D, Ginocchio CC, Bythrow M, Condon S.** 2006. Diminished susceptibility to daptomycin accompanied by clinical failure in a patient with methicillin-resistant *Staphylococcus aureus* bacteremia. *Infect Control Hosp Epidemiol.* 27(3):315-7. Epub 2006 Feb 23.
- Holtfreter S, Radcliff FJ, Grumann D, Read H, Johnson S, Monecke S, Ritchie S, Clow F, Goerke C, Bröker BM, Fraser JD, Wiles S.** 2013. Characterization of a Mouse-Adapted *Staphylococcus aureus* Strain. *PLoS One.* 8(9):e71142. doi: 10.1371/journal.pone.0071142.
- Huber MM, Huber TW.** 1989. Susceptibility of methicillin-resistant *Staphylococcus aureus* to lysostaphin. *J Clin Microbiol.* 27(5):1122-4.
- Huizinga TW, Roos D, von dem Borne AE.** 1990. Neutrophil Fc-gamma receptors: a two-way bridge in the immune system. *Blood.* 75(6):1211-4.
- Jabes D.** 2011. The antibiotic R&D pipeline: an update. *Curr Opin Microbiol.* 14(5):564-9. doi: 10.1016/j.mib.2011.08.002. Epub 2011 Aug 26.
- Janjic JM, Srinivas M, Kadayakkara DK, Ahrens ET.** 2008. Self-delivering nanoemulsions for dual fluorine-19 MRI and fluorescence detection. *J Am Chem Soc.* 130(9):2832-41. doi: 10.1021/ja077388j. Epub 2008 Feb 12.
- Janjic JM, Ahrens ET.** 2009. Fluorine-containing nanoemulsions for MRI cell tracking. *Wiley Interdiscip Rev Nanomed Nanobiotechnol.* 1(5):492-501. doi: 10.1002/wnan.35.
- Jawhara S, Mordon S.** 2004. In vivo imaging of bioluminescent *Escherichia coli* in a cutaneous wound infection model for evaluation of an antibiotic therapy. *Antimicrob Agents Chemother.* 48(9):3436-41.
- Jiang W, Li B, Zheng X, Liu X, Cen Y, Li J, Pan X, Cao H, Zheng J, Zhou H.** 2011 Artesunate in combination with oxacillin protect sepsis model mice challenged with lethal live methicillin-resistant *Staphylococcus aureus* (MRSA) via its inhibition on proinflammatory cytokines release and enhancement on antibacterial activity of oxacillin. *Int Immunopharmacol.* 11(8):1065-73. doi: 10.1016/j.intimp.2011.02.028. Epub 2011 Mar 21.
- Jin T, Bokarewa M, Foster T, Mitchell J, Higgins J, Tarkowski A.** 2004. *Staphylococcus aureus* resists human defensins by production of staphylokinase, a novel bacterial evasion mechanism. *J Immunol.* 172(2):1169-76.

**Johnson AP.** 2011. Methicillin-resistant *Staphylococcus aureus*: the European landscape. J Antimicrob Chemother. 66 Suppl 4:iv43-iv48. doi: 10.1093/jac/dkr076.

**Kadurugamuwa JL, Sin LV, Yu J, Francis KP, Kimura R, Purchio T, Contag PR.** 2003a. Rapid direct method for monitoring antibiotics in a mouse model of bacterial biofilm infection. Antimicrob Agents Chemother. 47(10):3130-7.

**Kadurugamuwa JL, Sin L, Albert E, Yu J, Francis K, DeBoer M, Rubin M, Bellinger-Kawahara C, Parr Jr TR Jr, Contag PR.** 2003b. Direct continuous method for monitoring biofilm infection in a mouse model. Infect Immun. 71(2):882-90.

**Kaim AH, Wischer T, O'Reilly T, Jundt G, Fröhlich J, von Schulthess GK, Allegrini PR.** 2002. MR imaging with ultrasmall superparamagnetic iron oxide particles in experimental soft-tissue infections in rats. Radiology. 225(3):808-14.

**Kaim AH, Jundt G, Wischer T, O'Reilly T, Fröhlich J et al.** 2003. Functional-morphologic MR imaging with ultrasmall superparamagnetic particles of iron oxide in acute and chronic soft-tissue infection: study in rats. Radiology 227(1): 169-174

**Katayama Y, Ito T, Hiramatsu K.** 2000. A new class of genetic element, staphylococcus cassette chromosome mec, encodes methicillin resistance in *Staphylococcus aureus*. Antimicrob Agents Chemother. 44(6):1549-55.

**Kehrl JH, Riva A, Wilson GL, Thévenin C.** 1994. Molecular mechanisms regulating CD19, CD20 and CD22 gene expression. Immunol Today. 15(9):432-6.

**Kennedy AD, Otto M, Braughton KR, Whitney AR, Chen L, Mathema B, Mediavilla JR, Byrne KA, Parkins LD, Tenover FC, Kreiswirth BN, Musser JM, DeLeo FR.** 2008. Epidemic community-associated methicillin-resistant *Staphylococcus aureus*: recent clonal expansion and diversification. Proc Natl Acad Sci U S A. 105(4):1327-32. doi: 10.1073/pnas.0710217105. Epub 2008 Jan 23.

**Khatri GS, Sharma R.** May 2005. Expression of recombinant mature lysostaphin. US patent 6,897,041 B1.

**Kielian T, Esen N, Liu S, Phulwani NK, Syed MM, Phillips N, Nishina K, Cheung AL, Schwartzman JD, Ruhe JJ.** 2007. Minocycline modulates neuroinflammation independently of its antimicrobial activity in *staphylococcus aureus*-induced brain abscess. Am J Pathol. 171(4):1199-214. Epub 2007 Aug 23.

**King MD, Humphrey BJ, Wang YF, Kourbatova EV, Ray SM, Blumberg HM.** 2006. Emergence of community-acquired methicillin-resistant *Staphylococcus aureus* USA 300 clone as the predominant cause of skin and soft-tissue infections. Ann Intern Med. 144(5):309-17.

**Kiri N, Archer G, Climo MW.** 2002. Combinations of lysostaphin with beta-lactams are synergistic against oxacillin-resistant *Staphylococcus epidermidis*. Antimicrob Agents Chemother. 46(6):2017-20.



**Klevens RM, Morrison MA, Nadle J, Petit S, Gershman K, Ray S, Harrison LH, Lynfield R, Dumyati G, Townes JM, Craig AS, Zell ER, Fosheim GE, McDougal LK, Carey RB, Fridkin SK; Active Bacterial Core surveillance (ABCs) MRSA Investigators.** 2007. Invasive methicillin-resistant *Staphylococcus aureus* infections in the United States. *JAMA*. 298(15):1763-71.

**Köck R, Becker K, Cookson B, van Gemert-Pijnen JE, Harbarth S, Kluytmans J, Mielke M, Peters G, Skov RL, Struelens MJ, Tacconelli E, Navarro Torné A, Witte W, Friedrich AW.** 2010. Methicillin-resistant *Staphylococcus aureus* (MRSA): burden of disease and control challenges in Europe. *Euro Surveill*. 15(41):19688.

**Köck R, Mellmann A, Schaumburg F, Friedrich AW, Kipp F, Becker K.** 2011. The epidemiology of methicillin-resistant *Staphylococcus aureus* (MRSA) in Germany. *Dtsch Arztebl Int*. 108(45):761-7. doi: 10.3238/arztebl.2011.0761. Epub 2011 Nov 4.

**Kolata G.** 2013. Mice Fall Short as Test Subjects for Some of Humans' Deadly Ills. *The New York Times*. 2013 Feb 2011. <http://www.nytimes.com/2013/02/12/science/testing-of-some-deadly-diseases-on-mice-mislead-report-says.html?emc=eta1& r=1&>

**Kokai-Kun JF, Chanturiya T, Mond JJ.** 2007. Lysostaphin as a treatment for systemic *Staphylococcus aureus* infection in a mouse model. *J Antimicrob Chemother*. 60:1051-1059.

**Kokai-Kun JF, Chanturiya T, Mond JJ.** 2009. Lysostaphin eradicates established *Staphylococcus aureus* biofilms in jugular vein catheterized mice. *J Antimicrob Chemother*. 64:94-100.

**Koplow DA.** 2003. Smallpox: the fight to eradicate a global scourge. Berkeley: University of California Press. ISBN 0-520-24220-3.

**Kossodo S, Zhang J, Groves K, Cuneo GJ, Handy E, Morin J, Delaney J, Yared W, Rajopadhye M, Peterson JD.** 2011. Noninvasive in vivo quantification of neutrophil elastase activity in acute experimental mouse lung injury. *Int J Mol Imaging*. 2011:581406. doi: 10.1155/2011/581406. Epub 2011 Sep 18.

**Kretschmer D, Gleske AK, Rautenberg M, Wang R, Köberle M, Bohn E, Schöneberg T, Rabiet MJ, Boulay F, Klebanoff SJ, van Kessel KA, van Strijp JA, Otto M, Peschel A.** 2010. Human formyl peptide receptor 2 senses highly pathogenic *Staphylococcus aureus*. *Cell Host Microbe*. 7(6):463-73. doi: 10.1016/j.chom.2010.05.012.

**Kroese FG, Opstelten D, Wubbena AS, Deenen GJ, Aten J, Schwander EH, de Leij L, Nieuwenhuis P.** 1985. Monoclonal antibodies to rat B lymphocyte (sub-)populations. *Adv Exp Med Biol*. 186:81-9.

**Kuklin NA, Pancari GD, Tobery TW, Cope L, Jackson J, Gill C, Overbye K, Francis KP, Yu J, Montgomery D, Anderson AS, McClements W, Jansen KU.** 2003. Real-time monitoring of bacterial infection in vivo: development of bioluminescent staphylococcal foreign-body and deep-thigh-wound mouse infection models. *Antimicrob Agents Chemother*. 47(9):2740-8.

- Ladhani S.** 2003. Understanding the mechanism of action of the exfoliative toxins of *Staphylococcus aureus*. FEMS Immunol Med Microbiol. 39(2):181-9.
- Langley R, Patel D, Jackson N, Clow F, Fraser JD.** 2010. Staphylococcal superantigen superdomains in immune evasion. Crit Rev Immunol. 30(2):149-65.
- LaPlante KL, Leonard SN, Andes DR, Craig WA, Rybak MJ.** 2008. Activities of clindamycin, daptomycin, doxycycline, linezolid, trimethoprim-sulfamethoxazole, and vancomycin against community-associated methicillin-resistant *Staphylococcus aureus* with inducible clindamycin resistance in murine thigh infection and in vitro pharmacodynamic models. Antimicrob Agents Chemother. 52(6):2156-62. Epub 2008 Apr 14.
- Lasa I, Penadés JR.** 2006. Bap: a family of surface proteins involved in biofilm formation. Res Microbiol. 157(2):99-107. Epub 2005 Dec 27.
- Lau D, Mollnau H, Eiserich JP, Freeman BA, Daiber A, Gehling UM, Brümmer J, Rudolph V, Münzel T, Heitzer T, Meinertz T, Baldus S.** 2005. Myeloperoxidase mediates neutrophil activation by association with CD11b/CD18 integrins. Proc Natl Acad Sci U S A. 102(2):431-6. Epub 2004 Dec 29.
- Ledbetter JA, Herzenberg LA.** 1979. Xenogeneic monoclonal antibodies to mouse lymphoid differentiation antigens. Immunol Rev. 1979;47:63-90.
- Leevy WM, Gammon ST, Jiang H, Johnson JR, Maxwell DJ, Jackson EN, Marquez M, Piwnica-Worms D, Smith BD.** 2006. Optical imaging of bacterial infection in living mice using a fluorescent near-infrared molecular probe. J Am Chem Soc. 128(51):16476-7.
- Leibovici L.** 1995. Bacteraemia in the very old. Features and treatment. Drugs Aging. 6(6):456-64.
- Lietzau S, Stürmer T, Erb A, Von Baum H, Marre R, Brenner H.** 2004. Prevalence and determinants of nasal colonization with antibiotic-resistant *Staphylococcus aureus* among unselected patients attending general practitioners in Germany. Epidemiol Infect. 132(4):655-62.
- Lorenz U, Hüttinger C, Schäfer T, Ziebuhr W, Thiede A, Hacker J, Engelmann S, Hecker M, Ohlsen K.** 2008 The alternative sigma factor sigma B of *Staphylococcus aureus* modulates virulence in experimental central venous catheter-related infections. Microbes Infect. 10:217-223.
- Love C, Tomas MB, Tronco GG, Palestro CJ.** 2005. FDG PET of infection and inflammation. Radiographics. 25(5):1357-68.
- Lowy FD.** 1998. *Staphylococcus aureus* infections. N Engl J Med. 339(8):520-32.

- Lutz AM, Weishaupt D, Persohn E, Goepfert K, Froehlich J, Sasse B, Gottschalk J, Marincek B, Kaim AH.** 2005. Imaging of macrophages in soft-tissue infection in rats: relationship between ultrasmall superparamagnetic iron oxide dose and MR signal characteristics. *Radiology*. 234(3):765-75. Epub 2005 Jan 21.
- Marzola P, Nicolato E, Di Modugno E, Cristofori P, Lanzoni A, Ladel CH, Sbarbati A.** 1999. Comparison between MRI, microbiology and histology in evaluation of antibiotics in a murine model of thigh infection. *MAGMA*. 9(1-2):21-8.
- Masihi KN.** 2000. Immunomodulators in infectious diseases: panoply of possibilities. *Int J Immunopharmacol*. 22(12):1083-91.
- McCaig LF, McDonald LC, Mandal S, Jernigan DB.** 2006. *Staphylococcus aureus*-associated skin and soft tissue infections in ambulatory care. *Emerg Infect Dis*. 12(11):1715-23.
- Meighen EA.** 1993. Bacterial bioluminescence: organization, regulation, and application of the lux genes. *FASEB J*. 7(11):1016-22.
- Meka VG, Pillai SK, Sakoulas G, Wennersten C, Venkataraman L, DeGirolami PC, Eliopoulos GM, Moellering RC Jr, Gold HS.** 2004. Linezolid resistance in sequential *Staphylococcus aureus* isolates associated with a T2500A mutation in the 23S rRNA gene and loss of a single copy of rRNA. *J Infect Dis*. 190(2):311-7. Epub 2004 Jun 9.
- Merino N, Toledo-Arana A, Vergara-Irigaray M, Valle J, Solano C, Calvo E, Lopez JA, Foster TJ, Penadés JR, Lasa I.** 2009. Protein A-mediated multicellular behavior in *Staphylococcus aureus*. *J Bacteriol*. 191(3):832-43. doi: 10.1128/JB.01222-08. Epub 2008 Dec 1.
- Moise PA, Sakoulas G, Forrest A, Schentag JJ.** 2007. Vancomycin in vitro bactericidal activity and its relationship to efficacy in clearance of methicillin-resistant *Staphylococcus aureus* bacteremia. *Antimicrob Agents Chemother*. 51(7):2582-6. Epub 2007 Apr 23.
- Mookherjee N, Rehaume LM, Hancock RE.** 2007. Cathelicidins and functional analogues as antiseptics molecules. *Expert Opin Ther Targets*. 11(8):993-1004.
- Montoya M, Gouaux E.** 2003. Beta-barrel membrane protein folding and structure viewed through the lens of alpha-hemolysin. *Biochim Biophys Acta*. 1609(1):19-27.
- Moore LJ, Pridmore AC, Dower SK, Read RC.** 2004. The glycopeptide vancomycin does not enhance toll-like receptor 2 (TLR2) activation by *Streptococcus pneumoniae*. *J Antimicrob Chemother*. 54(1):76-8. Epub 2004 Jun 9.
- Moore LJ, Gilbey AM, Dowson CG, Pridmore AC, Dower SK, Read RC.** 2007. Proinflammatory activation of Toll-like receptor-2 during exposure of penicillin-resistant *Streptococcus pneumoniae* to beta-lactam antibiotics. *J Antimicrob Chemother*. 59(1):35-42. Epub 2006 Oct 31.

**Morales G, Picazo JJ, Baos E, Candel FJ, Arribi A, Peláez B, Andrade R, de la Torre MA, Fereres J, Sánchez-García M.** 2010. Resistance to linezolid is mediated by the *cfr* gene in the first report of an outbreak of linezolid-resistant *Staphylococcus aureus*. *Clin Infect Dis*. 50(6):821-5. doi: 10.1086/650574.

**Morikawa K, Takemura AJ, Inose Y, Tsai M, Nguyen Thi le T, Ohta T, Msadek T.** 2012. Expression of a cryptic secondary sigma factor gene unveils natural competence for DNA transformation in *Staphylococcus aureus*. *PLoS Pathog*. 8(11):e1003003. doi: 10.1371/journal.ppat.1003003. Epub 2012 Nov 1.

**Murphy SL, Xu J, Kochanek KD.** 2013. Deaths: Final Data for 2010. *National Vital Statistics Reports*, Vol. 61, No. 4, May 8, 2013

**Nau R, Eiffert H.** 2005. Minimizing the release of proinflammatory and toxic bacterial products within the host: a promising approach to improve outcome in life-threatening infections. *FEMS Immunol Med Microbiol*. 44:1-16.

**Nijnik A, Madera L, Ma S, Waldbrook M, Elliott MR, Easton DM, Mayer ML, Mullaly SC, Kindrachuk J, Jenssen H, Hancock RE.** 2010. Synthetic cationic peptide IDR-1002 provides protection against bacterial infections through chemokine induction and enhanced leukocyte recruitment. *J Immunol*. 184(5):2539-50. doi: 10.4049/jimmunol.0901813. Epub 2010 Jan 27.

**Niska JA, Meganck JA, Pribaz JR, Shahbazian JH, Lim E, Zhang N, Rice BW, Akin A, Ramos RI, Bernthal NM, Francis KP, Miller LS.** 2012. Monitoring bacterial burden, inflammation and bone damage longitudinally using optical and  $\mu$ CT imaging in an orthopaedic implant infection in mice. *PLoS One*. 7(10):e47397. doi: 10.1371/journal.pone.0047397. Epub 2012 Oct 17.

**Oesterreich B, Lorenz B, Schmitter T, Kontermann R, Zenn M, Zimmermann B, Haake M, Lorenz U, Ohlsen K.** 2014. Characterization of the biological anti-staphylococcal functionality of hUK-66 IgG1, a humanized monoclonal antibody as substantial component for an immunotherapeutic approach. *Hum Vaccin Immunother*. 2014 Feb 4;10(4). [Epub ahead of print]

**Oeppen J, Vaupel JW.** 2002. Demography. Broken limits to life expectancy. *Science*. 296(5570):1029-31.

**Ohlsen K, Dandekar G, Schwarz R, Dandekar T.** 2008. New trends in pharmacogenomic strategies against resistance development in microbial infections. *Pharmacogenomics*. 9(11):1711-23. doi: 10.2217/14622416.9.11.1711.

**Ohlsen K, Lorenz U.** 2010. Immunotherapeutic strategies to combat staphylococcal infections. *Int J Med Microbiol*. 300(6):402-10. doi: 10.1016/j.ijmm.2010.04.015. Epub 2010 May 23.

**Oldham ER, Daley MJ.** 1991. Lysostaphin: use of a recombinant bactericidal enzyme as a mastitis therapeutic. *J Dairy Sci.* 74(12):4175-82.

**O'Neill E, Pozzi C, Houston P, Smyth D, Humphreys H, Robinson DA, O'Gara JP.** 2007. Association between methicillin susceptibility and biofilm regulation in *Staphylococcus aureus* isolates from device-related infections. *J Clin Microbiol.* 45(5):1379-88. Epub 2007 Feb 28.

**Pantosti A, Sanchini A, Monaco M.** 2007. Mechanisms of antibiotic resistance in *Staphylococcus aureus*. *Future Microbiol.* 2(3):323-34.

**Parcina M, Wendt C, Goetz F, Zawatzky R, Zähringer U, Heeg K, Bekeredjian-Ding I.** 2008. *Staphylococcus aureus*-induced plasmacytoid dendritic cell activation is based on an IgG-mediated memory response. *J Immunol.* 181(6):3823-33.

**Parcina M, Miranda-Garcia MA, Durlanik S, Ziegler S, Over B, Georg P, Foermer S, Ammann S, Hilmi D, Weber KJ, Schiller M, Heeg K, Schneider-Brachert W, Götz F, Bekeredjian-Ding I.** 2013. Pathogen-triggered activation of plasmacytoid dendritic cells induces IL-10-producing B cells in response to *Staphylococcus aureus*. *J Immunol.* 190(4):1591-602. doi: 10.4049/jimmunol.1201222. Epub 2013 Jan 16.

**Parisien A, Allain B, Zhang J, Mandeville R, Lan CQ.** 2008. Novel alternatives to antibiotics: bacteriophages, bacterial cell wall hydrolases, and antimicrobial peptides. *J Appl Microbiol.* 104(1):1-13. doi: 10.1111/j.1365-2672.2007.03498.x.

**Partlow KC, Chen J, Brant JA, Neubauer AM, Meyerrose TE, Creer MH, Nolte JA, Caruthers SD, Lanza GM, Wickline SA.** 2007. <sup>19</sup>F magnetic resonance imaging for stem/progenitor cell tracking with multiple unique perfluorocarbon nanobeacons. *FASEB J.* 21(8):1647-54. Epub 2007 Feb 6.

**Patron RL, Climo MW, Goldstein BP, Archer GL.** 1999. Lysostaphin treatment of experimental aortic valve endocarditis caused by a *Staphylococcus aureus* isolate with reduced susceptibility to vancomycin. *Antimicrob Agents Chemother.* 43:1754-1755.

**Peschel A, Otto M, Jack RW, Kalbacher H, Jung G, Götz F.** 1999. Inactivation of the *dlt* operon in *Staphylococcus aureus* confers sensitivity to defensins, protegrins, and other antimicrobial peptides. *J Biol Chem.* 274(13):8405-10.

**Peschel A, Jack RW, Otto M, Collins LV, Staubitz P, Nicholson G, Kalbacher H, Nieuwenhuizen WF, Jung G, Tarkowski A, van Kessel KP, van Strijp JA.** 2001. *Staphylococcus aureus* resistance to human defensins and evasion of neutrophil killing via the novel virulence factor MprF is based on modification of membrane lipids with L-lysine. *J Exp Med.* 193(9):1067-76.

**Pirofski LA, Casadevall A.** 2006. Immunomodulators as an antimicrobial tool. *Curr Opin Microbiol.* 9(5):489-95. Epub 2006 Aug 22.

- Polak J, Della Latta P, Blackburn P.** 1993. In vitro activity of recombinant lysostaphin-antibiotic combinations toward methicillin-resistant *Staphylococcus aureus*. *Diagn Microbiol Infect Dis.* 17(4):265-70.
- Prat C, Bestebroer J, de Haas CJ, van Strijp JA, van Kessel KP.** 2006. A new staphylococcal anti-inflammatory protein that antagonizes the formyl peptide receptor-like 1. *J Immunol.* 177(11):8017-26.
- Prat C, Haas PJ, Bestebroer J, de Haas CJ, van Strijp JA, van Kessel KP.** 2009. A homolog of formyl peptide receptor-like 1 (FPRL1) inhibitor from *Staphylococcus aureus* (FPRL1 inhibitory protein) that inhibits FPRL1 and FPR. *J Immunol.* 183(10):6569-78. doi: 10.4049/jimmunol.0801523. Epub 2009 Oct 21.
- Preziosi P.** 2004. Science, pharmacoeconomics and ethics in drug R&D: a sustainable future scenario? *Nat Rev Drug Discov.* 3(6):521-6.
- Proctor RA.** 2012a. Is there a future for a *Staphylococcus aureus* vaccine? *Vaccine.* 30(19):2921-7. doi: 10.1016/j.vaccine.2011.11.006. Epub 2011 Nov 21.
- Proctor RA.** 2012b. Challenges for a universal *Staphylococcus aureus* vaccine. *Clin Infect Dis.* 54(8):1179-86. doi: 10.1093/cid/cis033. Epub 2012 Feb 21.
- Projan SJ.** 2003. Why is big Pharma getting out of antibacterial drug discovery? *Curr Opin Microbiol.* 6(5):427-30.
- Projan SJ, Nesin M, Dunman PM.** 2006. Staphylococcal vaccines and immunotherapy: to dream the impossible dream? *Curr Opin Pharmacol.* 6(5):473-9. Epub 2006 Jul 25.
- Prokesová L, Potuzníková B, Potempa J, Zikán J, Radl J, Porwit-Bóbr Z, John C.** 1995. Cleavage of human immunoglobulins by proteinase from *Staphylococcus aureus*. *Adv Exp Med Biol.* 371A:613-6.
- Quickel KE Jr, Selden R, Caldwell JR, Nora NF, Schaffner W.** 1971. Efficacy and safety of topical lysostaphin treatment of persistent nasal carriage of *Staphylococcus aureus*. *Appl Microbiol.* 22:446-450.
- Rahman S, Manuel SL, Khan ZK, Wigdahl B, Acheampong E, Tangy F, Jain P.** 2010. Depletion of dendritic cells enhances susceptibility to cell-free infection of human T cell leukemia virus type 1 in CD11c-diphtheria toxin receptor transgenic mice. *J Immunol.* 184(10):5553-61. doi: 10.4049/jimmunol.0903226. Epub 2010 Apr 9.
- Reacher MH, Shah A, Livermore DM, Wale MC, Graham C, Johnson AP, Heine H, Monnickendam MA, Barker KF, James D, George RC.** 2000. Bacteraemia and antibiotic resistance of its pathogens reported in England and Wales between 1990 and 1998: trend analysis. *BMJ.* 320(7229):213-6.

**Richards MJ, Edwards JR, Culver DH, Gaynes RP.** 2000. Nosocomial infections in combined medical-surgical intensive care units in the United States. *Infect Control Hosp Epidemiol.* 21:510-515.

**Rocchetta HL, Boylan CJ, Foley JW, Iversen PW, LeTourneau DL, McMillian CL, Contag PR, Jenkins DE, Parr TR Jr.** 2001. Validation of a noninvasive, real-time imaging technology using bioluminescent *Escherichia coli* in the neutropenic mouse thigh model of infection. *Antimicrob Agents Chemother.* 45(1):129-37.

**Rossney AS, Shore AC, Morgan PM, Fitzgibbon MM, O'Connell B, Coleman DC.** 2007. The emergence and importation of diverse genotypes of methicillin-resistant *Staphylococcus aureus* (MRSA) harboring the Panton-Valentine leukocidin gene (pvl) reveal that pvl is a poor marker for community-acquired MRSA strains in Ireland. *J Clin Microbiol.* 45(8):2554-63. Epub 2007 Jun 20.

**Sakoulas G, Moise-Broder PA, Schentag J, Forrest A, Moellering RC Jr, Eliopoulos GM.** 2004. Relationship of MIC and bactericidal activity to efficacy of vancomycin for treatment of methicillin-resistant *Staphylococcus aureus* bacteremia. *J Clin Microbiol.* 42(6):2398-402.

**Sakoulas G, Moellering RC Jr.** 2008. Increasing antibiotic resistance among methicillin-resistant *Staphylococcus aureus* strains. *Clin Infect Dis.* 46 Suppl 5:S360-7. doi: 10.1086/533592.

**Sandanaraj BS, Kneuer R, Beckmann N.** 2010. Optical and magnetic resonance imaging as complementary modalities in drug discovery. *Future Med Chem.* 2(3):317-37.

**Savage VJ, Chopra I, O'Neill AJ.** 2013. *Staphylococcus aureus* biofilms promote horizontal transfer of antibiotic resistance. *Antimicrob Agents Chemother.* 57(4):1968-70. doi: 10.1128/AAC.02008-12. Epub 2013 Jan 28.

**Schaffner W, Melly MA, Koenig MG.** 1967. Lysostaphin: an enzymatic approach to staphylococcal disease. II. In vivo studies. *Yale J Biol Med.* 39:230-244.

**Schaumburg F, Köck R, Mellmann A, Richter L, Hasenberg F, Kriegeskorte A, Friedrich AW, Gatermann S, Peters G, von Eiff C, Becker K; study group.** 2012. Population dynamics among methicillin-resistant *Staphylococcus aureus* isolates in Germany during a 6-year period. *J Clin Microbiol.* 50(10):3186-92. doi: 10.1128/JCM.01174-12. Epub 2012 Jul 18.

**Schaumburg F, Idelevich EA, Peters G, Mellmann A, von Eiff C, Becker K; Study Group.** 2013. Trends in antimicrobial non-susceptibility in methicillin-resistant *Staphylococcus aureus* from Germany (2004-2011). *Clin Microbiol Infect.* 2013 Dec 27. doi: 10.1111/1469-0691.12519. [Epub ahead of print]

**Schindler CA, Schuhardt VT.** 1964. Lysostaphin: a new bacteriolytic agent for *Staphylococcus*. *Proc Natl Acad Sci U S A.* 51:414-421.

**Schindler CA.** 1966. Staphylococcal strains with relation to lysostaphin sensitivity. *Nature*. 209(5030):1368-9.

**ScienceDaily.** 2008 How Poxviruses Such As Smallpox Evade The Immune System, ScienceDaily, February 1, 2008

**Scott MG, Dullaghan E, Mookherjee N, Glavas N, Waldbrook M, Thompson A, Wang A, Lee K, Doria S, Hamill P, Yu JJ, Li Y, Donini O, Guarna MM, Finlay BB, North JR, Hancock RE.** 2007. An anti-infective peptide that selectively modulates the innate immune response. *Nat Biotechnol*. 25(4):465-72. Epub 2007 Mar 25.

**Schymeinsky J, Mócsai A, Walzog B.** 2007. Neutrophil activation via beta2 integrins (CD11/CD18): molecular mechanisms and clinical implications. *Thromb Haemost*. 98(2):262-73.

**Seale A, Finn A.** 2011. What is the best way to use conjugate vaccines? *Curr Opin Infect Dis*. 2011 Jun;24(3):219-24. doi: 10.1097/QCO.0b013e3283468996.

**Seok J, Warren HS, Cuenca AG, Mindrinos MN, Baker HV, Xu W, Richards DR, McDonald-Smith GP, Gao H, Hennessy L, Finnerty CC, López CM, Honari S, Moore EE, Minei JP, Cuschieri J, Bankey PE, Johnson JL, Sperry J, Nathens AB, Billiar TR, West MA, Jeschke MG, Klein MB, Gamelli RL, Gibran NS, Brownstein BH, Miller-Graziano C, Calvano SE, Mason PH, Cobb JP, Rahme LG, Lowry SF, Maier RV, Moldawer LL, Herndon DN, Davis RW, Xiao W, Tompkins RG; Inflammation and Host Response to Injury, Large Scale Collaborative Research Program.** 2013. Genomic responses in mouse models poorly mimic human inflammatory diseases. *Proc Natl Acad Sci U S A*. 110(9):3507-12. doi: 10.1073/pnas.1222878110. Epub 2013 Feb 11.

**Seybold U, Kourbatova EV, Johnson JG, Halvosa SJ, Wang YF, King MD, Ray SM, Blumberg HM.** 2006. Emergence of community-associated methicillin-resistant *Staphylococcus aureus* USA300 genotype as a major cause of health care-associated blood stream infections. *Clin Infect Dis*. 42(5):647-56. Epub 2006 Jan 25.

**Shaw, WH.** 2001. Cost and benefits of inflicting pain. *Nature* 414, 396–397 (2001).

**Sieprawska-Lupa M, Mydel P, Krawczyk K, Wójcik K, Puklo M, Lupa B, Suder P, Silberring J, Reed M, Pohl J, Shafer W, McAleese F, Foster T, Travis J, Potempa J.** 2004. Degradation of human antimicrobial peptide LL-37 by *Staphylococcus aureus*-derived proteinases. *Antimicrob Agents Chemother*. 48(12):4673-9.

**Sijbers J, den Dekker AJ, Raman E, Van Dyck D.** 1999. Parameter Estimation from Magnitude MR Images. *International Journal of imaging systems and technology* 10: 109–114



- Singh-Jasuja H, Thiolat A, Ribon M, Boissier MC, Bessis N, Rammensee HG, Decker P.** 2013. The mouse dendritic cell marker CD11c is down-regulated upon cell activation through Toll-like receptor triggering. *Immunobiology*. 218(1):28-39. doi: 10.1016/j.imbio.2012.01.021. Epub 2012 Feb 21.
- Sinha B, Francois P, Que YA, Hussain M, Heilmann C, Moreillon P, Lew D, Krause KH, Peters G, Herrmann M.** 2000. Heterologously expressed *Staphylococcus aureus* fibronectin-binding proteins are sufficient for invasion of host cells. *Infect Immun*. 68(12):6871-8.
- Sloan GL, Smith EC, Lancaster JH.** 1977. Lysostaphin endopeptidase-catalysed transpeptidation reactions of the imino-transfer type. *Biochem J*. 167:293-296.
- Smith EJ, Visai L, Kerrigan SW, Speziale P, Foster TJ.** 2011. The Sbi protein is a multifunctional immune evasion factor of *Staphylococcus aureus*. *Infect Immun*. 79(9):3801-9. doi: 10.1128/IAI.05075-11. Epub 2011 Jun 27.
- J. Snider, M. Rapids, B. Rivard.** 2012. Methicillin-resistant *Staphylococcus aureus*: a review of current antibiotic therapy. Spectrum Health Grand Rapids, 2012.
- Southworth R, Kaneda M, Chen J, Zhang L, Zhang H, Yang X, Razavi R, Lanza G, Wickline SA.** 2009. Renal vascular inflammation induced by Western diet in ApoE-null mice quantified by (19)F NMR of VCAM-1 targeted nanobeacons. *Nanomedicine*. 5(3):359-67. doi: 10.1016/j.nano.2008.12.002. Epub 2009 Jan 19.
- Spellberg B, Powers JH, Brass EP, Miller LG, Edwards JE Jr.** 2004. Trends in antimicrobial drug development: implications for the future. *Clin Infect Dis*. 2004 May 1;38(9):1279-86. Epub 2004 Apr 14.
- Spellberg B, Daum R.** 2012. Development of a vaccine against *Staphylococcus aureus*. *Semin Immunopathol*. 34(2):335-48. doi: 10.1007/s00281-011-0293-5. Epub 2011 Nov 14.
- Stark FR, Thornsvarð C, Flannery EP, Artenstein MS.** 1974. Systemic lysostaphin in man--apparent antimicrobial activity in a neutropenic patient. *N Engl J Med*. 291:239-240.
- Steinhuber A, Landmann R, Goerke C, Wolz C, Flückiger U.** 2008. Bioluminescence imaging to study the promoter activity of hla of *Staphylococcus aureus* in vitro and in vivo. *Int J Med Microbiol*. 298(7-8):599-605. doi: 10.1016/j.ijmm.2007.09.008. Epub 2008 Mar 7.
- Strauss A, Thumm G, Götz F.** 1998. Influence of Lif, the lysostaphin immunity factor, on acceptors of surface proteins and cell wall sorting efficiency in *Staphylococcus carnosus*. *J Bacteriol*. 180:4960-4962.
- Stryjewski ME, Corey GR.** 2014. Methicillin-resistant *Staphylococcus aureus*: an evolving pathogen. *Clin Infect Dis*. 58 Suppl 1:S10-9. doi: 10.1093/cid/cit613.

- Stuertz K, Schmidt H, Eiffert H, Schwartz P, Mäder M, Nau R.** 1998. Differential release of lipoteichoic and teichoic acids from *Streptococcus pneumoniae* as a result of exposure to beta-lactam antibiotics, rifamycins, trovafloxacin, and quinupristin-dalfopristin. *Antimicrob Agents Chemother.* 42(2):277-81.
- Talan DA, Krishnadasan A, Gorwitz RJ, Fosheim GE, Limbago B, Albrecht V, Moran GJ; EMERGENCY ID Net Study Group.** 2011. Comparison of *Staphylococcus aureus* from skin and soft-tissue infections in US emergency department patients, 2004 and 2008. *Clin Infect Dis.* 53(2):144-9. doi: 10.1093/cid/cir308.
- Tang JS, Gold RH, Bassett LW, Seeger LL.** 1988. Musculoskeletal infection of the extremities: evaluation with MR imaging. *Radiology.* 166(1 Pt 1):205-9.
- Tauber SC, Nau R.** 2008. Immunomodulatory properties of antibiotics. *Curr Mol Pharmacol.* 1(1):68-79.
- Temme S, Jacoby C, Ding Z, Bönner F, Borg N, Schrader J, Flögel U.** 2013. Technical Advance: Monitoring the trafficking of neutrophil granulocytes and monocytes during the course of tissue inflammation by noninvasive <sup>19</sup>F MRI. *J Leukoc Biol.* 2013 Dec 6. [Epub ahead of print]
- Thakker M, Park JS, Carey V, Lee JC.** 1998. *Staphylococcus aureus* serotype 5 capsular polysaccharide is antiphagocytic and enhances bacterial virulence in a murine bacteremia model. *Infect Immun.* 66(11):5183-9.
- Theuretzbacher U.** 2009. Future antibiotics scenarios: is the tide starting to turn? *Int J Antimicrob Agents.* 34(1):15-20. doi: 10.1016/j.ijantimicag.2009.02.005. Epub 2009 Apr 1.
- Theuretzbacher U.** 2012. Accelerating resistance, inadequate antibacterial drug pipelines and international responses. *Int J Antimicrob Agents.* 39(4):295-9. doi: 10.1016/j.ijantimicag.2011.12.006. Epub 2012 Feb 14.
- The World 120 Health Report 2004.** 2004. Annex Table 2: Deaths by cause, sex and mortality stratum in WHO regions, a estimates for 2002.
- Thomson CJ, Power E, Ruebsamen-Waigmann H, Labischinski H.** 2004. Antibacterial research and development in the 21(st) Century--an industry perspective of the challenges. *Curr Opin Microbiol.* 7(5):445-50.
- Thumm G, Götz F.** 1997. Studies on prolystaphin processing and characterization of the lysostaphin immunity factor (Lif) of *Staphylococcus simulans* biovar *staphylolyticus*. *Mol Microbiol.* 23:1251-1265.
- Tschierske M, Ehlert K, Strandén AM, Berger-Bächli B.** 1997. Lif, the lysostaphin immunity factor, complements FemB in staphylococcal peptidoglycan interpeptide bridge formation. *FEMS Microbiol Lett.* 153:261-264.

**Tseng JC, Kung AL.** 2013. In vivo imaging method to distinguish acute and chronic inflammation. *J Vis Exp.* 78. doi: 10.3791/50690.

**van Langevelde P, van Dissel JT, Ravensbergen E, Appelmelk BJ, Schrijver IA, Groeneveld PH.** 1998. Antibiotic-induced release of lipoteichoic acid and peptidoglycan from *Staphylococcus aureus*: quantitative measurements and biological reactivities. *Antimicrob Agents Chemother.* 42:3073-8.

**van Langevelde P, Ravensbergen E, Grashoff P, Beekhuizen H, Groeneveld PH, van Dissel JT.** 1999. Antibiotic-induced cell wall fragments of *Staphylococcus aureus* increase endothelial chemokine secretion and adhesiveness for granulocytes. *Antimicrob Agents Chemother.* 43:2984-9.

**Verkaik NJ, van Wamel WJ, van Belkum A.** 2011. Immunotherapeutic approaches against *Staphylococcus aureus*. *Immunotherapy.* 3(9):1063-73. doi: 10.2217/imt.11.84.

**Voyich JM, Braughton KR, Sturdevant DE, Whitney AR, Saïd-Salim B, Porcella SF, Long RD, Dorward DW, Gardner DJ, Kreiswirth BN, Musser JM, DeLeo FR.** 2005. Insights into mechanisms used by *Staphylococcus aureus* to avoid destruction by human neutrophils. *J Immunol.* 175(6):3907-19.

**Wang J, Maurer L.** 2005. Positron Emission Tomography: applications in drug discovery and drug development. *Curr Top Med Chem.* 5(11):1053-75.

**Wang R, Braughton KR, Kretschmer D, Bach TH, Queck SY, Li M, Kennedy AD, Dorward DW, Klebanoff SJ, Peschel A, DeLeo FR, Otto M.** 2007. Identification of novel cytolytic peptides as key virulence determinants for community-associated MRSA. *Nat Med.* 13(12):1510-4. Epub 2007 Nov 11.

**Wanner M.** 2013. Why mice may succeed in research when a single mouse falls short. [http://community.jax.org/genetics\\_health/b/weblog/archive/2013/02/13/why-mice-may-succeed-in-research-when-a-single-mouse-falls-short.aspx](http://community.jax.org/genetics_health/b/weblog/archive/2013/02/13/why-mice-may-succeed-in-research-when-a-single-mouse-falls-short.aspx)

**Willmann JK, van Bruggen N, Dinkelborg LM, Gambhir SS.** 2008. Molecular imaging in drug development. *Nat Rev Drug Discov.* 7(7):591-607. doi: 10.1038/nrd2290.

**Winston R.** 2013. Animal experiments deserve a place on drug labels. *Nat Med.* 19(10):1204. doi: 10.1038/nm1013-1204.

**Winter PM, Caruthers SD, Kassner A, Harris TD, Chinen LK, Allen JS, Lacy EK, Zhang H, Robertson JD, Wickline SA, Lanza GM.** 2003. Molecular imaging of angiogenesis in nascent Vx-2 rabbit tumors using a novel alpha(nu)beta3-targeted nanoparticle and 1.5 tesla magnetic resonance imaging. *Cancer Res.* 63(18):5838-43.

**Xiong YQ, Willard J, Kadurugamuwa JL, Yu J, Francis KP, Bayer AS.** 2005. Real-time in vivo bioluminescent imaging for evaluating the efficacy of antibiotics in a rat *Staphylococcus aureus* endocarditis model. *Antimicrob Agents Chemother.* 49(1):380-7.

- Xu SX, McCormick JK.** 2012. Staphylococcal superantigens in colonization and disease. *Front Cell Infect Microbiol.* 2:52. doi: 10.3389/fcimb.2012.00052. eCollection 2012.
- Yoshikawa TT.** 2000. Epidemiology and unique aspects of aging and infectious diseases. *Clin Infect Dis.* 30(6):931-3. Epub 2000 Jun 30.
- Yoshikawa TT.** 2002. Antimicrobial resistance and aging: beginning of the end of the antibiotic era? *J Am Geriatr Soc.* 50(7 Suppl):S226-9.
- Zhang X, Goncalves R, Mosser DM.** 2008. The isolation and characterization of murine macrophages. *Curr Protoc Immunol.* Chapter 14:Unit 14.1. doi: 10.1002/0471142735.im1401s83.
- Zhu J, Yamane H, Paul WE.** 2010. Differentiation of effector CD4 T cell populations (\*). *Annu Rev Immunol.* 28:445-89. doi: 10.1146/annurev-immunol-030409-101212.
- Zipfel PF, Skerka C.** 2009. Complement regulators and inhibitory proteins. *Nat Rev Immunol.* 9(10):729-40. doi: 10.1038/nri2620. Epub 2009 Sep 4.
- Zipfel PF, Skerka C.** 2013. *Staphylococcus aureus*: The multi headed hydra resists and controls human complement response in multiple ways. *Int J Med Microbiol.* 2013 Dec 1. pii: S1438-4221(13)00177-X. doi: 10.1016/j.ijmm.2013.11.004. [Epub ahead of print]
- Zygmunt WA, Harrison EF, Browder HP.** 1965. MICROBIOLOGICAL ACTIVITIES OF LYSOSTAPHIN AND PENICILLINS AGAINST BACTERIOPHAGE 80/81 STRAINS OF *STAPHYLOCOCCUS AUREUS*. *Appl Microbiol.* 13:491-3.



## Curriculum Vitae

**Full name:** Tobias Hertlein

### Education

Since 2008, August **Doctoral thesis:** "Visualization of *Staphylococcus aureus* infections and antibiotic therapy by bioluminescence and <sup>19</sup>F magnetic resonance imaging with perfluorocarbon emulsions"

University of Würzburg, Germany

Institute for Molecular Infection Biology

in the lab of PD Dr. Knut Ohlsen

2008, May **"Diplom Biologie"**

University of Würzburg, Germany

Diploma thesis in the lab of Prof. Dr. Joachim Morschhäuser

"Funktionale Analyse von Peptidtransportern in *Candida albicans*"

2002 – 2008 **program of study: "Biologie"**

University of Würzburg, Germany

2001, June **Abitur**

Simon-Marius-Gymnasium, Gunzenhausen, Germany

## Presentations (Selection)

T. Hertlein, V. Sturm, T. Basse-Lüsebrink, D. Haddad, K.Ohlsen, P.Jakob. 2010. In vivo monitoring of bacterial infections using high-field MRI. Poster presented at the 3<sup>rd</sup> ‚Gemeinsame Tagung der DGHM und VAAM‘ in Hannover, Germany

T. Hertlein, V. Sturm, T. Basse-Lüsebrink, D. Haddad, K.Ohlsen, P.Jakob. 2011. In vivo monitoring of bacterial infections using high-field MRI. Oral and poster presentation at the FEMS-Leopoldina-Symposium “Emerging Topics in Microbial Pathogenesis” in Würzburg, Germany

T. Hertlein, V. Sturm, T. Basse-Lüsebrink, D. Haddad, P.Jakob, K.Ohlsen. 2011. In vivo monitoring of bacterial infections using high-field MRI. Poster presented at the Gordon Research Conference ‘Staphylococcal diseases’ in Il Ciocco Tuscany Resort in Lucca, Italy

T. Hertlein, V. Sturm, T. Basse-Lüsebrink, D. Haddad, P.Jakob, K.Ohlsen. 2012. In vivo monitoring of *Staphylococcus aureus* infections in murine models by BLI and high-field MRI. Poster presented at the World Molecular Imaging Congress 2012 in Dublin, Ireland

T. Hertlein, V. Sturm, T. Basse-Lüsebrink, P.Jakob, K.Ohlsen. 2012. In vivo monitoring of *Staphylococcus aureus* infections by high-field MRI (and BLI). Short talk and poster presentation at the 2<sup>nd</sup> International Conference ‘Pathophysiology of staphylococci in the post-genomic era’ at Kloster Banz, Germany

## Publications

Hertlein T, Sturm V, Kircher S, Basse-Lüsebrink T, Haddad D, Ohlsen K, Jakob P. 2011. Visualization of abscess formation in a murine thigh infection model of *Staphylococcus aureus* by <sup>19</sup>F-magnetic resonance imaging (MRI). PLoS One. 6(3):e18246. doi: 10.1371/journal.pone.0018246.

Hertlein T, Sturm V, Jakob P, Ohlsen K. 2013. <sup>19</sup>F magnetic resonance imaging of perfluorocarbons for the evaluation of response to antibiotic therapy in a *Staphylococcus aureus* infection model. PLoS One. 8(5):e64440. doi: 10.1371/journal.pone.0064440. Print 2013.

Hertlein T, Sturm V, Lorenz U, Sumathy K, Jakob P, Ohlsen K. 2014. Bioluminescence and <sup>19</sup>F magnetic resonance imaging visualize the efficacy of lysostaphin alone and in combination with oxacillin against *Staphylococcus aureus* in murine thigh and catheter-associated infection models. Antimicrob Agents Chemother. 58(3):1630-8. doi: 10.1128/AAC.01422-13. Epub 2013 Dec 23.

